

UNIVERSITÀ DEGLI STUDI DI NAPOLI FEDERICO II

SCHOOL OF DOCTORATE IN INDUSTRIAL ENGINEERING



DOCTORATE IN MECHANICAL SYSTEM ENGINEERING

XXI CYCLE

PHILOSOPHY DOCTORATE THESIS

*Theoretical and experimental analysis of high temperature
solid oxide fuel cells (SOFC)*

ADVISERS

PROF. MASSIMO DENTICE d'ACCADIA

PROF. NIGEL SAMMES

CO-ADVISER

ING. FRANCESCO CALISE

CANDIDATE

GIULIO RESTUCCIA

COORDINATOR OF DOCTORATE

Prof. Raffaele TUCCILLO

Summary

The technology of solid oxide fuel cells (SOFC) at high temperature represents a particularly promising solution in the realization of innovative systems for energetic conversion at high efficiency, in particular for systems destined to the distributed energetic production on small-medium scale.

In such ambit has been carried out a theoretical analysis for the development of a one-dimensional simulation model of a solid oxide fuel cell stack, capable to predict the course and the variation of the main operational parameters of such systems and characterizing the main sources of irreversibility.

At the theoretical analysis has placed side by side an experimentation program on solid oxide fuel cells based on two main topic of search. First of all has been analyzed the global behavior of a cogenerative module of 5 kWe, manufactured by Acumentrics Corporation (Boston, MA - U.S.A.), with the aim to determine the total energetic performances in cogenerative arrangement for domestic applications. Successively the attention has been concentrated on the energetic performances of single tubular SOFC, through a campaign of tests realized on fuel cell of different dimension and manufactured with diverse materials; the activity has been carried out at the Colorado School of Mines in collaboration with the Prof. Nigel Sammes (Editor in Chief of Journal of Fuel Cells Science and Technology).

For the simulation activities, has been built a detailed axial symmetric model at finite volumes applied to a single tubular Solid Oxide Fuel Cell (SOFC) with internal reforming. The model, with relative 1-D discretization, was later extended to other components present within a fuel cell stack: pre-reformer and catalytic combustor placed on the top of the fuel cells bundle.

In developing the simulation model were applied detailed models related to the kinetics of shift, steam methane reforming and post-combustion reactions, the pressure drop, the heat transfer mechanisms, and overvoltage occurring within the fuel cells. The model is capable of analyzing the profiles of temperature, pressure, chemical composition and power within the single fuel cell as inside other components of the stack. This model was developed through the finite volume technique: the control volume was divided into elementary slice, and for each domain were applied mass, energy and moles balances. By implementing the exergetic analysis techniques were unable to identify the source and location of the irreversibility of the various components of the stack.

Unlike the existing paper in literature the model for the heat transfer was greatly improved by introducing the radiative heat exchange mechanism. The results show the great influence that the radiation has for these types of cells (high temperature).

Temperature, pressure, chemical composition, electrical parameters and exergy destroyed were assessed for each discretization domain of the single tubular SOFC and for pre-reformer and post-combustor components. A sensitivity analysis was developed in order to analyze the influence of the main design and operational parameters to the fuel cell performance.

The experimental activity is part of a research program for the establishment of a Fuel Cell Research Centre at the Ges.En. (Gestioni Energetiche) S.p.A. power plant, for conducting experimental campaigns aimed at determining the energetic and exergetic performance of different fuel cell based on different technologies, of different size and fed with different types of fuel (hydrogen, natural gas, biogas, etc.). The program is conducted in collaboration between the DETEC of University of Naples Federico II and the Ges.En. SpA, a company responsible for post-mortem managing of a landfill located in Schiavi Masseria del Pozzo, in the town of Giugliano in Campania (NA).

The Ges.En. S.p.A. owns with the D.I.M.S.A.T. of University of Cassino (Italy) a cogenerative module CP-SOFC-5000, manufactured by Acumentrics Corporation (Boston, MA - USA) and based on solid oxide fuel cell technology. The cogeneration unit is capable of delivering a maximum power of 5 kWe with an electric gross efficiency of around 30-35%. In addition, the module is capable of producing hot water at temperatures ranging 40-50 °C that could be used for cogeneration for domestic application.

In order to conduct experiments on that cogeneration unit, were first acquired fundamental knowledge for the operation of the same module, through a period of training at the Acumentrics Inc. (Boston, MA): in particular have deepened the issues concerning the design of the cell, the manufacturing and assembly processes of the various components, the solutions adopted for reforming and post-combustion processes and the solutions adopted for the module heat balance.

The module is also equipped with a DSP (Digital Signal Process) that acquire the signals from instruments placed on board of the unit and automatically adjust the operation during changes in electric load drawings.

The real testing program started at the Acumentrics factory, analyzing the various stages that compose the start-up procedure of the cogenerative module, and continued when the fuel cell unit was transferred to the Ges.En. Research Center in the town of Giugliano in Campania (NA), where it was connected to the electrical load line (composed of halogen lamps powered in AC ranging between 200W and 500W), and to the thermal loads (2 Fancoil fueled by a circuit of water at low temperature). An Ethernet line allows the remote control of the module.

The campaign has allowed testing the energetic performance of the cogenerative module in different conditions of electrical load, and verifying the response of cogeneration systems in transient operation. The gross electrical efficiency varies between 30% and 35% for variations in electrical load of between 2.1 kW and 3.8 kW, while the coefficient of fuel utilization varies between 60% and 85% respectively.

In the dynamic behavior the cell has shown good ability to adapt at electric load changes, due to the presence, on board of the module, of a series of batteries that act as buffer between the demands of the electrical load and the electricity provided by the tubular cells, interposing in sudden variations of the electrical load.

In parallel to the above mentioned experimental activities, has been conducted a research program involving the analysis of the energetic performance of single tubular solid oxide fuel cells manufactured and tested in the laboratory. The research program was conducted at the Colorado Fuel Cell Center (CFCC) and the Colorado Center for Advanced Ceramics (CCAC) of Colorado School of Mines (Golden, CO - USA) in collaboration with Prof. Nigel Sammes (Editor in Chief of Journal of Fuel Cells Science and Technology).

This experience has allowed acquiring essential information on manufacturing processes of different types of solid oxide fuel cells using conventional materials and new materials capable of ensuring superior performance and advantages in manufacturing processes. The tests conducted have allowed to analyze the energetic performance of different SOFC operating at different temperatures and with different fuel volume flow of gas entering the cell. Also has been analyzed the behavior of fuel cells when fed with different types of gas (hydrogen, methane, synthesis gas, etc.).

In particular, we were able to analyze the energetic performance of tubular SOFC at anodic support, with an electrolyte consisting of YSZ (yttria Stabilized Zirconia), an anode made with Cermet formed by NiO (Nickel Oxide) and YSZ, and a cathode made of LSM

(Strontium - doped Lanthanum Manganite). These cells were tested at operating temperatures ranging from 750 °C and 850 °C, fed with variables volume flow and different types of gas (hydrogen, methane, synthesis gas, etc.).

Subsequently, have been analyzed the energetic performance of anode supported micro-tubular SOFC, with an electrolyte realized in GDC (Gadolinum Doped Ceria), an cermet anode made by mixing NiO and GDC and a cathode in LSCF ($\text{La}_{0.6}\text{Sr}_{0.4}\text{Co}_{0.2}\text{Fe}_{0.8}\text{O}_{3-y}$). These cells were tested at operating temperatures ranging from 450 °C and 550 °C, fed by variables volume flow, using different types of gas (hydrogen, methane, synthesis gas, etc.).

The results show performance definitely much higher for these last types of SOFC with lower operating temperatures that allow lower start-up times (start-up) and greater simplicity in the "sealing" of the various stacks components. Tests conducted with different gas confirm the ability of the "Ceria" material to inhibit the phenomenon of carbon deposition in the anode. It should be remembered however, as the presence of nickel in the anode is still the main obstacle to the possibility of direct feed such types of cells with fuels that present levels of carbon more or less variables. Tests conducted in fact confirm the ability of the "ceria" to improve the performance of the cells when fed directly with hydrocarbon, but this behavior is guaranteed for a number of hours still insufficient. The research program conducted has allowed also learning important information about the main techniques used in laboratories to test the electrochemical performance of single fuel cells and methods used to measure key parameters that influence the behavior of these cells.

CHAPTER I

CHAPTER.I

A FINITE-VOLUME SIMULATION MODEL OF A TUBULAR SOLID OXIDE FUEL CELL STACK

Summary

1.1.	Introduction	2
1.2.	SOFC Stack	4
1.3.	Thermodynamic Assumptions and Thermo-physical Properties	6
1.4.	Electrochemical Model.....	13
1.4.1.	Open circuit voltage.....	14
1.4.2.	Activation polarization	15
1.4.3.	Ohmic polarization	18
1.4.4.	Concentration Polarization	21
1.5.	Polarization Curve	27
1.6.	Pre-Reformer	29
1.6.1.	One-Dimensional Model	31
1.6.2.	Chemical kinetics	33
1.6.3.	Calculation of pressure drop and heat exchange coefficients.....	39
1.6.4.	Heat exchange model.....	43
1.6.5.	Results and discussion	44
1.6.6.	Exergy Balances	48
1.7.	SOFC Model.....	50
1.7.1.	SOFC Chemical Kinetics (Internal Reforming)	52
1.7.2.	Convection Heat Transfer Coefficients and Friction Factors Models.....	54
1.7.3.	Radiative Heat Transfer Model	55
1.7.4.	Overall Simulation Model and Energy Balance Equations	59
1.7.5.	The Case Study	63
1.7.5.1.	<i>Chemical/Electrochemical and Thermodynamic Analysis</i>	63
1.7.5.2.	<i>Radiative Heat Transfer</i>	73
1.7.5.3.	<i>Exergy balance</i>	76
1.7.5.4.	<i>Exergy Analysis results</i>	78
1.7.6.	Sensitivity analysis	80
1.7.6.1.	<i>Cell Diameter</i>	80
1.7.6.2.	<i>Cell Length</i>	82
1.7.6.3.	<i>Cell Voltage</i>	84
1.7.6.4.	<i>Air inlet temperature</i>	86
1.7.6.5.	<i>Inlet pressure</i>	87
1.8.	Combustor Model.....	89
1.8.1.	Combustor exergy analysis.....	92
1.9.	Conclusions	94
1.10.	References	96

1.1. Introduction

Solid Oxide Fuel Cells (SOFCs) are considered one of the most promising technologies for distributed power/heat production, due to their peculiarities, such as: high electrical and thermal efficiencies, low emissions, large availability of high temperature heat for cogeneration purposes, good reliability [1, 2].

SOFCs have been investigated since 1970s, however they are very far from a real commercialization since a number of issues must still be solved [3]. Currently, a number of different SOFC configurations are under investigation, namely: tubular, planar, tubular High Power Density (HPD) and micro-tubular [2, 3]. The most mature and reliable configuration is probably the tubular one, developed by Siemens-Westinghouse since the 1970s [3]. Nevertheless, even this type of SOFC is still far from commercial availability, mainly due to problems such as: cost targets, operating life, system optimization and eventual integration with traditional devices in hybrid systems, aiming at maximizing the overall electrical efficiency [3].

A number of the above mentioned issues are going to be solved by implementing, designing and optimizing further configurations of SOFCs, such as the HPD [2, 3], the microtubular [3] or the DELTA 9. Such new configurations aim at solving the typical problem of the tubular one: charge transfer, high operating temperatures and manufacturing costs [3]. However these new configurations are very far from a prototypal stadium [1-3]. So, the SOFC tubular configuration can be still regarded as the most efficient, reliable and mature one, and was here considered [3-6].

The development of fast and accurate simulation models is important to support the research efforts on SOFC, aiming at achieving the efficiency and costs targets recently fixed by the SECA and DOE [3-14].

In the last few years, many researchers were involved in the investigation of such systems [4-6, 11, 14], aiming at developing the above mentioned simulation models. So, SOFCs have been analyzed with a number of different techniques and with different levels of accuracy [4, 11, 13, 14]. Many papers are available, presenting 0-D [11], 1-D [4] or CFD [15] simulation models for the entire SOFC tube or for some sub-components (anode, cathode or electrolyte), in transient or steady conditions [15]. Usually, the CFD models are very time consuming and are capable to determine parameter fields only for a restricted area of the fuel cell [15]; on the other hand, the 0-D model are very fast but they can only analyze the thermodynamic conditions at the inlet and outlet sections of each component [7-11, 13, 14]. The CFD approach could be very useful for local analysis [15]; the 0-D

approach can be effectively used in plant simulation codes [7-11, 13, 14]. Thus, even if the 0-D models showed a very good compromise between calculation accuracy and computational times [11], they are not able to determine the profiles of important thermodynamic parameters, such as temperature, pressure, chemical composition, current density, etc., along the component [11, 13, 14]. Consequently, the 0-D models cannot be used by industry in order to design and optimize the single component but only to analyze more complex power plants [11].

Therefore, a very detailed 1-D finite-volume simulation models were developed in order to determine the profiles of the local parameters along the components of the system, achieving a dramatic reduction of the computational times [10-12]. This approach allows one to achieve both good calculation accuracy and velocity. Therefore, it can be usefully adopted both for local analysis and for system analysis and optimization [10, 12].

In the absence of any commercial software that could reliably simulate the operation of a system based on technology of solid oxide fuel cells, was necessary to develop and build a model simulation with Matlab toolbox. This model is based on a thorough bibliographic investigation undertaken in order to understand the physical and chemical phenomena that are the basis of its functioning and to assess the best way to model these phenomena.

Also in the simulation of certain phenomena, especially the electrochemical, it is often preferred to use a semi-empirical approach rather than using the strict form of the equation that governs the phenomenon. In fact, the first approach can guarantee the same accuracy in calculation but with simulation time considerably lower.

All subsequently reported analysis are based on the following assumptions wholly general:

- Mono-dimensional flow;
- Steady State;
- Thermodynamic equilibrium;
- No loss of fluid from components;
- Loss of heat towards the environment negligible;
- Kinetic and gravitational terms are negligible in the energy balance equations.

Further assumptions may be necessary to simulate the individual components and will be recalled within the respective paragraphs.

1.2. SOFC Stack

The stack considered for the development of the 1-D model is part of a more complex Hybrid SOFC-GT system realized with internal reforming Solide Oxide Fuel Cells, an external pre-reformer system, anodic flux recirculation, including compressors, heat exchangers, etc. The entire system has been previously studied by the research group wherewith I have worked in the last 3 years [4-8].

It is clear that the performance of power plants based on SOFC technology is substantially influenced by the choice and design of the stacks section. It is the most delicate component which requires a more complex design, showing obvious integration difficulties with the other traditional components. Therefore, the analysis needs to define carefully and model all the chemical, electrochemical, electrical and thermodynamic phenomena taking place inside the stack.

The entire system is really complex consisting of a large number of components, such as IRSOFC (Internal Reforming Solid Oxide Fuel Cell), pre-reformer, by-pass valves, mixers, heat exchangers and post-combustion chamber. In particular, the typical configuration stack developed by Siemens-Westinghouse (Figure I.1) shown below, can be “dismembered” in components, more or less fictitious, which describe its operation (Figure I.2).

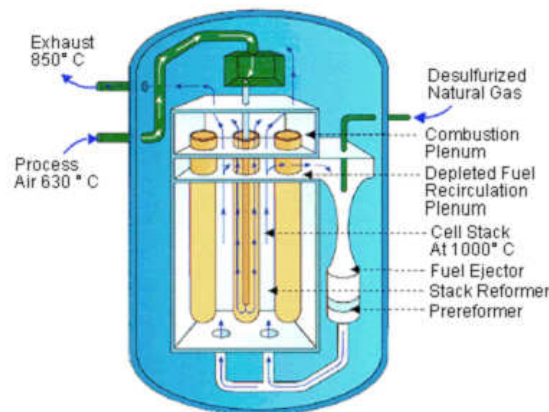


Figure I. 1: Siemens SOFC Stack configuration

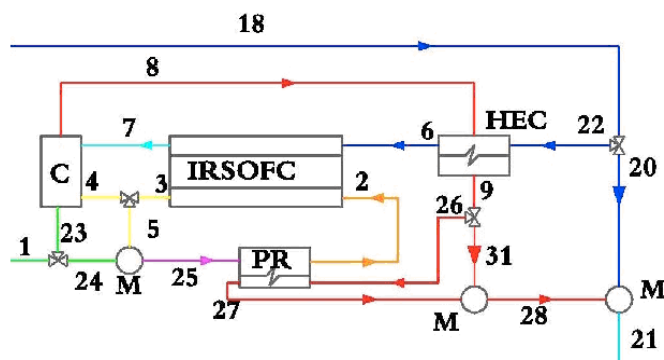


Figure I. 2: Schematization of SOFC stack

Starting from the configuration shown in Figure I.1, has been obtained the simplified layout of the stack, displayed in Figure I.3. On this stack has been developed the 1-D model. In particular, the typical configuration stack developed by Siemens-Westinghouse is investigated, not including the anode recirculation arrangement (e.g. [1-3]).

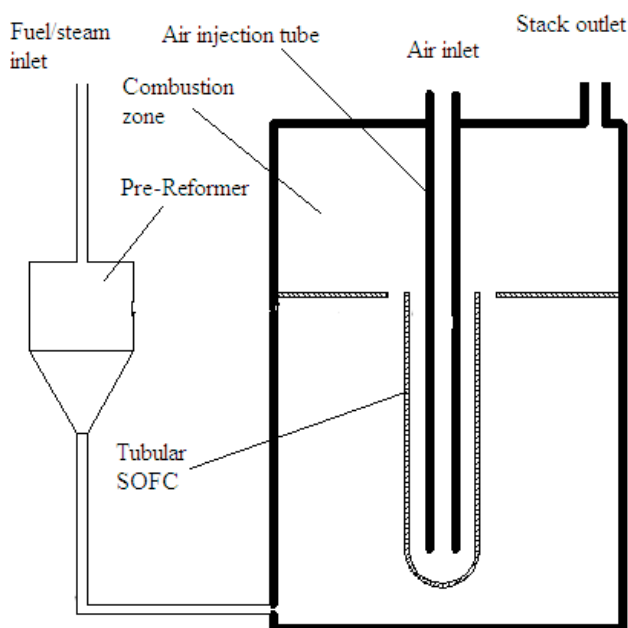


Figure I. 3: Studied SOFC Stack Layout

Obviously, the simulation of such a component is extremely complex because requires:

- calculation of the electrochemical performance of the cell, or calculate the real cell voltage changing the geometric and operational parameters of the system; obviously this calculation also requires evaluation of all the polarizations (ohmic, activation and concentration);

- calculating the degree of reaction of the reforming and shift reaction within the pre-reformer;
- calculating the degree of reaction of the reforming, shift and electrochemical reaction within the cell;
- calculation of heat exchange in SOFC;
- calculation of heat exchange in Pre-reformer;
- calculation of the heat exchange in the tube of air injection (HEC);
- calculation of the degrees of reaction in the combustion chamber.

In the following sections will be described and implemented 1-dimensional models and will be described the obtained result using such modeling procedure.

Afterwards will be therefore analyzed all the components of which the system is constituted and the phenomena that are at the base of its operation. For each component will be introduced the model adopted and implemented inside the simulation procedure.

1.3. Thermodynamic Assumptions and Thermo-physical Properties

The system under investigation is fed with two flows: on one side the fuel and on the other the air. Regarding the fuel, in this study it has been assumed to use the natural gas; in reality it is known that SOFC can be fed by a large fuel range as methane, hydrogen, propane, butane, syngas, biogas etc. However, between these, the natural gas appears the more favorite candidate, virtue of its highest methane content, of the capillary distribution on the territory, with its transport network, and its cost. The natural composition of gas varied according to many parameters as: origin place, environmental conditions, arranges of transport, etc. In this study has been assumed to use the typical gas extracted in Italy (Table I.1); it is clearly shown as the percentage of methane in the Italian natural gas is very high and that the sum of all the other hydrocarbons does not exceed 0.035%. Such value concurs to assume that methane is the only hydrocarbon contained in the natural gas simplifying also the calculation model. After all, it is assumed that the fuel is constituted only by N_2 , CO_2 and CH_4 , according to the proportions suggested on Table I.1.

substance	percentage
CH_4	99,728
Ethane	0,0006
Propane	0,0148
Isobutene	0,007

Butane	0,0019
Isopentane	0,0022
Pentane	0,00001
Hexane	0,0078
N ₂	0,207
CO ₂	0,0311

Table I. 1: Typical composition of the Italian natural gas (10² mol/mol)

At the cathodic section of the SOFC has been chosen to use air as oxidant, constituted by 21% of O₂ and 79% of N₂, being neglected the content in H₂O, Argon, H₂, He, etc.

The criterion of operation of the system is based on some important electrochemical and chemical reactions (pre-reforming reactions, reforming and electrochemical oxidation) that obviously realize a variation of the chemical composition compared with the flows at the inlet of each system. Analyzing the aforesaid reactions it can be assumed that, beginning from O₂ and CH₄ is possible the conversions in other substances as CO, CO₂, H₂ and H₂O. In general terms, therefore any node of the system can be considered like a mixture of seven various substances: H₂O, CO, H₂, O₂, N₂, CO₂ and CH₄. Named x the vector of the molar fractions, result:

$$x = \left[x_{H_2O} \quad x_{CO} \quad x_{H_2} \quad x_{O_2} \quad x_{N_2} \quad x_{CO_2} \quad x_{CH_4} \right] \quad (I.1)$$

The simulation of the system, based on I and II law of thermodynamics, is based on the choice of the model for the calculation of the properties of the substances. It can easily be verified that, with exception of the H₂O, the critical temperature of the substances previously listed is really under the ambient temperature and this substances can be considered in the gaseous phase.

substance	P _{critical} (bar)	T _{critical} (K)
H ₂ O	220,55	647,1
CO	34,99	132,9
H ₂	13,13	33,19
O ₂	50,43	154,6
N ₂	34	126,2
CO ₂	73,83	304,2
CH ₄	45,99	190,6

Table I. 2: Critical Pressure and Temperature

A more rigorous model should have to consider the behavior of real gases, because the ideal conditions are not all the time verified; however the implementation of such model would be extremely onerous without add particular precision to the calculation. It is possible to verify that assuming the ideal behavior of the mixture implies a calculation error of properties that are always inferior to 2%.

It will be assumed therefore the ideal gas behavior and the Dalton law will be considered valid:

$$p = \sum_i p_i \quad (\text{I.2})$$

$$p_i = p \cdot x_i \quad (\text{I.3})$$

For the water, it has been developed a model in order to estimate its properties in case it will be in the superheated steam, saturated steam or liquid condition; such model has been gained on the base of the IAPWS-IF97 equations and on the base of data reported in the tables in the case of saturated steam, implementing appropriate procedures of interpolation. The result is a model of calculation capable of estimating the properties of the water, in terms of pressure, temperature, entropy, enthalpy, internal energy and specific volume in a wide range of temperature and pressure (50-2000°C and 0,1-400 bar). However, it must also consider that if the ideal gas model had been adopted, in simplified way, also for the water, the error would not have been important. After all, using the additive property it is possible to calculate the total enthalpy, entropy, internal energy, specific heat coefficient and physical exergy of the gas mixture, using the following equations, respectively:

$$h = \sum_{i=1}^7 h_i \quad (\text{I.4})$$

$$s = \sum_{i=1}^7 s_i \quad (\text{I.5})$$

$$u = \sum_{i=1}^7 u_i \quad (\text{I.6})$$

$$v = \sum_{i=1}^7 v_i \quad (\text{I.7})$$

$$\text{ex}_{ph} = \sum_{i=1}^7 \text{ex}_{ph,i} \quad (\text{I.8})$$

In the sum of the previous equations, the first term ($i=1$, H_2O), is estimated by means of the model previously described. For the other species, whose behavior can be thought ideal, the enthalpy is function of the temperature. For the calculation of the specific heat it

has been realized the implementation of functions that express the dependency from temperature. As usual such functions have a polynomial expression:

$$c_p = \sum_{k=0}^N A_k T^k \quad (\text{I.9})$$

in which it is typically used a value of N equal to 3. However, such expressions introduce a validity field, in terms of temperature, too much limited regarding the effective range of operating temperature of the system; therefore it has been preferred to use an expression of the type brought back in (the 4,13) that, in the event under investigation it is rigorously valid at least till 1500 K.

$$c_{p,i} = \frac{R_o}{M_i} (A + BT + CT^2 + DT^{-2}) \quad (\text{I.10})$$

where:

R_o universal constant of gases;

M_i molecular mass of i species;

T temperature [K];

A, B, C and D are coefficient, function of the substance, reported on Table I. 3.

substance	Ai	Bi (K ⁻¹)	Ci (K ⁻²)	Di (K ²)
H ₂ O	3,47	1,450E-03	0	1,210E+03
CO	3,376	5,570E-04	0	-3,100E+03
H ₂	3,3249	4,220E-04	0	8,300E+03
O ₂	3,639	5,060E-04	0	-2,270E+04
N ₂	3,28	5,930E-04	0	4,000E+03
CO ₂	5,457	1,045E-03	0	-1,157E+05
CH ₄	1,702	9,081E-03	-2,164E-06	0

Table I. 3: A, B, C and D coefficients for different substances

The application of the specific heat model (4,13), also concurs, in an extremely easy way, to the calculation of the specific entalpy variation of the i species:

$$h_i = \int_{T_0}^{T_i} c_{pi} dT = \frac{R_o}{M_i} \left[A_i (T_1 - T_0) + \frac{B_i}{2} (T_1^2 - T_0^2) + \frac{C_i}{3} (T_1^3 - T_0^3) - D_i (T_1^{-1} - T_0^{-1}) \right] \quad (\text{I.11})$$

In completely analogous way it is possible to calculate the entropy of the i species:

$$s_i = \int_{T_0}^{T_i} c_{pi} dT - \int_{p_0}^{p_i} \frac{R_o}{M_i} dp = \frac{R_o}{M_i} \left[A_i \ln \left(\frac{T_i}{T_0} \right) + B_i (T_1 - T_0) + \frac{C_i}{2} (T_1^2 - T_0^2) - 2D_i (T_1^{-2} - T_0^{-2}) \right] - R_i \ln \left(\frac{p_i}{p_0} \right) \quad (\text{I.12})$$

For each substance, the state of reference is fixed to $T_0=273.15$ K and $p_0=1,00$ bar. The simulation code is also capable to estimate the exergetic performances of the system. The exergetic analysis mainly will be used for having a clear vision of the entity of the irreversibility and their localization inside the components. Therefore, besides the evaluation of the traditional thermodynamics properties it is also necessary to estimate the exergy, than as it is known is composed by two quotes: physical and chemical exergy. The first one is connected to the pressure and temperature gradient inside the system, the second one to the chemical composition of the mixture.

$$ex = ex_{ph} + ex_{ch} \quad (I.13)$$

$$ex_{ph,i} = (h_i - h_a) - T_a(s_i - s_a) \quad (I.14)$$

where, h_i ed h_a are specific entalpy of the i substance evaluated respectively at (t_i, p_i) and (t_a, p_a) . Similarly are valuated s_i ed s_a . The ambient condition are fixed at: $T_a=298,15$ K e $p_a=1,00$ bar.

In the event the flow is constituted by more substances the specific molar chemical exergy can be calculated as follows:

$$ex_{ch} = \sum_{i=1}^7 x_i \sum_{i=1}^7 (x_i ex_{ch,i}^0 + R_0 T_a \ln(x_i)) \quad (I.15)$$

In the equation (I.15) the terms representative of the specific molar chemical exergy, of each component in standard condition ($ex_{ch,i}^0$), are brought back in Table I.4.

substance	$ex_{ch,i}^0$ (kJ/kmol)
H ₂ O	11710
CO	275430
H ₂	238490
O ₂	3970
N ₂	720
CO ₂	20140
CH ₄	836510

Table I. 4: Specific Chemical exergy in standard condition

After all, the previous considerations were used to develop and successively implement 4 different subroutines, in MATLAB, of the type:

$$h = h(t, p, \vec{x}) \quad (I.16)$$

$$s = s(t, p, \vec{x}) \quad (I.17)$$

$$\text{ex}_{ph} = \text{ex}_{ph}(t, p, \vec{x}, t_a, p_a) \quad (\text{I.18})$$

$$\text{ex}_{ch} = \text{ex}_{ch}(\vec{x}) \quad (\text{I.19})$$

In many circumstances it is necessary to reverse these functions, but the previous functions are not explicitly reversible, so the corresponding inverse functions have been built by implementing the appropriate iterative procedures on MATLAB and TOMLAB able to find the zero of a nonlinear function. In this way it was possible to build powerful, fast and useful subroutines like this:

$$t = t(s, p, \vec{x}) \quad (\text{I.20})$$

$$t = t(h, p, \vec{x}) \quad (\text{I.21})$$

Finally, the calculation of heat transfer coefficients and friction coefficients, needed to solve the problems of heat exchange and evaluation of pressure drop, also requires the implementation of a calculating code for the viscosity and conductivity of the mixtures. Again it is considered valid the assumption of an ideal mixture of gases. It is known that the conductivity of the fluid is a function of temperature of the fluid itself. The functional dependence is often expressed through a polynomial equation, or in graphic form:

$$\begin{aligned} k_{\text{H}_2\text{O}} &= 0.00053 + 4.7093\text{e-}5T + 4.955\text{e-}8T^2 \\ k_{\text{CO}} &= 0.00158 + 8.2511\text{e-}5T - 1.9081\text{e-}8 T^2 \\ k_{\text{H}_2} &= 0.03951 + 4.5918\text{e-}4T - 6.4933\text{e-}8 T^2 \\ k_{\text{O}_2} &= 0.00121 + 8.6157\text{e-}5T - 1.3346\text{e-}8 T^2 \\ k_{\text{N}_2} &= 0.00309 + 7.5930\text{e-}5T - 1.1014\text{e-}8 T^2 \\ k_{\text{CO}_2} &= -0.012 + 1.0208\text{e-}4T - 2.2403\text{e-}8 T^2 \\ k_{\text{CH}_4} &= -0.00935 + 1.4028\text{e-}4T + 3.318\text{e-}8 T^2 \end{aligned} \quad (\text{I.22})$$

Similarly, you can find in literature reports that provide the functional dependence of the viscosity of substances with their temperature:

$$\begin{aligned}
\mu_{\text{H}_2\text{O}} &= -36.826 + 4.29e-1T - 1.62e-5T^2 \\
\mu_{\text{CO}} &= 23.811 + 5.3944e-1T - 1.5411e-4T^2 \\
\mu_{\text{H}_2} &= 27.758 + 2.12e-1T - 3.28e-5T^2 \\
\mu_{\text{O}_2} &= 44.224 + 5.62e-1T - 1.13e-4T^2 \\
\mu_{\text{N}_2} &= 42.6064 + 4.75e-1T - 9.88e-5T^2 \\
\mu_{\text{CO}_2} &= 11.811 + 4.9818e-1T - 1.0851e-4T^2 \\
\mu_{\text{CH}_4} &= 3.844 + 4.0112e-1T - 1.4303e-4T^2
\end{aligned} \tag{I.23}$$

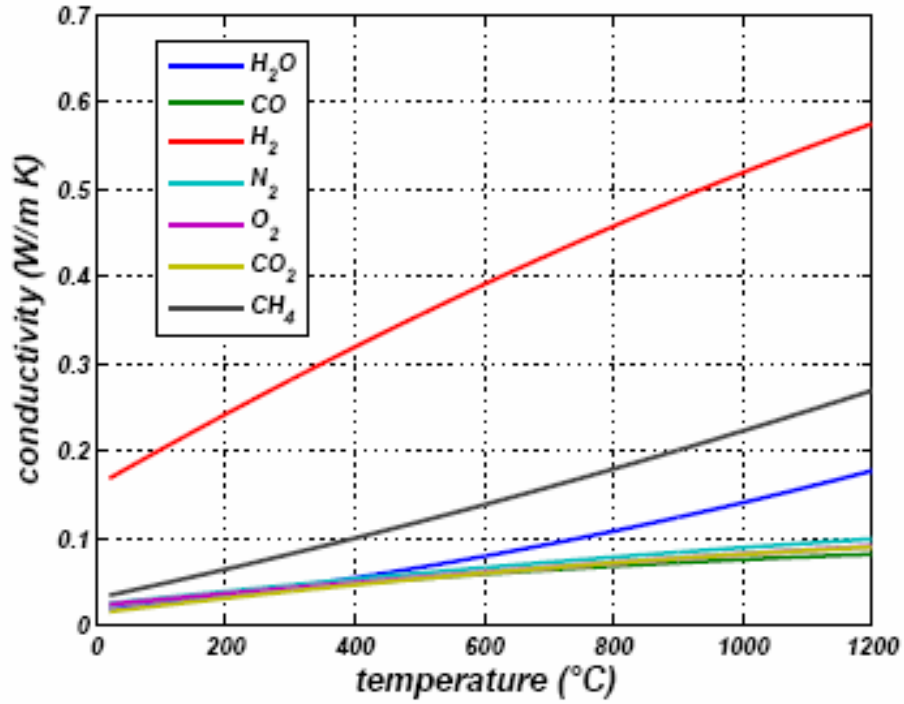


Figure I. 4: Conductivity of pure substances

The values obtained by the equations previously reported are related only to pure substances; when mixture of substances are considered, the calculation of the viscosity or conductivity of the total mixture is extremely complex because we need to introduce the kinetic theory of gases. The results derived from this theory are summarized in the Wilke's law, according to which:

$$\mu = \sum_{i=1}^7 \frac{x_i \mu_i}{\sum_{j=1}^7 x_j \phi_{ij}} \tag{I.24}$$

$$k = \frac{\sum_{i=1}^7 x_i k_i}{\sum_{j=1}^7 x_j \phi_{ij}} \quad (\text{I.25})$$

where the so-called intercollision factor is defined by the following equation:

$$\phi_{ij} = \frac{1}{\sqrt{8}} \left(1 + \frac{M_i}{M_j} \right)^{-\frac{1}{2}} \left[1 + \left(\frac{\mu_i}{\mu_j} \right)^{\frac{1}{2}} \left(\frac{M_i}{M_j} \right)^{\frac{1}{4}} \right]^2 \quad (\text{I.26})$$

1.4. Electrochemical Model

The overall simulation model of a tubular SOFC is mainly based on the evaluation of its electrochemical performance. A number of different electrochemical models are available in literature, characterized by different levels of accuracy [3-15, 17, 18]. However, these models are mostly based on simplifying assumptions that cannot be considered completely correct [5, 6, 11]. Such assumptions are often required to reduce the computational time and/or to implement simplified approaches, such as the 0-D simulations [11]. Typical examples are as follows: use of the Tafel equations to evaluate activation overvoltages, use of constant values for the exchange current densities, inappropriate arrangement of the electrical equivalent scheme in calculation of Ohmic overvoltage, use of constant values for the diffusion coefficients, concentration polarization not considering the real diffusion mechanisms, evaluation of overvoltages corresponding to average values of the cell thermodynamic properties, and so on [5, 6, 11, 13, 18].

Here, a special effort was spent to evaluate the suitability of all the above mentioned assumptions, removing all the ones that induced a significant loss in the model accuracy. This effort resulted in a very complex and complete electrochemical model relating the cell operating voltage to a number of parameters, such as:

- operating temperature;
- pressure;
- thickness of the anode, cathode, electrolyte and interconnections;
- fuel cell materials;
- geometry of the cell;
- length of the cell;
- fuel utilization coefficient;

- composition and mass flow of fuel;
- composition and air mass flow;
- current density.

The cell voltage was calculated on the basis of the open circuit reversible voltage and its overvoltages, shown in equations (I.27).

$$V = E - \eta_{act,A} - \eta_{act,C} - \eta_{\Omega} - \eta_{conc,A} - \eta_{conc,C} \quad (I.27)$$

where:

V	fuel cell voltage;
$\eta_{act,A}$	activation polarization anode;
$\eta_{act,C}$	activation polarization cathode;
η_{Ω}	Ohmic polarization;
$\eta_{conc,A}$	concentration polarization anode;
$\eta_{conc,C}$	concentration polarization cathode.

In the case of SOFCs, are usually negligible the losses for fuel crossover and internal currents, because in this case the electrolyte ceramic matrix enables an excellent insulation both as regards the flow of electrons that the fuel; it follows that the i_n value is so small that can be neglected without affecting the accuracy of the calculation of the fuel cell potential.

1.4.1. Open circuit voltage

As you know the Nernst equation gives the expression of open-circuit potential of a fuel cell under operating pressure other than standard:

$$E = \frac{-\Delta\bar{g}_f^0}{2F} + \frac{RT}{2F} \ln \frac{a_{H_2} a_{O_2}^{1/2}}{a_{H_2O}} \quad (I.28)$$

$$E = E_0 + \frac{RT}{2F} \ln \frac{a_{H_2} a_{O_2}^{1/2}}{a_{H_2O}} \quad (I.29)$$

In the case of high temperatures, as in the SOFC operating at about 1000 ° C, we can assume that the steam is in conditions of ideal gas and, setting $p_0 = 1$ bar, the Nernst equation becomes:

$$E = E_0 + \frac{RT}{2F} \ln \frac{p_{H_2} p_{O_2}^{1/2}}{p_{H_2O}} \quad (I.30)$$

The electrochemical performance is usually described by the polarization curve diagram obtained making a diagram of the cell potential function of the current density. In this type of chart are indicated the theoretical maximum reversible potential and the total losses according always to current density. Overall, the cell reaches the maximum value of reversible potential when current is not required outside.

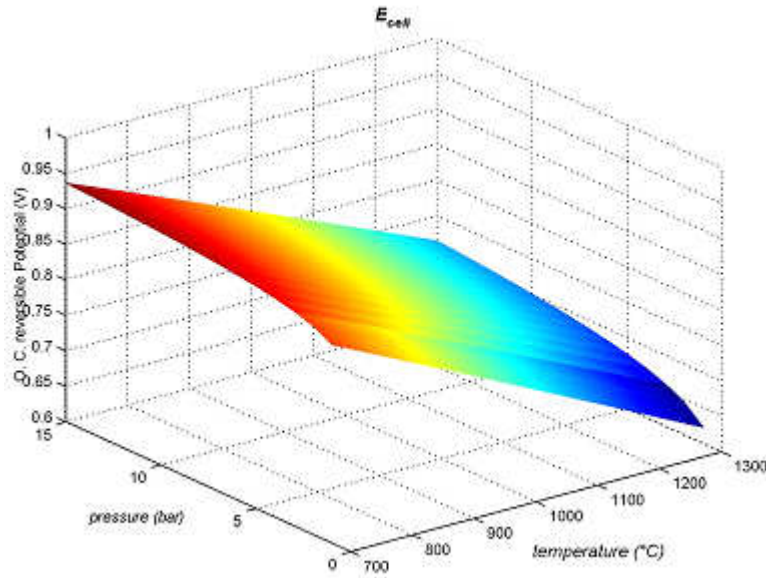


Figure I. 5: Fuel Cell Open Circuit Voltage function of pressure and temperature.

At this point we look in particular at the various types of losses, or polarization, which take place inside the cell.

1.4.2. Activation polarization

In the simulation model adopted in this study, the activation polarization, for both the anode and the cathode, is calculated by the Butler-Volmer equation:

$$i = i_0 \left[\exp \left(\alpha \frac{zF}{RT} \eta_{act} \right) - \exp \left(-(1 - \alpha) \frac{zF}{RT} \eta_{act} \right) \right] \quad (I.31)$$

The calculation of activation polarization with this equation is very difficult; it is necessary to proceed for iteration since you cannot explicit this loss in function of i , or you cannot invert the equation. It is not possible to decide in advance if the cell will work with very high or very low current density, so you cannot use the simplified expressions of Butler-Volmer reported in literature.

It is however important to note that the use of the Butler-Vomer equation, complex and costly in calculation terms, is justifiable only when the values of the exchange current density are provided with sufficient reliability. Precisely for this reason it was done a thorough research activity in literature to find the more reliable parameter values present on the equations (I.31).

To estimate the exchange current density of the two electrodes may refer to the formula derived semiempirically by Mogensen and by Yamamura:

$$i_{0,an} = \gamma_{an} \left(\frac{p_{H_2}}{p_0} \right) \left(\frac{p_{H_2O}}{p_0} \right)^m \exp \left(- \frac{E_{act,A}}{RT} \right) \quad (I.32)$$

$$i_{0,an} = \gamma_{an} \left(\frac{p_{H_2}}{p_{amb}} \right) \left(\frac{p_{H_2O}}{p_{amb}} \right)^m \exp \left(- \frac{E_{act,an}}{RT} \right) \quad (I.33)$$

$$i_{0,cat} = \gamma_{cat} \left(\frac{p_{O_2}}{p_{amb}} \right)^{0.25} \exp \left(- \frac{E_{act,C}}{RT} \right) \quad (I.34)$$

The values of γ , E_{act} and m are provided in literature. As shows these equations, the values of anode and cathode exchange current density vary greatly depending on the parameters γ and E_{act} . It is clear that even small changes in activation energies and pre-exponential factors determine considerable variations in the exchange current and then in the activation polarization. It is therefore essential to choose these parameters with extreme caution and if possible to refer to those values which are reflected in experimental data. This fact is also quite rare when you consider that most of the formulas provided in the literature are not accompanied by an experimental validation procedure.

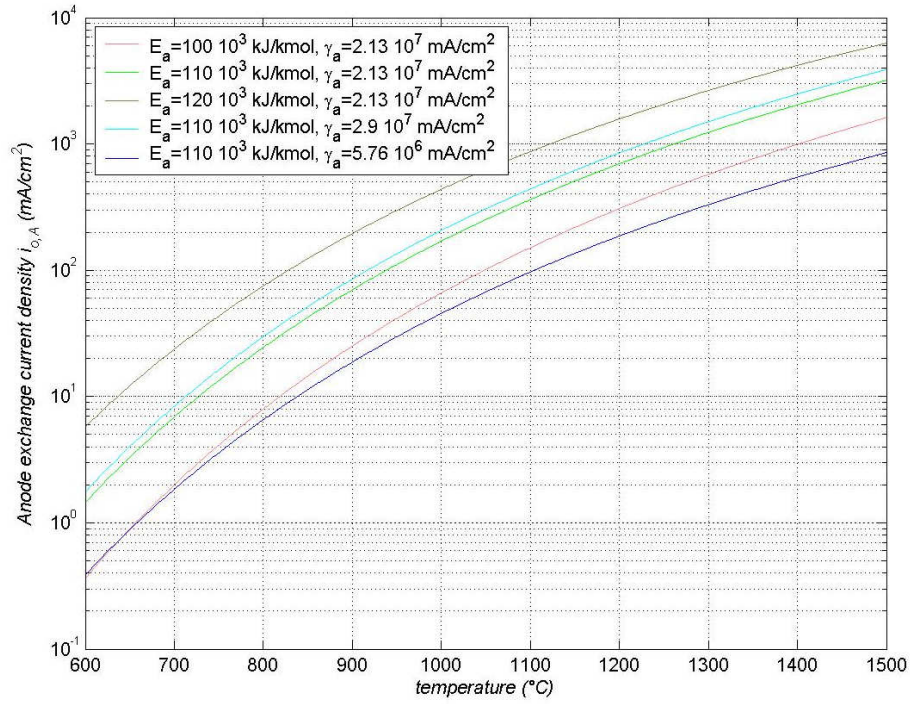


Figure I. 6: Anodic Exchange Current Density

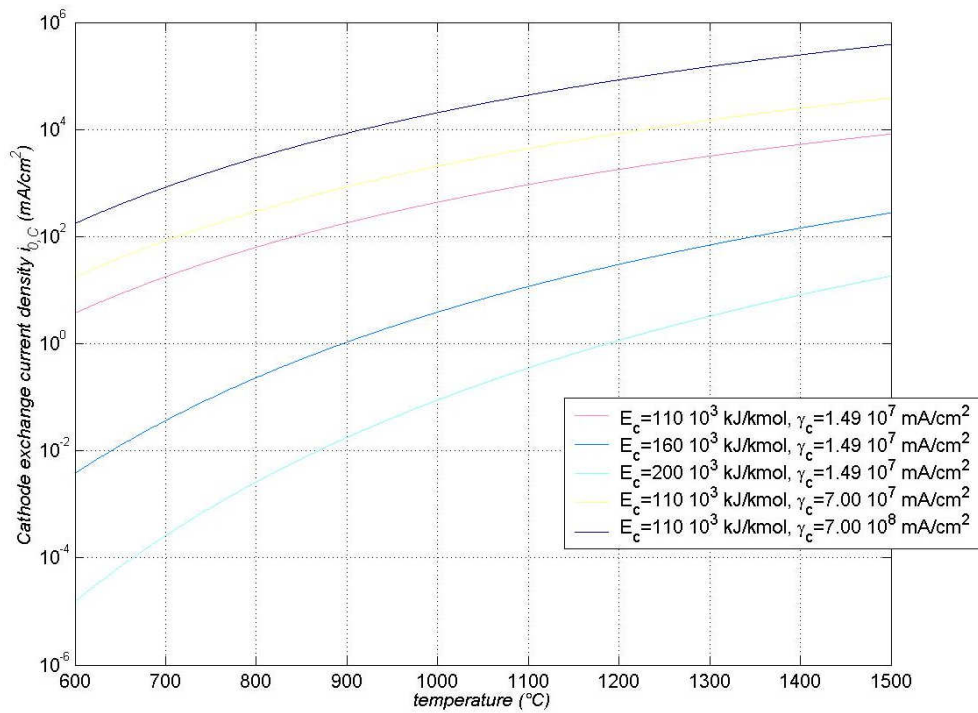


Figure I. 7: Cathodic Exchange Current Density

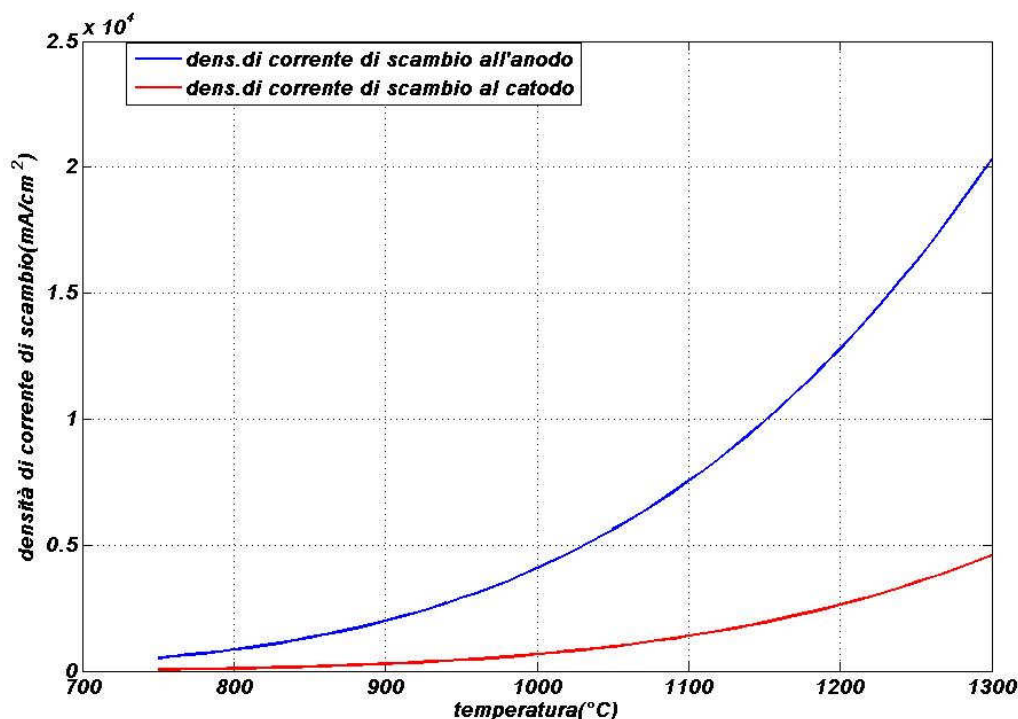


Figure I. 8: Anodic and cathodic current density in the model adopted

With the anodic and cathodic values of γ and E_{act} , selected in this work, result that the anodic exchange current density is greater than cathodic, or that the anode activation polarization is lower than cathode polarization, in full agreement with what is widely reported in the literature.

By implementing the Butler-Volmer equation and semi-empirical equations ((I.32)-(I.34)) in a special subroutine in MATLAB, once set the trends with the temperature of anode and cathode exchange current density, can be easily obtained the trend of anode and cathode activation losses with the current density, varying temperature and pressure.

1.4.3. Ohmic polarization

The Ohmic loss was evaluated on the basis of a complex electrical arrangement, taking into account the real paths of charges in the cell. So, a complex combination of parallel (circumferential path) and series (radial path) arrangements was considered [19].

It was proposed by Nisancioglu, a theory which gives expressions articulated but also more compact for the calculation of ohmic losses, with evident considerable advantages for its implementation in a calculation procedure. This model is based on the fact that the single cell can be studied from an electrical point of view as a combination serial and parallels its components. Therefore, ones obtained the resistance of a single cell, the electrical resistance value of the stack can be easily calculated through the simple application of the Kirchoff's law at the equivalent circuit representing the cell's stack. In most of SOFC,

components, carrying charges, are much more thin than the characteristic dimension in the direction of current flow ($\delta \ll L$); also, the resistivity of the electrodes are much smaller than those of the electrolyte and interconnections.

These characteristics allow considering the following assumptions:

- the effects of board are negligible;
- any changes through the electrode thickness is negligible, therefore it is possible to assume that the current flow is unidirectional along the characteristic dimension of the electrode;
- the passage of current through two parallel electrodes, through the electrolyte or through the interconnection occurs perpendicular to the electrode surface; in other words the passage of current through the electrolyte and interconnection is unidirectional in thickness. There is no significant current flows toward the length of these materials;
- the resistivity of the components of the cell are constant in the space.
- Under the symmetry in the distribution of current (do not have current flow through the plane of symmetry) into the analysis is taken in consideration only one half of the cylinder. Half orthogonal section of the cell is electrically equivalent to the cell shown in Figure I.9 and also the geometry can be represented by three types of "sub-unit" of the cell connected to each other in series as shown in the same figure. In this way the resistance of the cell is given by:

$$R = \frac{1}{2}(R_1 + R_2 + R_3) \quad (\text{I.35})$$

where R_1 , R_2 and R_3 are the resistance of three "sub-unit".

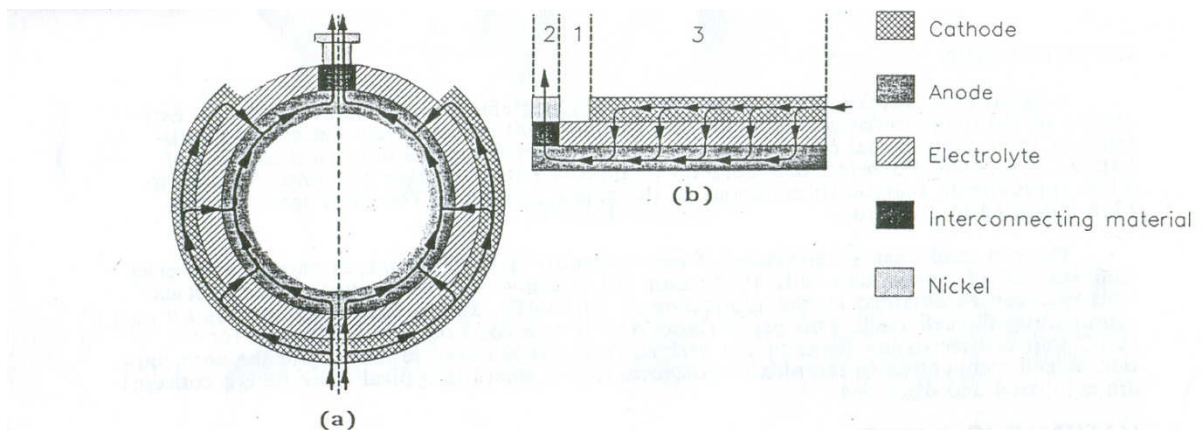


Figure I. 9: (a) Cross section of a tubular SOFC. (b) Geometrical model for Ohmic resistance calculation.

The formula for the resistance of the cell, ignoring the contribution to the resistance provided by "sub-unit" 1, i.e. neglecting R_{1} , is:

$$R = \frac{\left\{ \left(\frac{\rho_a}{\delta_a} \right)^2 + \left(\frac{\rho_c}{\delta_c} \right)^2 \right\} \cosh J_e + \frac{\rho_a \rho_c}{\delta_a \delta_c} (2 + J_e \sinh J_e)}{2 \left(\frac{1}{\rho_e \delta_e} \right)^{1/2} \left(\frac{\rho_a}{\delta_a} + \frac{\rho_c}{\delta_c} \right)^{3/2} \sinh J_e} + \frac{\sqrt{\rho_{\text{int}} \delta_{\text{int}} \left(\frac{\rho_c}{\delta_c} \right)}}{2 \tanh J_{\text{int}}} \quad (\text{I.36})$$

where:

$$J_e = \frac{L_e}{2} \sqrt{\frac{1}{\rho_e \delta_e} \left(\frac{\rho_a}{\delta_a} + \frac{\rho_c}{\delta_c} \right)} \quad (\text{I.37})$$

$$J_{\text{int}} = \frac{L_{\text{int}}}{2} \sqrt{\frac{\rho_c / \delta_c}{\rho_{\text{int}} \delta_{\text{int}}}} \quad (\text{I.38})$$

The value of resistance of the cell thus obtained is expressed in $\Omega \text{ cm}$; to switch to Ω it is necessary to divide the value obtained for the length of the cell.

Thus, obtained with this approach the value of the cell resistance in Ω , for the calculation of ohmic losses of the cell, simply it is necessary to multiply the resistance value to the current passing through the cell:

$$\eta_{\Omega} = IR_{\text{cella}} \quad (\text{I.39})$$

Referring to the model proposed by Nisancioglu the results in terms of overall resistance per unit area obtained, are shown in Figure I.10, compared to other models. Also for a more clear comparison between the results obtained using the different models, will be shown in Figure I.11, the percentage gap.

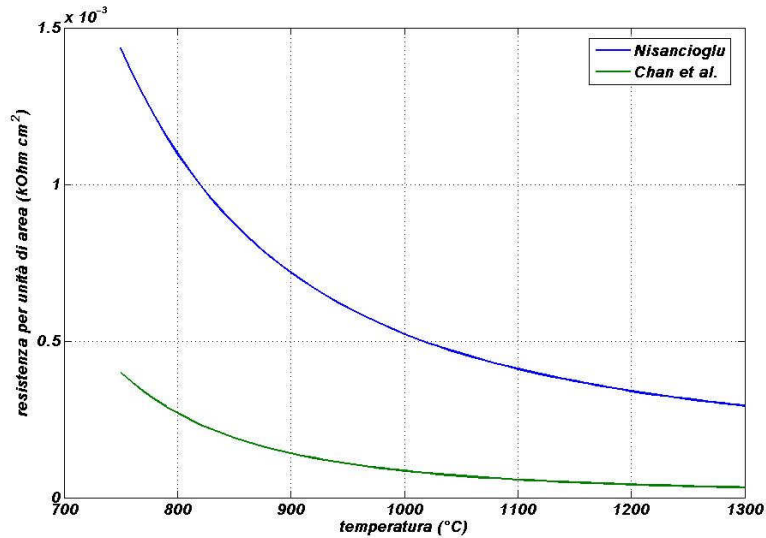


Figure I. 10: Ohmic Global Resistance for unit surface, obtained applying two different models

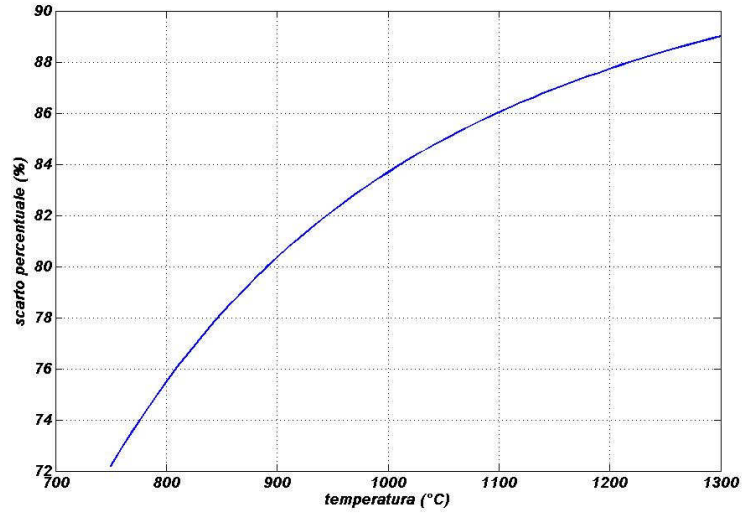


Figure I. 11: Percentage difference trend between the global resistance values obtained applying two different models

1.4.4. Concentration Polarization

Finally, the concentration overvoltage was calculated by means of a very accurate diffusion model based on both Knudsen and binary diffusion [11]. In particular, the binary diffusion coefficient was calculated on the basis of the Chapman-Enskog theory (equation (I.40) [20], also including the Lennard-Jones intercollision integral (equation (I.41)) [20].

$$D_{AB} = 1,858 \times 10^{-3} T^{3/2} \frac{\left[\frac{M_A + M_B}{M_A M_B} \right]^{1/2}}{p \sigma_{AB}^2 \Omega_D} \quad (\text{I.40})$$

where:

- M_A e M_B molecular mass;
- n number of molecule present in the mixture;
- k Boltzmann constant;
- T absolute temperature;
- Ω_D collision integral for the diffusion (non-dimensional), function of temperature, depending also by the choice of the intermolecular forces law between molecules that collide.
- σ_{AB} characteristic length (Angstrom), depending on the intermolecular forces law;

$$\Omega_D = \frac{A}{\left(\frac{kT}{\varepsilon_{AB}}\right)^B} + \frac{C}{\exp\left(D \frac{kT}{\varepsilon_{AB}}\right)} + \frac{E}{\exp\left(F \frac{kT}{\varepsilon_{AB}}\right)} + \frac{G}{\exp\left(H \frac{kT}{\varepsilon_{AB}}\right)} \quad (\text{I.41})$$

where:

$$\begin{aligned} A &= 1,06036 & B &= 0,15610 \\ C &= 0,19300 & D &= 0,47635 \\ E &= 1,03587 & F &= 1,52996 \\ G &= 1,76474 & H &= 3,89411 \end{aligned}$$

Whereas the Knudsen diffusion coefficient was calculated on the basis of the theory of diffusion in a cylindrical pore, by means of the average pore radius, that can be related to the porosity, porous media area and bulk density (equation (I.42)) [17, 18, 20-22].

$$D_K = 97,0 \bar{r} \sqrt{\frac{T}{M}} = 97,0 \frac{2\varepsilon}{S_A \rho_B} \sqrt{\frac{T}{M}} \quad (\text{I.42})$$

$$\bar{r} = \frac{2\varepsilon}{S_A \rho_B} \quad (\text{I.43})$$

where:

ε material porosity;

ρ_B “bulk-density”;

S_A area of porous material.

Finally, the real overall diffusion coefficient was calculated by considering material porosity and tortuosity and the combined mechanisms of ordinary and Knudsen diffusion (equation (I.44)) [18].

$$\frac{1}{D_{A,eff}} = \frac{\varepsilon}{\xi} \left(\frac{1}{D_{AB}} + \frac{1}{D_{AK}} \right) \quad (\text{I.44})$$

Such overall coefficient was used in the theory developed by Chan [18] in order to evaluate the overall anode and cathode concentration overvoltage (equations (I.45)).

$$\begin{aligned}
D_{a(eff)} &= \left(\frac{p_{H_2O}}{p_{H_2} + p_{H_2O}} \right) D_{H_2(eff)} + \left(\frac{p_{H_2}}{p_{H_2} + p_{H_2O}} \right) D_{H_2O(eff)} \\
\eta_{conc,a} &= -\frac{RT}{2F} \ln \left[\frac{1 - (RT/2F) \left(\delta_a / D_{a,eff} p_{H_2}^I \right) i}{1 + (RT/2F) \left(\delta_a / D_{a,eff} p_{H_2O}^I \right) i} \right] \\
p_{O_2} &= \frac{p_c}{\psi_{O_2}} - \left(\frac{p_c}{\psi_{O_2}} - p_{O_2}^I \right) \exp \left(\frac{\psi_{O_2} RT i \delta_c}{4FD_{cathode,eff} p_c} \right) \\
\eta_{conc,c} &= -\frac{RT}{4F} \ln \left[\frac{\left(p_c / \psi_{O_2} \right) - \left(\left(p_c / \psi_{O_2} - p_{O_2}^I \right) \exp \left[(RT/4F) \left(\psi_{O_2} \delta_c / D_{c,eff} p_c \right) i \right] \right)}{p_{O_2}^I} \right] \quad (I.45)
\end{aligned}$$

It can be immediately seen that the concentration polarization at the cathode are more important than those at the anode. In fact, the concentration polarization at the cathode, exceeded a certain value of current density, have an even asymptotic, which is not happening at all for losses at the anode. This asymptotic, which means concentration losses at the cathode practically tending to infinity, occur for a current density equal to the cathode limit current density, and thus the tension of the cell is practically zero. All this is due to the diffusion phenomena that occur during the motion of oxygen or air, which feeds the cathode to obtain the electrochemical reaction. The phenomena of diffusion interest also the hydrogen that feeds the anode compartment only that they are not so high to result in losses equal of those obtained at the cathode, which as we have seen in practice tend to infinity at certain values current density.

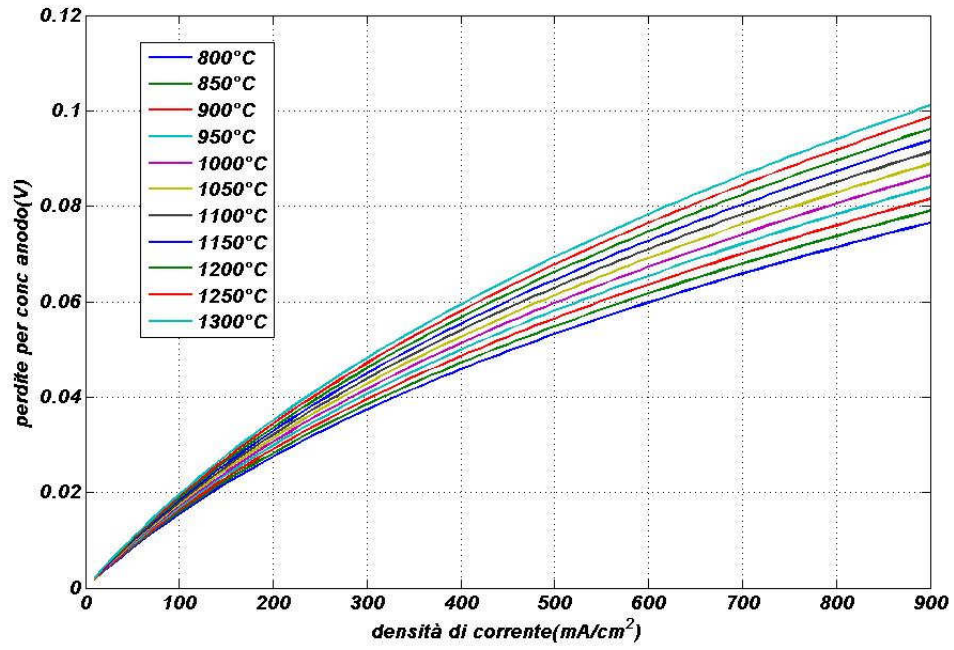


Figure I. 12: Anodic Concentration polarization function of Current density at various temperature.

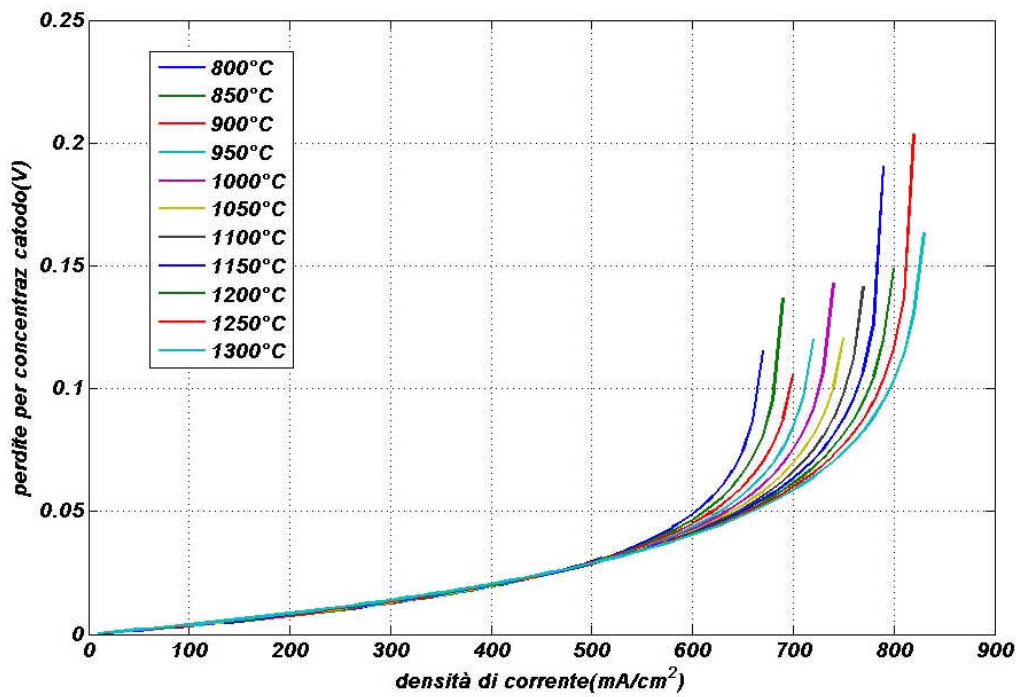


Figure I. 13: Perdite per concentrazione catodiche al variare della temperatura

	UM	1	2	3	4	5	6	7	8	9	10	present
A-electrolyte	ohm cm	0,00294	$10\exp(1092(1/T-1/1273,15))$	0,00294	/	/	/	0,00294	0,00294	/	/	0,00294
A- anode	ohm cm	0,00298	0,00298	0,00298	/	/	/	0,00298	0,00298	/	/	0,00298
A - cathode	ohm cm	0,00814	0,00814	0,00814	/	/	/	0,00811	0,00811	/	/	0,00811
A - interconn	ohm cm	/	/	0,1256	/	/	/	0,1256	0,1256	/	/	0,1256
B - electrolyte	K	-10350	$10\exp(1092(1/T-1/1273,15))$	-10350	/	/	/	-10350	-10350	/	/	-10350
B- anode	K	1392	1392	1392	/	/	/	1392	1392	/	/	1392
B - cathode	K	-600	-600	-600	/	/	/	-600	-600	/	/	-600
B - interconn	K	/	/	-4690	/	/	/	-4690	-4690	/	/	-4690
γ , anode	mA/ cm ²	2,13E+07	/	/	5,7E6/2, 9E7	/	/	/	/	/	/	2,90E+07
γ , cathode	mA/ cm ³	1,49E+07	/	/	7*E8/7E 7	/	/	/	/	/	/	7,00E+07
E_{act} , anode	kJ/K mol	110000	/	/	140000/ 120000	/	/	/	/	115781	/	110000
E_{act} , catode	kJ/K mol	110000	/	/	16000/1 20000	200000	/	/	/	157659	/	130000
δ anode	cm	0,03	0,01	0,01	0,01	0,01/0,0 05	0,075/0,00 5	0,015	0,015	/	/	0,01

δ cathode	cm	0,035	0,022/0,007/0,022	0,19	0,005	0,2/0,013	0,005	0,2	0,2	/	/	0,19
δ elettrol	cm	0,017	0,004	0,004	0,018	0,004/0,002	0,004/0,05	0,004	0,004	/	/	0,004
δ int	cm	/	/	0,004	/	0,004/0,007	/	0,004	0,01	/	/	0,004
L tube	cm	/	50/30/150	50	/	150/25	/	0,004	/	/	/	50
K anode	W/mK	11	/	/	2	4	/	/	/	/	/	/
Kcathode	W/mK	2,7	/	/	2	4	/	/	/	/	/	/
K electrolyte	W/mK	6	/	/	2	4	/	/	/	/	/	/
K tubesost	W/mK	1,1	/	/	/	/	/	/	/	/	/	/
K tubeair	W/mK	1,1	/	/	/	10,4	/	/	/	/	/	/
K interconn	W/mK	/	/	/	0,855	/	/	/	/	/	/	/
θ a anode		/	/	/	2	/	/	/	/	/	/	2
θ c anode		/	/	/	1	/	/	/	/	/	/	1
θ a cathode		/	/	/	1,4	/	/	/	/	/	/	1,4
θ c cathode		/	/	/	0,6	/	/	/	/	/	/	0,6
i_1	mA/cm ²	/	/	/	/	/	/	/	345	/	/	900

Table I. 5: Basic Parameters for the different simulation models

1.5. Polarization Curve

The analysis of any electrochemical fuel cell performance are usually summarized diagramming the well-known polarization curve that, expressing the characteristic trend of voltage as a function of current density, show qualitative and quantitative trend of losses and the total voltage of the cell, changing the project and operational parameters.

In the previous sections have been introduced models to simulate the fuel cell polarization. Therefore below will be discussed the results of the combination of these models:

- Butler-Volmer for activation polarization;
- Knudsen and binary diffusion for concentration polarization;
- Nisancioglu for ohmic polarization,

in order to obtain the highest possible level of detail in the modeling of one-SOFC reactor, as described in the next sessions.

The model is able to provide reliable results. The results obtained by this model were validated by the experimental data available in literature [Singhal (Figure I.14)].

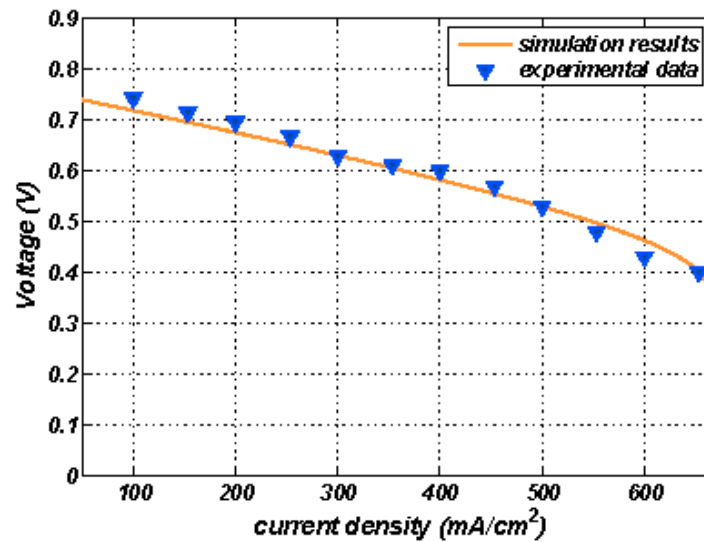


Figure I. 14: Validation of the Electrochemical model

A detailed approach that takes into account more accurate models for calculating the polarizations, is able to show how changes the electrochemical performance of fuel cell varying the most common geometric and constructive parameters of the SOFC (thickness of the anode, cathode, electrolyte, interconnections, length and diameter of the cell, tortuosity, porosity etc).

With this model can be realized a sensitivity analysis of the electrochemical performance of the cell. From a base configuration of the SOFC, it is possible to vary the geometric and operational parameters of the cell. The values of the parameters used in the case of a basic configuration are presented in Table I.6. Figure I.15 shows the trend of the open circuit voltage of the cell, as well as the various losses and then the effective cell voltage as a function of current density, once set the values of temperature and pressure of the cell.

Parameter	value	Measure Unit
Cell Length	100	cm
Tortuosity	5.5	/
Porosity	50	%
Anode Thickness	0.01	cm
Cathode Thickness	0.22	cm
Electrolyte Thickness	0.004	cm
Interconnection Thickness	0.0085	cm
Cell Diameter	1.56	cm
Ainterconn./Acell	0.097	/
Anode Pressure	10	bar
Cathode Pressure	10	bar
Cell Temperature	1000	°C
x_{H_2O} anode inlet	0.01	/
x_{H_2O} anode outlet	0.3	/
x_{H_2} anode inlet	0.2	
x_{H_2} anode outlet	0.15	/
x_{O_2} cathode inlet	0.21	/
x_{O_2} cathode outlet	0.17	/

Table I. 6: Basics parameters used for a SOFC simulation

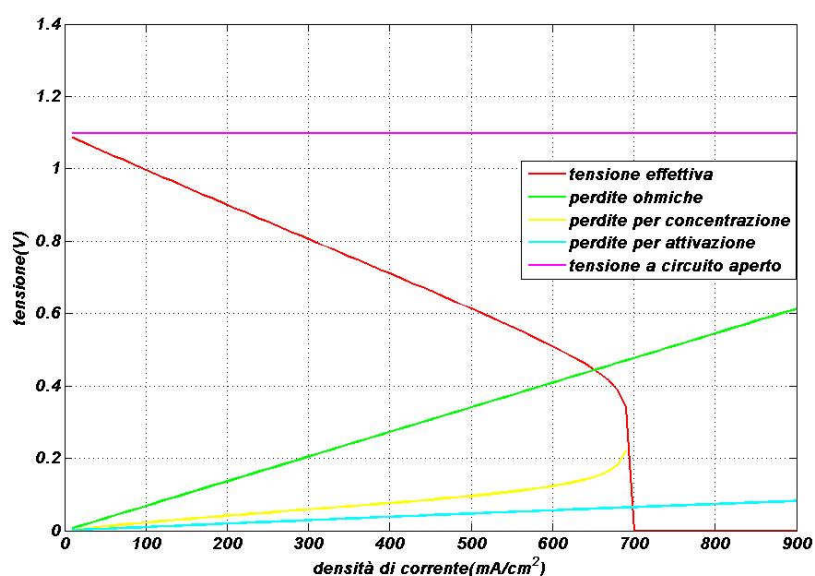


Figure I. 15: Effective SOFC voltage trend and fuel cell losses, function of current density (basic config.)

In this way it is possible to evaluate the influence that different types of losses have on the cell potential. It is clear that, for the type of fuel cell considered, the role of ohmic losses is dominant, at least until the operative current density approach the value of the limit current density where the concentration losses rises asymptotically.

The model can predict the behavior of the polarization curve as a function of operating parameters such as temperature and pressure inside the cell, molar flow of fluids, as well as geometric parameters such as diameter and length of the cell, tortuous and porosity of anode and cathode, thickness of anode, cathode and electrolyte, length of interconnections, etc.

1.6. Pre-Reformer

One of the main advantages of fuel cells operating at high temperature, and in particular of SOFC, is the possibility to realize the reforming process within the cell, supported by the heat produced by the cell's electrochemical reaction.

However, a reforming process entirely "internal" is very difficult to achieve in practice because of lead hazards for the safe operation of the cell and also lead to a reduction of efficiency. Indeed, we must consider that:

- natural gas also included a small fraction of complex hydrocarbons that must undergo a process of "cracking" before entering the cell, because they could not be efficiently converted to hydrogen inside the cell itself;
- if the reforming process occurs entirely within the fuel cell, in the initial part of the anode there is no hydrogen available for the electrochemical reaction, and on this part would be only an endothermic reforming reaction. This eventuality should to be avoided because it leads to a reduction in the active area of the cell.

Therefore, the gas mixture at the inlet of the anode will come from the outlet of a pre-reformer, where is already present partly H_2 , available for the electrochemical reaction, and all complex hydrocarbon have already undergone a process of "cracking".

The pre-reformer consists of a number of tubes placed inside an envelope (consisting of a coaxial tube) and filled with a special catalytic material. The fuel flows within the tubes, while outside the hot gases, coming from the combustion chamber, provide the heat necessary for the reforming process, which is generally strongly endothermic. The outline of a tube in the pre-reformer is shown in the Figure I.16.

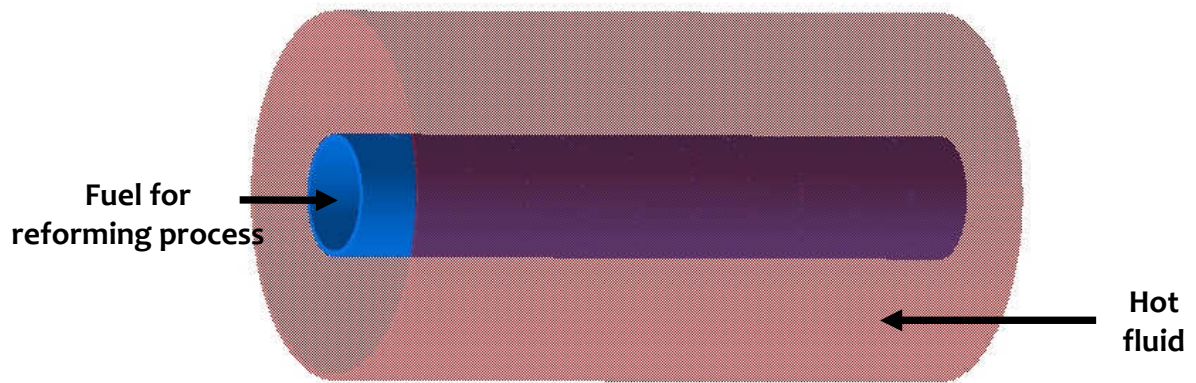


Figure I. 16: Pre-reformer tube scheme.

The "hot side" is feed with the flow at the outside of the combustion chamber placed on top of the SOFC stack, or the fluid at the end of the counter flow heat exchanger used to pre-heat the air in the injection tube.

The simulation of the pre-reformer component is extremely complex, because there are two different kinds of problems:

- Calculation of the degree of reaction of the process;
- Calculation of the heat exchange between reagent fluid and hot fluid.

In this case has been used an approach extremely detailed, based on a 1-D model using a system of algebraic non-linear equations that, though more costly in terms of complexity, is able to estimate the profiles of temperature, pressure and chemical composition in both sides of the component.

The calculation of the degree of reaction of the reforming process is based on the evaluation of the equilibrium constants. In this work these constants were evaluated by thermodynamic considerations, avoiding the use of correlations that have camps of validity often too limited.

The equation that define the equilibrium constant K is:

$$K = \exp\left(\frac{-\Delta G^o}{RT}\right) \quad (\text{I.46})$$

Often, can be used an alternative expression:

$$\ln K = \frac{-\Delta G^o}{RT} \quad (\text{I.47})$$

G_i^o is a property of the pure species, which in standard condition, to a certain pressure p_0 depends only on the temperature; it follows that ΔG^o and therefore K (equation (I.46)) are functions only of the temperature.

Despite its dependence on temperature, K is considered the equilibrium constant of reaction and ΔG^o the standard variation of the Gibbs energy of the reaction, easily calculable extracting the values of enthalpies and entropies.

Analyzing the trend of the constant of equilibrium with the temperature you may notice that when the reaction is exothermic, ΔG^o is growing and consequently K is decreasing, conversely if the reaction is endothermic, ΔG^o decreases and the constant of equilibrium grows (as shown in the figure below). Note that the only two reactions with a growing trend are the reactions of steam reforming showing a marked endothermic characteristic.

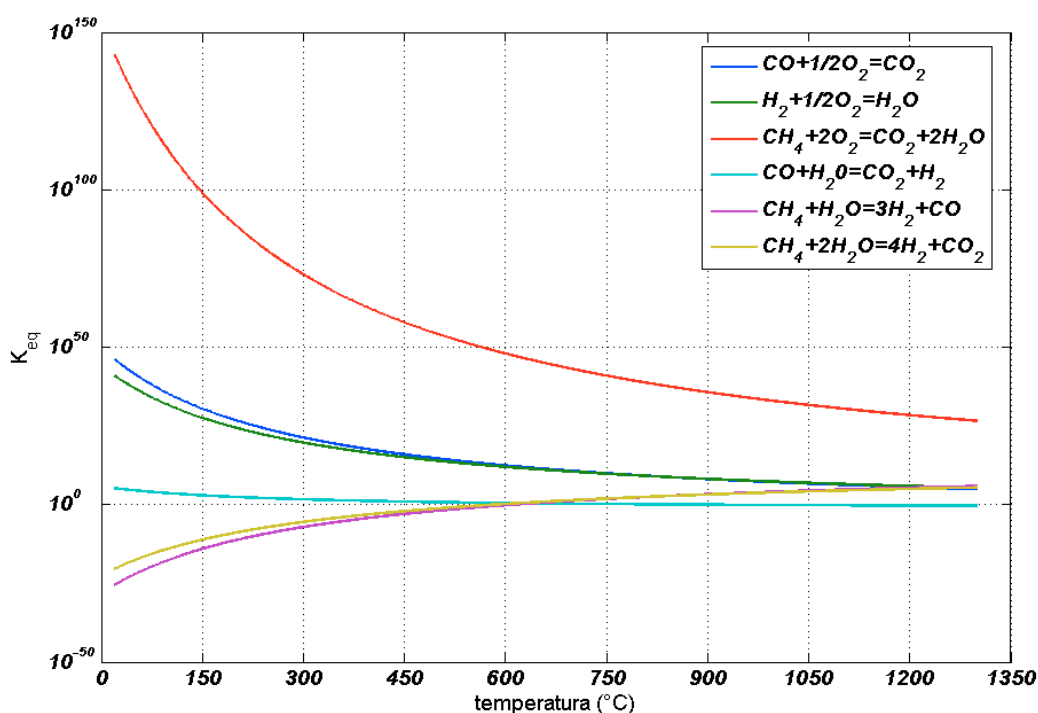


Figure I. 17: Trend of the equilibrium constant of reforming reaction with the temperature.

1.6.1. One-Dimensional Model

In this section it will be described accurately the theoretical formulation for the development of the 1-dimensional model of pre-reformer, paying particular attention to chemical-kinetic model, to heat exchange model and to the calculation of the pressure drop. These three models will be integrated in the simulation procedure of the entire component. The 1-dimensional model can simulate in an extremely fast and efficient way the pre-reformer operation, providing important information about trends in temperature, pressure and chemical composition along the pre-reformer itself. Such information is also

extremely important for the designer of the component that have to select the geometric and operational parameters in order to reduce the thermal stress, balance the speed of chemical processes and heat exchange, etc.

In general this model is a kind of simplified method of finite volumes: the component pre-reformer, or rather an elementary unit, is divided in n "slices", at each of which are applied mass and energy balances and calculation models of chemical kinetics and pressure drop. The difference between this discretization technique and method of finite volumes is that in this case the coefficients of transmission and pressure drop are evaluated through correlations without using the differential equations that govern the phenomenon from the thermo-fluid dynamic perspective.

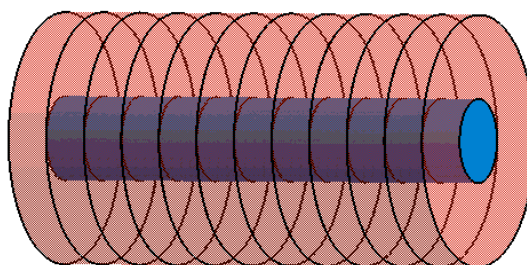


Figure I. 18: 1-D discretization of pre-reformer

In particular, it will establish a field of attempt temperature, at which, applying the model of pressure drop, will be possible to calculate the field of pressure; fields of temperature and pressure will be used by the kinetic-chemical model determining the chemical compositions of the fluid in each node. Finally, will be recalculated the temperature, based on the energy balance equations, using algorithms for iterative solution of systems of nonlinear equations.

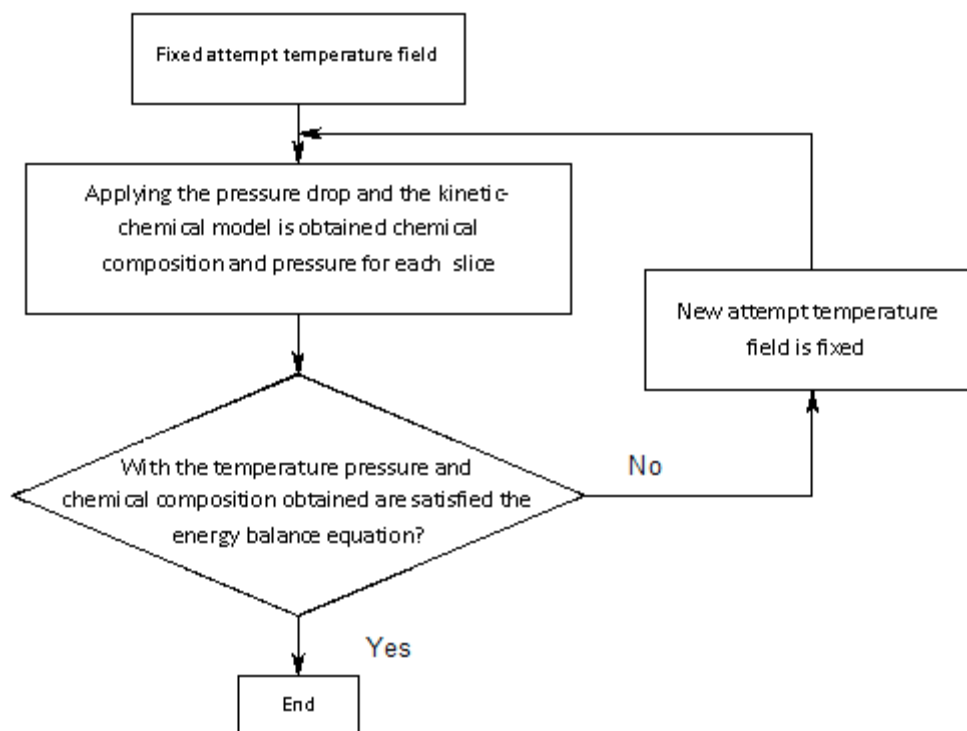


Figure I. 19: Simulation Flow Chart of the implemented model

Below will be described the theoretical formulation and some of the main results of this model.

1.6.2. Chemical kinetics

Assuming negligible the content of heavy hydrocarbons, the steam reforming process involves only methane.

However, in parallel with the above reaction may also be other phenomenon, often unwanted. Among these, the most dangerous is the so-called "carbon deposition": during the process of methane reforming, it could be, in lateral areas of the pre-reformer, or of the cell itself, small availability of steam that cause the carbon deposition phenomena, in accordance with the following equation:



This phenomenon must be absolutely avoided because, even if it is produced hydrogen for cell operation, the inert carbon, laying, occupies the chemical reaction sites (or electrochemical in SOFC) and inhibits the system operation, thereby reducing the useful volume of the reactor. The risk of carbon deposition can be avoided by working with an excess of steam; therefore, is considered the Steam to Carbon ratio:

$$SC = \frac{n_{H_2O}}{n_{CH_4}} \quad (I.49)$$

So to avoid this negative phenomenon of carbon deposition it is sufficient to operate in high Steam to Carbon ratio: usually is used at least a value equal to 2.

The Steam Methane Reforming is slow and strongly endothermic while the Shift Reaction is fast and weakly exothermic, so the whole process of reforming is dominated by the endothermic reforming reaction of methane which requires heat supplied by other sources.

The simplification assumptions used in the chemical kinetic simulation of pre-reformer are as follows:

- is analyzed a single tube of the reactor and all the tubes that form the reactor have a behavior independent of each other;
- gases have ideal behavior;
- the fuel flow inside the channels is the type plug-flow;
- there is no phenomenon of carbon deposition thanks to an adequate value of the steam to fuel ratio.

One of the main advantages of using a 1 dimensional model is the possibility of removing a number of simplifying assumptions that is necessary to implement in a 0-D model.

Indeed it is possible to remove the following assumptions:

1. use of average specific heat;
2. Using average coefficients of heat exchange;
3. Calculation of properties mediated between inlet and outlet;
4. kinetic calculation implemented at the average temperature and pressure of the pre-reformer;
5. assumptions of shift reaction at equilibrium;
6. parallel calculation of kinetic and equilibrium of reforming reaction.

In particular, steps 1 through 4 are a direct consequence of the implementation of a 1-D model, through which you can appreciate the change of property along the axial coordinated. The remaining points, however, refer to the possibility of using theories more accurate to calculate the degree of reaction of the reforming process.

The equilibrium of a chemical reaction is an asymptote, which can be reached only after an infinite time. It is also true that most chemical reactions will achieve values very close to those of equilibrium in engineering appreciable time: this circumstance is a direct

function of the slope of the curve of the degree of reaction, and how much tends to the asymptotic equilibrium value.

Therefore, in recent years, the theory of chemical kinetics will be abandoning the parallel kinetic-equilibrium technique, to move towards the use of models that simultaneously consider both equilibrium and chemical kinetics, structured in such a way that the value of equilibrium is achieved only asymptotically. The above consideration is clearly visible by qualitative representation provided in the figure below.

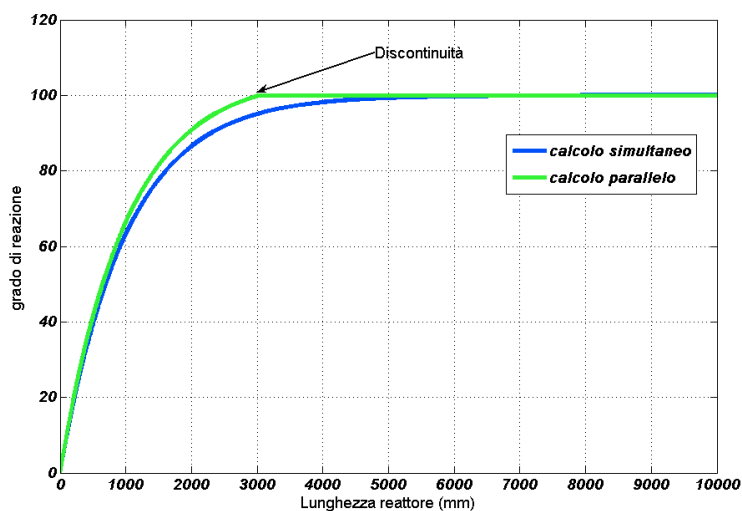


Figure 1.20: Qualitative representation of both methodologies for degree of reaction calculation

It must also consider that the basic assumptions of equilibrium of the shift reaction is approximate because, although the reaction occurs very quickly, in the early sections of the tube, however, it has not yet reached the condition of equilibrium. Moreover, while rapidly reaching that condition, it cannot be considered stable as it is continuously modified by changes in concentration of certain substances during the reaction of steam reforming.

To avoid that, was sought in literature a calculation model that condenses all the above requirements.

This is for example one that was developed by Zafir and Gavrilidis and that can be considered one of the most accurate and comprehensive currently available.

Are considered the three reactions of reforming, namely:

- Steam Methane Reforming;



- Shift Reaction;



- Demethanation.



Note that the reaction of Demethanation can be obtained by adding the reaction (4.238) and (4.239). Would be wrong to reach the conclusion that it is redundant, since we have to consider that the three aforementioned reactions are not at equilibrium. Please note, that you can make arbitrary linear combinations of chemical equations, when the reactions in question are at equilibrium. When this condition is not verified, it is clear that the equation (I.52) adds information to the (I.50) and (I.51).

The speeds of these reactions are provided by the following equations:

$$r_1 = \frac{\frac{k_1}{p_{H_2}^{2.5}} \left[p_{CH_4} p_{H_2O} - \frac{p_{H_2}^3 p_{CO}}{K_{eq_1}} \right]}{DEN^2} \quad (I.53)$$

$$r_2 = \frac{\frac{k_2}{p_{H_2}} \left[p_{CO} p_{H_2O} - \frac{p_{H_2} p_{CO_2}}{K_{eq_2}} \right]}{DEN^2} \quad (I.54)$$

$$r_3 = \frac{\frac{k_3}{p_{H_2}^{3.5}} \left[p_{CH_4} p_{H_2O}^2 - \frac{p_{H_2}^4 p_{CO_2}}{K_{eq_3}} \right]}{DEN^2} \quad (I.55)$$

where:

$$DEN = 1 + K_{CO} p_{CO} + K_{H_2} p_{H_2} + K_{CH_4} p_{CH_4} + K_{H_2O} \frac{p_{H_2O}}{p_{H_2}} \quad (I.56)$$

The frequency factors are often related to the temperature through of exponential equations, linked to the respective energies of activation:

$$k_i = A_i \exp\left(\frac{-E_i}{RT}\right) \quad (I.57)$$

Obviously:

$K_{eq,j}$ is the equilibrium constant of j reaction;

r_i is the speed of the i chemical reaction measured in $mol/(h \cdot g_{cat})$

Results also that $i = \text{reactions } 1, 2, 3; \quad j = CO, H_2, CH_4, H_2O.$

In this way, in order to calculate the speed of reactions, are important both the kinetic and the equilibrium of individual reactions thus avoiding the discontinuity of the function r_i , typical of parallel kinetic-equilibrium calculation.

The values of kinetic parameters are listed below:

Reaction N.	A_i $[mol \cdot MPa^{0.5} \cdot (g_{cat})^{-1} \cdot h^{-1}]$	E_i $[kJ \cdot mol^{-1}]$
1	$1,336 \cdot 10^{15}$	240,1
2	$1,955 \cdot 10^7$	67,13
3	$3,226 \cdot 10^{14}$	243,9

Table I. 7: Parameters of the Kinetic model

The mass balance is carried out for every component of the mixture and the three reactions under investigation, not having the same behavior, must be analyzed separately. Named r_1 the number of moles reacted by reaction 1, r_2 the number of moles reacted by reaction 2, and r_3 the number of moles reacted by reaction 3, it is possible to calculate the chemical composition at the outlet of the single slice by means of simple stoichiometric balances:

$$\forall i = 1 : n - 1 \quad \left\{ \begin{array}{l} n_{CH_{4,i+1}} = n_{CH_{4,i}} - r_{1,i} - r_{3,i} \\ n_{CO_{i+1}} = n_{CO_i} + r_{1,i} - r_{2,i} \\ n_{H_{2,i+1}} = n_{H_{2,i}} + 3r_{1,i} + r_{2,i} + 4r_{3,i} \\ n_{O_{2,i+1}} = n_{O_{2,i}} \\ n_{N_{2,i+1}} = n_{N_{2,i}} \\ n_{CO_{2,i+1}} = n_{CO_{2,i}} + r_{2,i} + r_{3,i} \\ n_{H_2O} = n_{H_2O_i} - r_{1,i} - r_{2,i} - 2r_{3,i} \end{array} \right. \quad (I.58)$$

The application of the model of Zanfir et al. turns out particularly interesting if implemented in a model such as described before, because is capable of showing, in extremely clear way, the trend of the speed of reactions along the axial direction of reactor. Therefore, the pre-reformer has been subdivided in n elementary cells, with regular spacing, obtained intersecting the coaxial tubes with $n - 1$ plans perpendicular to the axis of the cylinders. After all the structure brought back in Figure I.21 is obtained.

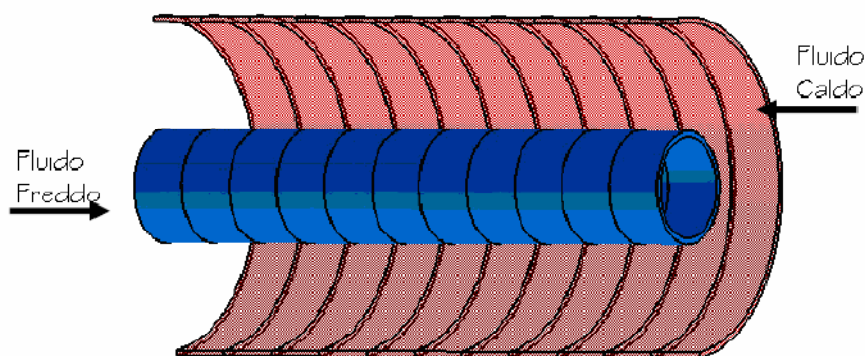


Figure I. 21: Discretization of pre-reformer section

Now it is possible to describe in the detail the type of discretization adopted for the pre-reformer. Fixed the inlet from the part of the tube where the fuel is introduced, that is the outlet of the hot fluid coming from the combustor, whose heat is used in order to sustain the process of reforming, we previously subdivide the obtained dominion in equidistant N slices; each one therefore will be constituted from a part that belongs to the external tube and another part that belongs instead to the inner one. For simplicity we suppose that the external wall of the tube is adiabatic and therefore there is no heat exchange with the outside.

By this point, starting from the first slice (fuel inlet), based on what said previously, are obtained, even if as attempt values, the temperature field and pressure. In fact, attempt temperature field is assigned at the beginning with the inlet pressures of the hot and cold fluid. Applying the pressure drop model, known the temperature field, the field of attempt pressures is gained. Always referring to the first slice, the mass flow and the chemical compositions of both the flows turn out known (boundary conditions). Applying therefore the previously equations it is possible to calculate the chemical composition of the fuel at the outlet of the first slice, that is the inlet of the second one. Such last data constitutes the boundary condition for the calculation of the chemical composition of the fuel at the outlet of the second slice. The procedure comes iterative till the n slice in which the pre-reformer has been subdivided. Formalizing:

$$\begin{aligned}
& \forall i = 1 : n - 1 \\
& \left\{ \begin{array}{l}
r_{1,i} = f\left(p_{k,i+1}, \frac{t_i + t_{i+1}}{2}\right) \quad k = 1 \dots 7 \\
r_{2,i} = g\left(p_{k,i+1}, \frac{t_i + t_{i+1}}{2}\right) \quad k = 1 \dots 7 \\
r_{3,i} = h\left(p_{k,i+1}, \frac{t_i + t_{i+1}}{2}\right) \quad k = 1 \dots 7
\end{array} \right. \\
& \left\{ \begin{array}{l}
n_{CH_{4,i+1}} = n_{CH_{4,i}} - r_{1,i} - r_{3,i} \\
n_{CO_{i+1}} = n_{CO_i} + r_{1,i} - r_{2,i} \\
n_{H_{2,i+1}} = n_{H_{2,i}} + 3r_{1,i} + r_{2,i} + 4r_{3,i} \\
n_{O_{2,i+1}} = n_{O_{2,i}} \\
n_{N_{2,i+1}} = n_{N_{2,i}} \\
n_{CO_{2,i+1}} = n_{CO_{2,i}} + r_{2,i} + r_{3,i} \\
n_{H_2O} = n_{H_2O_i} - r_{1,i} - r_{2,i} - 2r_{3,i}
\end{array} \right. \quad (I.59)
\end{aligned}$$

Note that the (4.246) is a system of nonlinear equations, not explicit because r_i function contain the partial pressures at the outlet that depends to the composition at the outlet, or by the same r_i . In order to apply the pressure drop model is necessary to know the properties at entry and exit of the single slice (including the chemical composition of output). It will therefore be necessary to use algorithms to solve systems of non-linear algebraic equations. It could be an explicit solution otherwise, if the r_i functions were evaluated at the partial pressure at the inlet of the i slice, but introducing an error of calculation that is greater as lower is the number of slices of discretization.

1.6.3. Calculation of pressure drop and heat exchange coefficients

As the pre-reformer is structured, we must distinguish the hot fluid side by the other side where the fuel is reformed: therefore, indicate with 1, the properties related to hot fluid and with 2 those relating to the fluid that need to be reformed.

Indicating with n the number of tubes that compose the pre-reformer, suppose that the mass of hot fluid and fuel at the inlet is divided equally within these tubes, then it is possible to write that both the hot fluid mass flow and fuel mass flow are given by:

$$\dot{m}_{1,2n} = \frac{\dot{m}_{1,2}}{n} \quad (I.60)$$

where $\dot{m}_{1,2}$ are the mass flow of hot fluid and fuel, respectively, which feed the entire pre-reformer.

It follows that the average velocity of the hot fluid and fuel within each slide is given by:

$$w_{1,2} = \dot{m}_{1,2n} / \rho_{1,2} A_{1,2n} \quad (\text{I.61})$$

where ρ_1 is the density of the fluid, mediated between input and output of single slice. Starting with the analysis of what happens in the zone where is flowing the hot fluid, indicate with A_{1n} the cross-section area passed by the hot fluid in his motion, or the area of circular cross section between the internal cylinder (where the fuel flows to be reformed) and external cylinder, where is flowing the hot fluid. So indicated with D_{react} the diameter of the internal cylinder and with D_{shell} the diameter of the outside cylinder will be:

$$A_{1n} = \pi \frac{(D_{shell}^2 - D_{react}^2)}{4} \quad (\text{I.62})$$

For the calculation of both heat exchange coefficients and friction factors it is necessary to use the Reynolds, Prandtl and Nusselt numbers, whose expression are reported below, in order to obtain these dimensional parameters.

D_1 is the equivalent diameter for the hot fluid:

$$D_1 = 4 \frac{A_{1n}}{P_{b1}} \quad (\text{I.63})$$

with P_{b1} perimeter lapped by the hot fluid equal to $\pi (D_{shell} + D_{react})$.

Regarding the number of Nusselt we must distinguish between two cases:

If $Re_1 < 2300$, then the number of Nusselt will be obtained by integration, on the length of the tube, of the local number of Nusselt provided by the following equation:

$$Nu_1 = 3,66 + \frac{(0,104 D_1 Re_1 Pr_1 / L_i)}{(1 + 0,016 (D_1 Re_1 Pr_1 / L_i)^{0,8})} \quad (\text{I.64})$$

and in this case the values of the coefficient of transmission and the friction factor are given respectively by:

$$h_1 = Nu_1 k_1 / L_i \quad (\text{I.65})$$

$$f_1 = 16 / Re_1 \quad (\text{I.66})$$

with L_1 axial length of the cylinder;

If $Re_1 \geq 2300$ than,

$$Nu_1 = 0,0214 (Re_1^{0,8} - 100) Pr_1^{0,4} \quad (\text{I.67})$$

and the values of the coefficient of transmission and the friction factor are given respectively by the equation (I.65) and

$$f_1 = 0,046 \text{ Re}_1^{-0,2} \quad (\text{I.68})$$

Turning now to the part of pre-reformer where the fuel flows to be reformed, the formulas to apply are almost the same except that we have to consider different expression of certain sizes such as:

- The cross-sectional area passed by the fuel and indicated with A_{2n} , that is precisely the area of the orthogonal section of the internal tube in the pre-reformer, is therefore equal to $A_{2n} = \pi \frac{D_{react}^2}{4}$;

- For the equivalent diameter will be always valid the formula $D_2 = 4 \frac{A_{2n}}{P_{b2}}$ but

this time, being $P_{b2} = \pi D_{react}$, it will be obtained that $D_2 = D_{react}$.

The correlation to be used to calculate the number of Nusselt is:

$$Nu_1 = 3,66 + \frac{(0,104 D_1 \text{Re}_1 \text{Pr}_1 / L_i)}{\left[1 + 0,016 (D_1 \text{Re}_1 \text{Pr}_1 / L_i)^{0,8}\right]} \quad (\text{I.69})$$

The friction factor is calculated using instead an equation like this:

$$\begin{aligned} \text{Re} < 2300 \quad f &= \frac{\Omega}{\text{Re}} \\ \text{Re} > 2300 \quad f &= 0.046 \text{ Re}^{-0.2} \end{aligned} \quad (\text{I.70})$$

The coefficient Ω depends on the ratio D_{ext} / D_{int} :

D_{ext} / D_{int}	Ω
$D_{ext} / D_{int} < 0.05$	86.3
$0.05 < D_{ext} / D_{int} < 0.1$	89.4
$0.1 < D_{ext} / D_{int} < 0.5$	95.2
$0.5 < D_{ext} / D_{int} < 0.75$	95.9
$D_{ext} / D_{int} > 0.75$	96

Table I. 8: Annulus Friction Factor calculation

At this point, can be calculated the heat transfer global coefficient, U:

$$UA = \frac{1}{\frac{1}{h_1 A_1} + \frac{1}{h_2 A_2} + \frac{s}{k A_{m \log}}} \quad (\text{I.71})$$

the pressure drop for both the side of the hot fluid and reforming fuel, can be calculated under the generic equation:

$$\Delta p_{1,2} = f_{1,2} \frac{L_i}{D_{1,2}} \frac{w_{1,2}^2}{2} \quad (\text{I.72})$$

The calculation of the friction factors and heat transfer coefficients is extremely accurate because it is possible to evaluate the properties locally without mediate along the control volume.

The correlations used for the calculation of these coefficients are referred to local values of the dimensional numbers. In summary the procedure for calculating the field of pressure and heat transfer coefficients can be summarized by the following equations:

$$\begin{aligned} \forall i &= n - 1 : -1 : 1 \\ \text{Re}_{h,i} &= f \left(\frac{t_{h,i} + t_{h,i+1}}{2}, p_{h,i}, \overrightarrow{\beta}_{h,i} \right) \\ \text{Pr}_{c,i} &= g \left(\frac{t_{h,i} + t_{h,i+1}}{2}, p_{h,i}, \overrightarrow{\beta}_{h,i} \right) \\ \text{Nu}_{h,i} &= h(\text{Re}_{h,i}, \text{Pr}_{h,i}) \\ \overline{h}_{h,i} &= \phi(\text{Nu}_{h,i}, k_{h,i}) \\ U_i &= \frac{1}{\frac{1}{\overline{h}_{h,i}} + \frac{s_{tubo}}{k_{tubo,i}} + \frac{1}{\overline{h}_{c,i}}} \\ p_{h,i+1} &= p_{h,i} - \Delta p_{h,i} \end{aligned} \quad (\text{I.73})$$

Obviously, on the hot side the procedure must be implemented steps backward:

$$\begin{aligned} \forall i &= 1 : n - 1 \\ \text{Re}_{c,i} &= f \left(\frac{t_{c,i} + t_{c,i+1}}{2}, p_{c,i}, \overrightarrow{\beta}_{c,i} \right) \\ \text{Pr}_{c,i} &= g \left(\frac{t_{c,i} + t_{c,i+1}}{2}, p_{c,i}, \overrightarrow{\beta}_{c,i} \right) \\ \text{Nu}_{c,i} &= h(\text{Re}_{c,i}, \text{Pr}_{c,i}) \\ \overline{h}_{c,i} &= \phi(\text{Nu}_{c,i}, k_{c,i}) \\ p_{c,i+1} &= p_{c,i} - \Delta p_{c,i} \end{aligned} \quad (\text{I.74})$$

Note that at each iteration should be applied at the same time the model of pressure drop and the chemical-kinetic model. In fact, for the generic i slice, the model of pressure drop provides the pressure at the entrance of the $i+1$ slice (data used for the chemical-

kinetic calculation of the slice $i+1$); similarly kinetic model will provide the chemical composition at the input of the slice $i+1$ that will be used for calculating the pressure drop in the slice $i+1$.

This condition makes the system of equations of the chemical-kinetic model to solve nonlinear not explicit requiring the implementation of algorithms for solving systems of nonlinear algebraic equations.

1.6.4. Heat exchange model

The model of heat exchange is the external loop of the logic cycle shown in Figure I.19. It is based on balance equations of energy along both the axial and the radial direction of each slice of pre-reformer. For each slice is written a first equation assessing the balance between the heat released by the hot fluid and received by the cold fluid (including consideration of "generations", due to chemical reactions); a second equation instead links the heat of the first equation to the temperature difference between hot fluid and cold fluid through the coefficient of heat exchange.

Obviously this two equations can be written only for half of the control volume, as shown by the plain in yellow in Figure I.22, being symmetrical from a point of view thermodynamic, geometric and of the boundary conditions, and can therefore be considered adiabatic.

Note also that since the discretization of pre-reformer was realized using n equally spaced parallel planes, were obtained $n - 1$ slices. It follows therefore that the temperature field consists of $2n$ values, however the unknowns are $2(n - 1)$ because the temperature of inlet hot fluid and cold fluid are known; simultaneously, the energy balances discussed before give 2 equations for each slice, or totally $2(n - 1)$ equations. Ultimately, it was obtained a system of $2(n - 1)$ equations in $2(n - 1)$ unknowns that allows the calculation of temperature unknowns. The resolution of this system is not the easiest because it is highly non-linear, under the complex dependencies of energetic terms from the temperature (the specific heats, pressures and chemical compositions are dependent on temperature). In general, then there is more than a solution of the system; will be considered acceptable the only one that meets the constraints of the second law of thermodynamic, namely that for each slice, the temperature of hot fluid is greater than the cold fluid. Again, the solution of the non-linear algebraic equations will be entrusted to a

special algorithm based on techniques of optimization of non-linear functions, providing quickly and with reliability the solution required (TOMLAB).

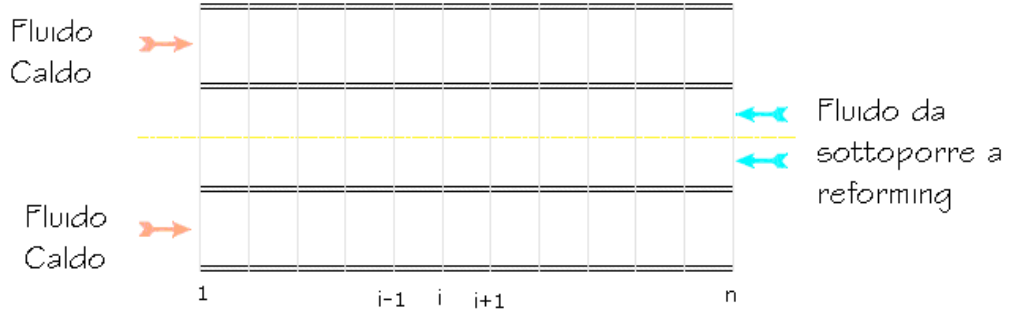


Figure I. 22: Discretization of pre-reformer section with a plane passing through the cylindrical axes

The previous considerations can be formalized by means of the following equations:

$$\forall i = 1 : n - 1$$

$$\begin{cases} \dot{m}_h \left[h_h(t_{h,i}, p_{h,i}, \vec{\beta}_{h,i}) - h_h(t_{h,i+1}, p_{h,i+1}, \vec{\beta}_{h,i+1}) \right] = \\ \sum_{j=1}^3 r_j \Delta h_j + \dot{m}_c \left[h_c(t_{c,i+1}, p_{c,i+1}, \vec{\beta}_{c,i+1}) - h_c(t_{c,i}, p_{c,i}, \vec{\beta}_{c,i}) \right] \\ \dot{m}_h \left[h_h(t_{h,i}, p_{h,i}, \vec{\beta}_{h,i}) - h_h(t_{h,i+1}, p_{h,i+1}, \vec{\beta}_{h,i+1}) \right] = \\ U_i A_i \left[\frac{t_{h,i} + t_{h,i+1}}{2} - \frac{t_{c,i} + t_{c,i+1}}{2} \right] \end{cases} \quad (I.75)$$

1.6.5. Results and discussion

On the base on what described in the previous paragraphs, have been implemented in MATLAB and in TOMLAB one-dimensional models of simulation of the pre-reformer.

The pre-reformer is simulated on the basis of the geometrical data and the thermodynamic boundary conditions, respectively shown in Table I. 9 and Table I. 10.

<i>Parameter</i>	<i>Unit</i>	<i>Value</i>
Tube length	m	0.60
Tube active length	m	0.060
Wall thickness	cm	0.10
Tube diameter	cm	1.70
Shell Diameter	cm	6.00
Number of slices		60

k_{wall} (Conductivity heat transfer coefficient)	W/mK	3
ρ_B catalytic bulk density	(kg/m ³)	50

Table I. 9: Pre-reformer design parameters

Note that it is assumed that a single pre-reformer tube supplies an entire bundle of cells, consisting of 24 SOFC tubes.

Parameter	Unit	Fuel	Hot Gas
Inlet pressure	bar	3.00	2.97
Inlet temp.	°C	800	1050
H_2O molar fract.	/	0.4444	0.0432
CO molar fract.	/	0.0478	0.0000
H_2 molar fract.	/	0.0714	0.0000
O_2 molar fract.	/	0	0.1784
N_2 molar fract.	/	0.0079	0.7572
CO_2 molar fract.	/	0.2063	0.0212
CH_4 molar fract.	/	0.2222	0.0000
Molar flow rate	kmol/s	1.29E-6	2.41e-5

Table I. 10: Pre-reformer boundary conditions

The simulation code allows one to calculate temperature, pressures and chemical compositions along the pre-reformer tube. In addition, results show negligible pressure drops.

: clearly shows that the chemical phenomena (reforming) is much faster than the thermal one (heat exchange between hot fluid and cold fluid).

The value of the temperature of the fluid at the outlet of pre-reformer must be close to the cell operating temperature to avoid heat stress which affects the functioning and durability of SOFC. Therefore, the length of the section devoted to the reforming reactions of the fuel (initial part of pre-reformer) is lower than the total length of the pre-reformer component, and the remaining part is dedicated solely for heat exchange.

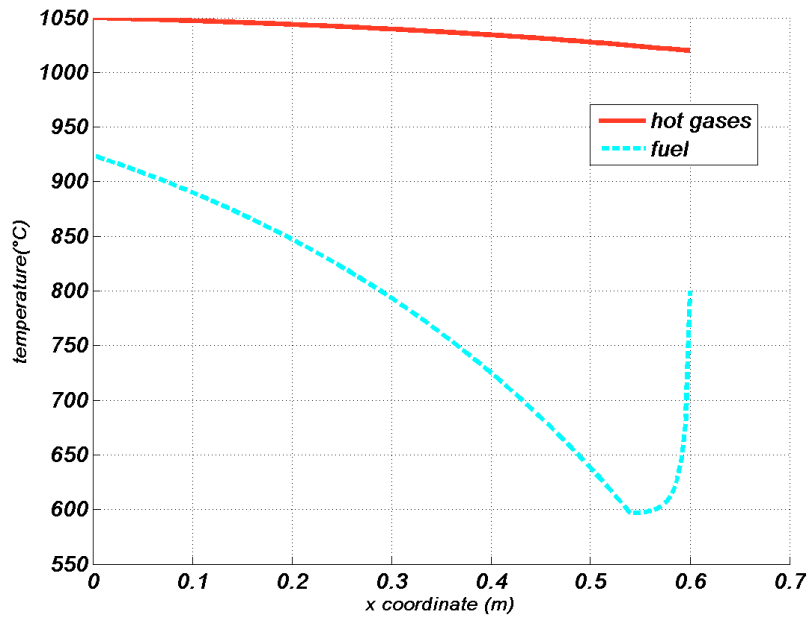


Figure I. 23: Pre-Reformer temperatures

: displays the magnitude of the reforming reactions, showing that the SMR is much faster than the demethanization one and that the shift reaction shows the opposite slope with respect to the remaining reactions. Furthermore, the trend displayed in : clearly depends on the dramatic fuel temperature reduction shown in :. In fact, the higher is the fuel temperature, the higher are the demethanization and SMR reaction rates and the lower is the shift reaction rate. This phenomenon is also emphasized by the reduction of the reactant partial pressures (not shown in figure) due to their consumption. The overall pre-reforming ratio is 27.6%.

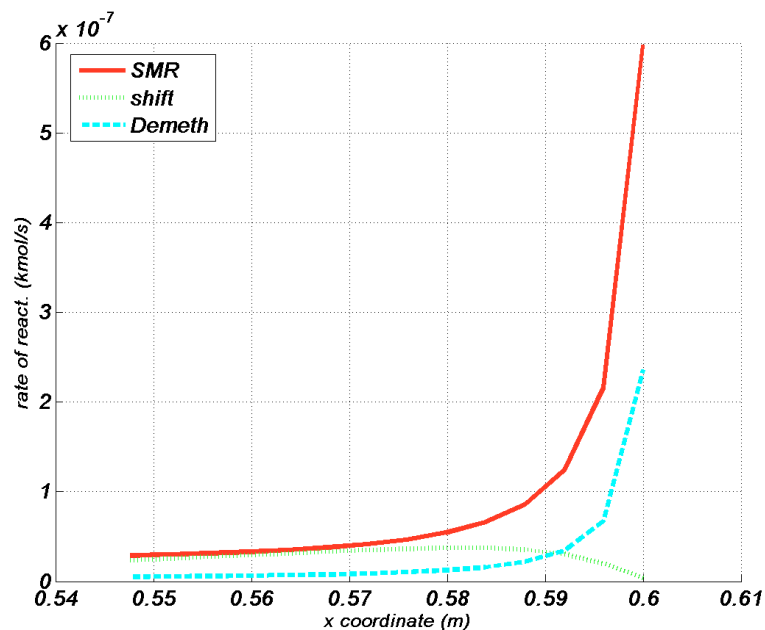


Figure I. 24: Pre-Reformer rates of reaction

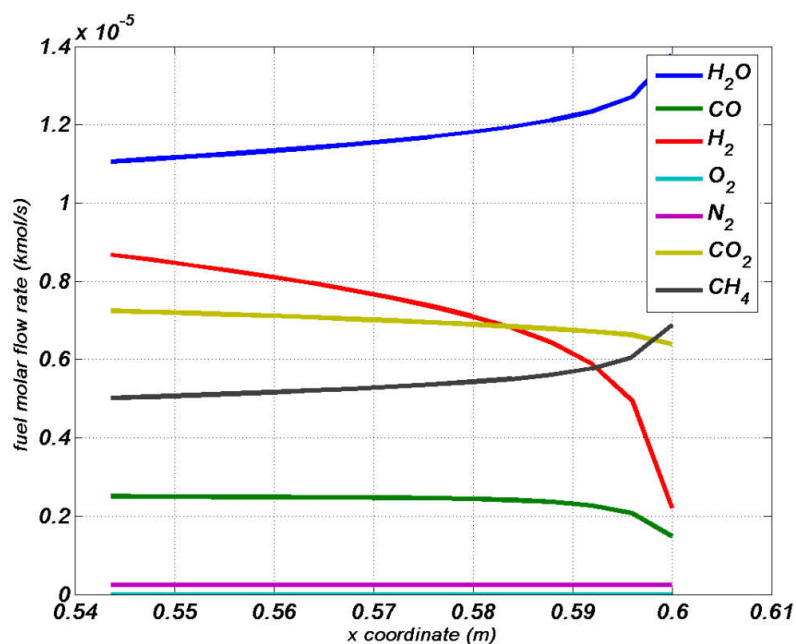


Figure I. 25: Fuel molar flow rate and composition

The Figure I.26 shows the heat absorbed, necessary for the reforming process; the thermal energy is pulled by both the hot fluid flowing in the pre-reformer and by sensitive heat of the reagent fluid. The evolution of this graph reflects the degree of reaction of the SMR. In fact, the heat required by the two reforming reactions is much greater than that yielded by the reaction of shift, so that the thermal power absorbed assume the same trend of the degree of reaction of the two reforming reactions.

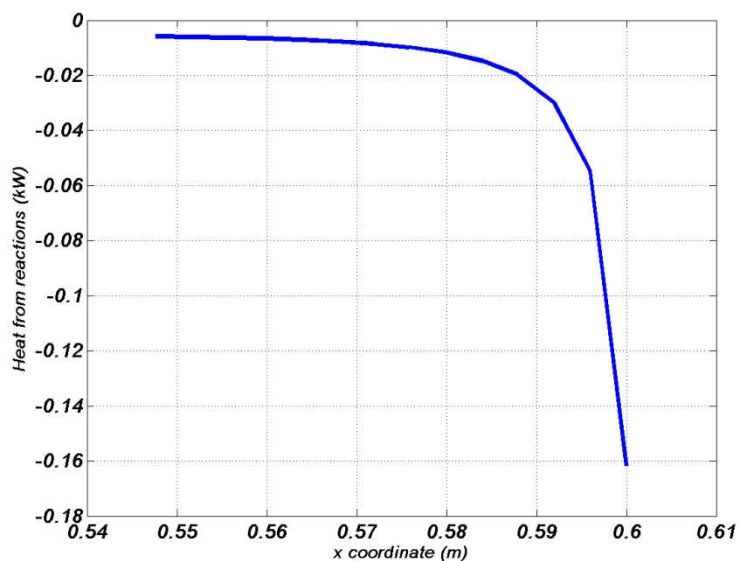


Figure I. 26: Heat produced by reactions

1.6.6. Exergy Balances

The above discussed simulation model returns the complete set of chemical, and thermodynamic parameters along the component pre-reformer. These data are subsequently used in order to perform the exergy [33] balances for each slice of the discretized computational domains. Such exergy balances allows to evaluate the magnitude of the exergy destruction [33]. The exergy balances are performed taking into account all the inlet and outlet exergy flows, concerning the control volume under investigation. Note that for the component under investigation these balances consist of two types of exergy flows:

- i) physical exergy depending on streams mass flow rate, temperature and pressure [6, 7, 33];
- ii) chemical exergy, depending on chemical composition and molar flow rate [6, 7, 14, 33].

No exergy flow due to the heat transfer is considered since all the control volume under investigation is delimited by adiabatic surfaces, as shown in :

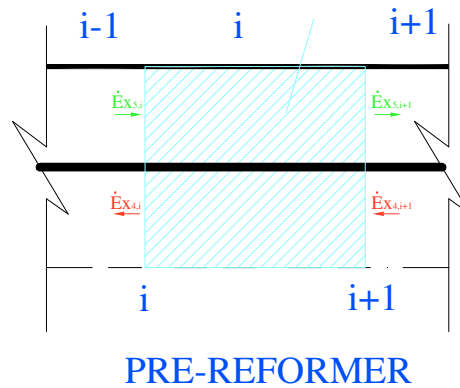


Figure I. 27: Exergy balances control volumes

The exergetic performance of the elementary cell under investigation is evaluated mainly determining the corresponding value of the exergy destruction rate, measuring the magnitude of its irreversibilities. In addition, an exergy efficiency is also defined in order to assess the relative exergetic performance of the elementary cell. Such efficiency is defined as the ratio between the desired exergy and the corresponding exergetic flow. Therefore, the pre-reformer, pre-reformer/heat-exchanger exergetic efficiencies are defined respectively as follows:

$$\eta_{ex,PR} = \Delta \dot{E}x_{chem, fuel} / \Delta \dot{E}x_{hot gases} \quad (I.76)$$

$$\eta_{ex,PR/HE} = \Delta\dot{E}x_{chem,fuel} / \left(\Delta\dot{E}x_{hot\ gases} + \Delta\dot{E}x_{ph,fuel} \right) \quad (I.77)$$

The thermo-chemical calculation allows one to evaluate the exergy (physical and chemical) flows along the component, as shown in .:

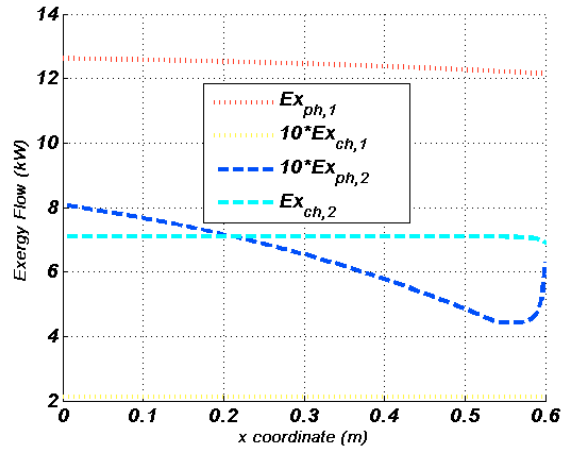


Figure I. 28: Pre-Reformer Exergy flows

Here, it is clearly shown that:

- i) hot gases physical exergy flows and fuel chemical exergy flows are dominant;
- ii) hot gases and fuel physical exergy flows dramatically depend on the corresponding temperatures (negligible pressure drops are detected);
- iii) the pre-reforming process slightly affects the chemical exergy flow of the reforming stream;
- iv) no chemical exergy flow is detected for the hot gases since this stream is not chemical reacting.

The exergetic performances of the pre-reformer are summarized in .:

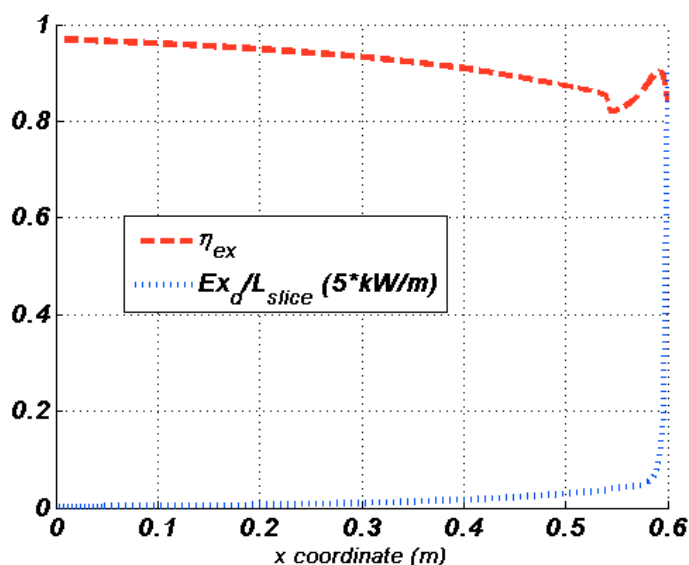


Figure I. 29: Pre-Reformer exergetic performances

Here it is clearly shown that the hot gases outlet section of the tube is featured by the largest inefficiency both due to the large radial temperature differences and to the dramatically fast rates of reforming reactions. These results also affect the exergetic efficiencies defined in **Errore. L'origine riferimento non è stata trovata.** and **Errore. L'origine riferimento non è stata trovata.**. In fact, the largest exergetic efficiencies are achieved at the hot gases inlet section of the tube, where low temperature differences are detected and no chemical reaction is occurring. On the other hand, the non-monotonic trend of the exergy efficiency, in the pre-reforming section is due to the combination of the dramatic reduction of the reaction rates shown in : and remarkable decrease of the fuel physical exergy, shown in :.

1.7. SOFC Model

The fuel cell considered in this study is the typical tubular SOFC, developed by Siemens-Westinghouse since 1970 (e.g. [3]). The same discretization technique adopted before is applied in order to assess thermodynamic, chemical, electrical and electrochemical parameters along the cell (Figure I.30).

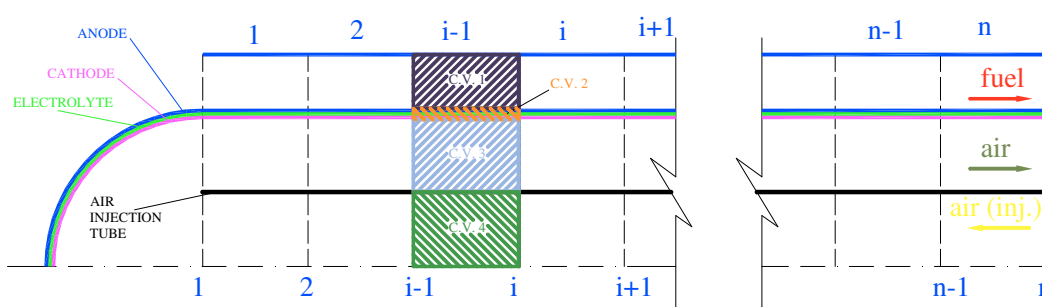


Figure I. 30: SOFC tube discretization

The core of the SOFC model is the electrochemical sub-model described before, implementing very accurate equations for the calculation of SOFC overvoltages:

- activation (Butler-Volmer and semi-empirical equations for the exchange current densities);
- concentration (combination of binary and Knudsen diffusion models and concentration equations);
- ohmic (temperature-dependent material resistivities and combined series/parallel electrical mechanism).

Furthermore, the above discussed innovative approach, for the simulation of the steam reforming process, was also calibrated in order to calculate the local rate of the internal reforming reactions internally at the fuel cell, as shown in detail in [8]. Friction factors and convective heat exchange coefficients are calculated by means of the correlations available in literature. A special effort was also performed in order to simulate the radiative heat exchange between the cathode compartment of the SOFC tube and the air injection tube, improving the model previously developed by the research group wherewith I have worked in the last 3 years [10, 14]. Such radiative model is based on a complex analytical calculation of the configuration factors among each surface of the cavity shown in Figure I.30. The various configuration factors are calculated on the basis of analytical relations and using the view factor algebra [15-20]. Thus, the cavity radiative model determines the radiosities and the slice-to-slice radiative heat flux [21]. Finally, the above described models are combined in an overall simulation code with the energy, mass, moles and momentum balances (with respect to the four control volume depicted in Figure I.30) for each slice of the computational model. Such set of equations forms the system of highly non-linear equations to be solved in the MATLAB® and TOMLAB® environments in order to determine thermodynamic, chemical and electrochemical parameters along the cell.

1.7.1. SOFC Chemical Kinetics (Internal Reforming)

In the IRSOFC the anodic section is designed in such way to being able to realize the reaction of Steam Methane Reforming and the shift reaction. After all the chemical reactions of Steam Methane Reforming, shift reaction and demethation must be taken in consideration simultaneously at the electrochemical reaction of oxidation of hydrogen inside the the cell. The kinetic of this last reaction, will be governed by the current produced by the same cell. The calculation of chemical kinetics inside the fuel cell can be developed in analogous way as described for the pre-reformer.

The methodological approach will completely remain unchanged: will be implemented a mono-dimensional model that allows to appreciate the variations of the physical-chemical properties along the axial direction of tube SOFC.

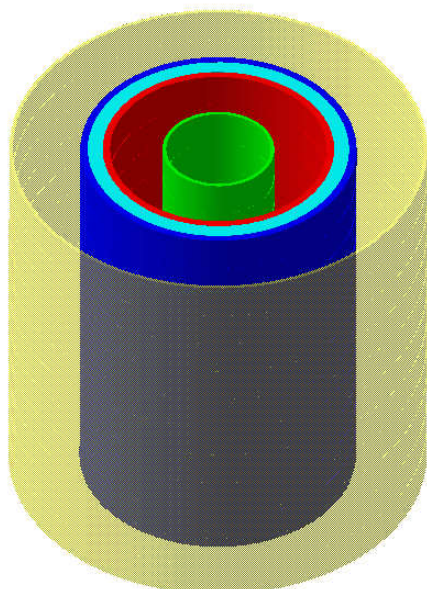


Figure I. 31: Elementary cell selection with two plane orthogonal to the axes

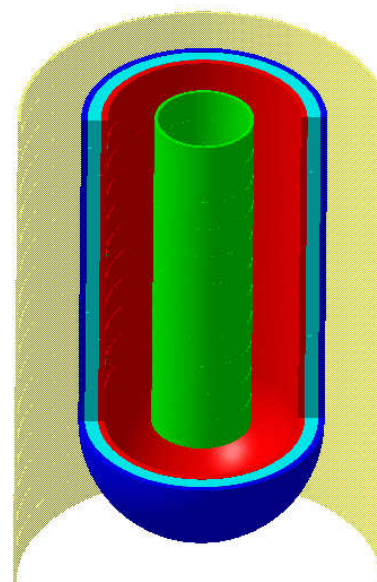
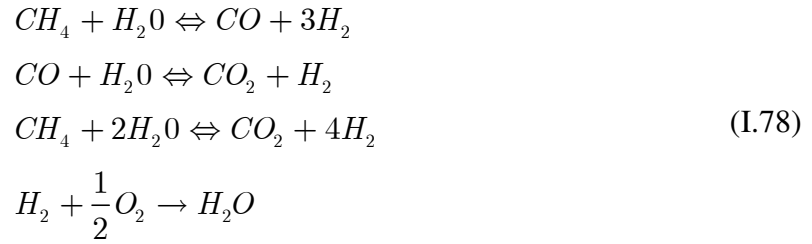


Figure I. 32: Section of a tubular SOFC cell

In completely analogous way at what described before for the pre-reformer it is possible to implement for the SOFC a mono-dimensional model for mass and energy exchange.

After all, the implementation of a 1-D stationary model for the SOFC, contemplate the development of the following points:

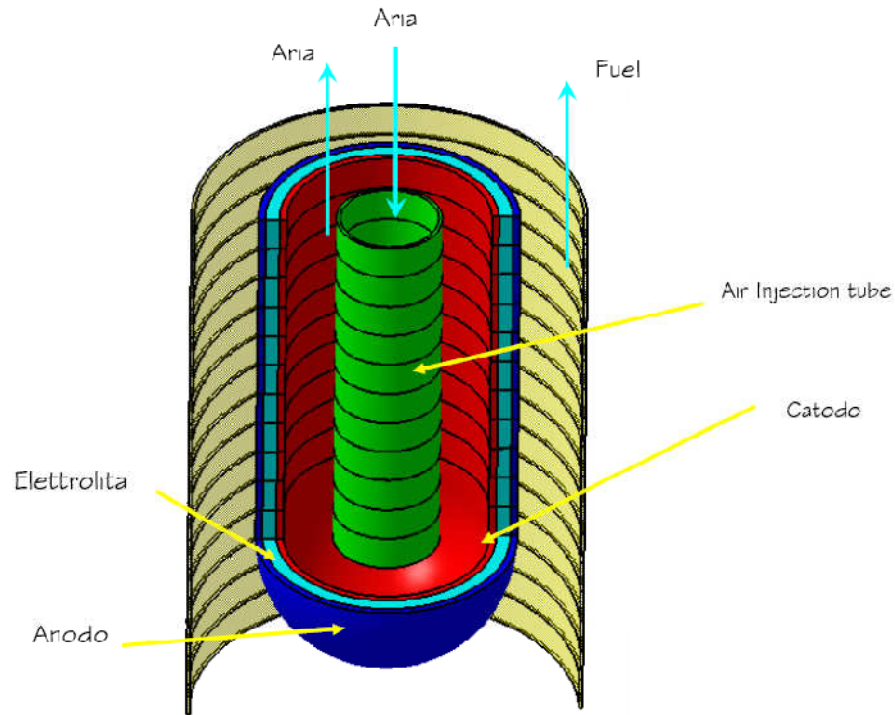
1. definition of the reactions that are necessary inside of the cell:



2. Molar balances for the calculation of the molar fractions at the outlet, on the base of the unknown degrees of reaction of the four previous reactions, respectively r_1 , r_2 , r_3 and r_4 :

$$\begin{aligned}
 n_{CH_4,o} &= n_{CH_4,i} - r_1 - r_3 \\
 n_{CO,o} &= n_{CO,i} + r_1 - r_2 \\
 n_{H_2,o} &= n_{H_2,i} + 3r_1 + r_2 + 4r_3 - r_4 \\
 n_{O_2,o} &= n_{O_2,i} - \frac{1}{2}r_4 \\
 n_{N_2,o} &= n_{N_2,i} \\
 n_{CO_2,o} &= n_{CO_2,i} + r_2 + r_3 \\
 n_{H_2O,o} &= n_{H_2O,i} - r_1 - r_1 - 2r_3 + r_4
 \end{aligned}
 \tag{I.79}$$

3. Discretization of the control volume according to plans perpendicular to the axis of the tubes, equidistant between them. It will be neglected the effect of edge however present in the inferior part of the tube;



1.

Figure I. 33: Discretization of an elementary SOFC cell

4. Adaptation of the Zafir and Gavriilidis model, for the calculation of the degrees of reaction of the first three reactions reported in (4,263).
5. The calculation of r_4 , that demands to couple, at the equations of the previous point, another equation that determine the degree of reaction of the electrochemical reaction. Such equation will be obtained following the procedure reported below:

- ✓ Is fixed the tension of the elementary cell (V_0);
- ✓ Supposing that every slice is in parallel with all the others (see Figure I.31 and Figure I.32), is possible to assert that every slice has the same tension and that the current distributed from the cell is the sum of the currents distributed from every slice.
- ✓ Note pressure, temperature field and chemical composition, for every slice is possible to invert the function polarization curve and to gain the value of the current density, and therefore also of the current, such to guarantee the value of the potential demanded (V_0). By means of iterative techniques of resolution of not linear equations, is obtained the value of i that satisfies the following equation:

$$V_0 - V_k \left(\begin{array}{l} i, \vec{\beta}_k, \vec{\beta}_{k+1}, t_k, t_{k+1}, p_k, p_{k+1}, \\ \text{geometria e materiali della SOFC} \end{array} \right) = 0 \quad (\text{I.80})$$

- ✓ from which it is gained, by means of simple budgets molars:

$$r_{H_2} = \frac{i}{2F} \quad (\text{I.81})$$

$$r_{O_2} = \frac{i}{4F} \quad (\text{I.82})$$

1.7.2. Convection Heat Transfer Coefficients and Friction Factors Models

Similarly to what has been done in the case of the pre-reformer, it is possible to apply, to the discretization control volume of the SOFC, the heat exchange and pressure drop models. Note that in the case of the SOFC, the discretization necessary to obtain the values of pressure, fuel and air composition at the exit of the cell, is slightly more complex than the case of pre-reformer, because of structure of the SOFC. Figure I.34 shows the geometrical

symmetry: this condition allows studying only half cell, assuming the central plan adiabatic.

In this control volume there are three streams:

- fuel undergoes reactions of reforming and electrochemical;
- air inside the cathodic compartment under the corresponding semi-reaction;
- air inside the injection tube, whose chemical composition remains constant.

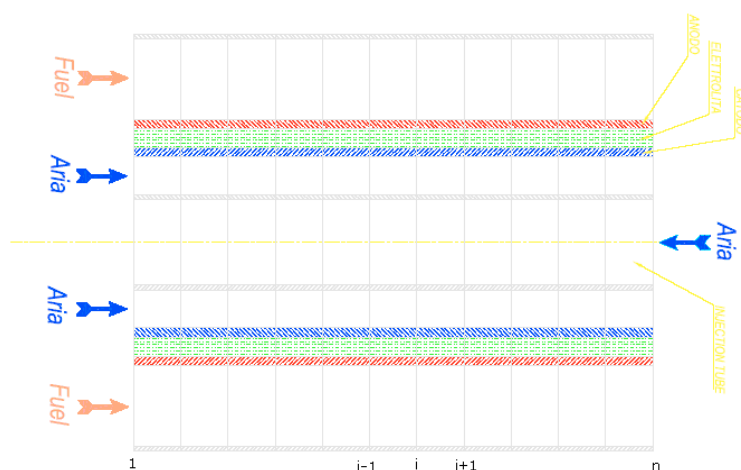


Figure I. 34: SOFC Discretization (heat Exchange model)

For the model that allows calculating the pressure drop and heat transfer coefficients it is possible to refer to what was provided in the case of the 1-D model of pre-reformer, because the correlations used are essentially the same, implemented using adequate definition of the equivalent diameter.

In most SOFC simulation models, pressure drops are neglected. This assumption is widely adopted because of the low viscosity of the fluids involved in the process. However, in this simulation a pressure drop model was also included, in order to evaluate the error determined by the previous assumption. This model is based on the calculation of the friction factor, depending on Reynolds number [25, 26]. Correlations for friction factor are taken in count for all the streams evolving in the SOFC [4, 11, 25].

Furthermore, the same procedure was also applied in order to calculate the convection heat transfer coefficient required to evaluate the energy balance equations in the SOFC. Here, correlations for the Nusselt number, as a function of Reynolds and Prandtl numbers were adopted, also taking into account the geometry of the fluid channel [4, 11, 25, 26].

1.7.3. Radiative Heat Transfer Model

In most of the papers available in literature, the radiative heat exchange between the air injection tube and the SOFC tube is neglected (e.g. [4, 5]). Moreover, the few papers

investigating the radiative heat transfer are mostly based on some significant simplifying assumption dealing with the calculation of the configuration factors [6]. However, the radiative heat transfer between the cathode compartment of the fuel cell and its injection tube is remarkable, because of the high operating temperatures typical of the tubular SOFC developed by Siemens [27-30].

The complexity of a complete radiative model of the SOFC tube is mainly due to the evaluation of the slice-to-slice configuration factors and the radiosities of the surfaces constituting the cavity included between the cathode compartment of the SOFC tube and the air injection tube [26].

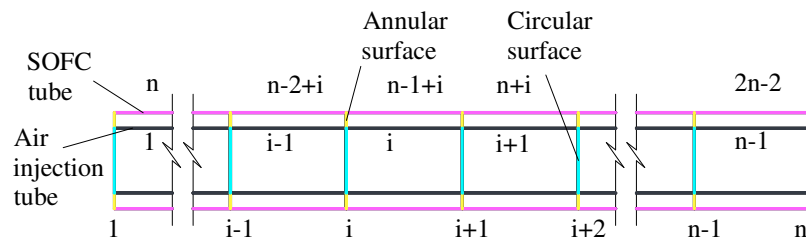


Figure 1. 35: SOFC radiative cavity

The areas of the top and bottom annular surfaces of the cavity are much lower than that of the tubes. Thus, such surfaces can be neglected and the resulting cavity consists of the $n-1$ surfaces of the external side of the air injection tube and the $n-1$ surfaces of the internal side of the SOFC tube. This results in a cavity consisting of $2n-2$ surfaces, and $(2n-2)^2$ configuration factors that have to be evaluated [26]. Thus, the simulation model must evaluate the square matrix $\bar{\bar{F}}$ of the $(n-1) \times (n-1)$ configuration factors. Such configuration factors can be calculated on the basis of the scheme reported in **Errore. L'origine riferimento non è stata trovata.**

The calculation of the above mentioned matrix requires to evaluate the following configuration factors:

- cylinder (external side) to cylinder (external side), same radius and axis, e.g. $F_{i,i+1}$ or $F_{i,i+2}$ and their reciprocal.
- cylinder (external side) to cylinder (internal side), different radius, same axis, e.g. $F_{i,n-1+i}$, $F_{i,n+i}$ or $F_{i,n+i+1}$ and their reciprocal.

- c. cylinder (internal side) to cylinder (internal side), same radius, same axis, with an inner cylinder inserted, e.g. $F_{n-2+i, n-1+i}$ or $F_{n-2+i, n+i}$ and their reciprocal.

It is very simple to recognize that all the view factors of the type a) are zero [26]:

$$F_{i=1:m, j=1:m} = 0 \quad m = n-1 \quad (1)$$

The configuration factors b) can be calculated only by means of a numerical integration, as shown below [28, 31]:

$$F_{i=1:m, j=m+1:m} = \frac{R_e}{R_i} \int_0^c f_{intext}(R_i, R_e, L_{slice}, \delta_{slice}) d\theta$$

$$c = a \cos(R_i / R_e)$$

$$L_{slice} = \delta_{slice} (j - i - m) \quad \delta_{slice} = \frac{L_{cell}}{m} \quad (I.83)$$

The integrating function is [28, 31]:

$$f_{intext} = \frac{1}{R_e \delta_{slice}} \left\{ \frac{B}{a^{\frac{3}{2}}} \left[(L_{slice} - \delta_{slice}) \operatorname{atan} \left(\frac{L_{slice} - \delta_{slice}}{a^{\frac{1}{2}}} \right) + (L_{slice} + \delta_{slice}) \operatorname{atan} \left(\frac{L_{slice} + \delta_{slice}}{a^{\frac{1}{2}}} \right) - 2L_{slice} \operatorname{atan} \left(\frac{L_{slice}}{a^{\frac{1}{2}}} \right) \right] \right\}$$

$$a = R_e^2 + R_i^2 - 2R_i R_e \cos \theta$$

$$B = \frac{R_i R_e}{\pi (R_e - R_i)^2} \left[R_e^2 + R_i^2 - R_i R_e (1 + \cos \theta) - 2R_i^2 \sin^2 \frac{\theta}{2} \right] \times$$

$$\left[R_e^2 + R_i^2 - R_i R_e (1 + \cos \theta) - 2R_e^2 \sin^2 \frac{\theta}{2} \right] \quad (I.84)$$

Obviously, the reciprocal configuration factors can be calculated by means of the well known reciprocity property [26]:

$$F_{i=m+1:2m, j=1:m} = \frac{R_i}{R_e} F_{i=1:m, j=m+1:2m} \quad (I.85)$$

It is noteworthy that the calculation of all the above described configuration factors is very time consuming since it is based on very complex equations and on numerical integration.

Finally, the calculation procedure of configuration factors c) is described in the followings. Here, some special procedures dealing with the view factors algebra were implemented. Such procedure is very complex as for the theoretical point of view, but permits a direct calculation, avoiding any numerical integration [32-34]. In general, the configuration factors

c) can be expressed as a function of internal and external radius, slice length and slice distances:

$$F_{i=m+1:2m, j=m+1:2m} = f_{\text{intint}}(R_i, R_e, L_{\text{slice}}, \delta_{\text{slice}}) \quad (\text{I.86})$$

Considering the scheme reported in : , the configuration factor c) is the $F_{1,3}$, and can be calculated by applying some rules of the view factor algebra, according to the following equation [31]:

$$F_{1,3} = \frac{R_e^2 - R_i^2}{2R_e \delta_{\text{slice}}} \left[(F_{5,9} - F_{6,9}) - (F_{5,10} - F_{6,10}) - F_{1,4} \right] \quad (\text{I.87})$$

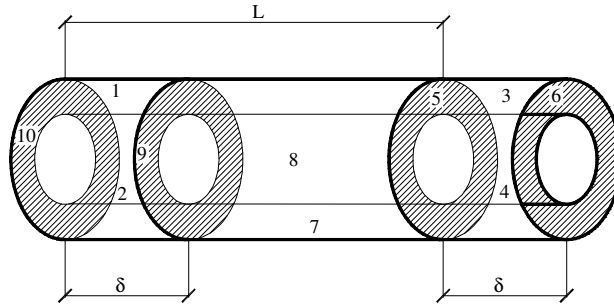


Figure I. 36: Scheme for the calculation of configuration factors c)

Here, it is possible to recognize that $F_{1,4}$ is a configuration factor a), whereas $F_{5,9}$, $F_{6,9}$, $F_{5,10}$ and $F_{6,10}$ are annulus to annulus configuration factors. Such parameters can be calculated using the well known equations available in literature [26, 31].

$$F_{i,j} = \frac{1}{2} \left\{ 1 + \left[1 + \left(\frac{R_j}{H} \right)^2 \right] \left(\frac{H}{R_i} \right)^2 - \left\{ \left[1 + \left(\frac{R_j}{H} \right)^2 \right] \left(\frac{H}{R_i} \right)^2 \right\}^2 - 4 \left(\frac{R_j}{H} \right)^2 \left(\frac{H}{R_i} \right)^2 \right\}^{\frac{1}{2}} \quad (\text{I.88})$$

Let us consider the scheme reported in **Errore. L'origine riferimento non è stata trovata.** The annulus to annulus configuration factor can be calculated by implementing some rules of the view factor algebra, as follows:

$$F_{1,2} = \frac{R_e^2}{R_e^2 - R_i^2} (F_{A,B} - F_{A,4}) - \frac{R_i^2}{R_e^2 - R_i^2} (F_{3,B} - F_{3,4}) \quad (\text{I.89})$$

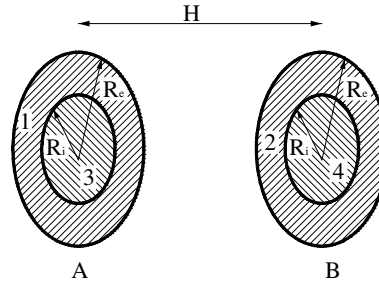


Figure I. 37: Scheme for the calculation of the annulus to annulus configuration factor

Thus, the overall above described procedure allows one to evaluate the configuration factor matrix. This matrix is subsequently adopted for the calculation of the radiations of each surface of the cavity. According to the well-known rules of the radiative cavity heat transfer [26], such radiosities can be calculated using the following equation:

$$r_{i=1:2m} = \varepsilon_i \sigma T_i^4 + \rho_i \left(\sum_{j=1:2m} F_{i,j} r_j \right) \quad (\text{I.90})$$

Equation (I.90) is a linear system of $2m$ algebraic equations in the $2m$ unknowns surface radiosities. Such system can be easily and quickly solved by implementing whatever method for the solution of linear equation systems. The values of the radiosities can be used to evaluate the radiative heat flux between the surface i and the overall cavity. Such flux will be subsequently used to evaluate the energy balance equations and can be evaluated implementing the well known rules of the radiative cavities, according to the following equation:

$$\dot{q}_{rad_{i,c}} = r_i - \sum_{j=1:2m} F_{i,j} r_j \quad (\text{I.91})$$

1.7.4. Overall Simulation Model and Energy Balance Equations

The previous sections clearly showed the complexity of a complete finite volume axial-symmetric model of a single tubular SOFC, due to the peculiarities of the phenomena occurring in the cell. In fact, all the above mentioned phenomena are ruled by highly non linear complex equations that are also highly coupled to each other.

The basic principle of the overall simulation model, developed in MATLAB, using the TOMLAB tool to solve non-linear constrained system of algebraic equations, will be summarized in the following.

A simplified flow chart of the simulation code, illustrating the procedure, is shown in :.

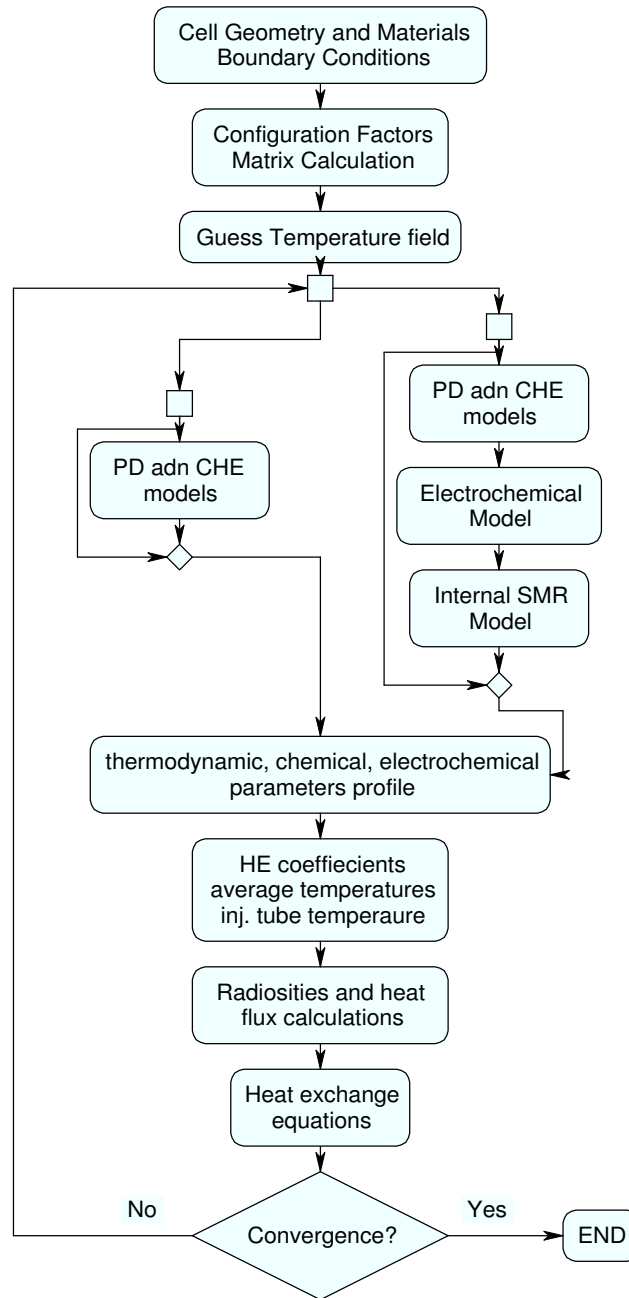


Figure I. 38: simplified flow chart of the overall simulation model

The geometry of the cell is an input fixed data. Thus, the first step of the simulation procedure is the calculation of the configuration factor matrix depending only on the geometrical parameters of the cell. Then, a guess temperature field for fuel (stream 1), air (cathode) (stream 2), air (injection tube) (stream 3) and solid is fixed. Starting from the air (injection tube) inlet, plane n , the pressure drops and convective heat exchange models (PD and CHE respectively) leads to the calculation of the slice outlet pressure and the slice convection heat exchange coefficients. Such procedure is iterated as for as the first slice of the discretization, calculating the overall profiles of stream 3 pressure and the convective heat

exchange coefficients. Then, starting from the first slice of the discretization, the same pressure drops and convective heat exchange models allow one to calculate the heat exchange coefficients and outlet pressures for streams 1 and 2. However, this calculation is much more complex, since streams 1 and 2 are chemical reacting. Thus, the calculation of their outlet chemical composition is also required. Such calculation is performed as follows: the fixed value of the operating voltage and the above discussed electrochemical model allow one to evaluate the slice operating current density. Such calculation is performed iteratively, using the TOMLAB package, since the current density is not an explicit function of the operating voltage. Such value of the current density can be used by the internal reforming SMR model to evaluate the outlet chemical composition of streams 1 and 2. This last calculation is also performed iteratively, using the TOMLAB package, since the chemical end electrochemical reaction rates are also function of the unknown outlet chemical compositions. Thus, iterating the above described procedure, the pressure and chemical compositions fields and heat transfer convective coefficients can be calculated. The values of chemical/electrochemical rates of reaction also allowed to determining the electrical power production and the heat generated/absorbed by the chemical/electrochemical process.

Therefore, once the guess temperature field has been fixed, the simulation procedure calculates the fields of pressure and chemical/electrochemical parameters in the cell. Finally, the guess temperature field is be iterated until the energy balance equations (described in the following) would be satisfied, according to a fixed convergence criterion. After this last iteration, all the parameters profiles in the cell are determined.

Energy balance equations were based on the scheme in \therefore . The computational domain was divided in n slices by the discretization procedure. Each slice was divided into 4 control volumes.

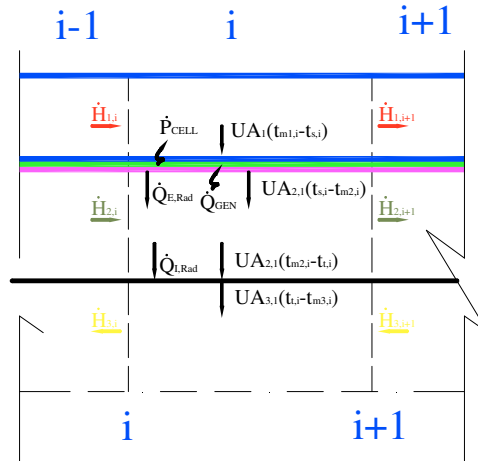


Figure I. 39: Scheme for the energy balance equations

Here, the overall thermal conductances UA reported in : can be calculated according to the following formula:

$$\begin{aligned} UA_{1,i=1:m} &= \frac{h_{1,i=1:m} \pi D_{cell} L_{cell}}{m} & UA_{2,1,i=1:m} &= \frac{h_{2,1,i=1:m} \pi D_{cell} L_{cell}}{m} \\ UA_{2,2,i=1:m} &= \frac{h_{2,2,i=1:m} \pi D_{inj} L_{cell}}{m} & UA_{3,i=1:m} &= \frac{h_{1,i=1:m} \pi D_{inj} L_{cell}}{m} \end{aligned} \quad (I.92)$$

These expression are obtained neglecting the conductive terms, of lower order of magnitude than the convective one.

Assuming that the discretization is based on a sufficiently large number of slices, the streams average temperatures can be calculated as follows:

$$\bar{t}_{j,i} = \frac{t_{j,i} + t_{j,i+1}}{2} \quad j = 1, 2, 3 \quad i = 1 : m \quad (I.93)$$

Then, the temperatures of the injection tube can be related to those of solid and streams, using a simple energy balance on the control volume including stream 2 and licking the air injection tube:

$$t_{t,i} = \bar{t}_{2,i} - (t_{s,i} - \bar{t}_{2,i}) \frac{UA_{2,1,i}}{UA_{2,2,i}} - \frac{\dot{H}_{2,i} - \dot{H}_{2,i+1}}{UA_{2,2,i}} \quad (I.94)$$

The configuration factor matrix, previously calculated, and the values of SOFC and injection tube temperatures can be used by the heat transfer radiative model in order to asses the radiative flux profile along the tube axis.

The guess temperature fields consists of $4m$ variables. These variables can be evaluated by solving the system of $4m$ algebraic equation, and by describing the energy balance for each

slice of the discretization. In fact, for each slice it is possible to write an energy balance equation for each of the 4 control volumes depicted in ::

$$\begin{aligned}
 \dot{H}_{1,i} - \dot{H}_{1,i+1} &= UA_{1,i} (\bar{t}_{1,i} - t_{s,i}) \\
 UA_{1,i} (\bar{t}_{1,i} - t_{s,i}) + \dot{Q}_{gen} - \dot{P}_{cell} &= UA_{2,1,i} (t_{s,i} - \bar{t}_{2,i}) + \dot{Q}_{rad} \\
 \dot{H}_{2,i} + UA_{2,2,i} (t_{s,i} - \bar{t}_{2,i}) + \dot{Q}_{rad} &= \dot{H}_{2,i+1} + UA_{3,i} (t_{t,i} - \bar{t}_{3,i}) \\
 UA_{3,i} (t_{t,i} - \bar{t}_{3,i}) + \dot{H}_{3,i+1} &= \dot{H}_{3,i}
 \end{aligned} \tag{I.95}$$

The highly non linear system of $4m$ equations on $4m$ unknowns temperatures was solved by using a fast and robust algorithm available in the TOMLAB package. It is noteworthy that the above displayed large system of algebraic equations consists of a number of sub-problems that require large computational times, because of:

- i) the high nonlinearity of the governing equation;
- ii) the need to solve nested system of highly non-linear algebraic equations in order to solve the electrochemical model (activation overvoltage and operating current density) and to predict the outlet slice chemical composition by means of the internal SMR model.

1.7.5. The Case Study

1.7.5.1. Chemical/Electrochemical and Thermodynamic Analysis

The simulation model, discussed in the first part of the chapter, was used in order to determine the trends of the main chemical, electrochemical, electrical and thermodynamic parameters along the SOFC axis for a specific case. The single tubular SOFC was simulated on the basis of data widely used in literature, listed in Tables I.11, I.12 and I.13. Namely: material and geometry are defined in Table I. 11.; the compositions of air and fuel at inlet conditions are resumed in Table I. 12.; the thermodynamic boundary conditions are displayed in Table I. 13.:

Parameter	Unit	Value
Anode thickness	cm	0.01
Cathode thickness	cm	0.22
Electrolyte thickness	cm	0.004
Interconnection thickness	cm	0.0085
Cell length	m	1.5
Interconnection versus cell area/		0,097
Equivalent r_b	kg/m3	0.6

Cell diameter	cm	1.56
Injection Tube Diameter	cm	1.2
Anode Pore Diameter	m	5.00E-07
Cathode Pore Diameter	m	5.00E-07
Anode porosity	%	50
Anode tortuosity	/	5.9
Cathode porosity	%	50
Cathode tortuosity	/	5.9
Anode conductivity	W/m K ²	
Cathode conductivity	W/m K ²	
Electrolyte conductivity	W/m K ²	
Interconnections conductivity	W/m K ²	
Cathode emissivity	/	0.7
Injection Tube emissivity	/	0.7

Table I. 11: SOFC material and geometrical parameters

species	fuel	air
H_2O	0,26803	0.00
CO	0,11111	0.00
H_2	0,33333	0.00
O_2	0	0,21
N_2	0,0065007	0,79
CO_2	0,18302	0.00
CH_4	0,09801	0.00

Table I. 12: Air and fuel inlet molar fractions

Parameter	Unit	Value
Cell Voltage	V	0.62
Number of slices	/	70
Fuel inlet pressure	bar	3
Air inlet pressure	bar	3

Fuel inlet temperature	°C	921
Air inlet temperature	°C	910
fuel molar flow rate	kmols/s	3.17E-06
air molar flow rate	kmols/s	3.17E-05

Table I. 13: Boundary and operating conditions

The results provided by the simulation are presented and discussed in the following. Special attention was paid to the effect of radiative heat transfer. To this scope, the results obtained with and without radiative heat transfer were compared.

Errore. L'origine riferimento non è stata trovata. shows the current density of each slice of the discretization. This graph clearly shows the same trend of the electrical power produced by each slice (:). It is noteworthy that in the tubular configuration arrangement the voltage along the tube axis can be assumed as a constant. In fact, each slice of the discretization can be considered in a parallel electrical arrangement (same voltage) with each other. **Errore. L'origine riferimento non è stata trovata.** also shows that current density varies along the SOFC tube. In fact, such parameter dramatically depends on the hydrogen partial pressure: the higher the x coordinate, the lower the hydrogen partial pressure (due to the consumption by the electrochemical reaction), determining lower values of the operating current density.

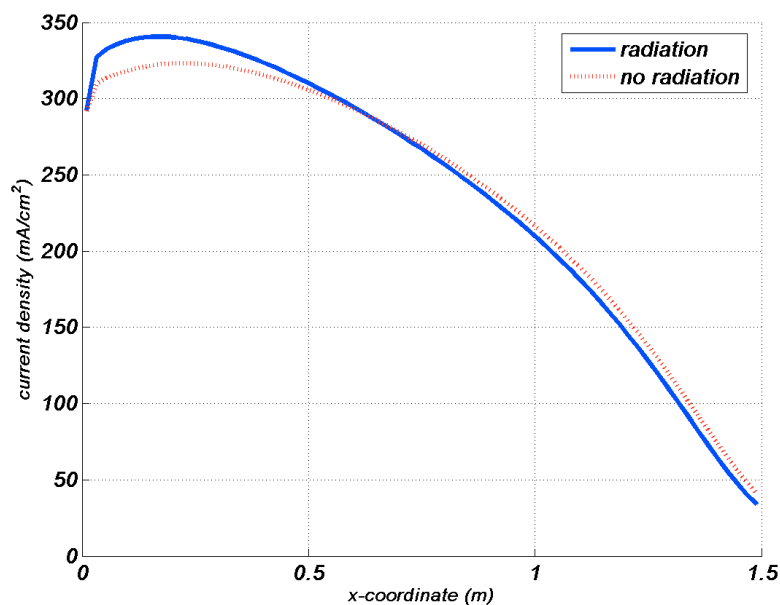


Figure I. 40: Operating current densities.

Therefore, the electrical power produced by the first slices of the tube is much larger than that produced by the others. Consequently, the results shown in **Errore. L'origine riferimento non è stata trovata.** suggest to pay special attention to the length of the SOFC tube, because of the scarce contribute to the overall power production provided by the last slices of the tube.

The results shown in **Errore. L'origine riferimento non è stata trovata.** are related to a number of design/operating parameters, such as: inlet chemical compositions, pressures and temperatures, SOFC materials, electrodes thicknesses, etc. Thus, the designer of the fuel cell can handle these parameters in order to achieve the desired current density profile.

The operating current density dramatically affects all the chemical, electrochemical and thermodynamic parameters of the cell. In particular, the distribution of the current densities along the SOFC axis affects the thermal balance, since the current density is strictly related to the rate of the electrochemical reaction. Thus, the larger the current density, the larger the amount of hydrogen reacted and the heat generated by the reaction. This latter is partly used by the endothermic internal steam methane reforming process. The net heat released by the chemical/electrochemical processes occurring in the cell is shown in \cdot . At low x coordinates, the rate of the SMR process is very high, consuming a large amount of the heat generated by the electrochemical process. This results in a low value of net heat generation. Subsequently, the rate SMR process remarkably decreases, resulting in a dramatic increase of the net heat generated.

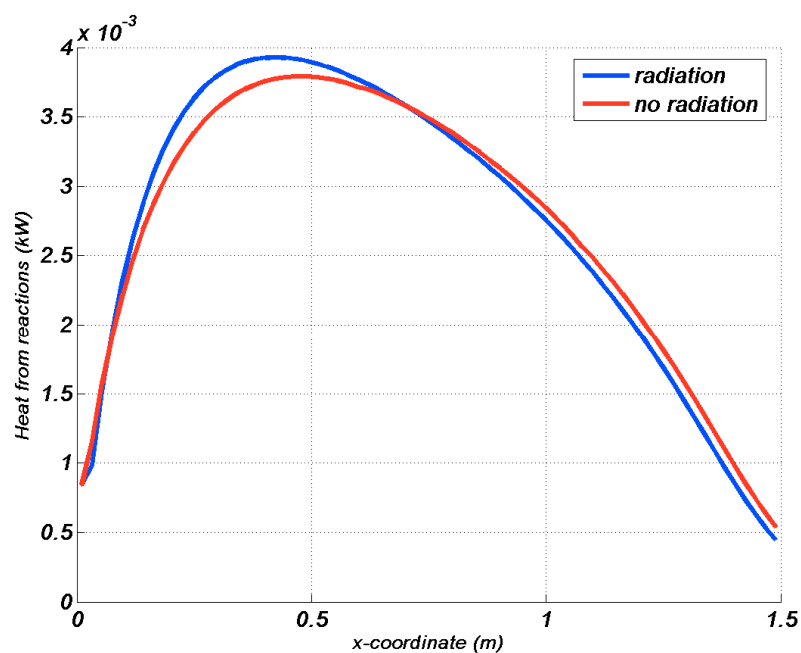


Figure I. 41: Heat Generated/absorbed by the chemical/electrochemical reactions.

Finally, at large x coordinates a remarkable decrease of the heat generated is detectable. Such decrease is mainly due to the reduction of the rate of the electrochemical process (low current densities).

The heat generated by the electrochemical reaction can be calculated as:

$$\dot{Q}_{H_2} = r_{H_2} \Delta h_{H_2} - VA_i i \quad (I.96)$$

The overall performance of the Fuel cell mainly depends on its polarization curve. The Nernst potential and the Ohmic overvoltage profiles are shown in : . Here, a remarkably low value of the Open Circuit Reversible Voltage is detected. Such value (close to 0.7 V) mainly depends on the high operating temperatures of the SOFC.

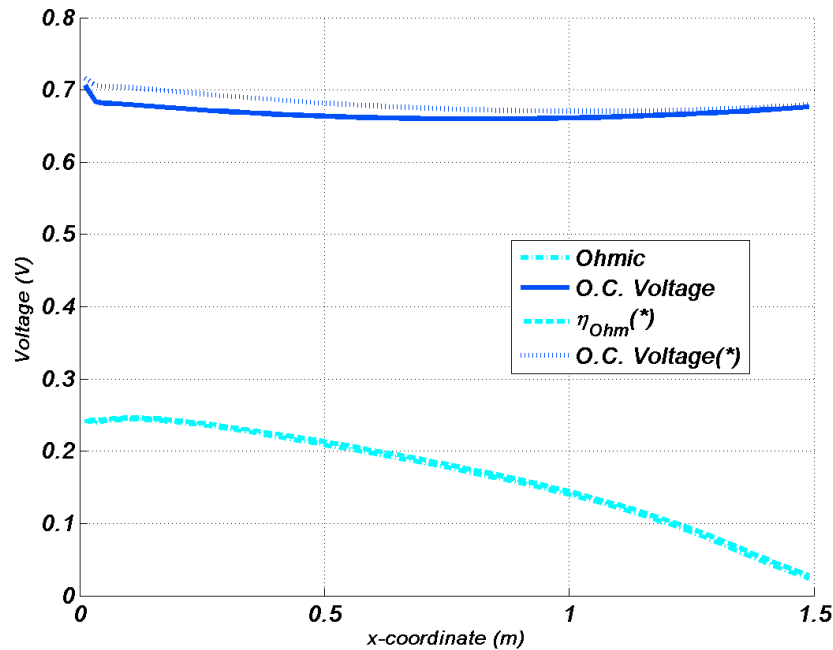


Figure I. 42: Nernst Potential and Ohmic Overvoltage, (* no radiation)

On the other hand, such high temperatures induce a reduction in the Ohmic overvoltage. In fact, the resistivities of the SOFC components are exponential functions of the operating temperatures [3-8, 10-13]. Such relationship is also clear from : : in fact, the operating temperature increases with the x coordinate, whereas the Ohmic overvoltage decreases. It is also noteworthy to emphasize that such reduction is also due to the reduction of the operating current density in the slice, shown in **Errore. L'origine riferimento non è stata trovata.** Finally, a comparison between the graphs displayed in : and **Errore. L'origine riferimento non è stata trovata.** clearly shows that in tubular SOFCs the Ohmic overvoltage is dominant. In fact, the curves in **Errore. L'origine riferimento non è stata trovata.** clearly show that concentration overvoltages are very low for the cell under investigation. Furthermore, the activation overpotential also shows a remarkable decrease along the SOFC axis (**Errore. L'origine riferimento non è stata trovata.**3). Such decrease is due both to the reduction of the operating current density and to the increase of the operating temperature.

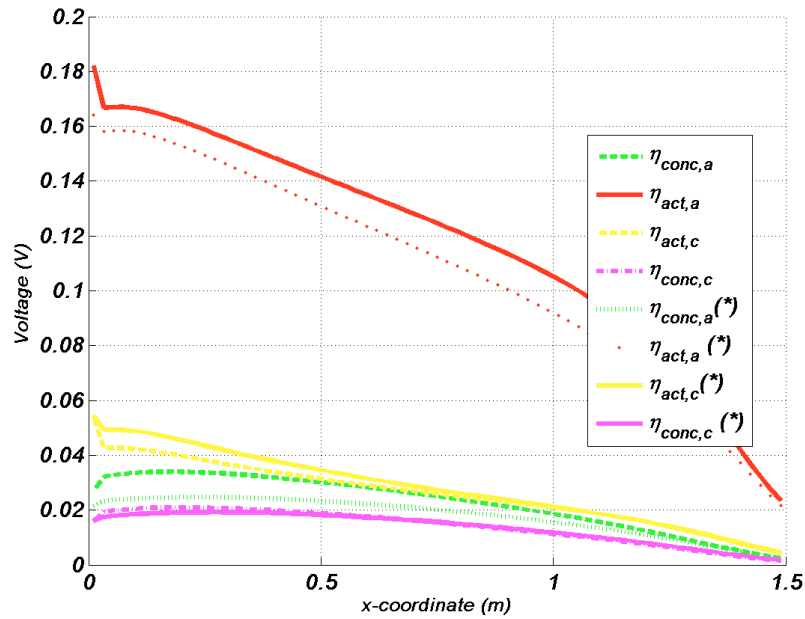


Figure I. 43: Concentration and Activation Overvoltages, (* no radiation)

The simulation model implemented in this chapter also performs an accurate calculation of the chemical composition of the streams reacting in the cell. Results of this calculation are shown in : and : : shows the trend of fuel molar fractions along the SOFC axis. The chemical composition of inlet fuel corresponds to the outlet state of the fuel exiting the pre-reformer, included in the stack [10]. Thus, it consist of N_2 , CO , CO_2 , H_2O , H_2 and CH_4 . The rates of the SMR process are very large in the bottom of the SOFC tube. In fact, the internal reforming process is very fast (:) because of the large operating temperature and the catalyst effect of the Nickel included in the anode compartment of the fuel cell. Thus, almost all the inlet methane is converted into hydrogen in the bottom of the Fuel cell. Furthermore, the hydrogen included in the fuel and produced by the SMR process is continuously consumed by the electrochemical reaction. As above mentioned, the rate of electrochemical reaction strictly follows the trend of the operating current density [10], as shown in :. Here, the rates of the chemical/electrochemical reactions are displayed for each slice of discretization. : also shows that the assumption widely adopted about the equilibrium of the shift reaction is not correct. Furthermore, it can be noted that the internal reforming process is very fast, so that the corresponding reactions approach very quickly the chemical equilibrium conditions.

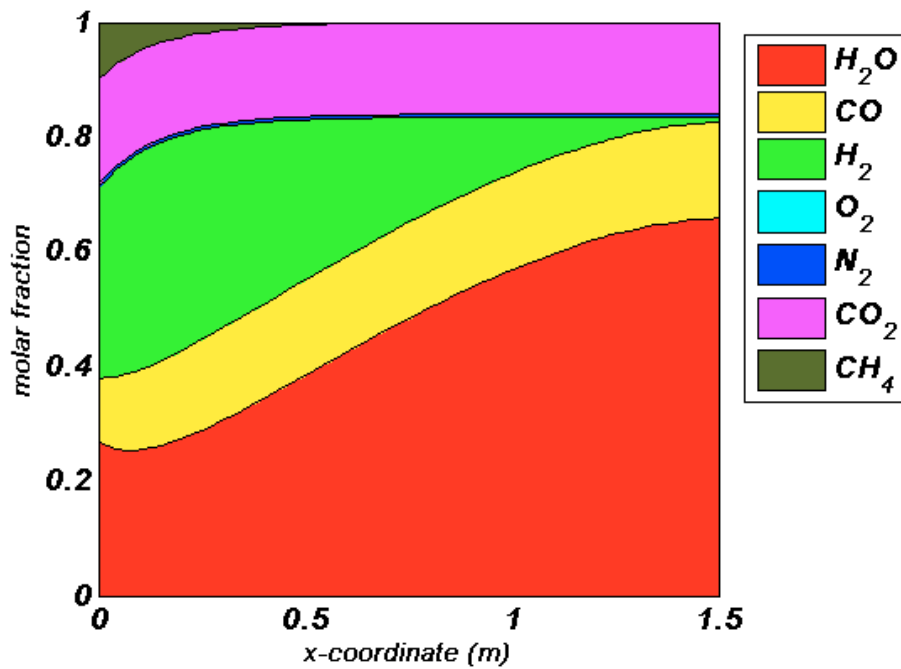


Figure I. 44: SOFC species molar flow rates

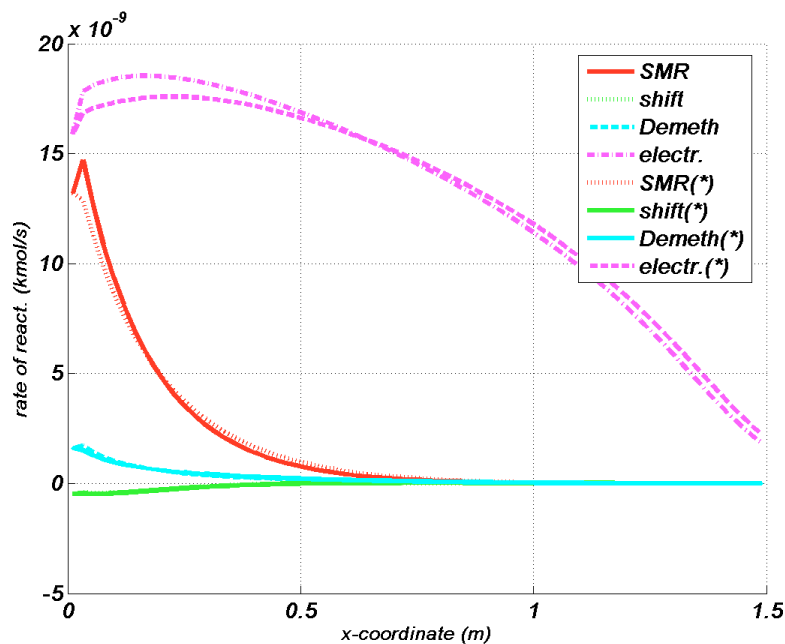


Figure I. 45: Rates of chemical/electrochemical reactions, (* no radiation)

The main result returned by the simulation code is the calculation of the temperature profiles in the cell. In particular, the code can determine fuel, air (cathode compartment), air (injection tube), SOFC tube and injection tube temperatures along the SOFC axis. These results are shown in :. It noteworthy to mention that the result shown in : was achieved by means an accurate adjustment of the operating/design parameters and boundary conditions. In fact, the SOFC thermal balance is very sensitive to any variation of those parameters. :

clearly shows that the cell cannot be considered isothermal. Large temperature gradients can be detected along both cell axis and radius. However, the above mentioned adjustment effort resulted in a slight longitudinal gradient in the solid of the fuel cell, according to the technological constraints of the manufacturer. In fact, one of the main issues avoiding the full commercialization of SOFC system is the reduction of the thermal stresses in the cell. In particular, the results provided by the simulations show that the reduction of the thermal stresses in the cell can be achieved:

- i) by optimizing the fuel to air ratio;
- ii) by increasing as much as possible the air inlet temperature;
- iii) by optimizing the pre-reforming ratio;
- iv) by promoting the heat exchange in the air injection tube.

: shows that a remarkable pre-heating is achieved in the air injection tube, reducing the temperature gradients in the cell. Furthermore, remarkable radial temperature gradients among the streams and among the solid and the injection tube are present, especially at the top of the fuel cell.

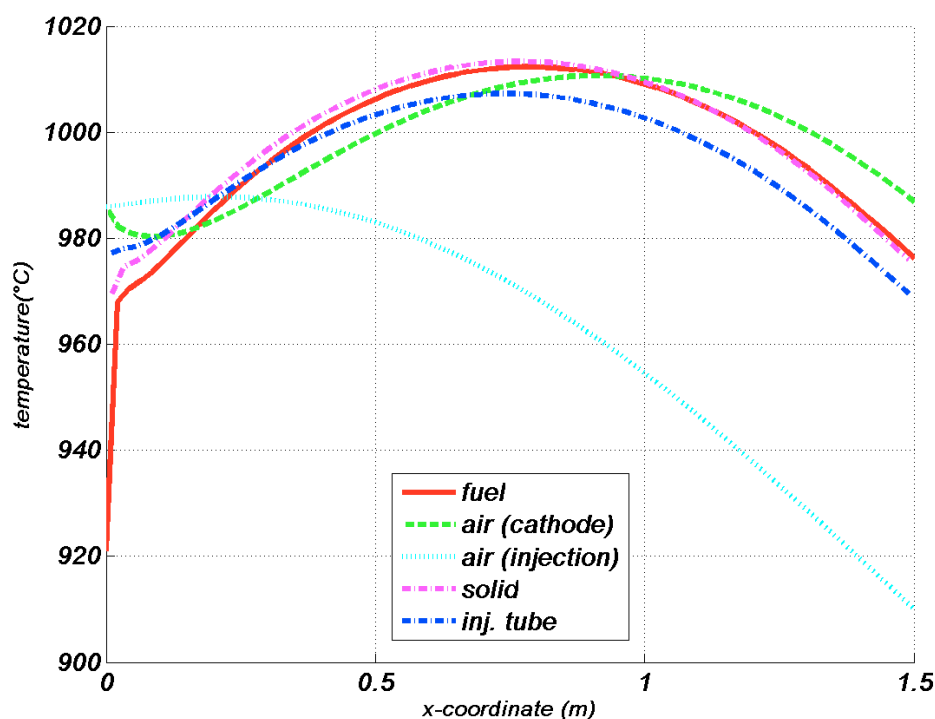


Figure I. 46: Streams and solids temperatures.

The simulation code also returns the calculation of some global parameters, such as electrical efficiency and fuel utilization factor. In particular, the combination of design/operating parameters set in the case study corresponds to quite high values of electrical efficiency

(39,3%) and fuel utilization factor (86,4 %). These latter parameters are strictly correlated, since higher values of the fuel utilization factor correspond to larger amount of fuel converted into the cell, determining higher electrical efficiency. Obviously, a SOFC can achieve even higher values of electrical efficiency, by optimizing the design and the operating conditions of the cell, as shown in the last part of the chapter (sensitivity analysis).

As for pressure drops, : shows that they are negligible, due the velocities and viscosities of the streams flowing in the cell.

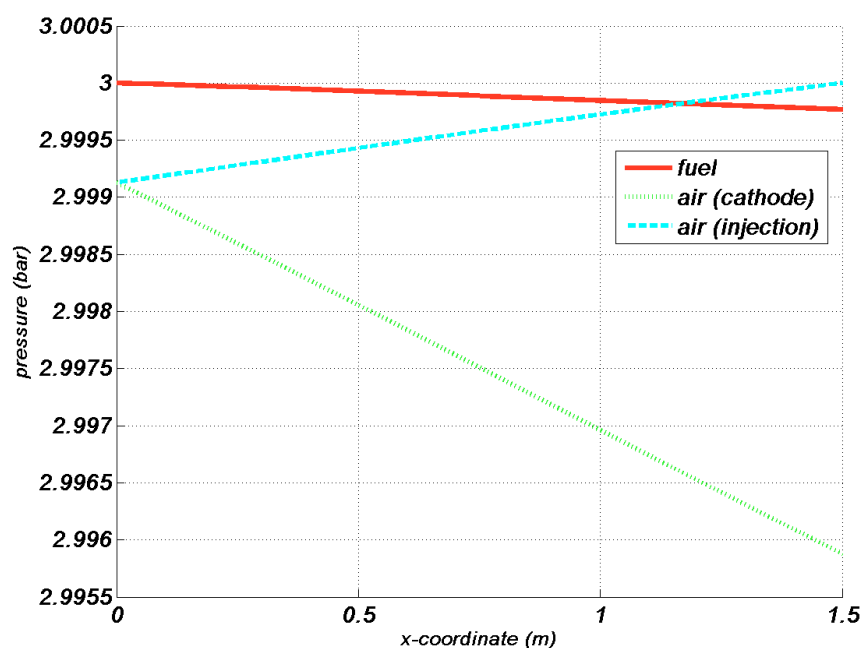


Figure I. 47: Streams pressures

The results provided by the model show that a number of the simplifying assumptions widely adopted in the simulation models available in literature (e.g. [11, 12]) are not completely correct:

- SOFC overvoltages, current densities and temperatures are not constant along the SOFC axis, also showing non-linear trends; therefore, the evaluation of chemical and electrochemical properties of the cell cannot be referred to its outlet conditions;
- fuel, solid and air outlet temperatures are quite different: hence, the assumption diffusely implemented in 0-D models, considering the same outlet air, fuel and solid temperature is not correct.

Therefore, the above discussed results clearly showed that an accurate calculation of the overall cell performance and outlet chemical/thermodynamic properties requires to

implement at least a 1-D model, in order to properly consider all the phenomena occurring in the cell.

1.7.5.2. Radiative Heat Transfer

One of the main aim of this study was the calculation of the radiative heat transfer between the air injection tube and the SOFC tube. This calculation was developed in order asses the magnitude of such heat transfer mechanisms and to verify the correctness of the simulation models available in literature neglecting the radiative heat transfer between the SOFC and the air injection tubes [5, 10].

Radiative heat transfer is mainly due to the radial temperature gradients between the slices of the SOFC and the slices of the air injection tube. In theory, such heat transfer mechanism can occur among whatever slice of the SOFC and air injection tube, and not only between two slices presenting the same x coordinate, as assumed in [6].

Errore. L'origine riferimento non è stata trovata. shows the configuration factor among the two surfaces placed respectively on the injection and on the SOFC tube and the remaining surfaces of the cavity. Such figure clearly shows that the simplifying assumption adopted in [6] is actually correct, for the geometrical configuration presented in this case. However, the following analysis will be performed considering the complete radiative model presented in the first part of this chapter, avoiding the adoption of any simplifying assumption.

Fig. 11 shows the configuration factor among two surfaces placed, respectively, on the injection and on the SOFC tube and the remaining surfaces of the cavity. Here, considering the scheme reported in Fig. 2, it is possible to detect that $F_{i,n-i+1} = 0.9193$, whereas $F_{i,n+1} = F_{i,n+i-2} = 0.0402$. Therefore, the radiative heat exchange among slices with different x coordinates cannot rigorously considered negligible since it is close to the 10% of the total radiosity of the slice.

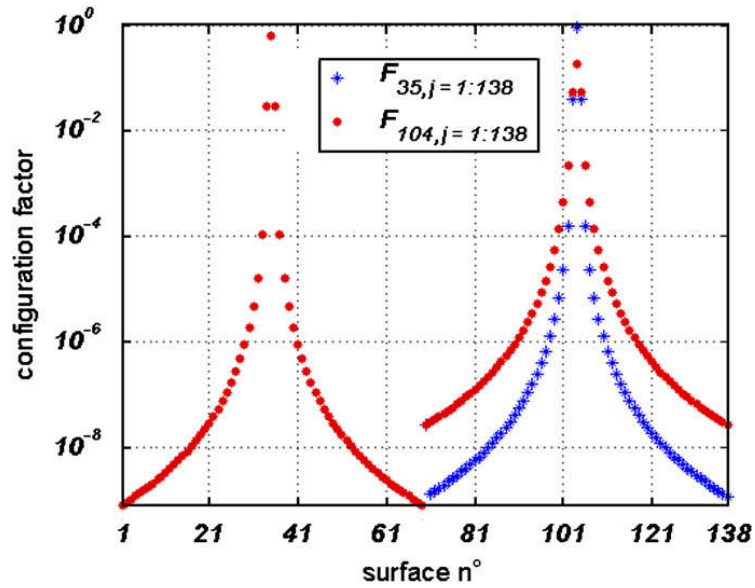


Figure I. 48: Configuration factors.

The radiative heat transfer model allows one to calculate surface radiosities, whose values are shown in :. Here, it is clearly that the radiosities are larger in the SOFC than in the injection tube, since in the SOFC the temperatures are higher, in most of the slices of the discretized computational domain. The values of SOFC and injection tube radiosities are really noteworthy, because of the extremely large values of the SOFC operating temperature. Such radiosities determine a significant radiative heat transfer along the tube axis, as shown in :. Here, the radiative heat transfer shows the same order of magnitude of the convective heat transfer.

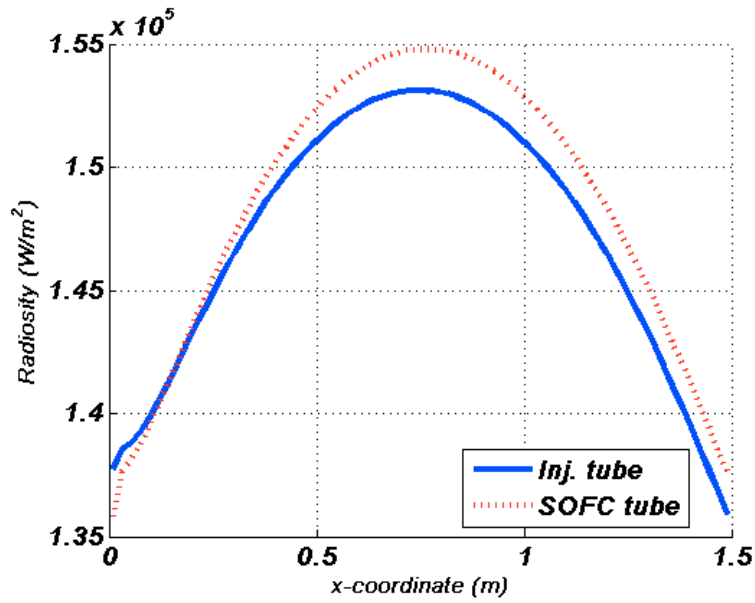


Figure I. 49: SOFC and injection tube radiosities

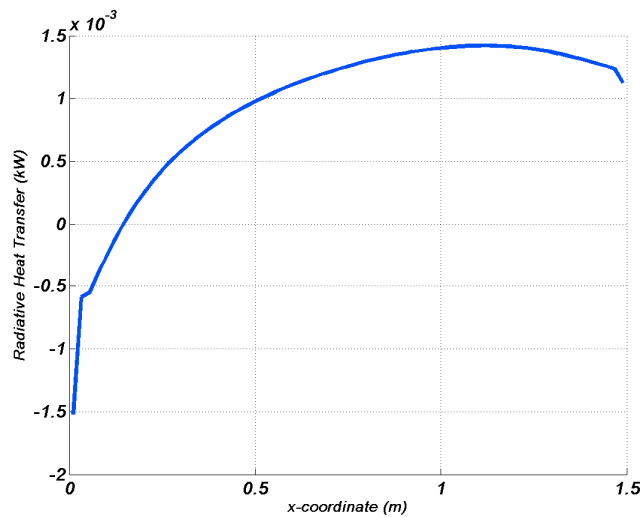


Figure I. 50: Radiative Heat Transfer

Such circumstance suggests that the radiative heat transfer is not negligible for the SOFC configuration under study. Such conclusion is clearly displayed in : , showing the temperature profiles calculated with and without radiative heat exchange. Such figure clearly shows that the radiative heat transfer is significant for the calculation of the temperature distributions in the cell.

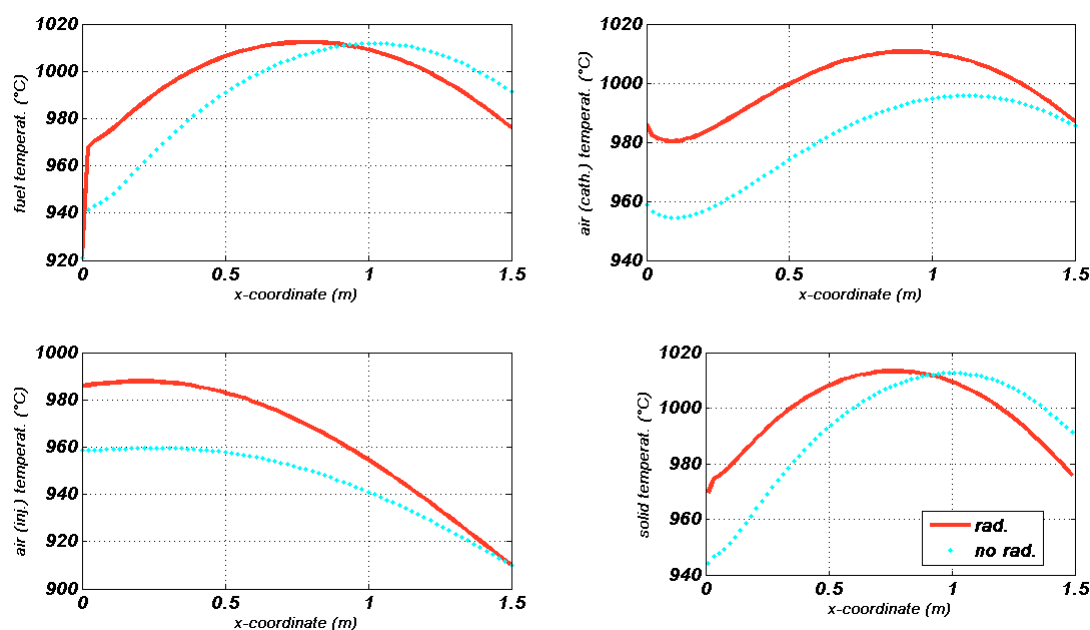


Figure I. 51: Radiative vs non-Radiative models

In particular the radiative heat transfer significantly promotes the air pre-heating in the injection tube and in the air compartment of the fuel cell. Consequently, such heat transfer mechanism strongly contributes to the reduction of temperature gradients along the SOFC tube. However, it is important to remind that thermal radiation is just an internal heat transfer mechanism: radiative and non-radiative models show the same outlet temperatures (:). Consequently, the radiative heat transfer can be neglected in any type of 0-D model.

1.7.5.3. Exergy balance

One of the aim of the study was the analysis of irreversibility distribution along the SOFC tubular cell, by means of an exergy analysis. Such analysis aimed at: i) calculating the magnitude of the irreversibilities; ii) determining their distribution along the cell; iii) determining the source of irreversibility.

Thus, the above discussed simulation model was used to calculate the physical and chemical exergy flows for each slice of the computational domain and then the corresponding local exergy destruction rate, using the exergy balance of eq. (4).

In the process under study, the sources of exergy destruction are:

- i) heat exchange;
- ii) chemical/electrochemical processes;
- iii) pressure drops.

SOFC fuel cells show mainly irreversibilities of types i) and ii), since very low pressure drops are detectable (:). Thus, the magnitude and the distribution of only thermal and chemical/electrochemical irreversibilities along the SOFC axis was investigated.

The exergy balance for any single slice of the discretization was then performed, in order to evaluate the local exergy destruction rate and to evaluate the level of thermodynamic irreversibility along the SOFC axis.

In SOFC analysis, both physical and chemical components of the exergy flow related to streams of matter must be considered. In fact, most streams evolving in the fuel cell are chemical reactive: so, variations in the chemical composition and consequently in the corresponding chemical exergy flows occur within the cell. Chemical and physical exergy can be calculated on the basis of the general relations available in literature. In this work, using the assumptions of ideal gas and ideal mixtures, as discussed before, the physical and chemical exergy flows were expressed as follows:

$$\dot{E}x_{ph} = \dot{m} \cdot ex_{ph} = \dot{m} \sum_{i=1}^7 \left\{ c_{p,i} (T_i - T_0) - T_0 \left[c_{p,i} \ln \left(\frac{T_i}{T_0} \right) - R_i \ln \left(\frac{p_i}{p_0} \right) \right] \right\} \quad (\text{I.97})$$

$$\dot{E}x_{ch} = \dot{n} \cdot ex_{ch} = \dot{n} \cdot \sum_{i=1}^7 x_i \sum_{i=1}^7 (x_i ex_{ch,i}^0 + R_0 T_a \ln(x_i)) \quad (\text{I.98})$$

Standard values for the chemical exergy of pure substances are reported in table I.4. The overall exergy flow related to the stream of matter i , is:

$$\dot{E}x_i = \dot{E}x_{ch,i} + \dot{E}x_{ph,i} \quad (\text{I.99})$$

The exergy balance for the slice i of the discretization can be written on the basis of the well-known rules of the exergy analysis. Considering the slice i , the exergy balance for the control volume displayed in : is:

$$\dot{E}x_{1,i-1} + \dot{E}x_{2,i-1} + \dot{E}x_{3,i} = \dot{E}x_{1,i} + \dot{E}x_{2,i} + \dot{E}x_{3,i-1} + \dot{E}x_{d,i} + \dot{P}_{cell,i} \quad \forall i = 1 : n \quad (\text{I.100})$$

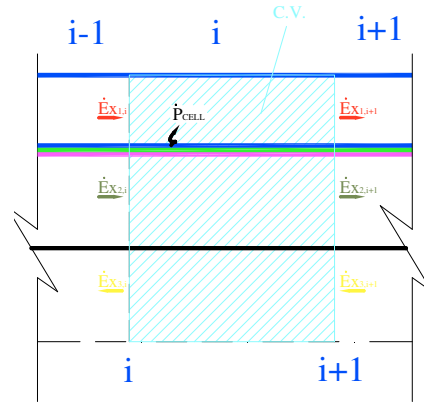


Figure I. 52: Control Volume for the exergy balance

The local exergy performance at slice i can be evaluated by means of the corresponding exergy destruction rate. However, this value just represents an absolute measure of the irreversibility level in the slice under investigation. In fact, the local contribution of a single slice to the overall power production varies significantly along the cell, and, in general, the local exergy destruction rate will increase with the local power production.

Therefore, the local exergy performance is better evaluated through the local exergy efficiency, defined as the ratio between the useful exergy flow (Product) and the exergy required to obtain it (Fuel).

In our case, for any slice of the cell, the Product is always represented by the local power production, whereas the Fuel was calculated as the difference between the exergy content of inlet and outlet streams, as shown in eq **Errore. L'origine riferimento non è stata trovata.**:

$$\eta_{ex,i} = \frac{\dot{P}_{cell,i}}{\dot{E}x_{1,i-1} + \dot{E}x_{2,i-1} + \dot{E}x_{3,i} - (\dot{E}x_{1,i} + \dot{E}x_{2,i} + \dot{E}x_{3,i-1} + \dot{E}x_{d,i})} \quad \forall i = 1:n \quad (I.101)$$

1.7.5.4. Exergy Analysis results

The results are shown in : and :, displaying the exergy destruction rates and the exergetic efficiencies of each slice, respectively. : clearly shows that exergy destruction rate dramatically decreases along the SOFC tube. Thus, the irreversibilities shown by the first slices are higher than those of whatever slice of the control volume. However, this result does not necessarily imply that the first slices are more efficient, from an exergetic point of view. In fact, the local exergy destruction rate also depends on the product provided locally, that is, on the local power production that decreases along the cell. Therefore, the local exergy efficiency, defined in **Errore. L'origine riferimento non è stata trovata.**, is more useful to

evaluate the performance of a slice. The profile of this parameter is shown in [Figure I. 53](#), displaying a trend remarkably different from [Figure I. 52](#).

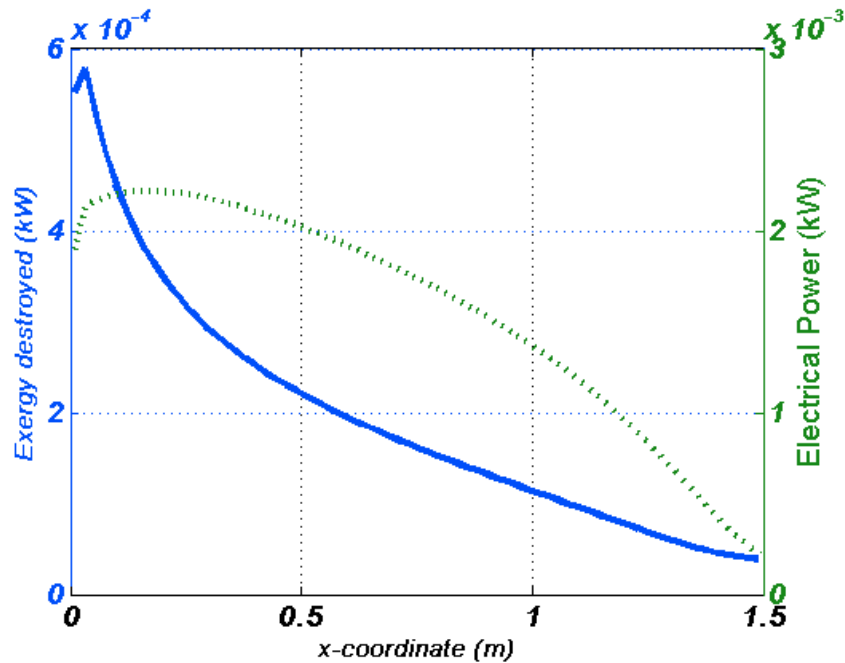


Figure I. 53: Local exergy destruction rates and electrical power production.

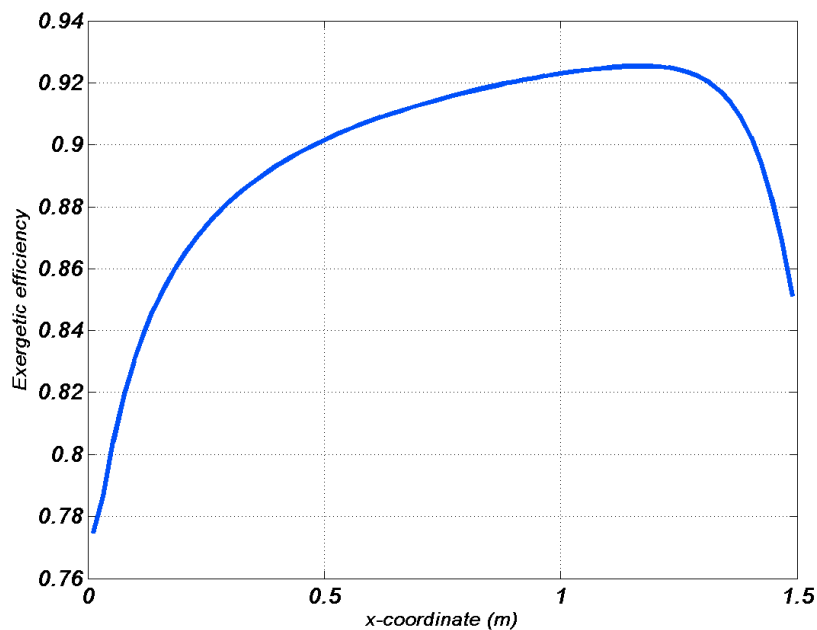


Figure I. 54: Exergetic Efficiency

The results can be explained as follows:

- The first third of the control volume shows remarkably large exergy destruction rates and also low exergy efficiencies. In other words, this part of the fuel cell

produces large electrical power but also large irreversibilities (low exergetic efficiency); in fact, \dot{E}_{ex} and \dot{E}_{ex} show that this part of the fuel cell is distinguished by high values of chemical/electrochemical reaction rates (reforming process and electrochemical reaction). On the other hand, the radial temperature gradients are low, so that the irreversibilities of this part of the fuel cell are mainly due to the chemical/electrochemical processes.

- In the second third of the control volume, the exergy destruction rates are much lower (\dot{E}_{ex}). This is due both to the reduction of power production and to an increase of the performance, since the slope of the exergy destruction curve is higher than that of power production.. This result is in agreement with the fact that chemical and electrochemical reaction rates in this part of the cell are very low (\dot{E}_{ex}). On the other hand, remarkable radial temperature differences between the solid and the air in the injection tube are detectable. Therefore, the irreversibilities of this part of the cell are mainly due to heat transfer phenomena.
- Finally, in the last part of the cell low values of both exergy destruction rates and low exergy efficiencies can be observed (\dot{E}_{ex} and \dot{E}_{ex}). Here, the electrical power production is low, but the reaction rate of electrochemical phenomena are also quite low, and the reforming process can be considered complete (\dot{E}_{ex}). Therefore, the high level of irreversibility is mainly due to high radial temperature gradient (\dot{E}_{ex}).

1.7.6. Sensitivity analysis

The simulation model described before was also implemented in order to perform a sensitivity analysis, aiming at investigating the variations of chemical/electrochemical and thermodynamic properties in the cell as a function of the main design/operating variables. In addition, the sensitivity analysis also aimed at investigating the influence of operating/design variables on the magnitude and location of irreversibilities along the cell.

The sensitivity analysis was only performed for the operating/design parameters showing a remarkable influence on the performance of the cell.

1.7.6.1. Cell Diameter

Cell diameter is one of the most important design parameters, since it dramatically affects: electrochemistry (that depends on the active area of the cell), internal reforming process (sensitive to the catalyst mass), heat exchange (depending on streams velocities and heat

exchange area), and pressure drops (depending on the friction factors). In addition, cell diameter also affects the cell capital costs, increasing with the cell diameter (and therefore with the active area).

This is clearly shown in [Fig. I.54](#). Larger cell diameters correspond to active area, inducing an increase of both electrochemical and internal reforming reaction rates. In fact, the larger the cell diameter, the larger the chemical/electrochemical reaction rates detectable in the first part of the cell. In other words, SOFCs equipped with large cell diameter accomplish both chemical and electrochemical processes in the first part of the cell. This circumstance also dramatically affects the solid temperature profiles. In fact, the heat generated by the chemical/electrochemical process, increase with the active area, especially in the first part of the cell. Therefore, the larger the cell diameter, the higher the SOFC solid temperature in the first part of the cell, and the lower the solid temperature in the second part. Furthermore, a larger cell area also implies a higher fuel consumption in the cell, due to an increase in the chemical/electrochemical reaction rates. This result is clearly depicted in [Fig. I.55](#), showing that the fuel utilization factor is an increasing function of the cell diameter. However, such figure also shows that the slope of the fuel utilization curve rapidly decreases with the cell diameter.

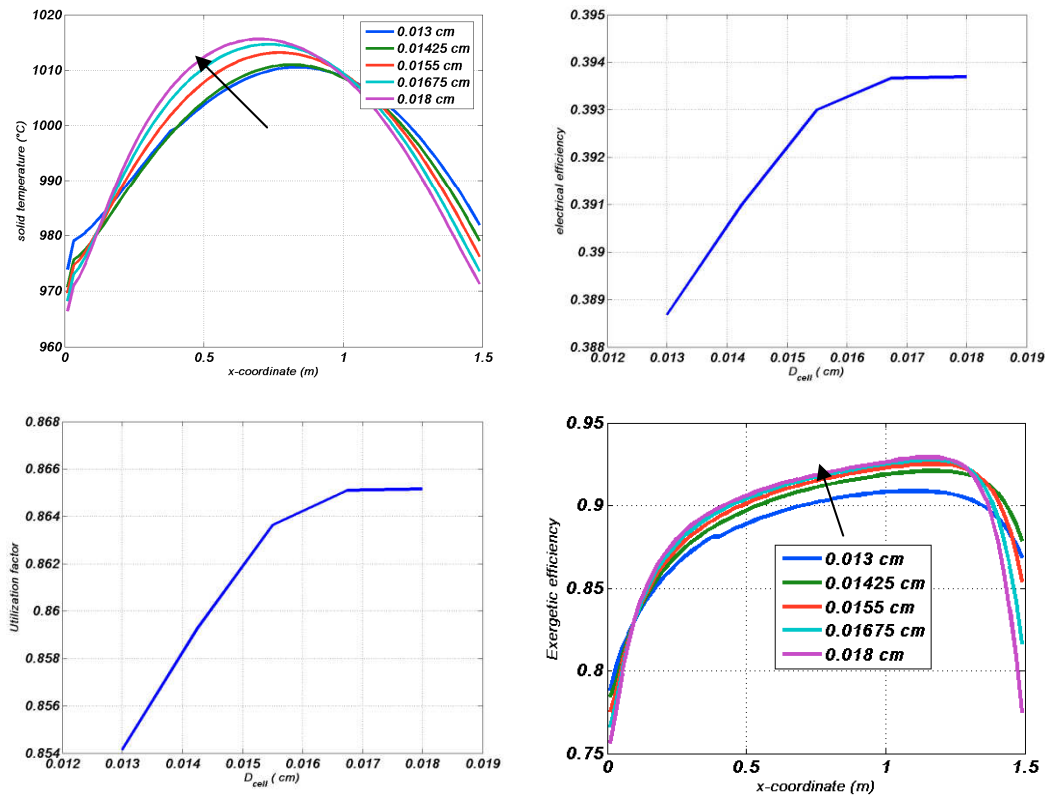


Figure I. 55: Sensitivity analysis: D_{cell}

In fact, a larger cell diameter corresponds to higher chemical/electrochemical reactions, but such reactions mainly occur in the first part of the cell. Therefore, remarkably low hydrogen partial pressures are detectable in the second part of the cell, determining significant overvoltages and consequently low current densities and low fuel consumption. The trend of the fuel utilization factor also influences the electrical efficiency: in fact the larger the cell diameter, the larger the fuel consumed in the cell, increasing its overall electrical efficiency. It is also noteworthy to mention that the variations of fuel utilization and electrical efficiency shown in : are very slight. On the other hand, an increase of the cell diameter dramatically affects the capital costs of the cell. Therefore, results shown in : clearly show that the best value of the cell diameter depends on the fixed objective function: in particular a future thermoeconomic optimization could allow one to determine the value of the cell diameter that minimizes the overall cost of the cell. Finally, : also shows some results of the exergy analysis. For example, it can be observed that the larger is the cell diameter, the larger is the overall exergy efficiency. In particular, larger cell diameters would imply:

- i) higher temperatures in the first part of the cell;
- ii) lower temperatures in the second part of the cell;
- iii) larger overvoltages in the second part of the cell.

Therefore, larger cell diameters would lead to larger exergy efficiency in the first part of the cell (higher temperatures, lower overvoltage and lower temperature differences) and lower exergy efficiencies in the second part of cell, where large irreversibilities are detectable.

1.7.6.2. Cell Length

The Siemens tubular SOFC is featured by a remarkable large cell length (1.5 m). However, the cell length is one of the design parameters that Siemens is going to optimize in order to achieve:

- i) larger electrical and thermal efficiencies;
- ii) lower longitudinal thermal gradients;
- iii) larger power densities;
- iv) lower capital costs.

In fact, in the last few years Siemens has been involved in the development of a 0.75 m cell in order to achieve the above mentioned goals.

Obviously, variations of the cell length dramatically affect all the chemical, electrochemical, thermal and thermodynamic processes occurring in the cell. In fact, a lower cell length also implies:

- i) lower electrochemical active area;
- ii) lower mass of catalyst available for the internal reforming processes;
- iii) lower heat exchange area;
- iv) lower pressure drops.

The simulation model described before allows to investigate the influence of the cell length on the main chemical, electrochemical, electrical and thermodynamic parameters of the cell. Results of this analysis are shown in :. Here, it is clearly shown that the larger the cell length the larger its operating temperature. In fact, large cell lengths would also imply large chemical and electrochemical reaction rates determining a larger amount of heat released by these reactions. Furthermore, : also shows that the larger the cell length the larger the cell length the larger also the longitudinal temperature gradients detectable along the cell. Therefore, taking into account the reduction of capital costs and temperature gradients, a cell designer could be addressed to the development of lower cell lengths. However, a lower length would also imply lower reaction rates determining lower fuel utilization factors and consequently lower electrical efficiencies.

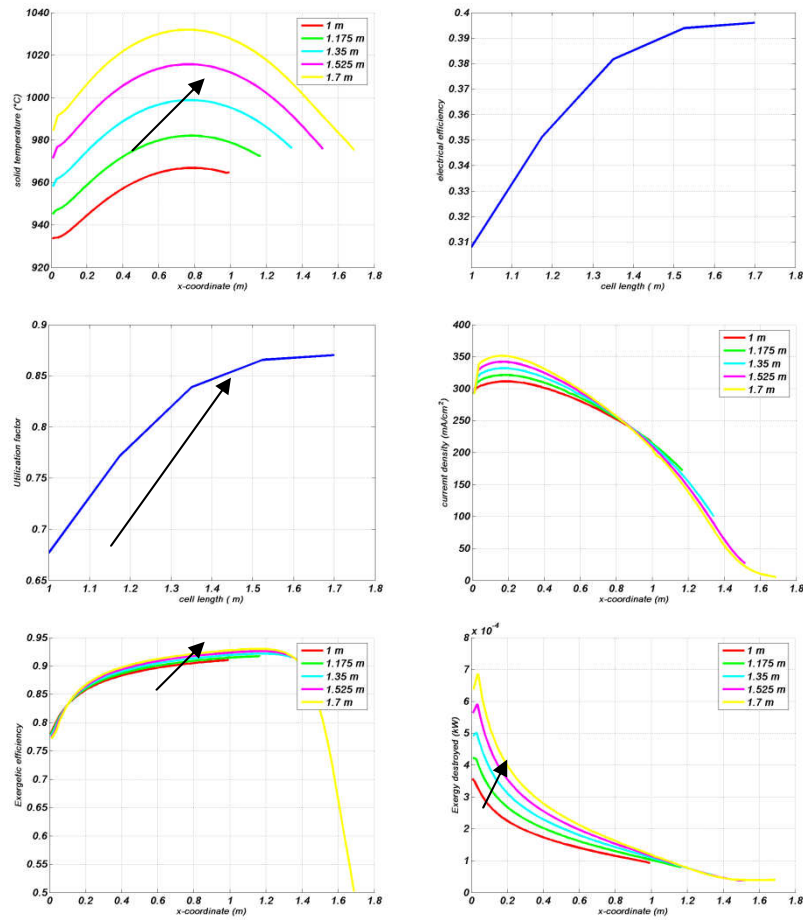


Figure I. 56: Sensitivity analysis: L_{cell}

Hence, the optimal cell length must be accurately chosen in function of the fixed objective function (maximum cell efficiency or minimum total cost), taking into account all the technological constraints in terms of longitudinal and radial temperature gradients. Finally, the exergy analysis displayed in Fig. I. 56, also shows that the larger the cell length the larger the corresponding local exergy destruction rate. However, taking into account that the exergy product is an increasing function of the cell length, the corresponding local exergy efficiency will show the trend displayed in Fig. I. 56. Here, it is clearly displayed that lower cell lengths would imply remarkably high exergy efficiency all over the cell. In fact, in this case both low radial temperature differences and overvoltages can be achieved. On the other hand, SOFCs equipped with larger lengths, will show larger exergy efficiencies in the first part of the cell (due to the higher operating temperature) and dramatically lower exergy efficiencies in the second part of the cell (due to the higher radial temperature gradients and overvoltages).

1.7.6.3. Cell Voltage

According to the discretization procedure implemented, the slices were assumed in electrical parallel arrangement with each other. Therefore, the voltage can be considered constant along the SOFC tube. Obviously, the operating cell voltage depends on the load connected to the cell. Hence, the operating cell voltage can be considered as an external parameter in the simulation code. : shows the influence of this parameter on the thermodynamic, chemical, electrochemical, electrical and exergetic performance of the cell. Obviously, the shape of the typical polarization curve shows that a larger operating voltage implies lower current densities, also determining lower electrochemical reaction rates. Therefore, the larger the operating voltage, the lower also the amount of heat released by the electrochemical reaction. This circumstance dramatically affects the cell thermal balance, resulting in a significant reduction of the cell operating temperature all over the cell. On the other hand, larger operating voltages would also result in lower radial and longitudinal temperature gradients, due to the low electrochemical reaction rate. Furthermore, the variations on the cell operating temperature slightly affect the local internal reforming reaction rates. Therefore, the operating voltage dramatically affects the hydrogen consumption in the cell. In fact, taking into account that the internal steam reforming process shows similar rates of reaction in function of the cell voltage, the lower the operating voltage, the lower the electrochemical reaction rates, determining a lower hydrogen consumption in the cell. This result is clearly shown in : 7, where the fuel utilization factor is shown as a decreasing function of the operating voltage. Moreover, the larger is the operating voltage, the higher is the operating temperature (increasing the electrical efficiency) and the lower the fuel utilization factor (decreasing the electrical efficiency). This trade-off is clearly shown in : 7, displaying a non-monotonic plot of the electrical efficiency in function of the operating voltage. Finally, the exergy analysis showed that the exergy efficiency decreases for low operating voltages, especially in the last part of the cell. Here, the overvoltages and the radial temperature gradients dramatically increase, determining a significant reduction of the corresponding exergy efficiency.

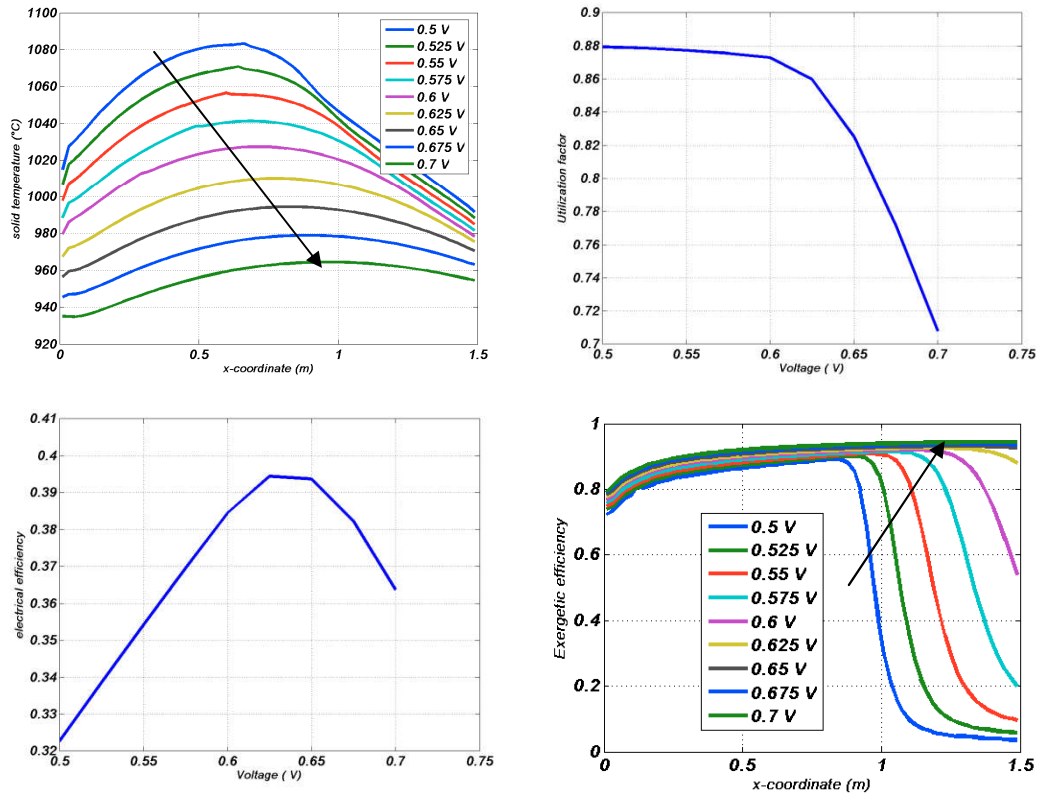


Figure I. 57: Sensitivity analysis: Cell Voltage

1.7.6.4. Air inlet temperature

The cell thermal balance is remarkably affected by the air inlet temperature. Such parameter can be externally controlled, using an external heat exchanger or the air injection tube included in the catalytic burner placed on the top of the fuel cell stack. The air inlet temperature is crucial in order to achieve large operating temperature and in order to control temperature gradients along the cell. The effects of the variations of the air inlet temperature on the performance of the cell are shown in . Here, it is clearly shown that higher inlet temperatures imply higher operating temperature for the solid. : also shows that the shape of the solid temperature curves are not affected by the air inlet operating temperature. Obviously, the higher the air inlet temperature (and solid temperature), the lower the overvoltages, determining higher rates of the electrochemical reactions, especially in the first part of the cell.

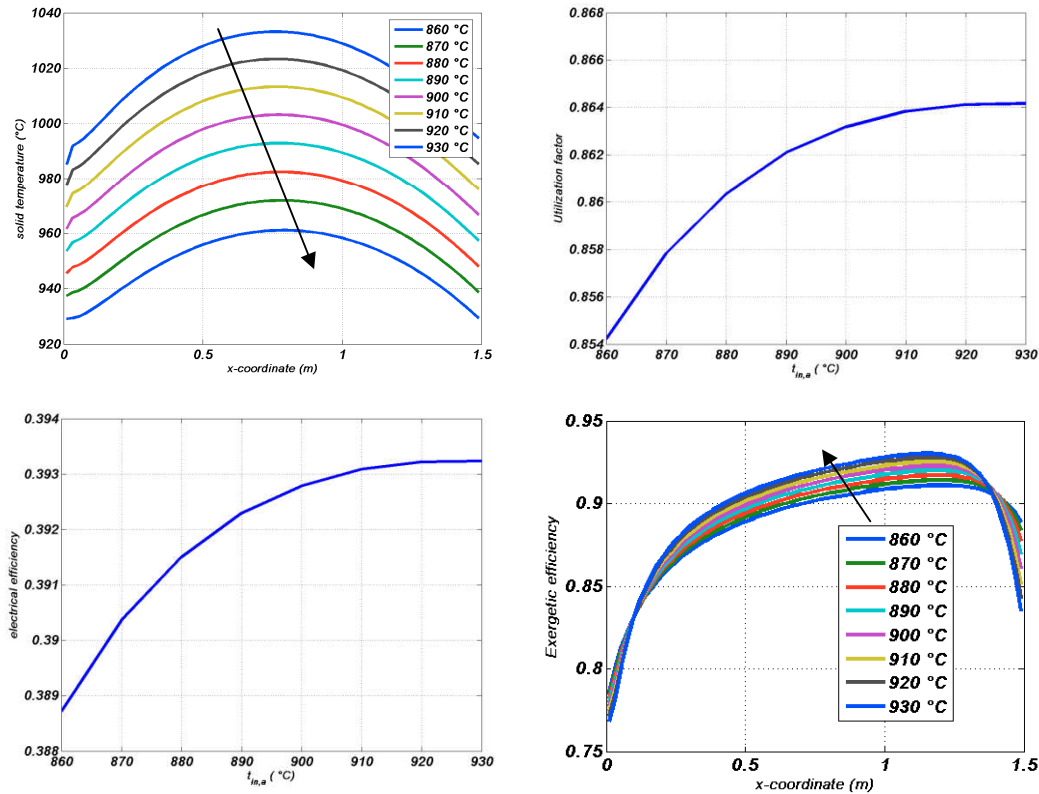


Figure I. 58: Sensitivity analysis: air inlet temperature

This results in a higher fuel consumption, i.e.: a higher fuel utilization factor. Obviously, the larger the current density and the fuel utilization factor, the larger the overall electrical efficiency of the fuel cell. Finally, the exergy analysis shows that an increase of the air inlet temperature increases the exergy efficiency, especially in the first part of the cell, due to the reduction of the corresponding overvoltages. On the other hand, a cell fed by high temperature inlet air stream would achieve high current densities in the first part of the cell, where most of the fuel is consumed. Consequently, the second part of the cell shows low hydrogen partial pressures (and current densities), achieving high overvoltages. Such overvoltages determine values of the exergy efficiencies lower than those achieved by cells fed by air at lower temperature.

1.7.6.5. Inlet pressure

Usually, SOFC systems operate at pressures slightly higher than the environmental one. However, a number of SOFC systems are also designed to operate at high pressures, e.g. in case of hybrid SOFC-GT power plants. It is well known that high operating pressures induce an increase in the following parameters:

- i) the rate of the internal reforming;

- ii) the rate of diffusion through the electrodes;
- iii) the activation of the electrochemical reaction;
- iv) the open circuit reversible voltage.

Furthermore, the increase of the cell operating pressure determines a number of other benefits, as shown in .:

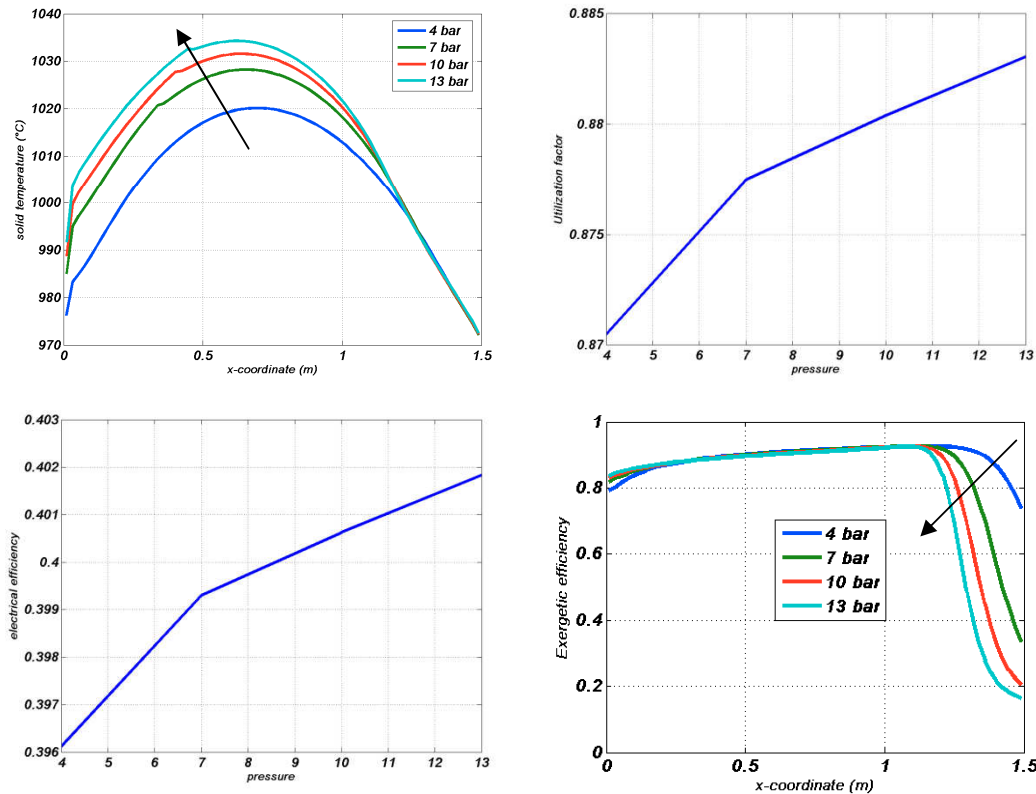


Figure I. 59: Sensitivity analysis: inlet pressure

In fact, the larger the operating pressure, the higher the cell operating temperature. This is mainly due to the significant increase of the electrochemical rate of reaction, also determining a larger amount of heat release. This heating effect is mainly located in the first part of the cell. Therefore, higher operating temperatures would also determine higher radial and longitudinal temperature gradients. Obviously, the higher the operating pressure, the higher the electrochemical reaction rate, causing better fuel utilization factors and electrical efficiencies. Finally, the exergy analysis shows that an increase of the operating pressure determines a remarkable reduction of the exergy efficiency. This result is mainly due to the reduction of the hydrogen partial pressure detectable in the second part of cell operating at high pressures. On the other hand, the effect of the variations of the radial temperature gradients is very slight, as shown in .:

1.8. Combustor Model

The simulation procedure also implements a detailed 1-D axial symmetric model of the catalytic burner located on the top of the fuel cell stack (**Errore. L'origine riferimento non è stata trovata.**), not included in the models previously developed by the authors [10, 13, 15]. This component is usually analyzed by means of a 0-D approach, due to the velocity and the magnitude of the combustion reactions [4-7]. However, in this case this assumption is not considered aiming at determining the distribution and the magnitude of irreversibilities along the cell. A special effort was performed in order to design appropriately this component and determining the corresponding simulation models. Usually, the combustion process, occurring in the traditional power plants, are carried out by means of flame-assisted combustions, whose simulation models are well-known in literature [26]. However, such technology is not commonly used in SOFC systems, where the catalytic flame-less combustion is usually selected. In fact, the catalytic flame-less combustion can occur spontaneously at the top of the cell, whereas the flame-assisted combustion would require an external properly designed component. The simulation of the catalytic combustion is usually carried out determining the set of elementary surface and gas reaction mechanisms [27, 28]. However, such approach is not suitable for the aim of this simulation since the number of elementary reactions is dramatically huge (e.g. [29]). Therefore, a special effort was performed in order to find papers presenting simplified apparent reaction mechanisms [30-32], calculating the kinetics of the combustion process implementing a reduced number of elementary equations. Such simplified reaction models allow one to achieve both good calculation accuracy and computational time. In particular, in [31] detailed kinetics of CO, CH₄ and H₂ are provided for the HA catalytic combustion. Therefore, the catalytic combustor is simulated by means of the above discussed 1-D discretization procedure.

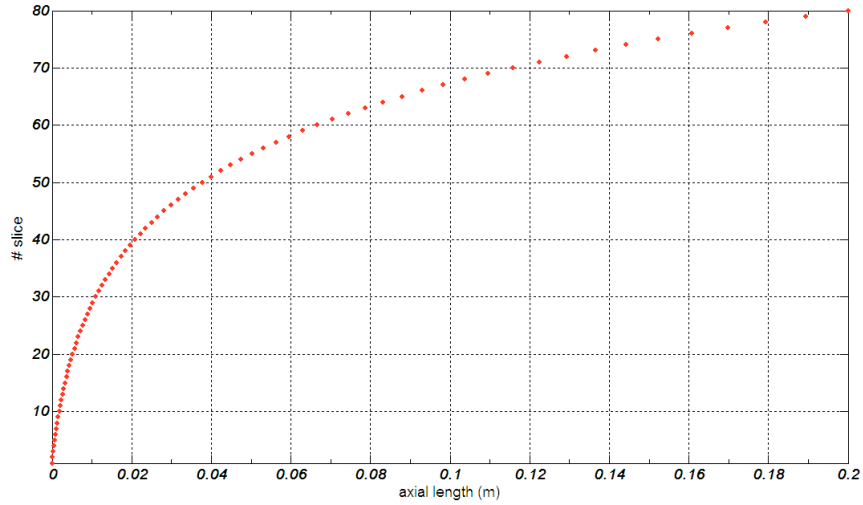
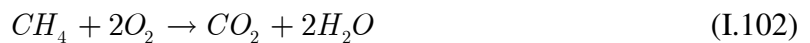


Figure I. 60: Combustor discretization

However, the combustion process determines dramatic gradients in the initial part of the combustion zone. Thus, an homogeneous discretization (same size for each slice) would require a huge number of elementary cells in order to achieve sufficient calculation accuracy. Hence, the combustor simulation is performed implementing a not-homogeneous discretization, as shown in : . The basic principle of the combustor simulation model can be summarized as follows. The mass flow rate, chemical composition, temperature and pressure of the stream flowing outside the tubes is calculated assuming an adiabatic instantaneous mixing between the SOFC cathode and anode outlet streams. Then, proper correlations are implemented to determine the corresponding friction factors and convective heat exchange coefficients. Simultaneously, the catalytic combustion model is implemented in order to determine chemical composition profiles and the heat released by the combustion reactions along the computational domain. On the other hand, the friction factors and convective exchange coefficients of the stream flowing inside the tube are calculated as previously discussed. Finally, energy, mass, moles and momentum balance equations are implemented in order to form the system of algebraic equations to be solved in order to determine temperature, pressure and chemical composition profiles in this component.

We now describe in detail the type of discretization adopted for the combustor. The component is simulated by simple energy, mass and moles balances, based on the following combustion reactions:





The speed of these three reactions are provided by the following equation (mol/cm³ s):

$$\xi_1 = r_{CH_4} = K_{CH_4} C_{CH_4} \quad (I.105)$$

$$\xi_2 = r_{CO} = K_{CO} C_{CO}$$

$$\xi_3 = r_{H_2} = K_{H_2} C_{H_2}$$

with:

$$K_i = A_i \exp\left(\frac{-E_{act,i}}{RT}\right) \quad (I.106)$$

i = 1, 2, 3 reaction

C_i = molar concentration of i species;

The values of kinetic parameters are listed below:

Reaction N.	A_i	$E_{act,i}$ [cal · mol ⁻¹]
1	$1,58 \cdot 10^{13}$	23900
2	$3,98 \cdot 10^{14}$	15300
3	$2,196 \cdot 10^{12}$	13000

Table I. 14: Parameter of kinetics model

The mass balance is realized for each component of the mixture; the three reactions considered, not having the same behavior, must be analyzed separately. Named ξ_1 , ξ_2 and ξ_3 the speed of reactions, it is possible to calculate the outlet chemical composition of a single slice using simple stoichiometric balances. Or:

$$\forall i = 1 : n - 1 \quad \left\{ \begin{array}{l} n_{CH_{4,i+1}} = n_{CH_{4,i}} - \xi_{1,i} \\ n_{CO_{i+1}} = n_{CO_i} - \xi_{2,i} \\ n_{H_{2,i+1}} = n_{H_{2,i}} - \xi_{3,i} \\ n_{O_{2,i+1}} = n_{O_{2,i}} - 2\xi_{1,i} - \frac{1}{2}(\xi_{3,i} + \xi_{2,i}) \\ n_{N_{2,i+1}} = n_{N_{2,i}} \\ n_{CO_{2,i+1}} = n_{CO_{2,i}} + \xi_{2,i} \\ n_{H_2O} = n_{H_2O_i} + 2\xi_{1,i} + \xi_{3,i} \end{array} \right. \quad (I.107)$$

Once obtained the molar compositions inbound and outbound of the single slice, and the temperatures and pressures at the inlet, through an energy balance is possible to calculate the enthalpy at the outlet and thus the temperature output.

$$\forall i = 1 : n - 1$$

$$\left\{ \begin{array}{l} \xi_{1,i} = f\left(p_i, \frac{t_i + t_{i+1}}{2}\right) \\ \xi_{2,i} = g\left(p_i, \frac{t_i + t_{i+1}}{2}\right) \\ \xi_{3,i} = h\left(p_i, \frac{t_i + t_{i+1}}{2}\right) \end{array} \right.$$

$$\left\{ \begin{array}{l} n_{CH_{4,i+1}} = n_{CH_{4,i}} - \xi_{1,i} \\ n_{CO_{i+1}} = n_{CO_i} - \xi_{2,i} \\ n_{H_{2,i+1}} = n_{H_{2,i}} - \xi_{3,i} \\ n_{O_{2,i+1}} = n_{O_{2,i}} - 2\xi_{1,i} - \frac{1}{2}(\xi_{3,i} + \xi_{2,i}) \\ n_{N_{2,i+1}} = n_{N_{2,i}} \\ n_{CO_{2,i+1}} = n_{CO_{2,i}} + \xi_{2,i} \\ n_{H_2O} = n_{H_2O_i} + 2\xi_{1,i} + \xi_{3,i} \end{array} \right. \quad (I.108)$$

Note that the (4.246) is a system of nonlinear equations, not explicit, because the ξ_i functions contain the partial pressures at the outlet of the slices that depend by the composition at the outlet of the slices, or by the same ξ_i values. In order to apply the pressure drop model it is in fact necessary to know the properties at entry and exit of single slice (including the output chemical composition). It will be therefore necessary to use algorithms to solve systems of non-linear algebraic equations. It could be obtained an explicit solution otherwise, if the ξ_i functions had been evaluated with the partial pressure at the inlet of the slice, but introducing a greater error of calculation for lower number of slices of discretization .

1.8.1. Combustor exergy analysis

The above discussed simulation code also returns the 1-D energy and exergy analysis of the catalytic burner, displayed in the following figures. The energetic and exergetic performance of the catalytic burner mainly depends on the value of the SOFC fuel utilization factor. In fact, the lower U_f , the larger the amount of fuel combusted in the catalytic burner.

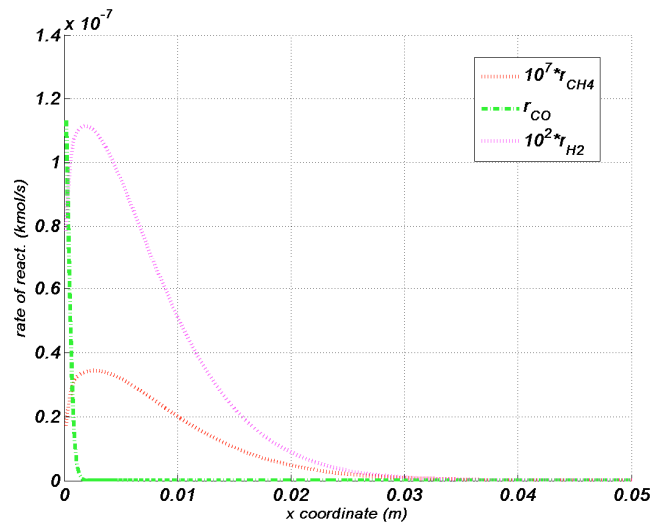


Figure I. 61: Combustor rates of reaction

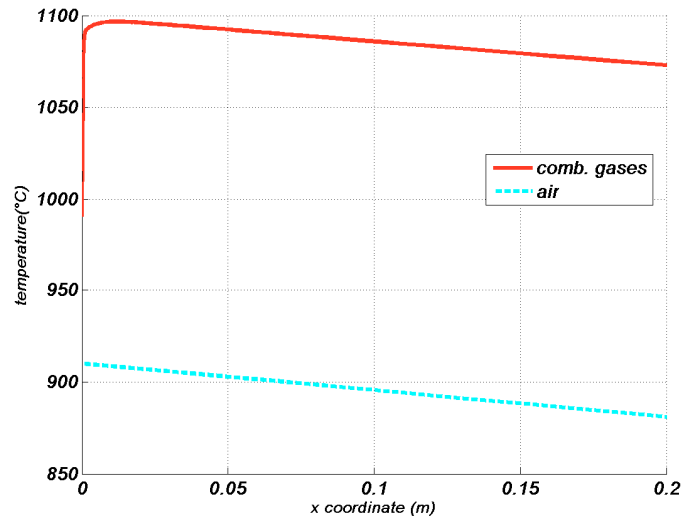


Figure I. 62: Combustor temperatures

Results of the kinetic model are displayed in : . Here, it is clearly shown that the catalytic combustion reactions are dramatically fast. In particular the CO combustion reaction is much faster than the H₂ and CH₄ reactions. In fact, the rate of the CH₄ reacted is remarkably low due to the low amount of CH₄ entering the catalytic burner (the inlet CH₄ molar fraction is 3.9 10⁻⁶ %). On the other hand, a significant amount of CO can be detected at the combustor inlet (the inlet CO molar fraction is 1.24%), determining large amount of CO reacted in the catalytic burner (:). It also noteworthy emphasize the circumstance that such rates of reaction are also due to the high operating temperature of the catalytic burner. Thus, the above discussed rates of combustion reactions dramatically affect the temperature trends shown in

Errore. L'origine riferimento non è stata trovata., where it is clearly shown the dramatic heating effect due to the combustion reactions, occurring in the initial part of the component.

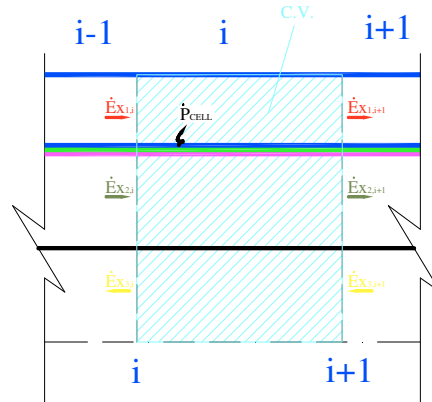


Figure I. 63: Control Volume for the exergy balance

The local exergy performance at slice i can be evaluated by means of the corresponding exergy destruction rate. However, this value just represents an absolute measure of the irreversibility level in the slice under investigation. In fact, the local contribution of a single slice to the overall power production varies significantly along the cell, and, in general, the local exergy destruction rate will increase with the local power production.

Therefore, the local exergy performance is better evaluated through the local exergy efficiency, defined as the ratio between the useful exergy flow (Product) and the exergy required to obtain it (Fuel).

In our case, for any slice of the cell, the Product is always represented by the local power production, whereas the Fuel was calculated as the difference between the exergy content of inlet and outlet streams, as shown in eq **Errore. L'origine riferimento non è stata trovata.**:

$$\eta_{ex,i} = \frac{\dot{P}_{cell,i}}{\dot{E}x_{1,i-1} + \dot{E}x_{2,i-1} + \dot{E}x_{3,i} - (\dot{E}x_{1,i} + \dot{E}x_{2,i} + \dot{E}x_{3,i-1} + \dot{E}x_{d,i})} \quad \forall i = 1:n \quad (I.109)$$

1.9. Conclusions

A very detailed simulation model, based on a finite-volume discretization of a tubular Solid Oxide Fuel Cell Stack, was presented. In the first part of the chapter, the model was accurately described and in the second part, the main results of the simulation were presented. The simulation model allows to accurately calculating the trends of all the main physical, chemical, electrical and electrochemical properties, such as temperature, pressure, chemical composition, overvoltages, current, etc.

The simulation code includes a number of detailed models for the calculation of electrochemistry, kinetics of the internal reforming process, heat exchange process and pressure drop phenomena. The model also includes a detailed radiative model for the calculation of the radiative heat transfer inside the cell. The model shows both good calculation accuracy and computational times. The simulation model was used in order to implement an energetic and exergetic analysis of the stacks components reported in Figure I.3.

A complete local exergy analysis of the tubular SOFC stack was presented. The magnitude and the distribution of irreversibilities along the components were evaluated. The results of the case study showed that the main source of irreversibilities is due to the chemical and electrochemical reactions occurring in the three components. In particular, the combustor shows the largest local exergy destruction rate, due to the velocity of the combustion reactions. Similarly, large irreversibilities are also detected in the initial sections of the SOFC tube and pre-reformer, due to the magnitude of the corresponding reaction rates. The present exergy model could be usefully adopted by system designers and manufacturers in order to localize and minimize the sources of irreversibilities in the components.

A sensitivity analysis was also performed, in order to investigate the influence of the most important design variables (e.g. cell diameter, cell length, pressure, inlet temperature and operating voltage) on the performance of the fuel cell. The results of the case study also showed that many design/operation variables can be optimized, in order to improve the thermodynamic and/or thermoeconomic efficiency of the system.

1.10. References

- [1] Singhal S.C., Kendall, K., 2003, High temperature Solid Oxide Fuel Cells, Elsevier.
- [2] Larminie, J., Dicks, A., 2004, Fuel cell system explained, John Wiley & sons LTD.
- [3] Fuel cell handbook (sixth edition), 2002, U.S. Department of Energy.
- [4] Calise F., Dentice d'Accadia M., Palombo A., Vanoli L., Simulation and exergy analysis of a SOFC-gas turbine system, accepted for publication on Energy: the international Journal /ECOS 04 special issue
- [5] Calise F., Palombo A., Vanoli L., Design and partial load exergy analysis of a hybrid SOFC-GT power plant, Journal of Power Sources (in press)
- [6] Calise F., Dentice d'Accadia M., Vanoli L., von Spakovsky M.R., Single-Level Strategy for the Optimal Synthesis/Design of A Hybrid SOFC-GT Power Plant, accepted for publication on Journal of Power Sources
- [7] Calise F. , Dentice d'Accadia M., Palombo A., Vanoli, L., Vanoli, R., 2004, “Modelling, simulation and exergy analysis of a hybrid SOFC - Gas Turbine System”. 3rd International Symposium Energy and environment 2004, Sorrento, 30th September to 2nd October.
- [8] Calise F. , Dentice d'Accadia M., Palombo A., Vanoli, L., Vanoli, R., 2006, “One-Dimensional Model of a Tubular Solid Oxide Fuel Cell”, in press ASME Journal of Fuel Cell Science and Technology, August 2006
- [9] P.Costamagna, L.Magistri, A.F.Massardo, Design and part-load performance of a hybrid system based on a solid oxid fuel cell reactor and a micro gas turbine, Journal of Power Sources 96 (2001) 352-368.
- [10] S.H. Chan, H.K.Ho ,Y.Tian, Multy-level modelling of SOFC-gas turbine Hybrid system, International Journal of Hydrogen Energy 28 (2003) 889-900.
- [11] Chan, S. H., Low, C. F. , Ding, O. L., 2002, “Energy and exergy analysis of a simple solid – oxide fuel cell power system.”, Journal of Power Sources, vol. 103, pp.188-200.
- [12] Campanari S., Iora P., Definition and sensitivity analysis of a finite volume SOFC model for a tubular cell geometry, Journal of Power Sources 132 (2004) 113—226

-
- [13] Cristoph Stiller, Bjorn Thorud, Steiner Seljebo, Oistein Mathisen, Havard Karoliussen, Olav Bolland, Finite volume modelling and hybrid-cycle performance of planar and tubular solid oxid fuel cells, *Journal of Power Sources* 141 (2005) 227-240.
- [14] Chan S.H., Kior K.A., Xia, Z.T., “a complete polarization model of a solid oxide fuel cell and its sensitivity to the change of cell component thickness, *Journal of Power Sources* 93 (2001) 130-140
- [15] Kemal Nisancioglu, Natural gas fuelled solid oxide fuel cells and systems, ohmic losses, Workshop on mathematical modelling, Charmey/Switzerland, july 2 to 6 1989.
- [16] Reid, Prausnitz, *The Properties of gases and liquids*, Mc Graw Hill, 1977
- [17] *Chemical Properties Handbook*, 1999, McGraw Hill, pp. 531-556.
- [18] Free Molecule (Knudsen) in porous media (www.fuelcellknowledge.org)
- [19] Diffusion vs Mass Transfer by Bulk Motion, Fick’s Law and Mass transfer rate equation, CEIC0010
- [20] Todd B., Young J.B., Thermodynamic and transport properties of gases for use in solid oxide fuel cell, *Journal of power Sources* 110 (2002) 186-200
- [21] Gallucci, F., Paturzo, L. , Basile, A. , 2004, “A simulation study of the steam reforming of methane in a dense tubular membrane reactor”, *International Journal of Hydrogen Energy*, vol. 29, pp. 611 – 617.
- [22] Xu, J., Froment, G. F., 1989, “Methanes-steam reforming: methanation and water-gas shift: I. Intrinsic kinetics”, *AIChE Journal*.
- [23] Suwanwarangkul, R., Croiset, E., Pritzker, M.D., Fowler, M.W., Douglas, P.L., Entchev, E., 2006, Mechanistic modeling of a cathode-supported tubular solid oxide fuel cell, *Journal of Power Sources* 154 (2006), pp. 74–85
- [24] Damm, D., Fedorov, A.G., 2005, Radiation heat transfer in SOFC materials and components, *Journal of Power Sources* 143 (2005)158–165
- [25] Murthy, S., Fedorov A.G., 2003, Radiation heat transfer analysis of the monolith type solid oxide fuel cell, *Journal of Power Sources* 124 (2003)453–458
- [26] Xue, X., Tanga, J., Sammes N., Dub, Y., 2005, Dynamic modeling of single tubular SOFC combining heat/mass transfer and electrochemical reaction effects, *Journal of Power Sources* 142 (2005) 211–222

- [27] Stiller, C., Thorud, B., Bolland, O., Kandepu, R., Imsland, L., 2006, Control strategy for a solid oxide fuel cell and gas turbine hybrid system, *Journal of Power Sources* 158 (2006) 303–315
- [28] Brockmann H., 1994, Analytic angle factors for the radiant interchange among the surface elements of two concentric cylinders, *International Journal of Heat and Mass Transfer*, vol.37, no.7, pp-1095-1100, 1994
- [29] Reid, R. L., Tennant, J. S., Anular Ring View Factors, *AIA Journal* vol.11 no.10, pp. 1446-1448
- [30] Tso, C. P., Mahulikar, S. P., 2000, Combined evaporating meniscus-driven convection and radiation in anular microchannels for electronics cooling application, *International Journal of Heat and Mass Transfer*, 43 (2000), pp-1007-1023,
- [31] Litke, P.J., 2002, An investigation into the directionality of heat transfer through stacked cylindrical elements in an enclosed gas environment, *ME* 608, Spring 202
- [32] Tso, C. P., Mahulikar, S. P., View Factors between finite length rings on an interior cylindrical shell, *Journal of thermophysics*, vol.13 no.3, pp. 375-379
- [33] Tso, C. P., Mahulikar, S. P., View Factors for ring elements on coaxial cylinders, *Journal of thermophysics*, vol.13 no.1, pp. 155-158.

CHAPTER II

CHAPTER II.

EXPERIMENTAL ANALYSIS OF THE ENERGETIC PERFORMANCE OF A 5 KW MICRO-TUBULAR SOFC'S COGENERATIVE MODULE

Summary

2.1.	Introduction.....	2
2.2.	The experience of Ges.En. S.p.A.....	2
2.3.	Description of the experimental plant.....	7
2.4.	The CP-SOFC-5000 module.....	9
2.5.	Gas distribution inside the cogenerative module.....	20
2.6.	The Stacks.....	26
2.7.	START UP of the CP-SOFC- 5000 module.....	28
2.8.	Shut-down of the CP-SOFC-5000 module.....	31
2.9.	Fabrication process of the tubular fuel cells.....	32
2.10.	Measuring instruments installed on board of the CP-SOFC-5000 module.....	36
2.11.	Thermocouples.....	41
2.12.	First results of the experimental activities.....	44
2.13.	Conclusion.....	55
2.14.	Acknowledgments.....	56
2.15.	Referenses.....	56

2.1. Introduction

The experimental activity conducted is part of a research program with the specific target of realizing a fuel cell research center at the Ges.En. (Gestioni Energetiche) S.p.A. power plant, for conducting experimental campaigns aimed at determining the energetic and exergetic performance of fuel cells, manufactured with different technology and size, fed by fossil fuels (natural gas), bio-fuels (biogas from landfills) and hydrogen.

Compared to cells at low temperature, the Solid Oxide Fuel Cells and Molten Carbonate Fuel Cells are much more suitable to be fed through non-conventional fuels, guaranteeing the achievement of greater efficiency with less exposure to impurities such as hydrogen sulphides, heavy metals, halogens, etc., whose removal requires, consequently, less complex and expensive systems. The problem of purification of biogas used in the cells is obviously an integral part of ongoing research activities.

The extensive testing is part of a research program born from collaboration between the DETEC (Department of Energetic, Applied Thermal fluid-dynamics and Environmental Controls) of the University of Naples Federico II and the Ges.En. (Gestioni Energetiche) S.p.A., a company responsible of post-mortem managing of a waste landfill site, located in urban location Schiavi-Masseria del Pozzo, in the town of Giugliano in Campania (NA, Italy).

This chapter presents the first results of tests conducted on a 5 kW_e CP-5000-SOFC cogenerative module, fueled by natural gas, manufactured by Acumentrics Corporation (Westwood – MA, USA), based on the solid oxide fuel cell technology. The experimental activity has allowed verifying the performance of the cogeneration unit in different conditions of electrical load, considering the resulting change in the main operational parameters (volume flow, temperature, coefficient of fuel utilization, etc.). Here are presented the first experimental data collected.

2.2. The experience of Ges.En. S.p.A.

The Ges.En S.p.A. is the company responsible of post-mortem managing of a waste landfill site located in Schiavi-Masseria del Pozzo in the town of Giugliano in Campania (NA).

It was founded as actuator subject of the project “analysis and experimentation of high temperature fuel cells fueled by natural gas and biogas” as operating arm of the Consortium Napoli 1 for the reclamation of the landfill site of Schiavi-Masseria del Pozzo in Giugliano in Campania (NA). The primary aim of these activities is testing of high temperature fuel cells (molten carbonate cells, MCFC, and solid oxide cells, SOFC), fed by

fossil fuels (natural gas) and bio-fuels (biogas). The main target of such experimentation is to improve the level of current knowledge on the behavior of the systems under consideration, in cogenerative applications and in case of feeding through non-conventional fuels.

The landfill of Schiavi-Masseria del Pozzo, is located within the territory of the Municipality of Giugliano in Campania (Na) and consists of three separate sites which occupy an area of nearly rectangular shape of about 30 hectares, as follows:

- 14 He Masseria del Pozzo;
- 6.5 He Schiavi;
- 4.5 He Masseria del Pozzo expansion;
- 5 He devoted to plant.

The height of the landfill body fluctuates around 50 meters above sea level.

Before the conferment of waste, it had to proceed at the waterproofing of the bottom of the landfill (rolling terrain, laying on the bottom and on the sides of a bentonitic mattress, 2 mm of polyethylene geo-membrane, 1 layer of geo-textile) and the installation of a drainage network for the leachate (high resistance polyethylene pipes, micro-fissured at the top, with a central collection). To protect this network of drainage, was performed the laying of river gravel pebbles, and then was spread a layer of large sand, and finally one of crushed stone, to facilitate the drainage of leachate.

The edges of the landfill have been shaped to ensure a slope of 1%, favoring the sliding of rainwater; at the escarpments were given a slope, in 1:3 ratio, so as to avoid possible yielding.

The conferment, within the landfill, of the coming waste from the "District Na1" of the Metropolitan area of Naples, has happened between February 1995 and February 2002.

The waste deposition was realized for layers, with subsequent waste covering, in order to recover the biogas produced by the landfill body and avoid that the same could be freely released, polluting the atmosphere (biogas is composed primarily of methane and carbon dioxide, both greenhouse gases).

Since February 2002 started the post-mortem managing of the landfill, which was entrusted to Ges.En. SpA: the main purposes of this management are the elimination of the major sources of pollution, namely biogas and leachate, and the production of electricity from renewable sources.

The collection of biogas is done through 216 vertical wells with a depth equal to 80% of the landfill height. The layout of the plant, with the extracting biogas wells, their radius of

influence and their link to the regulation stations, is shown in Figure II.1.

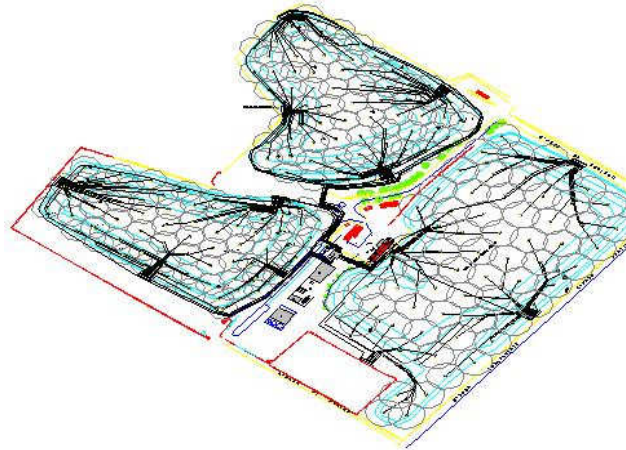


Figura II.1: Landfill's planimetry and wells representation

The biogas picked up arrives to the 12 regulation stations (4 for each of the three areas of the landfill) where at first happens the moisture evaporation and then it is channeled within a single pipe connected to the suction system. The latter has a total prevalence of 650 mbar, 250 mbar aspiration and 400 mbar in delivery: with this value, a direct cogeneration group feeding is possible. To prevent the corrosion of the engines mechanical parts, have been realized a line of pre-treatment, composed by a line of dust abatement, an anti-condensation trap and a dehumidifier.

According to the expected production of biogas from the landfill body and taking into account the choice adopted for the plant of treatment of the leachate (with the use of portion of the recovering heat produced by the energy plant), it was installed a cogeneration system that consists of four internal combustion engines (Jenbacher), designed to operate with landfill gas, with a guaranteed minimum power of 1048 kW each (figure II.2).



Figura II.2: Engine Cogenerator of 1.048 kW

To ensure the elimination of the biogas produced by the landfill body, in the event of interruption of the power plant functioning, has been realized a section of combustion with torches.

With the internal combustion engine system are pursued different objectives:

- Exhaustion of the biogas produced by the landfill body, alternatively or in parallel with the burning in torch;
- Production of electricity used for the auxiliary on the power plant and sold on the electric grid at favored fare;
- Production of the heat necessary for the leachate treatment plant and for building's air-conditioning and cooling systems.

The main problems occurring in the combustion of biogas from landfill are:

- a) significant changes in the volume flow and gas composition of biogas;
- b) presence of high concentrations of micro-pollutant;
- c) the need to limit emissions of pollutants in exhaust fumes.

During the power plant operation, the biogas coming from each line reaches the control centre, where the turbo aspirants provide to send the gas at the pre-treatment system and after at the CHP plant (or torches), where the mechanical energy of the engines is converted into electricity by alternators, before being sent to the electric grid through the MV cabins.

The heat recovery occurs by heat exchangers exploiting the energy content of the exhaust fumes and of the engine's cooling and lubrication circuit. The hot fluids are then sent to the leachate treatment plant and to the air conditioning system during the winter and summer (adsorption chiller).

The Ges.En. S.p.A. is a company since always very sensitive to energy and environmental issues, which is confirmed on the other hand by the presence within their plant of a photovoltaic field, with total electrical potentiality of 81 kW (output voltage of 400 V), consisting of over 650 modules in polycrystalline silicon.

It is in such context that was born the research program that consist in the realization of a Fuel Cells Research Center to carrying out experimental campaigns directed to determine the energetic and exergetic performance of different fuel cells, realized with various technology and size, fed both by fossil fuel (natural gas), bio-fuels (landfill gas and syngas) and hydrogen.

Inside the research center is currently installed:

- a 5 kW cogenerative module SOFC-CP-5000, fueled by natural gas, produced by Acumentrics Corporation (Boston, MA - USA) - the subject of the experimental activities reported in this chapter;



Figure II. 3: Acumentrics CP-SOFC-5000 cogenerative module of 5 kW

are being installed:

- a 1 kW MCFC module, fed directly with biogas from landfill (produced by the consortium IPASS), endowed by a biogas clean-up system.



Figure II. 4: 1 kW MCFC manufactured by IPASS Consortium

- 2 PEMFC of 5 kWe, fed directly with hydrogen and manufactured by Nuvera Corporation (Cambridge, MA – U.S.A.)

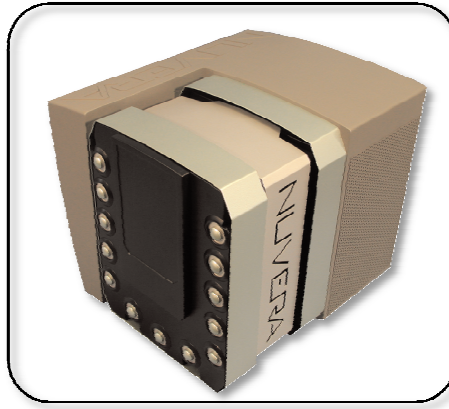


Figure II.5: 5 kW PEMFC manufactured by NUVERA Inc.

In this chapter is first described in detail the working principle of the CP-SOFC-5000 cogenerative module and subsequently are presented the first results of tests conducted on it. The experimental activity has allowed verifying the performance of the cogeneration unit in different conditions of electrical load, considering the resulting change in the main operational parameters (volume flow, temperature, coefficient of fuel utilization, etc.).

In order to conduct the experimental campaign on the cogeneration unit, first of all, has been performed a period of training at the Acumentrics Corporation Factory (Westwood, MA). At this stage were acquired fundamentals knowledge for the operation of the module: in particular have been deepened the issues relating to the design of the unit, the manufacturing and assembly processes of the various components, the solutions adopted for the reforming processes and post-combustion, the solutions for the unit thermal balance. The module is also equipped with a DSP (Digital Signal Process), device capable to acquire the signals coming from measurer placed on board of the unit and automatically to regulate the operation of the module at the varying load conditions. Contextually to the period of training, has been assisted to the various stages of the cogenerative unit start-up procedure with test of the corrected operation of the same one.

Successively an experimentation program has been begun that is continued when the cogenerative unit has been transferred in the Ges.En plant (Giugliano, NA). It has been predisposed the preparation, in the site that accommodates the cogenerative module, of all the necessary equipment to the measurement and the control of the useful parameters to the evaluation of the energetic-exergetic performances of unit (volume flow, pressures, temperatures, chemical compositions, voltage, electric current, etc.).

2.3. Description of the experimental plant

The cogeneration system, object of the first activities of research and experimentation, is

based, as mentioned before, on a SOFC module, of Acumentrics construction, that gives approximately 5 kW of electrical power.

In order to lead an experimentation aimed to determine the energetic performance of the cogenerative module, has been realized an appropriate circuit of thermal loads (Figure II.6-7), constituted of two hydraulic terminal (fancoils) fed by means of a circulator (pump) capable of supplying a water volume flow comprised between 5 Sdm³/min and 10 Sdm³/min.



Figure II.6: SOFC cogenerative plant installed at Ges.En. S.p.A.-Giugliano in Campania (NA, Italy)

The circuit has been opportunely instrumented by means of a thermal energy meter (C.E.T.) and measurer of pressure and temperature on the forward and return pipes.

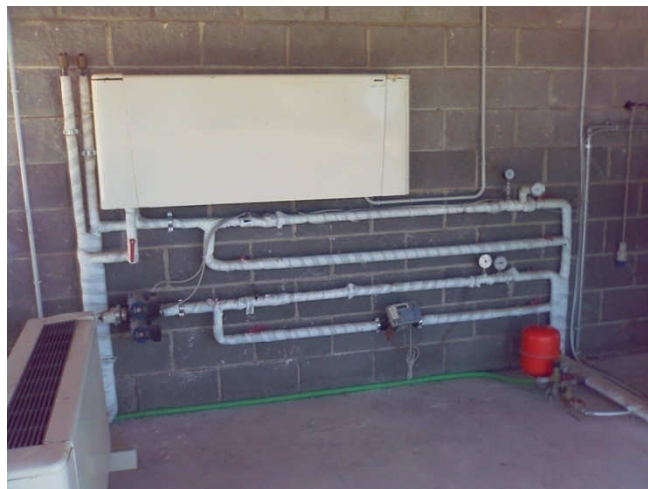


Figure II.7: Thermal loads connected to the CP-SOFC-5000 cogenerative module

It has been moreover predisposed a circuit for the electrical loads, made by 2 series of halogen lamps of different power (200-500 W), with each lamp endowed of a specific

switch, connected together to the inverters installed aboard the CP-SOFC-5000 module, through an electrical panel with inertial and magneto-thermic switches.



Figure II.8: Electric loads connected to the CP-SOFC-5000 cogenerative module

The supply of natural gas is guaranteed by 2 cylinder packages connected to a mixer-reducer, capable of changing autonomously the cylinders packages when the internal pressure falls below a certain threshold.

The CP-SOFC-5000 unit is also connected to a cylinder, containing a mixture formed by 3% of H_2 and 97% of N_2 (purge gas), essential in the event of sudden shutdown of the cogenerative module. The mixture, sent within the anode compartment of the cell, avoids that the nickel present on the anodic compartment may re-oxidize during the cooling phase, resulting in an expansion and possible disruption of tubular cells.

2.4. The CP-SOFC-5000 module

The design of the cogeneration unit is based on solid oxide fuel cells (SOFC) of tubular geometry, realized with anodic support. The solution adopted for the reforming operations of the inlet fuel of the module, allow to carrying out the whole reactions outside the stacks of fuel cells (external reformer), and only a minimum quantity (less than 1% of fuel inlet), in some cases, could carry out the reaction inside the anodic compartment of tubular cells.

The scheme shown in Figure II.9 displays an overview of the main components and the various streams inside the cogenerative module.

Essentially the fuel (natural gas, but also propane), once removed the content of sulfur (desulfurizer), undergoes reforming reactions with consequent production of a mixture composed primarily of hydrogen (H_2) and carbon monoxide (CO); the reforming operations take place either through partial oxidation reactions (CPOX) that through SMR (Steam Methane Reforming): in order to allow the development of CPOX reactions the fuel is pre-mixed with the air coming from the POX air blower. For this reason, the mixture of gas at the outlet of the reformer will be partly diluted by the nitrogen (N_2) present in the air that, not participating at the partial oxidation reaction, keeps intact the value of its volume flow even at the end of the reforming process.

This mixture entering inside the tubular SOFCs, placed inside the stacks, reacts with O^{2-} ions coming from the cathodic compartment, producing electricity on direct current (DC) and simultaneously heat.

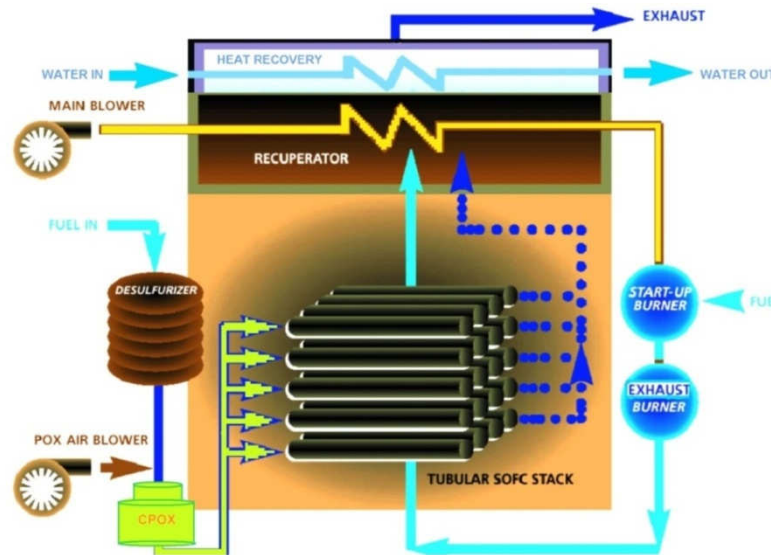


Figure II.9: Functioning scheme of the CP-SOFC-5000 module

The gas mixture, at the exit of SOFCs, consists essentially of steam (H_2O), carbon dioxide (CO_2), nitrogen (N_2) and the fraction of hydrogen (H_2) and carbon monoxide (CO) which, according to the value of the fuel utilization coefficient, that has not participated to the electrochemical reactions within the stacks.

Such gases, afterwards, are mixed with the cathodic air coming from the “main blower”, and sent to the external “exhaust burner” where, the fraction of H_2 and CO that has not reacted previously, complete the combustion process. The mixture, leaving the external burner, is still rich of oxygen and is sent to the cathodic section of the tubular cells, carrying out the cathodic reaction for the production of the O^{2-} ions. The passage of such

gas flow on the external surface of the tubular cells (cathodic section) moreover allows to remove the heat produced during the electrochemical reactions in the stacks.

The thermal energy adsorbed by the gas mixture is used in the two heat recovery sections, constituted of the heat exchanger (recuperator) for the preheating of the cathodic air (coming from main blower) and the section of cogeneration dedicated to the production of water at warm temperature. The exhausted gases finally are released in atmosphere at temperature lower than 100°C.

The unit is equipped moreover with an appropriate starting section constituted of a “start-up burner” that, directly fed by natural gas, warm up the entire module till the attainment of a minimal temperature inside the stacks of 680°C. The burner is placed in the same collector where the post-combustion reactions happen. In fact inside the collector is inserted an appropriate natural gas diffuser (Figure II.10) that, by means of an igniter, allows the development of the combustion process.



Figure II.10: Natural gas diffuser for the start-up burner

At the beginning of the cogenerative module starting phase, all the natural gas is sent to the start-up burner, but already when the maximum temperature in the stacks reaches 300 °C, the unit changes its operating status, sending much more natural gas to the CPOX while only a small fraction continues to feed the start-up burner. In doing so, the hot gas mixture leaving the start-up burner continues to invest outside the tubular cells, heating them, while the gas mixture formed by the reforming reaction, react electrochemically inside the tubular cells, producing additional heat needed to reach the minimum temperature of 680 °C, necessary condition to consider completed the start-up phase of the cogenerative module.

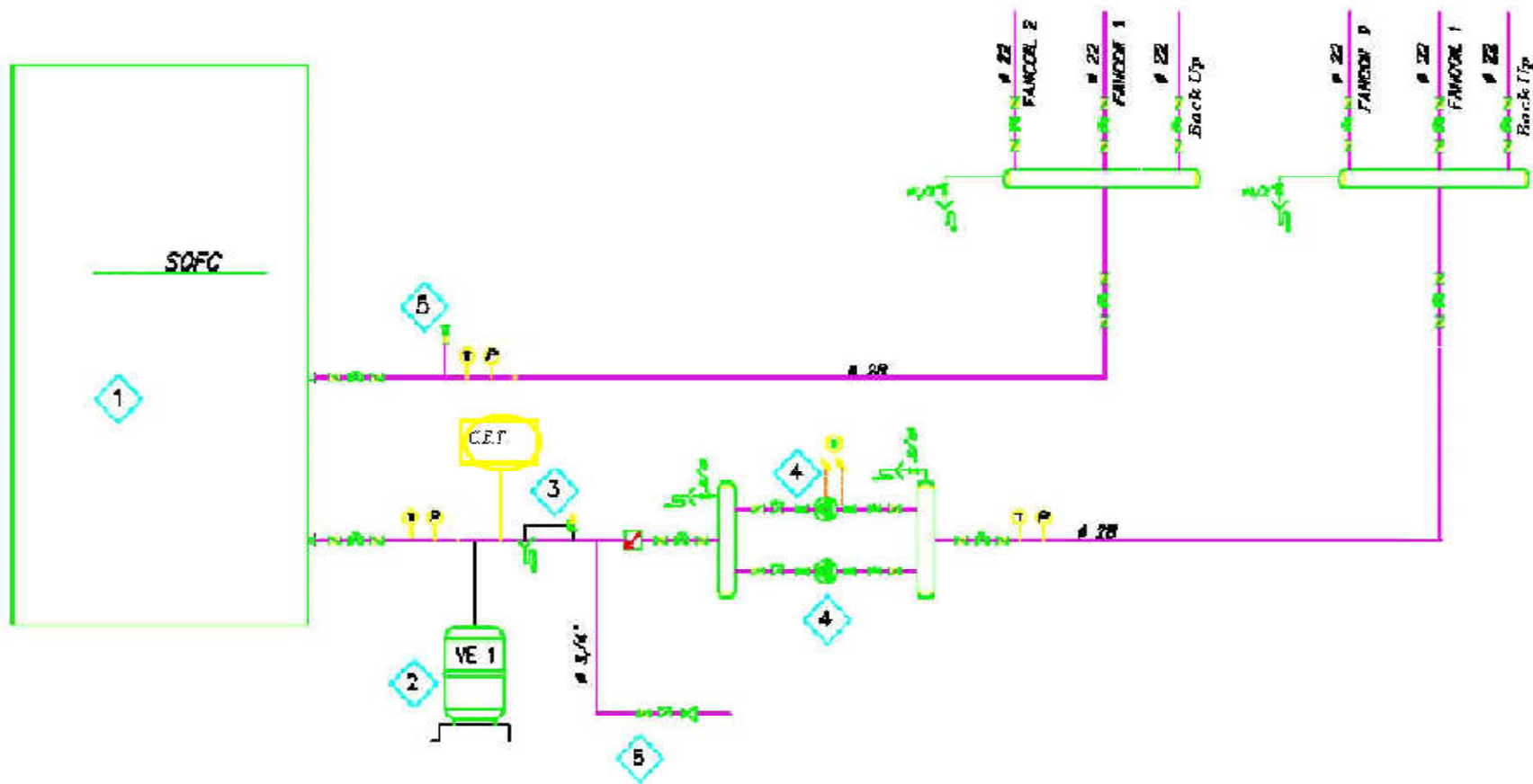


Figure II.11: Cogenerative section scheme

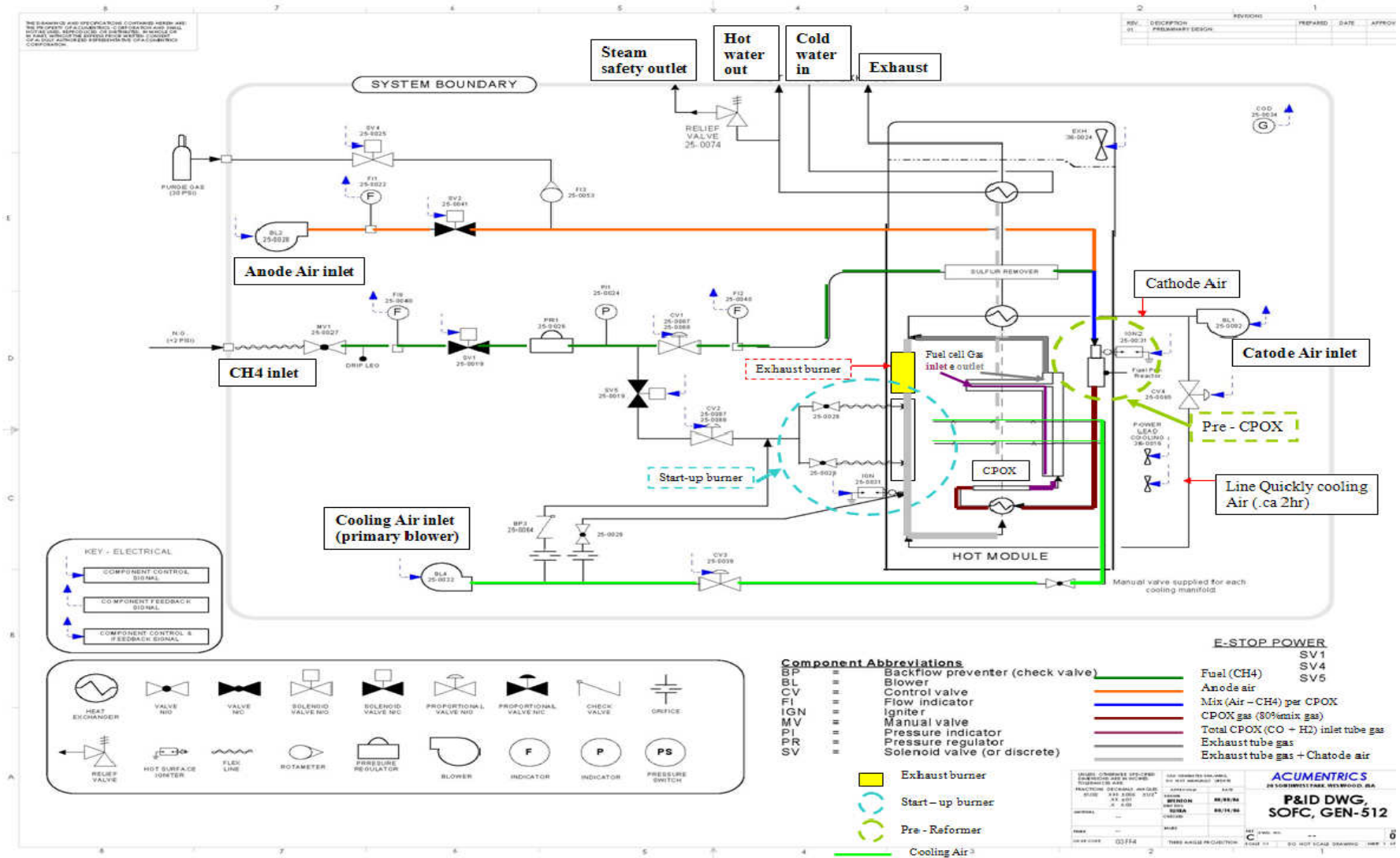


Figure II.12: Gases distribution scheme inside the CP-SOFC-5000 module

In steady state operative condition the cogenerative unit is fed with a volume flow of natural gas ranging between 6.5 Sdm³/min and 20 Sdm³/min, depending on the electrical power required by the electrical load. The partial oxidation process occurs with an O/C ratio of approximately 1.3 (slight excess of air than the stoichiometric ratio required by the reaction, in order to guarantee complete conversion of the inlet natural gas), with a volumetric flow of the inlet anode air ranging between 20.1 Sdm³/min and 65 Sdm³/min.

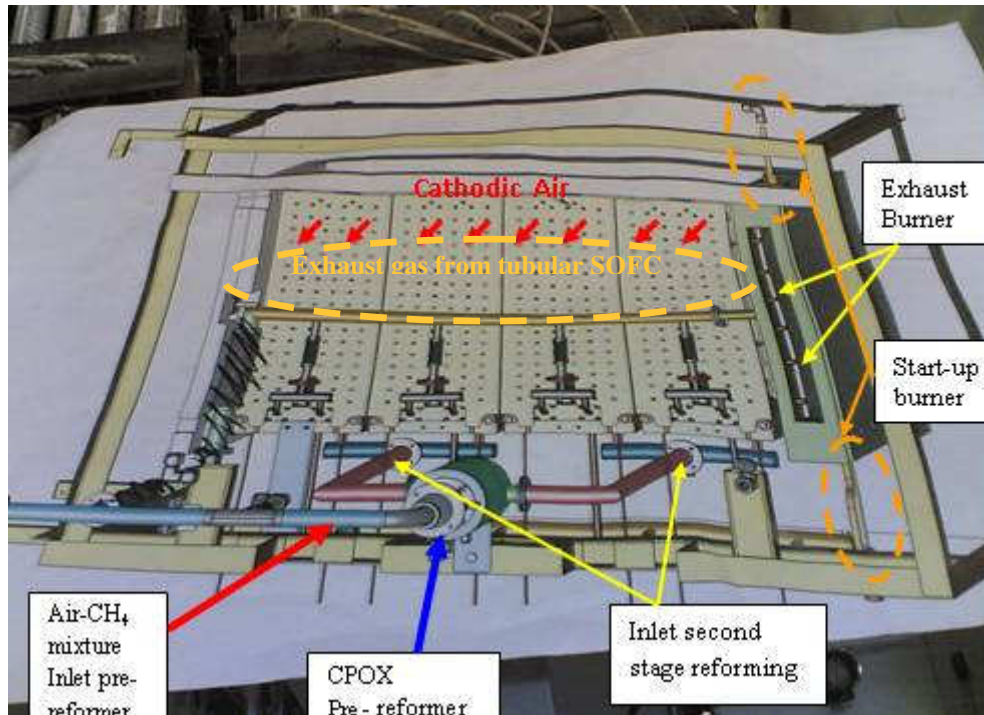
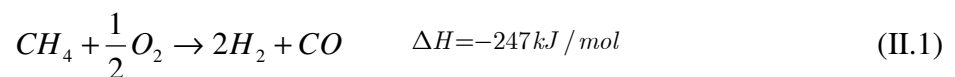
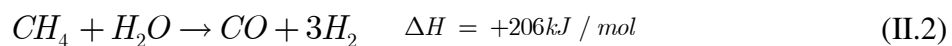


Figure II.13: Gases distribution inside the CPOX, the Start-up Burner and the Exhaust Burner

Analyzing more in detail the reforming process is possible to identify 3 distinct phases: the first stage of reaction takes place inside a catalytic reactor of cylindrical geometry (Figure II.14-15), made in rhodium with an alumina (Al₂O₃) support, where about 90% introduced natural gas is converted through the reaction of partial oxidation:



For any moles of CH₄ reacted are produced 2 moles of H₂ and 1 mole of CO. This process, less efficient if compared to steam methane reforming (capable of producing from 1 mole of CH₄, 3 moles of H₂ and 1 mole CO),



is nevertheless, unlike this last, an exothermic process that doesn't require therefore particular solutions of thermal exchange section to guarantee the necessary heat and temperatures to the SMR reactions.

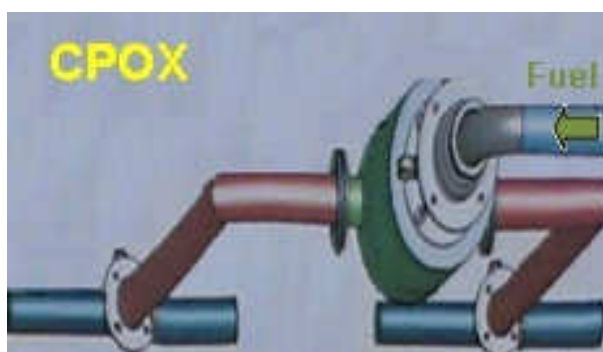


Figure II.14: Cylindrical Catalytic Partial Oxidation Reactor for natural gas reforming (CPOX)

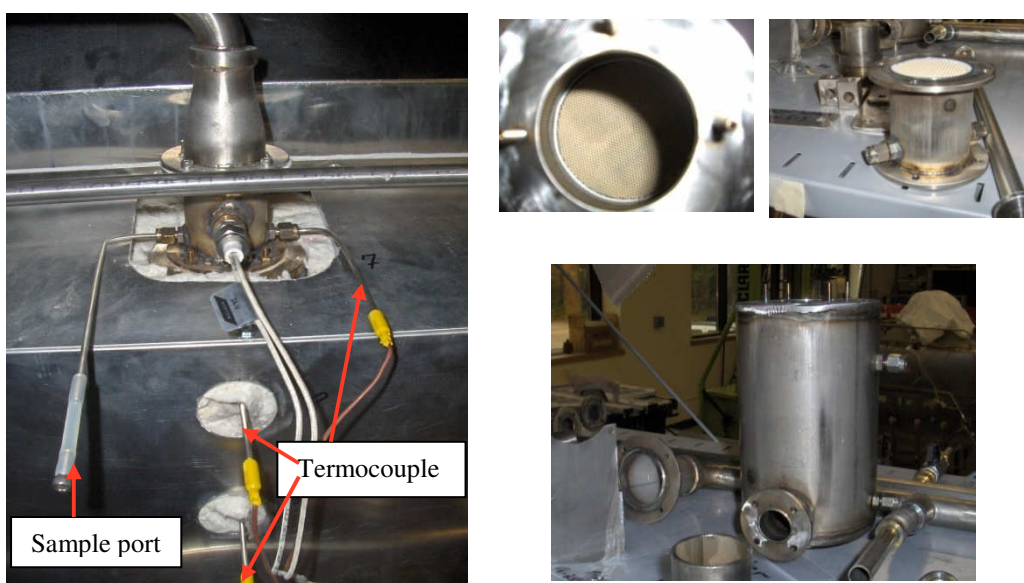


Figure II.15: CPOX cylindrical reactor: rhodium with alumina support with a honeycomb structure

The excess air, however, produces a deleterious effect in part because, the residual oxygen, reacting with the hydrogen and carbon monoxide just formed, prevents them from reaching the anodic compartment of fuel cells (to react inside the fuel cell) and produce electricity and heat.



All this implies a reduction in the efficiency of the natural gas reforming process. This gap, as mentioned before, is partly offset by the greater simplicity on the cogenerative module design thanks to the catalytic partial oxidation solution, which does not require any section of heat exchange (exothermic process).

The second stage of reforming (Figure II.16) occurs at the base of the 4 stacks, within 5 tubes (1 of forward and 4 of return), made of nickel, where the remaining quote of natural gas not yet reacted (about 10%) ends his conversion process through the steam methane reforming reaction, utilizing the steam formed in the oxidation reaction of the H_2 . The SMR solution adopted helps to increase the ratio of converting natural gas into H_2 and CO slightly increasing the efficiency of the process of conversion of natural gas.

The heat necessary for the steam reforming reaction is guaranteed by the gas mixture coming by the “exhaust burner” that invests the 5 tubes from the bottom, before crossing the cathodic section of the stacks.

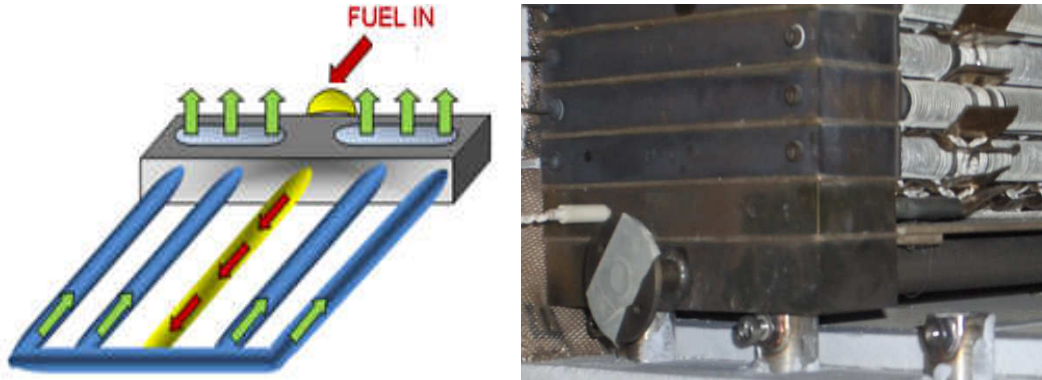


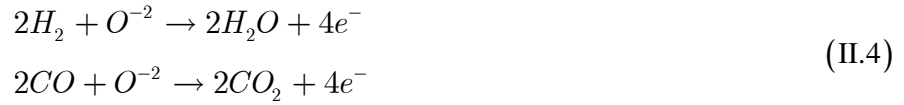
Figure II.16: Second stage of natural gas reforming - SMR

A percentage less than 1% of natural gas used by the cogenerative module could not react in the two preceding sections, and will end the process of reforming in the third stage, constituted by the anodic compartment of a tubular solid oxide fuel cell.

Most of the time, the third stage is not necessary and the reforming operation is completed in the two previous stages.

At this point, a mixture made up for more than 50-55% by H_2 and CO ($2/3 H_2$, $1/3 CO$), by approximately 30% of N_2 and the remainder by CO_2 , H_2O and CH_4 not reacted, is sent to the anode compartment of fuel cells, where the potential chemical energy of the gas

reagents mixture (H_2 and CO) is converted electrochemically into electricity and heat, through the following reactions:



with consequent production of steam and carbon dioxide (Figure II.17).

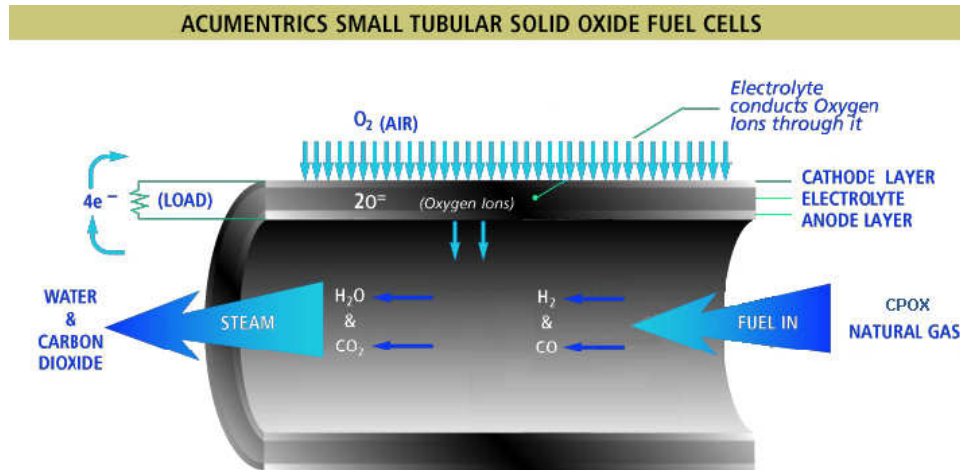


Figure II.17: Illustrative Scheme of a tubular SOFC Acumentrics at anodic support

The output gas coming from the stacks are then mixed with the cathode air coming from the "main blower" and sent to the external exhaust burner where the quote of residual reagent gases that did not participate at the electrochemical reactions, complete the combustion process: this amount (25-35%) changes, depending on the value of the fuel utilization coefficient adopted inside the anodic compartment of tubular cells. The combustion process yield thermal energy to the gas mixture that is used partly for the operations of steam reforming: the gas mixture reaches a temperature of about $750-850\text{ }^\circ\text{C}$ lapping outside the nickel tubes placed at the bottom of the stacks, where internally, the gases are subjected to steam reforming reactions.

The gas mixture, at the end of the post-combustion reactions, still possesses elevated oxygen content. Investing the external surface of the tubular SOFCs it allows the development of the cathodic reaction with production of O^{2-} ions:



These last ones crossing the electrolyte will react to the anode with the H_2 and the CO , according to the reactions (4), producing both electric power and heat.

Lapping externally the tubular cells, the mixture increases its thermal energy content which will be subsequently used in the two sections of heat exchange.

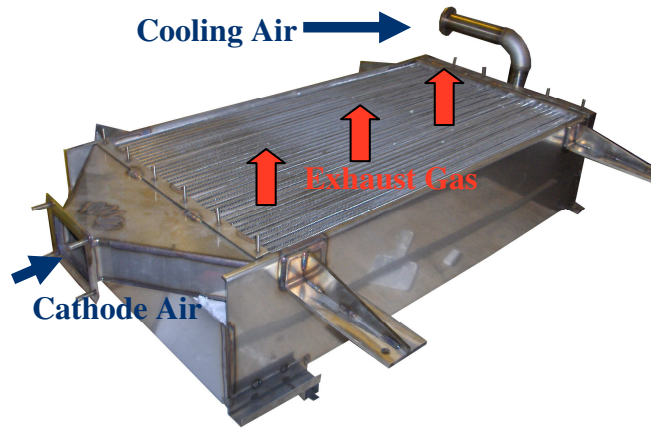


Figure II.18: Heat exchanger to preheat the cathodic air

The first section, consisting of a gas-gas heat exchanger (Figure II.19) with cross streams, uses the energy content of the mixture to preheat the cathode air at the inlet of the cogenerative module that subsequently is sent inside the exhaust burner.

The second section of recovery, consisting of an air-water heat exchanger (Figure II.20), uses the residual energy content of the gas mixture to produce water at warm temperature ($40-50\text{ }^{\circ}\text{C}$).

Through a chimney, the exhaust gases are finally channeled into the atmosphere at temperatures below $100\text{ }^{\circ}\text{C}$.



Figure II.19: Cogenerative section – hot water production.

The configuration adopted inside the cogenerative module CP-SOFC-5000 to arrange the position of the fuel cells in the stacks, is represented in the picture: totally there are 4 stacks accommodating 288 tubular SOFC. Each individual cell has a tube length of 33 cm and an effective reactive area equal to 133 cm^2 , with operating temperatures between $750 \text{ }^\circ\text{C}$ and $850 \text{ }^\circ\text{C}$.



Figure II.20: Electrical configuration and tubular cell arrangement in the Stack

In each stack, there are 12 rows of fuel cells; each row contains 6 tubular cells mounted on a collector (manifold) that allows the spread of both the fresh charge of gases and the exhausted gas coming out from the cells. The electrical configuration provides that the 6 cells on a single row are connected between them in parallel while the 12 rows in the stack are linked together in series. Every single stack is connected in series with the other 3 stacks, so a total of 48 rows of cells are connected in series and each row of 6 cells is electrically connected in parallel (Figure II.20).

The module produces electricity on direct current (DC); the conversion in alternating current (AC) takes place through two inverters installed onboard the cogenerative module.

For thermal balancing of the unit, the fuel utilization coefficient (U_f) varies between 65% and 85%; the CP-SOFC-5000 module is equipped with a DSP (Digital Signal Processor), which behaves as a real digital processor that elaborates the signals coming from the electrodes present on board of the module changing the operation parameters in case of need according to operating conditions of the module. In the CP-SOFC-5000 unit in fact has been placed 42 thermocouples capable to provide in real time operating temperature in different sections of the cogenerative module; the DSP, processing such data, is able to modify the volume flow of fuel, anodic and cathodic air.

2.5. Gas distribution inside the cogenerative module

The cogenerative module CP-SOFC-5000 has the great advantage of being able to be connected directly to the natural gas pipeline, making the unit directly usable for domestic application.

Once connected to the pipeline distribution, the natural gas (red line) in succession go through the mass flow meter, the solenoid valve, the pressure reducer and the pressure gauge.

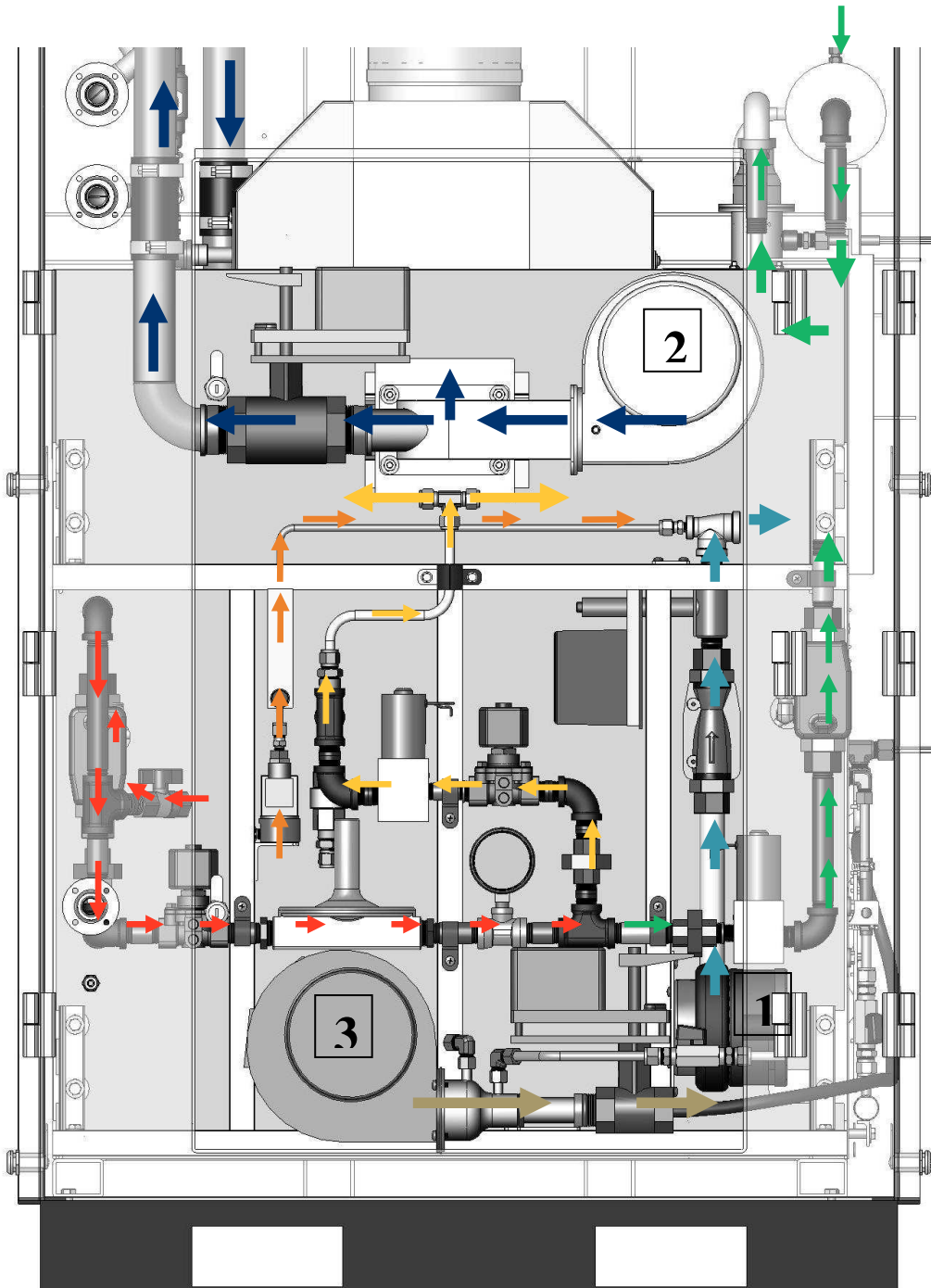
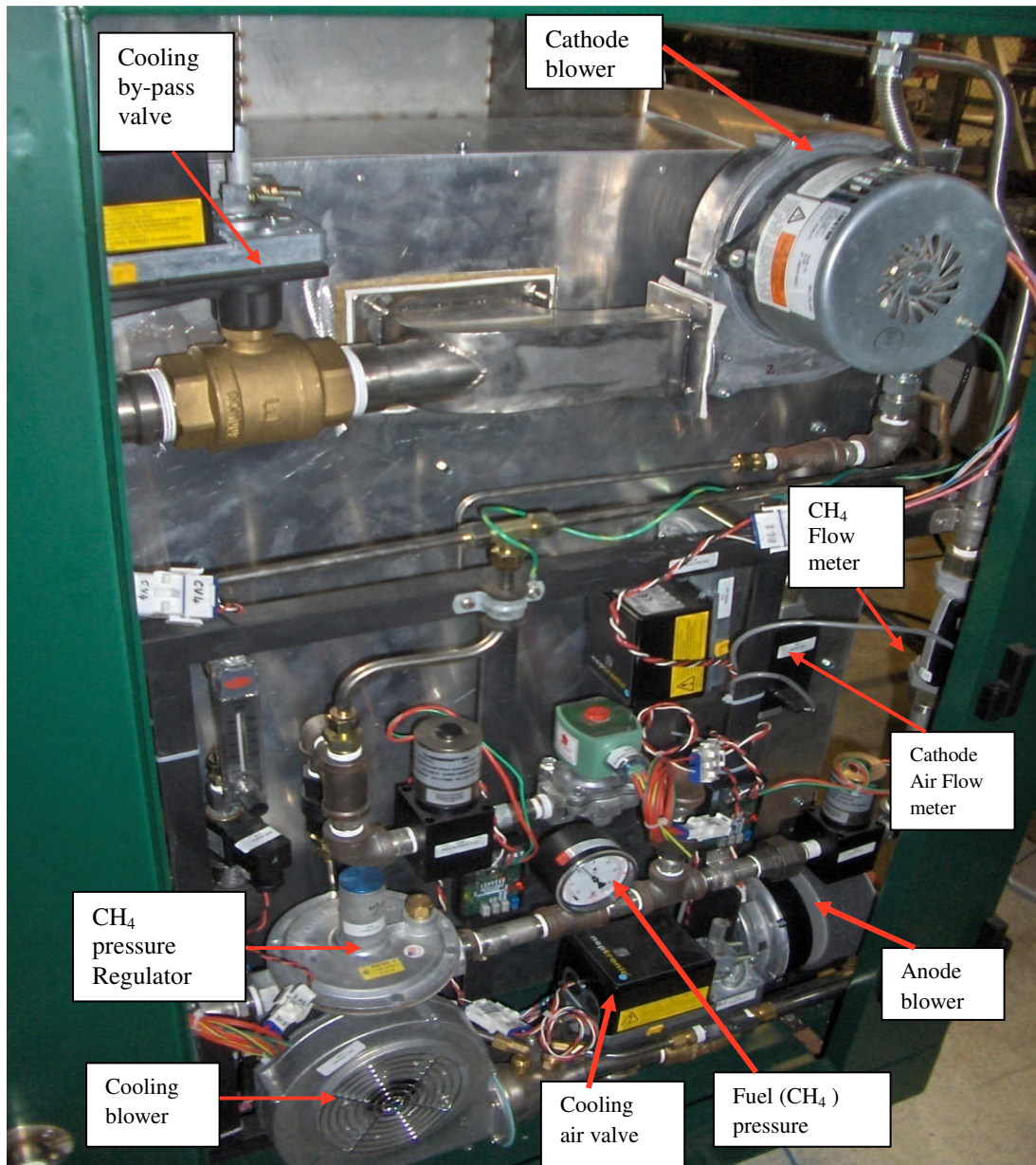


Figure II.21: Gases distribution panel – Path of each gas present inside the CP-SOFC-5000 module



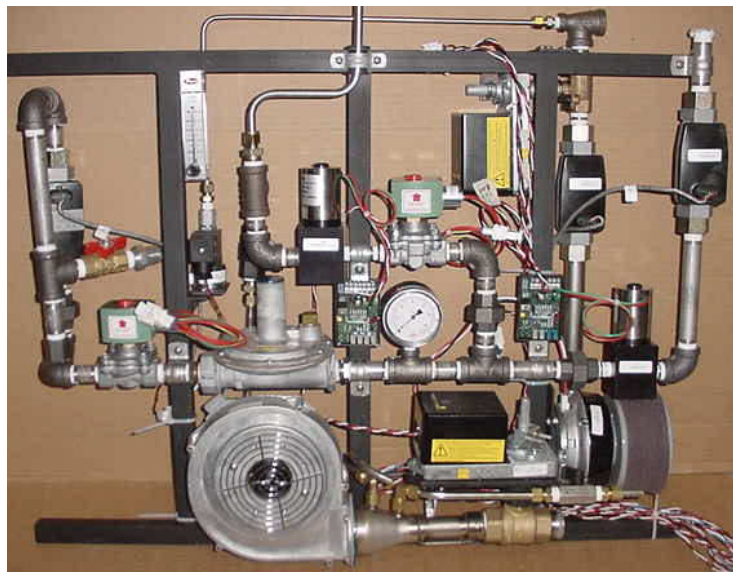


Figure II.22: Gases distribution panel with the instrumentation installed on board of the CP-SOFC-5000 module.

The flow at this point is split along two different routes: the first route (**green line**) is natural gas that is sent to the anode compartment of fuel cells, the second route (**orange line**) represents the percentage of natural gas sent to the start-up burner.

Following the path of natural gas used for the SOFC anode compartment (**green line**), the gas flow after crossing the proportional valve and the mass flow meter, is then sent to the desulfurizer, then mixed with the anode air flow (**sky blue line**) required to the CPOX reaction (figure II.23).

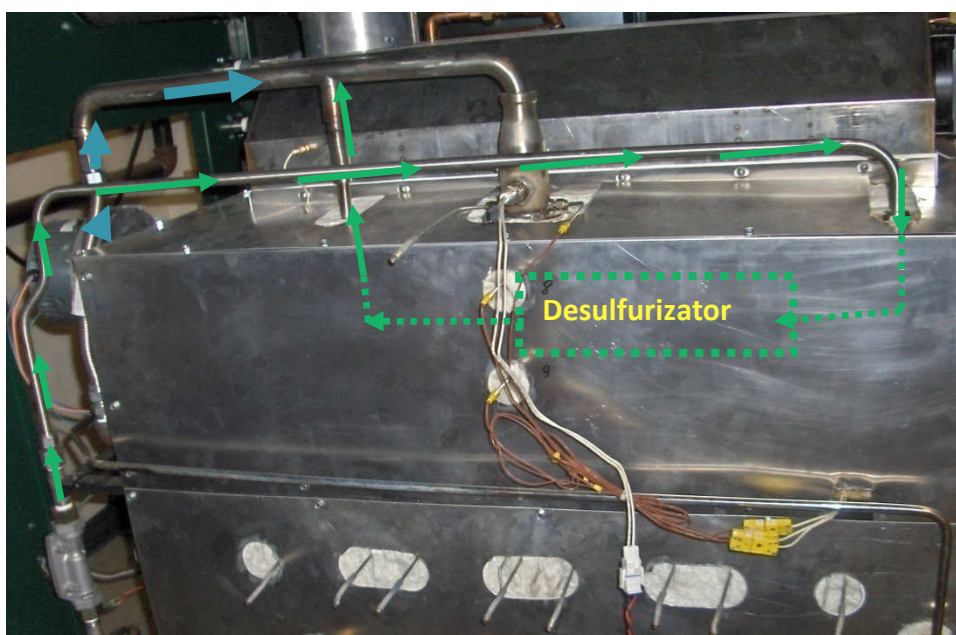


Figure II.23: Anodic fuel gas path before the CPOX reactor

This flow (**sky blue line**, Figure II.21), come into the system through a specific fan, going across the mass flow meter and the 2-way valve. When it is necessary to activate the emergency shut-down procedure, the air flow is mixed with the purge gas, coming from its cylinder (**brown line**) through a solenoid valve and a rotameter.

Returning to observe the natural gas line, the gas quote devoted to the start-up burner (**orange line**), crossing the appropriate solenoid valve and the proportional valve, is properly divided into two different lines (right and left), resulting in the two points, put one above the other, corresponding to the input of natural gas in the start-up burner. As will be clear later, the difference in the flame temperature inside the start-up burner is one of the conditions to be observed in order to consider finished the start-up procedure of the cogeneration module.

The cathodic air flow (**blue line**, Figure II.21), coming from the blower, is divided into two parts: the preponderant part enters directly in the hot module and it is pre-heated, inside the cross flow heat exchanger present on the hot module, receiving thermal energy from the exhausted gas outgoing from the exhaust burner. A more or less consisting part instead is sent downstream of the heat exchanger and is used in order to cool the gas flow outgoing from the exhaust burner and eventually in order to increase the tenor of oxygen cathodic gas mixture (Figure II.18 – II.21).

The third blower, placed at the bottom of the gas distribution panel, is used in order to control the temperature of the hot module, introducing fresh air (**sand line**) for the intermediate cooling of the stacks.

The intermediate cooling is necessary to avoid too large differences in the temperature profiles along the stacks, considering that the cathode gas stream, investing from the bottom the tubular SOFC, tends to accumulate heat produced by electrochemical reactions that occur in the fuel cells. To such purpose were inserted properly perforated tubes (Figure II.24) at half height of the stacks (Figure II.24-25),

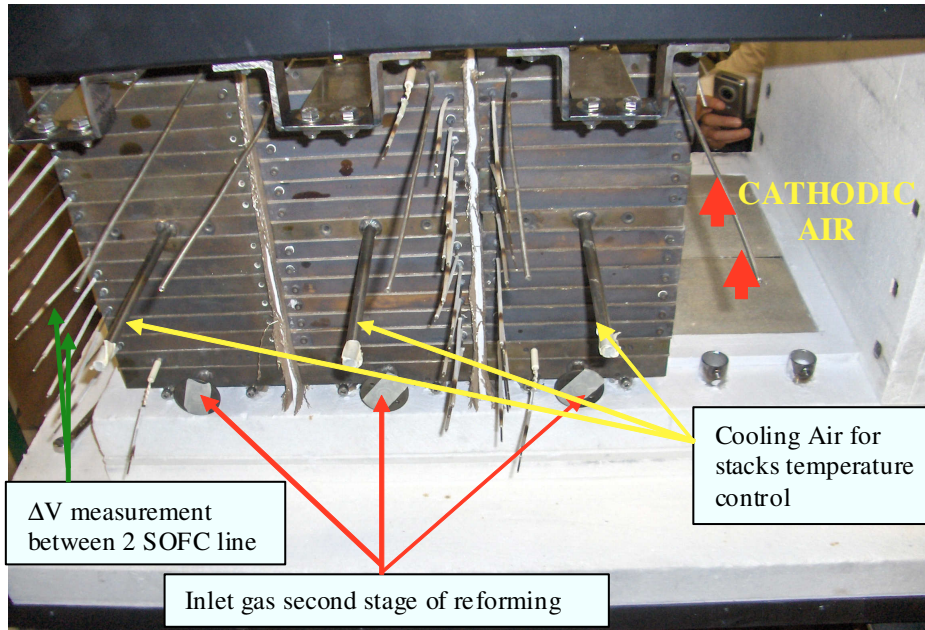


Figure II.24: Cooling air, cathodic air and reforming gas distribution inside the stacks



Figure II.25: Cooling air pipes for intermediate control of temperature's stacks

Along the cooling line (**sand line**, Figure II.21) are moreover present two orifices used in order to draw small amounts of air; such small volume flow are respectively sent to the start up burner and downstream the exhaust and start up burner for eventual gas flow cooling. The air destined to the start-up burner, once mixed with the natural gas, allows the development of the combustion reaction during the start-up procedure.

As regards the gas distribution of reactants in the anode compartment of tubular fuel cells, the mixture, once the reforming process at the bottom of the stack (5 tubes in nickel)

is completed, is sent in a specific manifold for the distribution. Such collector has two columns of distribution on one side allowing the distribution of the fresh charge and from the other to carry out the exhausted gas produced by the electrochemical reactions inside the fuel cells. The collector is realized collecting into a pile, one over the other, the appropriate structures of support of the rows of fuel cells (Figures II.24, II.26, II.30); every row is opportunely isolated from the other electrically through the interposition of appropriate material that guarantees also the absence of gas leakage.

The tubular SOFCs are with one end closed, so the release of the reacting gases, coming from the manifold, within the tubes takes place through the use of a thin steel tube that have a really small hole at the end. The hole is placed near the closed edge of the tube: the gases are so evenly distributed along the whole length of the SOFC tube until they reaches the exhaust manifold (Figure II.26).

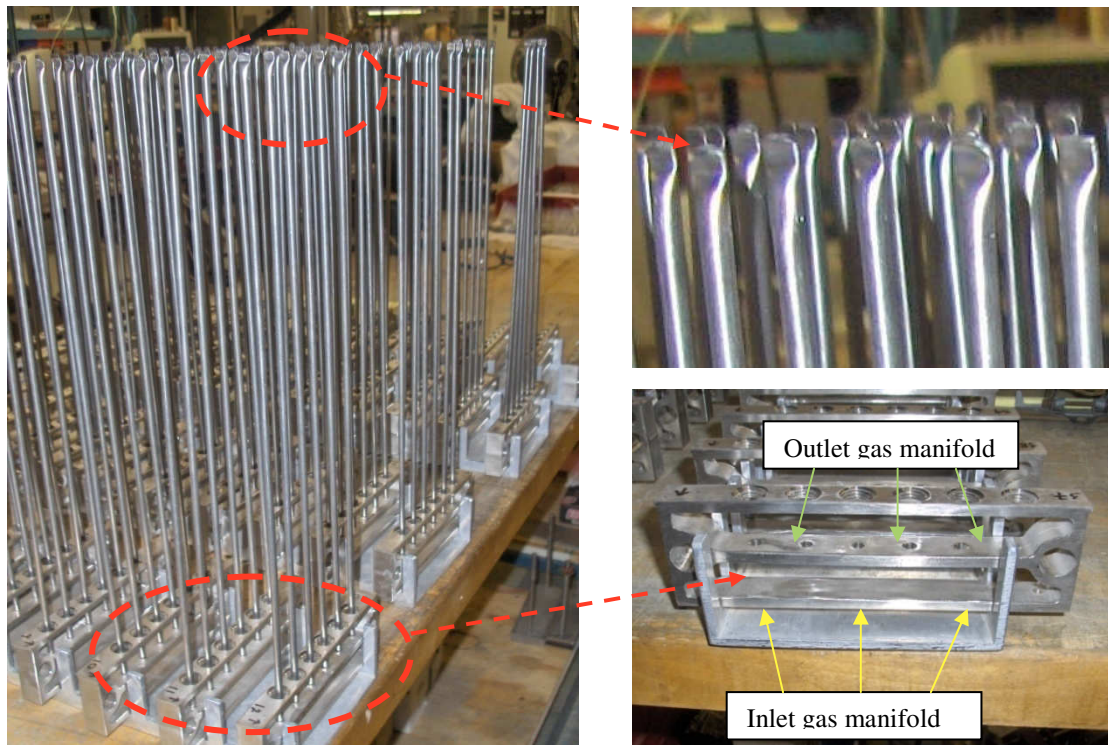


Figure II.26: Thin steel tubes for reactant gases distribution inside the tubular fuel cells

The exhausted gases of every single stack are gathered in the higher part of the manifold, for being carried out in a specific collector (Figure II.27) connected to the exhaust burner. Here these gases are mixed with the cathodic air coming from the heat exchanger placed to the top of the stacks, for the development of the combustion reactions of the reagent gas quota that has not participated to the electrochemical reactions inside of the anodic section of the fuel cells.

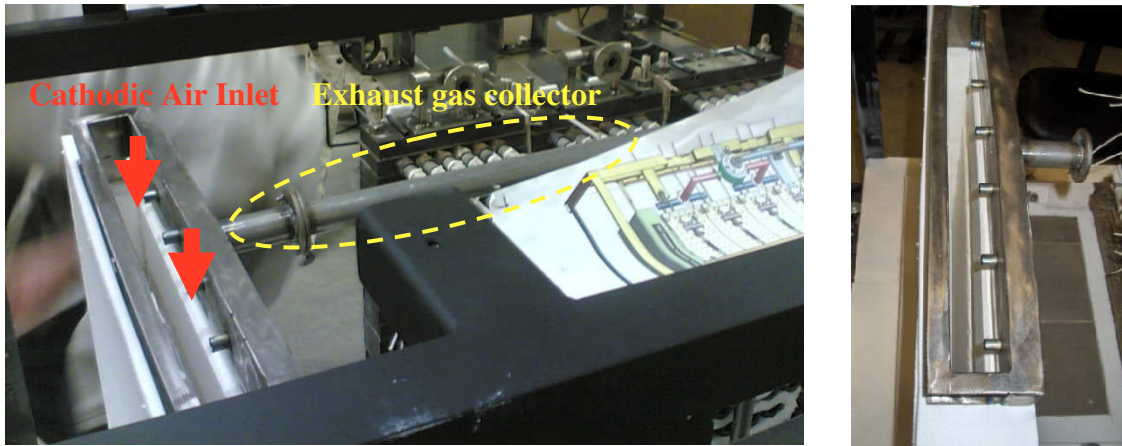


Figure II.27: Collector with exhaust burner and start-up burner

Once completed the combustion reactions within the exhaust burner, the mixture, still with a high oxygen content, crosses the honeycomb structure placed at the bottom of the stacks (which allows better air distribution, Figure II.24), and invests the steam methane reforming section (nickel tubes), lapping subsequently the tubular cells externally (cathode side). The high oxygen content, allows to carrying out the electrochemical reactions at the cathode side, freeing the O^- ions that passed through the electrolyte, reacting with the H_2 and CO in the anode compartment. The mixture receives the heat produced by the electrochemical reaction and cedes the thermal energy, through the heat exchange section, to the cathodic air coming inside the cogenerative module; the exhausted subsequently are discharged into the atmosphere at a temperature below $100\text{ }^\circ\text{C}$.

2.6. The Stacks

As mentioned before the cogenerative module CP-SOFC-5000 contains 4 stacks, where have been assembled 288 tubular fuel cells (12 lines of cells, connected in series: each row houses 6 tubular cells linked together in parallel).



Figure II.28: Tubular fuel cells distribution inside the stack and electrical connection

At the edge of the gas manifold has been made appropriate electrical connections which allow measuring the voltage of 48 files of tubular cells placed inside the stacks (Figure II.24).

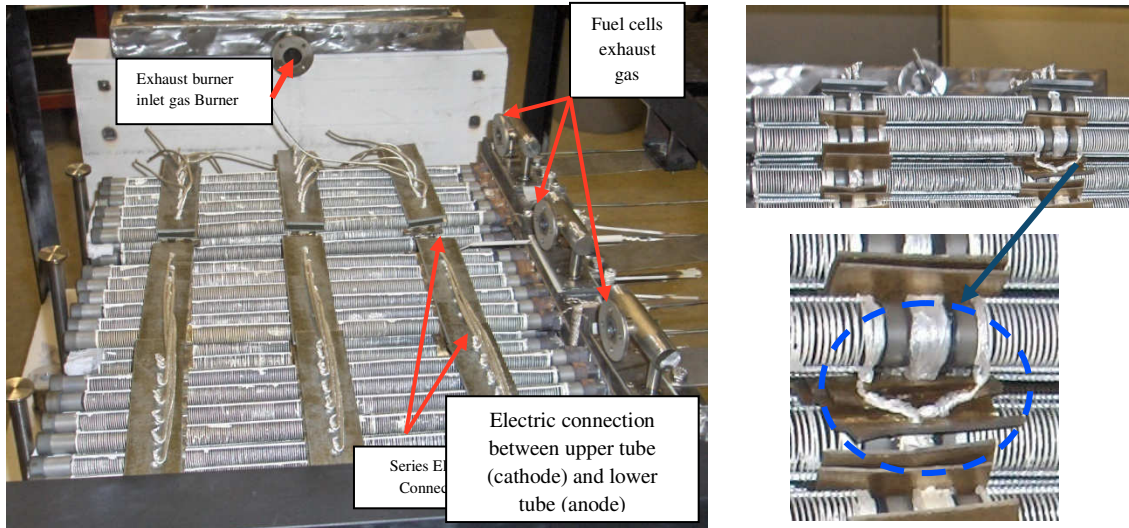


Figure II.29: Series and parallel electrical connection of tubular fuel cells e between different stacks

The electrical connection of the anodic and cathodic compartment of a single tubular cell, necessary to convey the electrical charges that are generated during the electrochemical reactions, is realized in different ways for the two compartments. The anode is directly screwed, through a metal threaded head, inside the gas manifold (metal): consider that the anode is made for about 50% by nickel allowing the passage of electrons internally to reach the end of the tube connected to the gas manifold. The cathodic connection happens through a real electric winding realized around the tubular cell, constructed with silver wire and subsequently connected to the anodic compartment of the tubular cell placed at the row below, thereby connecting in series (Figure II.29).

This solution also enables to reduce the path of electric charges: 2 interconnections have been placed along the tubular cells (see paragraph 2.9). They have precisely the task of connecting electrically smaller portions of cell, reducing the ohmic losses that for this type of fuel cells, we have seen, are dominant.

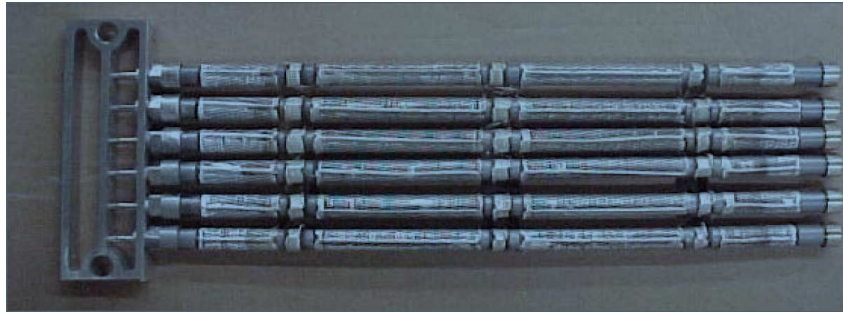


Figure II.30: Physical and electrical connection between tubular fuel cells and the gas manifold

The tubular fuel cells produce electricity in direct current. For this reason it has been installed, on board of the the cogenerative module, an electrical panel with 2 inverter in order to realize the DC-AC electricity conversion. The framework also hosts 4 batteries (12 V) connected in series, acting as buffer between the variations of electrical load and the electricity that the module is capable of providing: in particular the batteries are involved in sudden changes in the electrical load and only in the second time the module intervene to supply the power demanded by the electrical load.

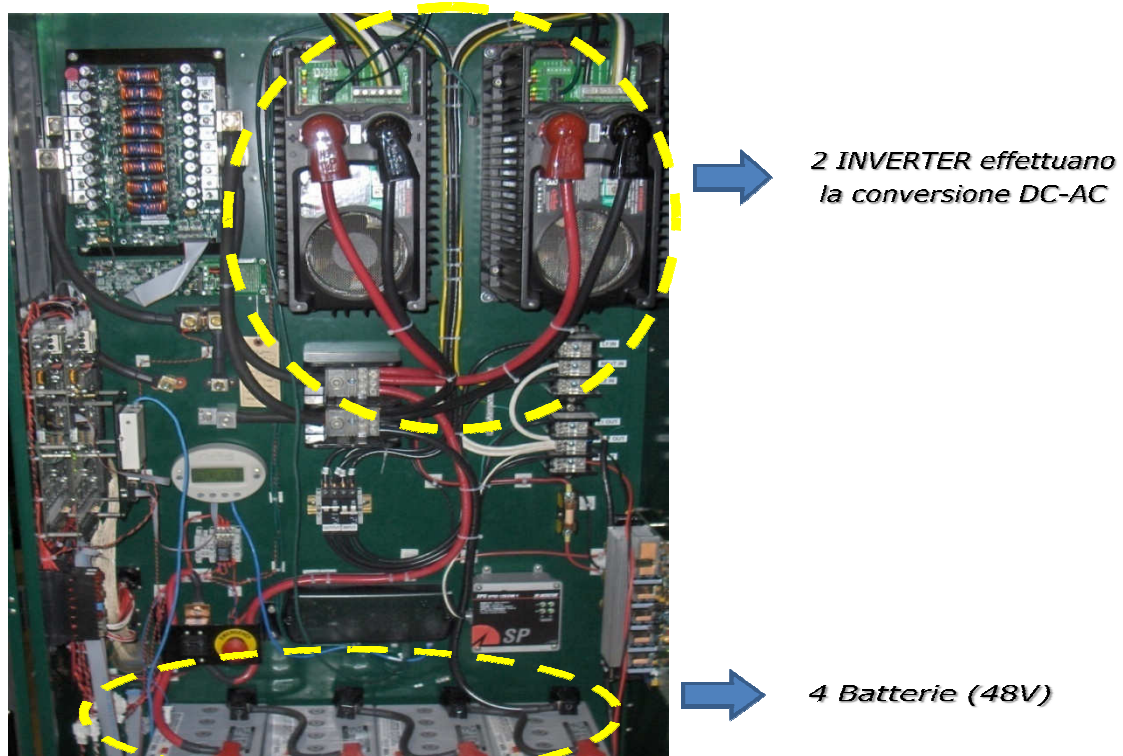


Figure II.31: Electric panel on board of the CP-SOFC-5000 module: Inverters and batteries

2.7. START UP of the CP-SOFC- 5000 module

The CP-SOFC-5000 module is equipped with a management software that through the DSP (Digital Signal Processor), is able to control its operation. The processor examines the

variables related to the control of the various inlet gases, the temperature inside the cogeneration module and the electronic power system, allowing independent operation of the CP-SOFC-5000 module without any supervision of the system. The software, through an Ethernet connection, also allows the management and control of the system remotely.

The phases of start-up and shut-down, begin simply by turning the key (on-off switch) mounted on the outer panel of the module. Once the ignition stage ("run state") was launched, the system automatically is able to carry out the sequence of start-up through the following steps:

- Ignition (Ignitor);
- Heating (Heat-up);
- Charging batteries (battery charge);
- Condition requested to connect the electric load (load state);
- Turned on inverter DC / AC;
- AC loads connected.

Turning the key the start-up phase happens automatically; during this phase the initial control parameter of the system is the Temperature of Plenum (at the bottom of module). Almost simultaneously take place the following operation automatically:

- The cathode Blower supply air into the cogenerative unit at the maximum velocity: the aim is to clean up the stacks from residues and provide oxygen to realize the combustion in the "start-up Burner";
- The valve of the gas (methane) opens;
- The others blowers start to operate;
- It happens the spark ignition (flame) in the start-up Burner "for about 2-3 minutes, in order to stabilize the combustion within the Burner;
- Start the exhausted release;

In the various stages of ignition, the cathode blower speed changes from high ($\approx 100\%$) during first ignition, to become lower ($\approx 60\%$) during the flame stable phase inside the start-up burner, to increase again when the temperature rises above 300°C .

The temperature of Plenum grows very rapidly during the flame stable (red line). The temperature in the lowest part of the stacks ("Bottom stack") higher than the temperature of the upper part of the stacks, grows much more gradually.



Figure II.32: Temperature trends during the start-up procedure

Initially all the fuel (30-40 Scm^3/min natural gas) is sent in "start-up burner" until the flame has not stabilized (1-2 minutes), during this period the O/C ratio is equal to 1.5. Subsequently the "start-up Burner" is still in operation but about 10 Scm^3/min will be sent to the CPOX for carrying out the reforming reactions. From this moment the O/C ratio drops and stabilizes at $1.2 \div 1.3$. The transition between stable flame and CPOX operation occur when the stack temperature exceeds $300\text{ }^\circ\text{C}$ (generally the phenomenon happens however within 5 minutes from ignition).

During all this phase the parameter that controls the system is the maximum temperature of the stack. Sending the fuel to the anodic compartment of the stacks it happens the progressive increasing of the cell voltages (till to exceed 0,7 V), placed in the bottom of the stacks, and the recharges of the batteries. When the maximum temperature of the stacks achieves the $810\text{ }^\circ\text{C}$, the control parameter changes and becomes the minimal temperature of the stack. When this parameter exceeds the $680\text{ }^\circ\text{C}$ is possible to connect the electric load:

- *System:* Passes from Charges batteries to \longrightarrow Refloat;
- *Enable AC Output:* It is possible to connect the electric load;
- It is sufficient to turn on the electric load switch (Switch on Output);
- *Cell Voltages:* They come down as the current sent to the electric load increases (coming down along the polarization curve).

The battery voltage passes from 55 V (maximum value) to inferior values according to the electric current amount absorbed in that moment by the electric load. The lowest temperature of the stack continues to grow. When such parameter achieves the $700\text{ }^\circ\text{C}$ changes the target relative to the maximum temperature of the stack that, passes from $810\text{ }^\circ\text{C}$ to $845\text{ }^\circ\text{C}$. With this change the maximum temperature of the stack (approximately $808\text{ }^\circ\text{C}$) start again to grow trending to the new target temperature ($845\text{ }^\circ\text{C}$). When it has been

achieved the 680 °C minimum temperature of the stack, it is possible to extinguish the “Start-up Burner”. Indeed it is necessary that an ulterior condition takes place:

- *Conditions for the Extinction of the “ start-up burner”:*
 - Minimal temperature of the stack > 680 °C;
 - Output Current > 20 A (that it is equivalent to connect the electric load),
- *or alternatively:*
 - The temperature difference inside the “Start-up Burner” = $\Delta T_{\text{flame}} < 30 \text{ °C}$;

The ΔT flame is calculated by the system as difference between the temperature measured downstream and upstream of both the Burners (Start-up and Exhaust); in fact are present 4 thermocouples downstream and upstream of the two Burners.

The shutdown of the Start-up Burner happens when both the first two conditions occurs, or if the alternative condition occurs alone.

When the temperature of the cell became greater than 730 °C there will be the temperature inversion in the stack, so the top of the stack will become hotter than the bottom of the stack. For this reason, as mentioned before it was provided the inclusion of cooling tubes placed at half height of the stacks.

Finally, it is important to note that the shutdown of the “start-up burner” is not definitive but could be the need to turn it back for thermal balance reasons. All this happens automatically and is regulated by the cathodic gas temperature.

2.8. Shut-down of the CP-SOFC-5000 module

Turning the key in the opposite direction (switch off) starts the shut-down procedure, with immediate disconnecting of the inverters that no longer feed the electrical load. During the shut-down procedure, a small amount of fuel (methane) continues to be fed within the module to protect the cell until the minimum temperature security threshold is reached, under of which there is no longer risk that the nickel, in the anodic compartment, may re-oxidize. It is essential that the fuel valve will remain opened during the period of shut-down.

The following are the main stages of shut-down procedure:

- | | | | |
|---|--------------------------------------|---------------|-----------------|
| - | The key is brought into off position | —————> | Key switch off; |
| - | <i>System:</i> | Run —————> | Shut down; |
| - | <i>Load:</i> | Output —————> | Off; |
| - | <i>Temperature</i> | —————> | Shut down; |
| - | <i>Fuel:</i> | CPOX —————> | Off |

at the same time:

Cathode Blower \longrightarrow full On ($\approx 100\%$)

Auxiliary Blower \longrightarrow full On ($\approx 100\%$)

The fuel continues, in minimal part, to being distributed until:

$T_{\max} \text{ stack} < 250\text{ }^{\circ}\text{C}$ \longrightarrow fuel shut down

Regarding the fuel, it is well to clarify that, in case it necessary to begin the automatic shut-down procedure, associated with some fault, it is automatically turned on the control valve that release the Purge Gas, allowing to use the same instead of the natural gas. This event does not occur during normal shutdown operation of the cogenerative module.

The shutdown procedure could be considered in both the case ended when the $T_{\max} \text{ stack} < 90\text{ }^{\circ}\text{C}$.

2.9. Fabrication process of the tubular fuel cells

The materials used in the manufacture of the tubular cells produced by Acumentrics are those typically used in the manufacture of solid oxide fuel cells. The anode is composed by 50% of NiO and 50% of Ytria Stabilized Zirconia (YSZ). The electrolyte is made entirely of YSZ while the cathode is made up with CrMnO_3 . The tubular cell is an anodic support fuel cell; the anode is produced by extrusion and then subjected to sintering process.

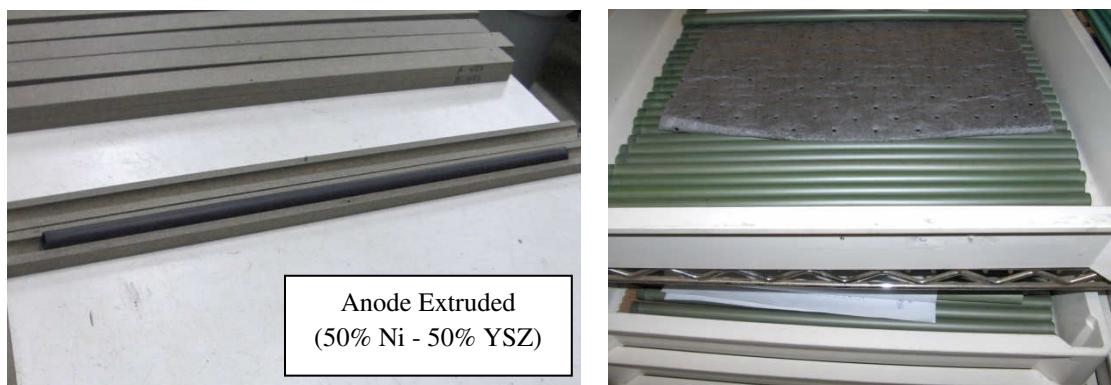


Figure II.33: Anode extrusion before and after sintering process

The electrolyte deposition is realized by vacuum infiltration. The machine consists of a head, placed at the top, that have small tubes where are placed the tubular cells, in order to suck in the air, causing the vacuum in the tube. The lower part consists of a reservoir containing the solution of electrolyte materials (YSZ). The head rotates on itself, allowing the immersion of the tube in the solution. The air sucked from the inside, creating vacuum in the pipe, facilitate the adherence and the penetration of the electrolyte in the anode

porous structure outer surface. This greatly increases the surface area available for carrying out the reactions (three phase boundary). Afterwards occurs the sintering process of the electrolyte.

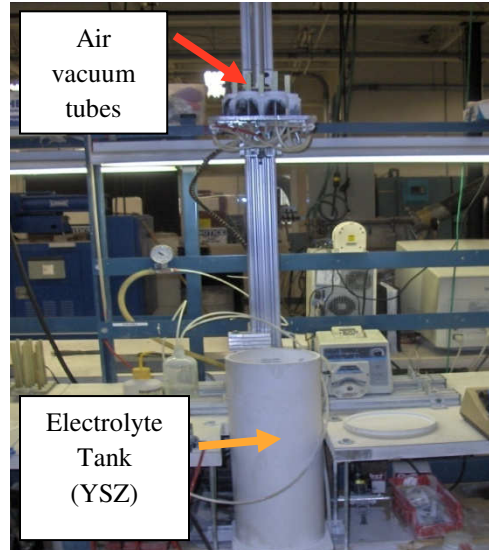


Figure II.34: Machinery for electrolyte deposition

Before the cathode deposition are realized the electric interconnection. As mentioned before, the electrical connection, at the anode compartment, occurs at the edge of the cell through a threaded head properly connected to the gas manifold. But to reduce the path of electric charges and consequently reduce ohmic losses have been realized two interconnections along the tubular cell appropriately removing the layer of electrolyte deposited and applying a layer of interconnection (LaCrO_2 , conductor ceramic material).

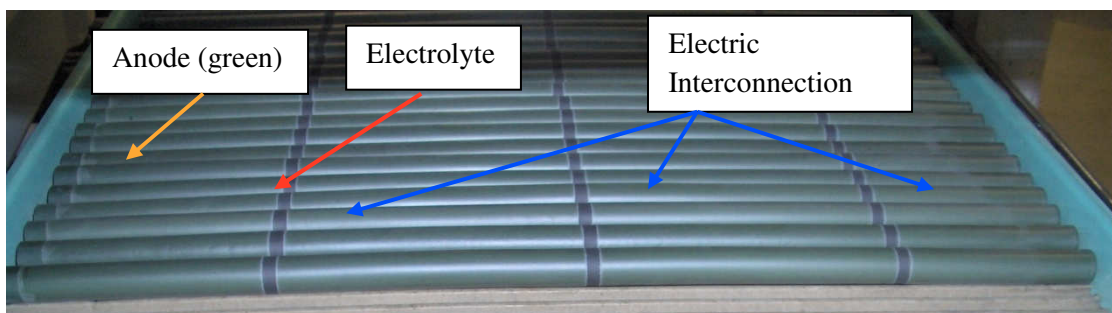


Figure II.35: Tubular cells with electric interconnection deposition

The cathode deposition takes place for dip coating through the use of machinery represented in the next figure. The tubular cell is sustained and driven by a rotary head while approaching, for the subsequently tube dip, of the tank that contains the cathodic material.

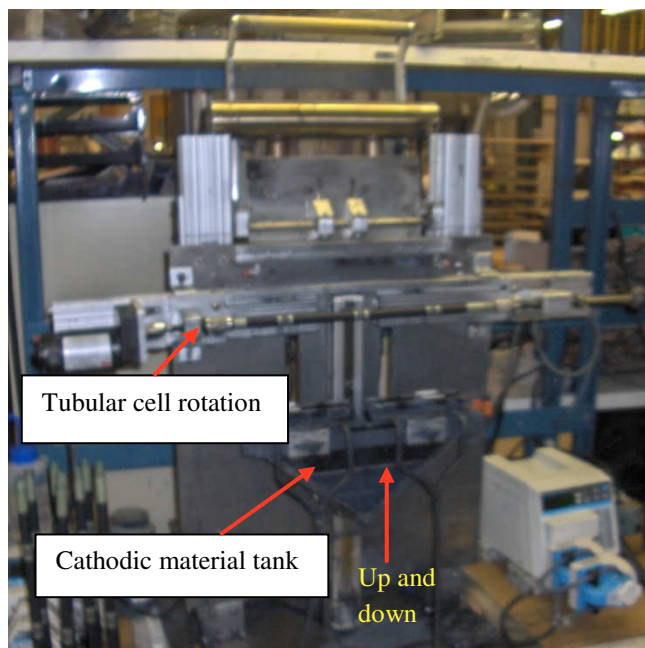


Figure II.36: Machinery for cathode deposition

After the deposition the tubes are subject to a sintering process in reduced atmosphere, with sintering of the cathode and reduction of the anode that change therefore color becoming gray.



Figure II.37: Fabricated tubular fuel cell before the reducing process (green anode)

The realization of the electrical connection electrical at the cathodic compartment takes places through appropriate machinery that automatically places longitudinally a silver wire and successively realizes the winding around the tubular cell (silver wires).



Figure II.38: Machinery for cathodic electrical connection application (silver wires)

The figures II.29 and II.38 show moreover the electrical connection realized in correspondence of the interconnection, with the application of a silver wire that allows the successive connection in series with the cathode side of the successive tubular cell, mounted in the stack.

Finally, as said before, the tubular cell have an extremity closed, by means of the application of a cap, and another quarry extremity on which is applied an appropriate threaded head for the electric connection at the reagent gas distribution manifold. In order to being able to realize the application of the closing cap and the threaded head, were applied a copper layer to the extremities of the tube with the application of a magnetic field (through appropriate machinery, Figure II.39), with a very high induced current, that produces the welding of extremities and tube (anode metallic material, NiO).



Figure II.39: Machinery for the application of the closing cap and the threaded head at the end of the cell

2.10. Measuring instruments installed on board of the CP-SOFC-5000 module

The cogenerative unit CP-SOFC-5000 is equipped with a measuring system devoted to regulation and control of it. The instrumentation available is sufficient to obtain a first complete energetic analysis of the system. However, in order to allow a more detailed and precise investigation of the cogeneration module's performance will need to place side by side in the future, at the instruments currently available, a set of additional measurement devices of both electrical and thermal fluid-dynamic property.

Module CP-SOFC-5000 is fed with gas natural coming from the network. The optimal inlet pressure must be ranging between 19.93 mbar and 34.88 mbar (gauge pressure), while the permissible maximum pressure is 137 mbar. The connector is a 1/2" type NTP female.

The module moreover is connected to a cylinder of "Purge gas" (a mixture having volumetric composition of 97% of nitrogen and the remaining 3% of hydrogen). The connector is a 1/4" type SwageLock. Such gas is necessary in the emergency "shut-down" procedure to preserve the integrity of the tubular cells, covering the anode, essentially by an inert substance such as nitrogen, which inhibits the oxidation chemical reactions of the nickel at the anodic compartment. The cylinder, thanks to an electro-valve expressly set, starts to feed the purge gas in the event of malfunctions in the natural gas line and in the shut-down procedures caused by faults. The feeding pressure of the Purge gas is at least 4.0 bars.

The CP-SOFC-5000 module is equipped with a cogeneration section fed with a water volumetric flow comprised between 3.8 Scm³/min and 9.5 Scm³/min: the maximum pressure in the pipe line is 170 kPa. The module is capable of producing between 2.5 and 4.5 kW of heat, in optimal operative conditions. The circuit also has a safety device that discharges the possible steam produced through a valve set at 210 kPa. The connectors of the hot and cold side are 3/4 "type NTP female; for venting the steam eventually produced has been realized an exit hole of the same size.

The CP-SOFC-5000 unit produces an electric nominal power of 5 kVA at a voltage of 220V, using 2 inverters installed on board of the module. In order to connect the electrical load is available a three terminal wires, where can be connected single-phase loads (of the three bus present, two represent the phases while the third acts as a neutral). The electricity produced can be used to directly power loads, but cannot be placed on the electric grid, because there is not safety device that is able to intervene, if anomalies occur and automatically isolate the cell.

The CP-SOFC-5000 unit is itself connected to the electric grid at low voltage (220 V) receiving the power needed to recharge the 4 batteries (each one of 12 V and 75 A) installed on board of the module, during prolonged arrest.

It also installed a network adapter that enables remote management of the module.

The CP-SOFC-5000 module is equipped with a series of measurer necessary to its regulation and to its corrected operation. The measures available are both of electric and thermo fluid dynamic properties. The electrical parameters measured and monitored by the equipment installed on board of the module are as follows:

- Current;
- Voltages;
- Electrical power.

The 4 stacks are connected in series and the current produced is directed towards the three terminal wires where the electric load is connected. The module's instrumentation allows the measurement of the current totally distributed by all stacks through the DSP device (Digital Signal the Processor), placed inside the electric panel on board of the cogenerative module. The DSP is capable to elaborate each signal coming from the electrodes with a temporal scanning of 15 second ones. In addition to perform the duties of data logger, the DSP acts by a real digital processor, modifying at the occurrence the operation parameters, based on the operating conditions of the module. The DSP is manageable via personal computer by Ethernet connection. The metrological characteristics concerning the current measurement by the DSP, are listed below:

		Incertezza in % attribuibile alla deriva del sensore (tempo di funzionamento 1 anno a 25 ± 5 °C)		Incertezza in % attribuibile all'influenza della temperatura ($0^\circ \div 20$ °C e $30^\circ \div 50$ °C)	
	Campo di misura	Incertezza in % della lettura	Incertezza in % del fondo scala	Incertezza in % della lettura	Incertezza in % del fondo scala
Corrente	$0 \div 100$ A	0,050	0,020	0,0002	0,0005

Table II.1: Metrological characteristics of electrical current measurement by DSP

The measures of voltages obtainable by the instrumentation currently installed include:

- the voltages of 48 files of tubular cell contained in the 4 stacks;
- the global tension of the stacks;
- the voltages of batteries.

Similarly at what happens for the current, the measures of voltages are detected by the DSP, which processes the signals coming from the module setting the operation parameters accordingly with the operating condition.

As mentioned before the 4 stacks accommodate 48 lines of tubular cells and for each of them has been installed a connector to be able to detect the voltage. The values of the voltages of 48 lines of tubular cells in addition to being recognized by the DSP can be measured directly, via multimeter, through a terminal installed on the module easily accessible from the outside. The terminal also allows calibrating in advance the values of the voltage read from the DSP during the phase of restart after long periods of arrest.

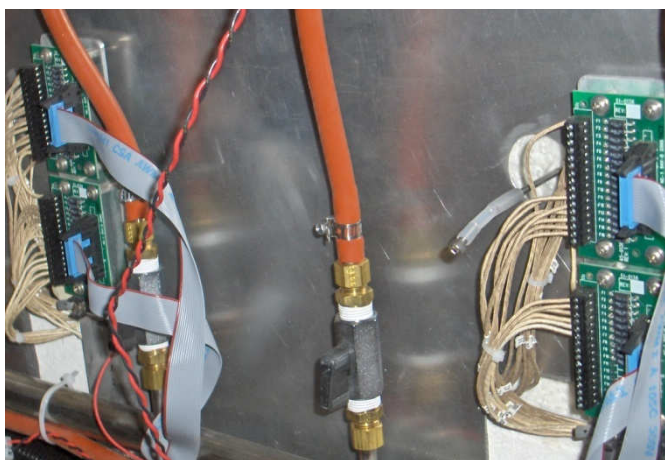


Figure II.40: Terminal that allows calibrating the voltages inside the stacks

The DSP allows monitoring also the voltages at the heads of the batteries. In the Table II.2 the range of measure and the typical uncertainties of the DSP are shown, for two different ranges of tension:

		Incertezza in % attribuibile alla deriva del sensore (tempo di funzionamento 1 anno a $25 \pm 5 \text{ }^\circ\text{C}$)		Incertezza in % attribuibile all'influenza della temperatura ($0^\circ \div 20 \text{ }^\circ\text{C}$ e $30^\circ \div 50 \text{ }^\circ\text{C}$)	
		Campo di misura	Incertezza in % della lettura	Incertezza in % del fondo scala	Incertezza in % della lettura
“Bassa” Tensione	$0 \div 100 \text{ mV}$	0,0050	0,0035	0,0005	0,0005
“Alta” Tensione	$1 \div 100 \text{ V}$	0,0045	0,0006	0,0005	0,0001

Table II.2: Metrological characteristics of electrical voltages measurement by DSP

The value of the electric power is obtained instead banally having at disposal the voltages and the current distribute by the module and registered by the DSP. It is possible moreover to read the power absorbed in alternating current by the electric load, that allows obtaining the net electrical efficiency Unlike the other measures discussed before, the value of the AC electrical output can be viewed only via a display mounted on the electric panel placed on the module; at the time this information is not acquired through the PC.



Figure II.41: Display mounted on board of the cogenerative module that allows monitoring the electric power absorbed by the electric loads

With the instruments installed on board of the CP-SOFC 5000 module is possible to control the following thermo- fluid dynamic properties listed below in different sections of the unit:

- *temperature;*
- *pressure;*
- *Volume flow.*

Like the electric measures, the thermo fluid dynamic ones are also acquired through the DSP, which in this case, however, requires the addition of dedicated "sensors".

The pressure of the fuel at the inlet of the cogenerative module is made downstream of a pressure regulator, via an analog Bourdon tube. The presence of a digital pressure transducer allows processing the data with a PC.

The Bourdon tube is a gauge pressure measurer. Its measurement range is comprised between $0 \div 8$ mbar with an uncertainty equal to $\pm 1\%$. The transducer is also a relative, and its range is comprised between $0 \div 7$ mbar with an uncertainty equal to 1% of full scale. Table II.3 summarizes the information on the pressure measurement system.

	Campo di misura	Incertezza
Tubo Bourdon	$0 \div 8$ mbar	$\pm 1\%$ V.L.
Trasduttore di pressione	$0 \div 7$ mbar	1% F.S.

Table II.3: Table with the metrological characteristics of the pressure measurement system

The fuel cell module is equipped with three mass flow meters, two of which are positioned on the line of the fuel, and the other one on the anodic air line. The fuel flows measured are:

- the total fuel at the inlet of the module;
- the quote sent directly to the anodic compartment of tubular cells.

The quote of fuel that doesn't go at the anodic compartment is used to feed the start-up burner to bring up the temperature of the cogenerative unit during the start-up phase.

The upper limit for the range of measurement of the flow meters used for natural gas is $50 \text{ Scm}^3/\text{min}$ (standard 273.15 K and 101.325 Pa), with an uncertainty of 4% of the reading value, or absolute of 0, 15 Scm^3/min , depending on whichever is greater. For the air, however, the maximum limit is $200 \text{ Scm}^3/\text{min}$ with a relative uncertainty equal to 2% of the reading value.

According to the specifications of the instruments, for both the fuel sensors and the air one, we have to add another uncertainty due to operating temperature. All the metrological characteristics of the instruments used for measuring the masses flow are briefly summarized in Table II.4:

	Campo di misura	Incertezza	Incertezza aggiuntiva dovuta alla temperatura
Flussometro gas naturale	1 ÷ 50 sL/min	4 % V.L. o 0,15 sL/min V.A.	0,1% V.L. per ogni °C da 21°C
Flussometro aria anodica	2 ÷ 200 sL/min	2 % V.L.	0,1% V.L. o 0,005 sL/min per ogni °C da 21°C

Table II.4: Table of the metrological characteristics of the mass flow measurer for fuel and anodic air

The figure II.42 shows the graph of further uncertainty due to operational pressure, which must be taken into account. The diagram refers to both fuel and air:

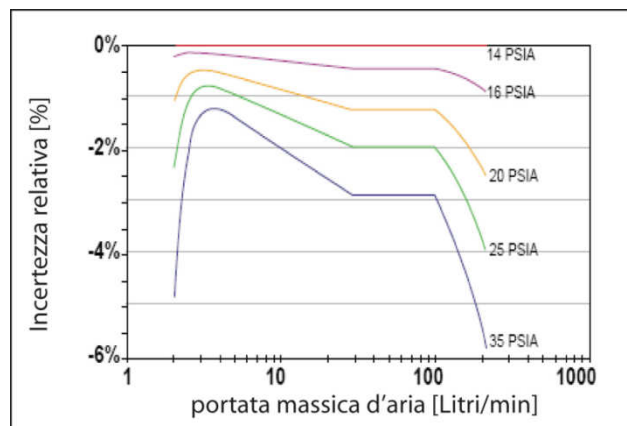


Figure II.42: Correction to be made due to the operational pressure, the curves are parameterized according to the operational pressure.

As regards the scope of mass flow measures, it is important to assess the pressure drop induced by the presence of these gauges, to prevent too low fuel pressure in the cell. For this reason, in Figure II.43 is reported the trend of these losses varying the mass flow measured by the instrument itself.

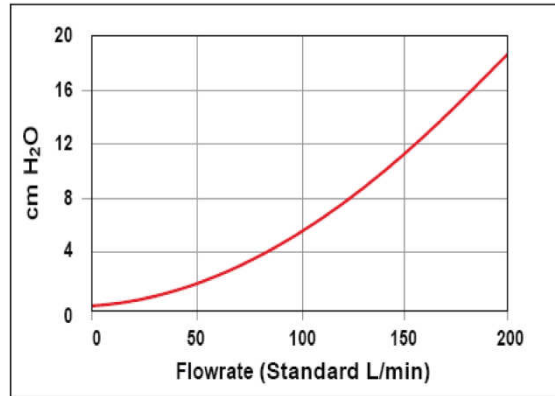


Figure II.43: Pressure drop induced by the flow meter

For the fuel flow elaborated, the losses inducted by the flowmeter are between 9.0 ÷ 10.0 mbar.

2.11. Thermocouples

Within the cogeneration unit have been installed 42 thermocouples, positioned in different sections (Figure II.45) and linked to the DSP, which read the values with a scan time of four values per minute. The temperature sensors mounted on CP-SOFC-5000 are thermocouples of type "R" (Platinum / Platinum rhodium 13% Rh) which, being composed of noble metals, show high accuracy over 500 ° C. The typical uncertainties of such sensors stand around ± 1 °C [28]. The sensors insulation are made of magnesia and alumina (Al_2O_3). The thermocouples are arranged in such a way as to measure the temperature in strategic and critical point for the operation of the cogeneration module and that, as described above, the DSP uses to be able to regulate its functioning. In order to conduct a complete energetic analysis of the CP-SOFC-5000 module, are of particular importance thermocouples arranged in the cogeneration section. They are installed upstream and downstream of the heat exchanger (number 22 and 22), as shown in figure II.44.

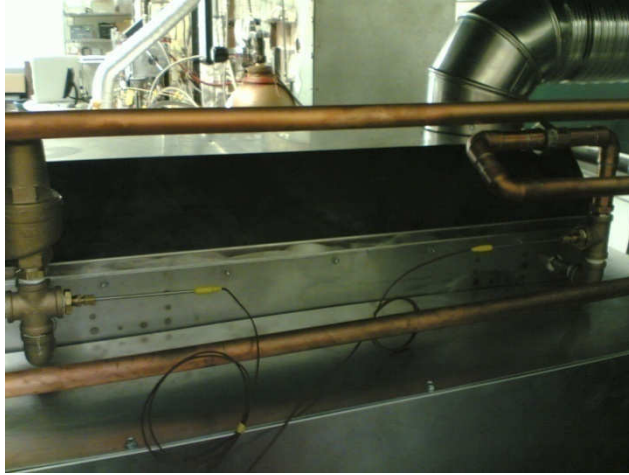


Figure II.44: Thermocouples installed into the cogenerative section of the CP-SOFC-5000 module

The thermocouple number 20 provides the value of the exhaust gas temperature at the output of cogenerative module. Inside the partial oxidation reactor 3 thermocouples are mounted with the task of controlling the temperature of the natural gas at the inlet and the outlet temperature of the mixture subjected to reforming; the third thermocouple measures the temperature of the top of the bed of reaction.

Inside the stacks section are mounted 24 thermocouples (3-14, 25-26, 29-30, 32-35, 37-40) respectively placed at the bottom, middle and the top of the hot module.

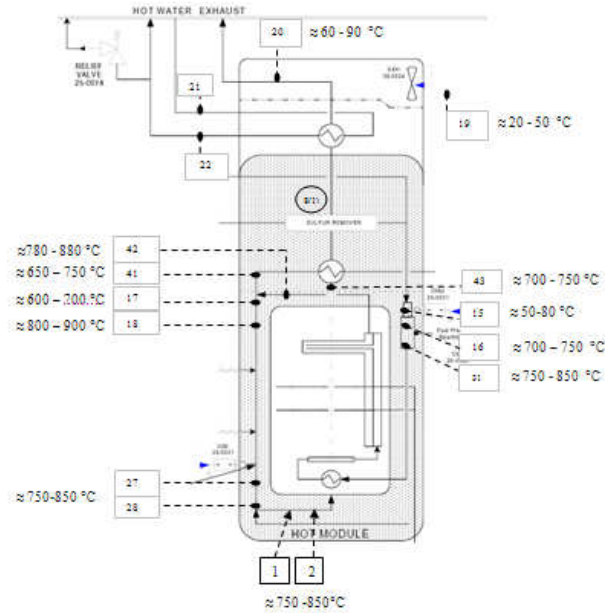
Both upstream and downstream of the exhaust burner and the start-up burner are mounted 4 thermocouples (17-18, 27-28), useful for controlling the start-up phase of the cogenerative module. Also 2 thermocouples (1-2) are installed at the bottom of the hot module (plenum) in order to control the start-up phase of the cogeneration module and to verify that the cathodic air has a thermal energy content sufficient for carrying out the steam reforming reactions at the bottom of the stacks.

The 43 thermocouple measures the temperature of exhaust gases leaving the cathodic compartment of tubular cells (upstream the area of heat exchange) while the 17-18 and 41-42 thermocouples measure the temperature in the area where the exhausted from the tubular cell and the cathodic air are mixed (exhaust burner) and happen the post-combustion reactions of hydrogen and carbon monoxide not yet reacted. The 27-28 thermocouples measure the temperature of gases downstream the exhaust burner and the start-up burner allowing the DSP to operate on the auxiliary blower to control the temperature of the gases sent to the cathodic compartment of the tubular cells.

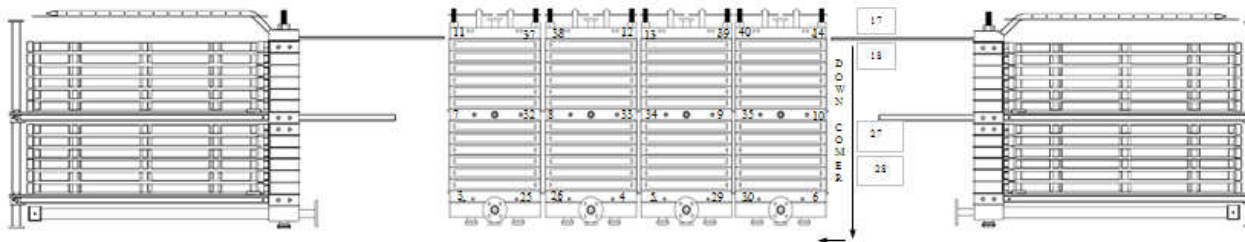
Thermocouple Map

File: Gen512_Tc_Map_Rev1_05-09-2006
SYSTEM THERMOCOUPLES

Generator 512



Thermocouples from 3 to 14, 25-26, 29-30, 32-35, 37-40 are inside the 4 stacks



Thermocouple List:

Thermocouple

- TI_01 1. Air Plenum - Right Stack (Manifold End)
- TI_02 2. Air Plenum - Right Stack (Cell End)
- TI_03 3. Below Left Stack
- TI_04 4. Below Left Center Stack
- TI_05 5. Below Right Center Stack
- TI_06 6. Below Right Stack
- TI_07 7. Left Stack, CM1
- TI_08 8. Left Center Stack, CM1
- TI_09 9. Right Center Stack, CM1
- TI_10 10. Right Stack, CM1
- TI_11 11. Above Left Stack
- TI_12 12. Above Left Center Stack
- TI_13 13. Above Right Center Stack
- TI_14 14. Above Right Stack
- TI_15 15. Reactor Inlet
- TI_16 16. Reactor Bed Top
- TI_17 17. Heat Exchanger & Off gas #1 (Manifold End)
- TI_18 18. Heat Exchanger & Off gas #2 (Cell End)
- TI_19 19. Exhaust Fan In
- TI_20 20. Exhaust Duct
- TI_21 21. Water Coil Inlet
- TI_22 22. Water Coil Outlet
- TI_23 23. Batteries
- TI_24 24. PE Compartment -Top
- TI_25 25. Below Left Stack
- TI_26 26. Below Left Center Stack
- TI_27 27. Downcomer #1
- TI_28 28. Downcomer #2
- TI_29 29. Below Right Center Stack
- TI_30 30. Below Right Stack
- TI_31 31. Reactor Outlet
- TI_32 32. Left Stack, CM 1
- TI_33 33. 16. Left Center Stack, CM 1
- TI_34 34. 17. Right Center Stack, CM1
- TI_35 35. Right Stack CM1
- TI_36 not used
- TI_37 37. Above Left Stack
- TI_38 38. Above Left Center Stack
- TI_39 39. Above Right Center Stack
- TI_40 40. Above Right Stack
- TI_41 41. Offgas Collection
- TI_42 42. HX & Offgas collection
- TI_43 43. Stack HX Center

Figure II.45: Thermocouples distribution inside the CP-SOFC-5000 module

2.12. First results of the experimental activities

The operating temperature of tubular cells, comprised between 750 °C and 850 °C, allows obtaining start-up times reduced respect to SOFC units that work at higher temperatures (900-1000 °C). The condition imposed by the DSP, to consider completed the start-up phase and to be able to provide the electric power, is reaching the minimum temperature inside the 4 stacks of 680 °C.

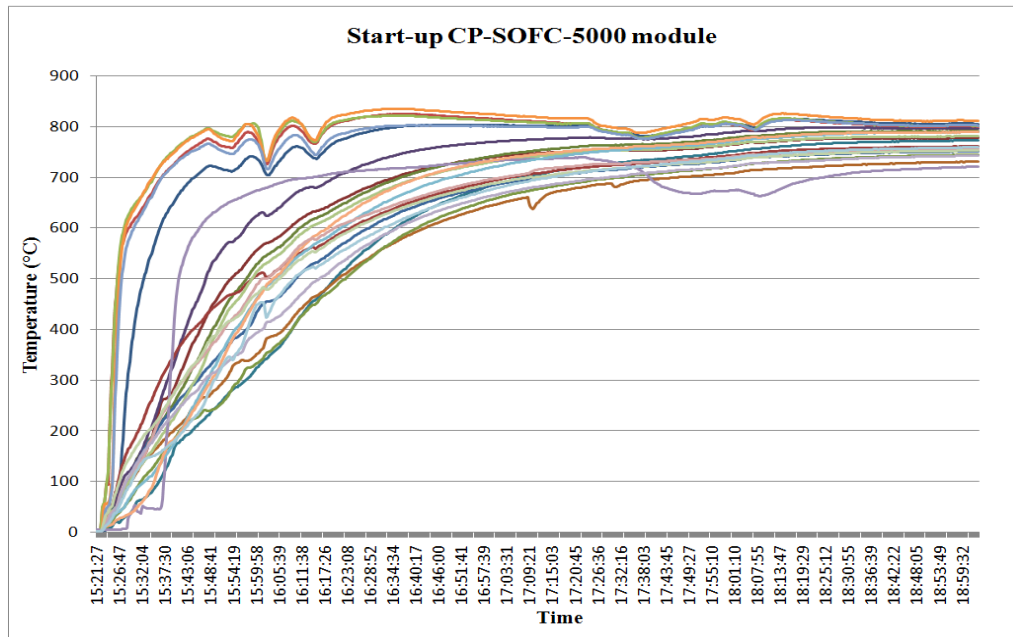


Figure II.46: Temperature trend, of the 24 thermocouples placed inside the stacks, during the start-up procedure

Figure II.46 shows the trend during the start-up procedure of the temperature inside the stacks, and it is possible to see clearly how after about 2 - 2.5 hours this condition has been reached and is therefore possible to supply the electrical load.

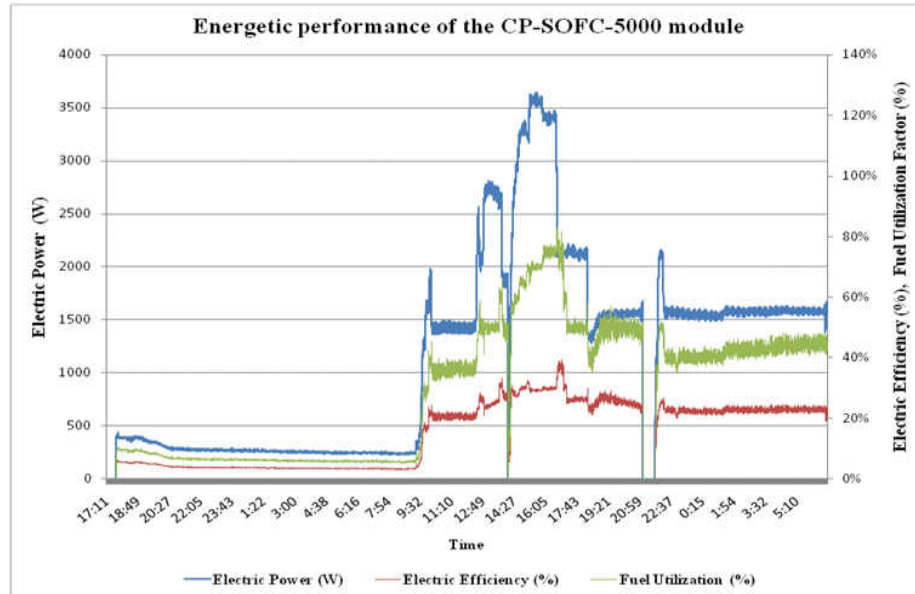


Figure II.47: Performance of the CP-SOFC-5000 module during the first start procedure

Figure II.47 shows the first start-up made on the CP-SOFC-5000 module, operated at the Acumentrics Factory (Westwood, MA – U.S.A.), where for over 12 hours cogenerative unit has worked in the absence of electric power in order to verify the congruency of all the parameters of control of the same one. The electrical adsorption during this phase is represented exclusively by the auxiliary (blowers, flow meters, solenoid valves, microprocessor and data acquisition system, etc.) and varies between 200 W and 400 W respectively.

The DSP gives back a calculation sheet where are reported the main operating parameters of the module that allows obtaining useful property for conducting exhaustive analysis of the energetic performance (Tables II.5, II.6).

In particular, are given:

- a) Value of the 42 thermocouples installed inside the cogenerative module;
- b) Value of voltages of the 48 files of tubular cells inside of the 4 stacks;
- c) Volume flow of natural gas at the inlet of the cogenerative unit and volume flow sent to the anodic compartment of fuel cells;
- d) Volume flow anodic air;
- e) Voltage and current output from the stacks;
- f) Percentage of operation of both cathodic air blower and cooling blower;
- g) battery voltage;
- h) Electric power output in direct current from stacks.

Time	TI_01	TI_02	TI_03	TI_04	TI_05	TI_06	TI_07	TI_08	TI_09	TI_10	TI_11	TI_12	TI_13	TI_14	TI_15	TI_16	TI_17	TI_18	TI_19	TI_20	TI_21	TI_22	TI_23	TI_24	TI_25	TI_26	TI_27	TI_28	TI_29	TI_30	TI_31	TI_32	TI_33	TI_34	TI_35	TI_37	TI_38	TI_39	TI_40	TI_41	TI_42	TI_43
09/11/2007 8.10	737.2	758.9	723.7	745.4	744.5	755.8	771.2	780.9	786	779.6	721.9	755.9	755.1	762.5	79.1	695.5	636.3	820	53.1	83	40.6	49.6	37.8	38.4	735.3	735.1	752.2	768.3	754.1	746.2	786.2	773.8	677.2	788.6	794.5	747.9	745.9	758.8	763.6	670.5	788.5	674.4
09/11/2007 8.10	736.9	758.4	723.9	745.4	744.6	755.9	771	780.8	785.9	779.3	722.1	755.8	755.3	762.5	79	695.5	636.2	819.5	53	82.8	40.8	49.6	37.5	38.4	735.6	735.1	752.3	768.2	754.2	746.2	786.3	773.9	677.4	788.6	794.7	748.1	745.8	759	763.7	670.7	788.3	674.5
09/11/2007 8.10	736.9	758.6	723.7	745.3	744.6	755.7	770.5	780.8	785.9	779.5	721.9	755.8	755.2	762.4	78.5	695.6	636.2	819.5	52.6	82.8	40.9	49.5	37.2	38	735.4	735	751.9	768.3	754.2	746.2	786.5	773.9	677.2	788.4	794.5	748	745.9	759.2	763.8	670.5	787.4	674.2
09/11/2007 8.11	736.7	758.4	723.8	745.3	744.5	755.7	770.9	780.8	785.7	779.4	721.9	755.8	755.1	762.3	78.9	695.8	636.2	819.5	52.6	82.8	40.9	49.5	37.2	38	735.4	735	751.9	768.3	754.2	746.2	786.5	773.9	677.2	788.4	794.5	748	745.9	759.2	763.8	670.5	787.4	674.2
09/11/2007 8.11	736.7	758.6	723.7	745.5	744.6	755.8	770.9	780.7	785.8	779.5	721.9	755.9	755.3	762.5	78.9	695.9	636.2	819.5	52.6	82.8	41	49.7	37.2	37.9	735.2	735	752	768.3	754	746.2	786.4	773.6	677.1	788.5	794.5	747.8	745.7	759.1	763.5	670.4	788.3	674.2
09/11/2007 8.11	736.8	758.5	723.9	745.3	744.6	755.8	771	780.9	785.9	779.6	722	755.7	755.1	762.5	79	696.1	636.3	820.5	52.7	82.5	40.9	49.8	37.5	38.4	735.4	735	752.1	768.6	754.1	746.1	786.3	773.8	677.2	788.4	794.6	747.9	745.7	759	763.5	670.5	788.3	674.3
09/11/2007 8.11	736.6	758.3	723.5	745.2	744.4	755.8	770.8	780.6	785.5	779.2	721.5	755.6	754.9	762.4	78.9	695.6	636	821.2	52	82.2	40.8	49.7	36.9	37.6	735.2	735	752.4	768.8	754.3	746.4	786.2	773.7	677	788.3	794.5	748	745.9	759	763.6	670.3	789	674.3
09/11/2007 8.12	736.8	758.5	723.6	745.3	744.3	755.8	770.9	781	785.5	779.3	721.7	755.7	754.9	762.4	78.9	695.8	636.1	821.2	52.4	82.3	40.7	49.7	36.9	38.1	735.3	735.1	752.6	769	754.2	746.4	786.5	773.8	677.1	788.4	794.6	747.9	746	759.2	763.6	670.3	788.5	674.4
09/11/2007 8.12	737.1	758.9	723.8	745.5	744.8	756	771	780.9	785.6	779.4	721.9	755.8	755.2	762.6	79.1	695.7	636.1	821.7	52.7	82.6	41.1	49.9	37.3	38.1	735.6	735.1	753	769.3	754	746.2	786	773.7	677.3	788.4	794.5	747.8	745.7	758.9	763.5	670.6	789.5	674.5
09/11/2007 8.12	737.3	758.8	723.5	745.4	744.7	755.8	770.8	780.8	785.8	779.3	721.4	755.6	755.1	762.4	78.8	695.5	636.3	822	52.2	82.4	41	49.7	36.8	38	735.5	735.2	753.3	769.6	754.4	746.4	786.3	773.9	677.3	788.5	794.7	748	745.9	758.9	763.6	670.5	789.8	674.7
09/11/2007 8.13	737.2	759	723.8	745.6	744.7	756	771	781.1	785.5	779.3	721.7	755.9	755.1	762.5	79	695.7	636.1	823	52.4	82.5	41	49.8	37.3	38.2	735.8	735.4	753.4	770	754.4	746.5	786.3	774.1	677.5	788.6	794.7	748.1	745.9	759.1	763.9	670.7	791.1	674.7
09/11/2007 8.13	737.3	759	724	745.5	744.6	755.9	770.9	780.7	785.6	779.3	721.9	755.7	755	762.3	78.8	695.5	636.2	822.5	52.3	82.2	41	49.7	37	38.1	735.7	735.3	753.3	769.9	754.5	746.5	786.3	774.1	677.4	788.4	794.5	748.2	745.9	759.1	763.8	670.7	790.5	674.4
09/11/2007 8.13	737.3	759.4	723.8	745.5	744.8	755.9	770.9	780.8	785.6	779.6	721.7	755.6	755.1	762.4	78.9	695.7	636.2	823.2	52.3	82.3	41	49.8	37.2	38.1	735.7	735.3	753.3	769.8	754.5	746.4	786.1	773.9	677.5	788.4	794.6	748	745.8	759	763.7	670.7	789.5	674
09/11/2007 8.13	737.6	759.3	724	745.5	744.6	756	770.9	780.9	785.9	779.4	721.8	755.6	754.9	762.5	78.9	695.9	636.3	823.2	52.3	82.2	40.9	49.8	37	38.2	735.8	735.4	753.2	769.8	754.6	746.6	786.2	773.9	677.5	788.5	794.6	748.1	746	759	763.7	670.8	789.7	674.5
09/11/2007 8.14	737.6	759.7	723.9	745.7	744.9	756	771	780.8	786	779.6	721.7	755.9	755.2	762.5	79	695.8	636.4	823.2	52.2	82.5	41.2	49.8	37.1	38.1	735.9	735.5	753.4	769.7	754.6	746.6	786.4	773.8	677.6	788.5	794.9	748.2	745.9	759.2	763.7	670.9	789.3	674.8
09/11/2007 8.14	737.2	759.2	723.9	745.6	744.7	756	770.9	780.8	785.7	779.5	721.7	755.7	755	762.4	79	695.8	636.2	820	52.1	82.3	40.9	49.8	37.3	38.2	735.8	735.4	752.8	768.8	754.5	746.6	786.2	773.9	677.4	788.4	794.7	748.1	746	759	763.7	670.6	788.8	674.5
09/11/2007 8.14	737	758.9	723.8	745.5	744.7	756.1	770.9	780.8	785.7	779.5	721.7	755.7	755.2	762.5	79	695.6	636.2	819.8	52.1	82.3	41	49.9	37.3	38.3	735.6	735.3	752.6	768.7	754.4	746.4	786.2	773.8	677.3	788.3	794.6	748.1	745.8	759	763.7	670.6	788.7	674.4
09/11/2007 8.14	736.8	758.8	723.8	745.5	744.6	756	770.8	781	785.6	779.5	721.8	755.7	755	762.5	79	695.8	636.1	818.5	52.3	82.4	40.9	49.9	37.3	38.6	736	735.6	752.3	768.4	754.5	746.5	786.4	773.9	677.6	788.5	794.6	748.1	745.8	759.3	763.8	670.9	788.3	673.8
09/11/2007 8.15	736.8	758.4	723.7	745.7	744.8	756.2	770.7	780.7	785.7	779.3	721.6	755.8	755.2	762.7	78.9	695.8	636	818.6	52.1	82.6	41.2	50.2	37.2	38.3	735.7	735.3	752.1	768.3	754.5	746.6	786.2	773.8	677.4	788.3	794.7	748.1	745.9	759.1	763.7	670.7	788.2	674.4
09/11/2007 8.15	736.7	758.3	723.9	745.7	744.9	756.2	770.9	780.8	785.7	779.3	721.9	755.9	755.3	762.6	79.1	695.9	636.1	818.9	52.2	82.8	41.3	50.2	37.4	38.4	735.6	735.3	751.7	768.2	754.5	746.5	786.3	773.8	677.4	788.4	794.6	748.2	745.9	759.1	763.7	670.6	787.9	674.4
09/11/2007 8.15	736.5	758.3	723.7	745.6	744.7	756	770.9	780.7	785.6	779.4	721.6	755.9	755.1	762.5	79.2	695.8	636	818.2	52.2	82.9	41.3	50.1	37.7	38.5	735.7	735.2	751.6	767.9	754.4	746.4	785.8	773.7	677.4	788.4	794.6	747.9	745.9	758.9	763.6	670.7	787.2	674.4
09/11/2007 8.15	736.6	758.4	724	745.7	744.7	756.1	770.8	781	785.7	779.6	721.8	756	755.2	762.6	79.1	695.9	636.2	818.8	52.3	82.8	41.3	50.1	37.5	38.8	735.8	735.3	751.8	767.9	754.4	746.5	786.2	773.8	677.4	788.3	794.7	748.1	745.9	759.1	763.7	670.6	787	674.4
09/11/2007 8.16	736.7	758.4	723.9	745.7	744.8	756	771.3	781.1	785.8	779.6	721.8	755.9	755.2	762.6	79.5	696.1	636.3	819.3	52.4	82.6	41.4	50.1	38.2	39.2	735.7	735.5	751.8	767.9	754.5	746.5	786.1	773.9	677.4	788.7	794.7	748.2	746	759.1	763.7	670.7	787.3	674.5
09/11/2007 8.16	737	758.6	724.3	745.8	744.9	756.4	771.3	781.2	786.2	779.7	722.1	756	755.4	762.8	79.7	695.9	636.6	819.8	52.7	83	41.5	50.4	38.1	39.1	735.8	735.1	751.9	768.3	754.6	746.6	786.1	774	677.5	788.2	794.8	748.3	746.1	759.1	763.9	670.7	787.4	674.4
09/11/2007 8.16	736.9	758.7	724.1	745.7	744.9	756.2	770.9	781	785.9	779.6	722	755.9	755.3	762.7	79.3	695.5	636.3	819.7	52.8	82.9	41.3	50.3	37.6	39	735.7	735.3	752.2	768.2	754.3	746.4	786	773.7	677.3	788.3	794.6	748	745.7	758.9	763.5	670.6	788.5	674.2
09/11/2007 8.16	737	758.5	723.9	745.8	745	756.3	771.1	781	785.9	779.5	721.7	755.9	755.3	762.7	79.4	694.9	636.2	819.6	52.6	82.8	41.5	50.3	37.9	38.7	735.9	735.4	752.3	768.2	754.5	746.7	785.9	774	677.5	788.3	794.5	748.1	746	759	763.9	670.6	788.8	674.2
09/11/2007 8.17	737.2	758.9	724.3	746	745	756.4	771.2	781	785.9	779.8	722.1	756.2	755.4	762.8	79.5	694.8	636.3	820.2	53	83.4	41.5	50.5	38.1	38.7	735.9	735.5	752.5	768.5	754.7	746.8	786.4	774	677.6	788.4	794.7	748.2	746	759.4	763.8	670.8	788.8	674.4
09/11/2007 8.17	737.4	758.9	724.3	745.9	745.1	756.5	771.2	781.2	786.2	779.8	722.1	756	755.3	762.8	79.5	695.1	636.6	820	53.2	83.2	41.6	50.5	37.9	38.8	736	735.7	75															

Time	V_01	V_02	V_03	V_04	V_05	V_06	V_07	V_08	V_09	V_10	V_11	V_12	V_13	V_14	V_15	V_16	V_17	V_18	V_19	V_20	V_21	V_22	V_23	V_24	V_25	V_26	V_27	V_28	V_29	V_30	V_31	V_32	V_33	V_34	V_35	V_36	V_37	V_38	V_39	V_40	V_41	V_42	V_43	V_44	V_45	V_46	V_47	V_48
09/11/2007 8.10	0.7205	0.7606	0.7596	0.7795	0.7594	0.7914	0.7521	0.8004	0.7525	0.7493	0.6958	0.6932	0.733	0.7272	0.7529	0.8125	0.7744	0.802	0.7479	0.7866	0.7549	0.763	0.7494	0.7517	0.81	0.764	0.8117	0.7793	0.7727	0.7845	0.778	0.8013	0.7822	0.7942	0.7449	0.7406	0.7527	0.7199	0.7844	0.7694	0.7925	0.7755	0.7745	0.7971	0.7761	0.8043	0.7678	0.7774
09/11/2007 8.10	0.7205	0.7575	0.7555	0.7775	0.7574	0.7904	0.7511	0.7974	0.7515	0.7463	0.6927	0.6861	0.7311	0.724	0.7518	0.8105	0.7734	0.7992	0.7429	0.7824	0.7529	0.7581	0.7494	0.7507	0.807	0.762	0.8107	0.7813	0.7697	0.7835	0.779	0.7994	0.7778	0.7933	0.7411	0.733	0.7476	0.7159	0.7795	0.7674	0.7925	0.7755	0.7705	0.7961	0.7751	0.8023	0.7659	0.7774
09/11/2007 8.10	0.7225	0.7575	0.7606	0.7755	0.7604	0.7884	0.7511	0.7944	0.7536	0.7463	0.6969	0.6851	0.7311	0.7283	0.7508	0.8085	0.7775	0.8001	0.7459	0.7814	0.7549	0.7572	0.7515	0.7477	0.803	0.7651	0.8098	0.7843	0.7736	0.7815	0.7811	0.7994	0.7822	0.7913	0.743	0.7276	0.7416	0.7179	0.7795	0.7684	0.7896	0.7775	0.7715	0.7971	0.7741	0.8004	0.7678	0.7734
09/11/2007 8.11	0.7215	0.7585	0.7596	0.7775	0.7564	0.7884	0.75	0.7964	0.7505	0.7432	0.6948	0.681	0.7311	0.724	0.7497	0.8095	0.7744	0.8001	0.7449	0.7804	0.751	0.7591	0.7484	0.7468	0.803	0.762	0.8107	0.7793	0.7697	0.7835	0.779	0.7985	0.7789	0.7865	0.7411	0.7308	0.7416	0.7199	0.7775	0.7684	0.7887	0.7755	0.7725	0.7971	0.7741	0.8033	0.7659	0.7744
09/11/2007 8.11	0.7205	0.7595	0.7586	0.7795	0.7584	0.7904	0.75	0.7984	0.7494	0.7483	0.6938	0.6861	0.7301	0.7229	0.7497	0.8105	0.7734	0.8001	0.7459	0.7824	0.7519	0.7611	0.7473	0.7497	0.807	0.763	0.8117	0.7783	0.7707	0.7815	0.779	0.7994	0.7789	0.7933	0.7402	0.7395	0.7456	0.7179	0.7814	0.7674	0.7925	0.7736	0.7725	0.7951	0.7731	0.8023	0.7669	0.7734
09/11/2007 8.11	0.7215	0.7564	0.7596	0.7755	0.7564	0.7884	0.7521	0.7984	0.7515	0.7473	0.6948	0.6871	0.7311	0.7272	0.7508	0.8095	0.7734	0.7992	0.7439	0.7814	0.7549	0.762	0.7494	0.7527	0.807	0.7651	0.8107	0.7803	0.7717	0.7825	0.7769	0.7994	0.78	0.7913	0.7402	0.7373	0.7466	0.7208	0.7795	0.7684	0.7915	0.7765	0.7735	0.7961	0.7741	0.8023	0.7649	0.7744
09/11/2007 8.11	0.7205	0.7564	0.7616	0.7755	0.7574	0.7874	0.7521	0.7944	0.7525	0.7442	0.6958	0.682	0.7272	0.7261	0.7497	0.8075	0.7755	0.7992	0.7449	0.7804	0.7539	0.7572	0.7494	0.7448	0.802	0.7651	0.8098	0.7803	0.7717	0.7795	0.779	0.7975	0.7789	0.7865	0.7421	0.7286	0.7416	0.7199	0.7766	0.7684	0.7877	0.7775	0.7696	0.7961	0.7751	0.8023	0.7669	0.7764
09/11/2007 8.12	0.7205	0.7585	0.7586	0.7775	0.7564	0.7914	0.7511	0.7974	0.7525	0.7452	0.6958	0.6861	0.7311	0.725	0.7508	0.8085	0.7765	0.8001	0.7439	0.7814	0.7549	0.7601	0.7525	0.7487	0.807	0.7651	0.8107	0.7813	0.7717	0.7815	0.779	0.7994	0.7767	0.7894	0.7411	0.7363	0.7446	0.7159	0.7814	0.7684	0.7906	0.7765	0.7705	0.7971	0.7731	0.8023	0.7678	0.7754
09/11/2007 8.12	0.7185	0.7585	0.7586	0.7785	0.7564	0.7874	0.7511	0.7974	0.7494	0.7473	0.6948	0.6861	0.732	0.724	0.7487	0.8075	0.7734	0.8001	0.7449	0.7814	0.7519	0.7601	0.7484	0.7477	0.804	0.763	0.8107	0.7803	0.7717	0.7815	0.7769	0.8003	0.7789	0.7933	0.7402	0.7395	0.7446	0.7179	0.7795	0.7684	0.7906	0.7755	0.7725	0.7951	0.7751	0.8014	0.7678	0.7744
09/11/2007 8.12	0.7215	0.7554	0.7596	0.7765	0.7564	0.7884	0.7521	0.7974	0.7515	0.7463	0.6948	0.684	0.7281	0.725	0.7508	0.8065	0.7744	0.7992	0.7439	0.7814	0.7519	0.7601	0.7484	0.7517	0.803	0.7651	0.8107	0.7803	0.7717	0.7815	0.779	0.7985	0.7811	0.7894	0.7421	0.7352	0.7436	0.7199	0.7795	0.7694	0.7877	0.7765	0.7715	0.7941	0.7741	0.8014	0.7678	0.7734
09/11/2007 8.13	0.7235	0.7595	0.7616	0.7805	0.7584	0.7904	0.7553	0.7954	0.7525	0.7463	0.6938	0.6861	0.7301	0.7261	0.7518	0.8105	0.7755	0.802	0.7449	0.7814	0.7539	0.7601	0.7494	0.7497	0.805	0.764	0.8126	0.7793	0.7736	0.7835	0.7801	0.7975	0.78	0.7904	0.7411	0.7352	0.7456	0.7179	0.7805	0.7664	0.7906	0.7765	0.7735	0.7951	0.7741	0.8062	0.7678	0.7754
09/11/2007 8.13	0.7185	0.7564	0.7565	0.7785	0.7584	0.7904	0.7521	0.7964	0.7515	0.7422	0.6958	0.683	0.7301	0.724	0.7497	0.8075	0.7755	0.7992	0.7439	0.7814	0.7539	0.7601	0.7494	0.7458	0.804	0.764	0.8107	0.7803	0.7707	0.7815	0.7801	0.7975	0.78	0.7923	0.7402	0.733	0.7416	0.715	0.7785	0.7664	0.7887	0.7775	0.7715	0.7951	0.7721	0.8004	0.7688	0.7734
09/11/2007 8.13	0.7215	0.7585	0.7596	0.7775	0.7584	0.7884	0.7521	0.7984	0.7525	0.7463	0.6979	0.6861	0.7301	0.7261	0.7508	0.8075	0.7765	0.7992	0.7459	0.7824	0.7539	0.7601	0.7515	0.7497	0.806	0.7671	0.8126	0.7803	0.7707	0.7805	0.7801	0.7975	0.78	0.7933	0.7421	0.7352	0.7456	0.7208	0.7805	0.7694	0.7906	0.7775	0.7715	0.7961	0.7741	0.8023	0.7678	0.7734
09/11/2007 8.13	0.7205	0.7564	0.7586	0.7785	0.7584	0.7894	0.75	0.7994	0.7505	0.7483	0.6938	0.682	0.733	0.7261	0.7508	0.8075	0.7744	0.8001	0.7439	0.7824	0.7529	0.7591	0.7473	0.7497	0.805	0.764	0.8136	0.7803	0.7707	0.7785	0.7801	0.7985	0.78	0.7884	0.7402	0.7373	0.7466	0.7189	0.7785	0.7664	0.7925	0.7746	0.7725	0.7941	0.7741	0.8052	0.7659	0.7744
09/11/2007 8.14	0.7205	0.7543	0.7616	0.7775	0.7574	0.7894	0.7511	0.7964	0.7536	0.7483	0.6958	0.6871	0.7291	0.7261	0.7529	0.8075	0.7775	0.8011	0.7439	0.7814	0.7539	0.7572	0.7504	0.7497	0.807	0.764	0.8098	0.7803	0.7736	0.7825	0.7801	0.7975	0.78	0.7894	0.7421	0.7319	0.7466	0.7199	0.7814	0.7694	0.7887	0.7765	0.7735	0.7961	0.7761	0.8033	0.7659	0.7734
09/11/2007 8.14	0.7215	0.7575	0.7616	0.7775	0.7594	0.7904	0.7532	0.7954	0.7525	0.7463	0.699	0.6892	0.732	0.7304	0.7518	0.8075	0.7765	0.8001	0.7449	0.7824	0.7549	0.7601	0.7504	0.7497	0.808	0.7651	0.8117	0.7813	0.7736	0.7805	0.7832	0.7994	0.7811	0.7923	0.744	0.7373	0.7496	0.7208	0.7795	0.7694	0.7906	0.7794	0.7735	0.7961	0.7771	0.8023	0.7678	0.7744
09/11/2007 8.14	0.7215	0.7595	0.7626	0.7775	0.7594	0.7904	0.7532	0.7974	0.7515	0.7452	0.6969	0.6871	0.733	0.7261	0.7529	0.8105	0.7755	0.8001	0.7469	0.7824	0.7539	0.7601	0.7484	0.7497	0.806	0.764	0.8107	0.7813	0.7717	0.7825	0.7811	0.7975	0.78	0.7962	0.743	0.7352	0.7476	0.7208	0.7824	0.7684	0.7896	0.7785	0.7735	0.7981	0.7761	0.8023	0.7708	0.7744
09/11/2007 8.14	0.7215	0.7564	0.7596	0.7785	0.7594	0.7884	0.7511	0.7964	0.7536	0.7452	0.6958	0.6871	0.7291	0.7283	0.7529	0.8095	0.7755	0.8001	0.7449	0.7824	0.7519	0.762	0.7504	0.7468	0.804	0.7651	0.8098	0.7823	0.7727	0.7805	0.778	0.7985	0.78	0.7884	0.7392	0.7363	0.7436	0.7208	0.7795	0.7694	0.7887	0.7775	0.7735	0.7941	0.7741	0.8004	0.7688	0.7734
09/11/2007 8.15	0.7245	0.7575	0.7586	0.7775	0.7584	0.7874	0.7511	0.7954	0.7525	0.7483	0.6958	0.6861	0.733	0.7283	0.7529	0.8085	0.7755	0.8011	0.7459	0.7793	0.7539	0.7581	0.7504	0.7487	0.804	0.7651	0.8117	0.7813	0.7746	0.7815	0.778	0.7994	0.7811	0.7904	0.7421	0.7363	0.7466	0.7208	0.7795	0.7704	0.7906	0.7775	0.7735	0.7971	0.7761	0.8033	0.7659	0.7744
09/11/2007 8.15	0.7215	0.7564	0.7596	0.7795	0.7584	0.7904	0.749	0.7954	0.7505	0.7463	0.6948	0.6871	0.7291	0.7283	0.7518	0.8085	0.7744	0.8001	0.7439	0.7824	0.7539	0.7581	0.7473	0.7497	0.807	0.764	0.8107	0.7813	0.7727	0.7815	0.779	0.7975	0.78	0.7923	0.7402													

Time	Anode Fuel Flow Scm ³ /min	Anode Fuel Valve (%)	Anode Air Flow Scm ³ /min	Anode Air Blower (%)	Stack Amps	Stack Volts	Burner Valve	Cathode Blower (%)	Cooling Valve (%)	Battery Volts	Primary Air Blower (%)	Bypass Valve Override (%)	Fuel Totalizer Scm ³ /min	Pressure Sensor	G512 DC Power (W)
09/11/2007 8.10	11.195712	34.634876	35.116916	19.415569	57.434082	36.4	0	51.127911	17.999935	54.415848	0	0	10.812701	-5.459561	2090.600586
09/11/2007 8.10	11.155202	34.714127	35.422871	19.443512	59.020996	36.43	0	51.127911	17.999935	54.515864	0	0	10.842164	-5.47152	2150.134888
09/11/2007 8.10	11.516116	34.72414	35.082921	19.443512	58.441162	36.37	0	51.127911	17.999935	54.494432	0	0	10.831115	-5.464793	2125.505066
09/11/2007 8.11	11.354073	34.739399	35.071589	19.43779	57.922363	36.43	0	51.127911	17.999935	54.530152	0	0	10.91582	-5.473015	2110.111694
09/11/2007 8.11	11.427729	34.717274	35.184906	19.424725	58.47168	36.43	0	51.127911	17.999935	54.487288	0	0	11.00789	-5.455824	2130.123291
09/11/2007 8.11	11.46824	34.698009	34.969604	19.440842	58.532715	36.38	0	51.127911	17.999935	54.444424	0	0	10.661706	-5.486468	2129.420166
09/11/2007 8.11	11.405632	34.735966	35.978124	19.452095	58.105469	36.35	0	51.127911	17.999935	54.58016	0	0	10.764825	-5.480489	2112.133789
09/11/2007 8.12	11.505068	34.759808	35.717495	19.471359	57.952881	36.34	0	51.127911	17.999935	54.537296	0	0	10.790604	-5.473015	2106.00769
09/11/2007 8.12	11.203078	34.756565	35.740159	19.453907	59.051514	36.41	0	51.127911	17.999935	54.530152	0	0	10.89004	-5.498427	2150.065613
09/11/2007 8.12	11.486654	34.739494	35.490862	19.473457	57.556152	36.34	0	51.127911	17.999935	54.551584	0	0	11.059449	-5.467035	2091.590576
09/11/2007 8.13	11.309879	34.768105	35.638174	19.463539	58.837891	36.39	0	51.127911	17.999935	54.465856	0	0	10.893723	-5.438633	2141.11084
09/11/2007 8.13	11.394584	34.747124	35.388876	19.48452	58.227539	36.36	0	51.127911	17.999935	54.537296	0	0	10.842164	-5.456571	2117.15332
09/11/2007 8.13	11.2841	34.795761	35.320886	19.465446	58.288574	36.36	0	51.127911	17.999935	54.551584	0	0	10.978427	-5.458066	2119.372559
09/11/2007 8.13	11.309879	34.770679	35.252896	19.473839	58.837891	36.4	0	51.127911	17.999935	54.58016	0	0	11.004207	-5.513376	2141.699219
09/11/2007 8.14	11.280417	34.794807	35.717495	19.44561	58.929443	36.33	0	51.127911	17.999935	54.61588	0	0	10.886357	-5.450592	2140.906677
09/11/2007 8.14	11.306196	34.777164	35.626842	19.451332	57.861328	36.4	0	51.127911	17.999935	54.494432	0	0	10.816384	-5.444612	2106.152344
09/11/2007 8.14	11.339342	34.758759	35.218901	19.45076	58.319092	36.43	0	51.127911	17.999935	54.487288	0	0	10.831115	-5.484226	2124.564514
09/11/2007 8.14	11.457191	34.787083	35.388876	19.433403	57.891846	36.43	0	51.127911	17.999935	54.501576	0	0	10.875309	-5.484973	2108.999939
09/11/2007 8.15	11.25832	34.800053	35.6835	19.449425	57.70874	36.41	0	51.127911	17.999935	54.494432	0	0	10.856895	-5.452834	2101.175232
09/11/2007 8.15	11.361438	34.79538	35.037594	19.435215	58.349609	36.38	0	51.127911	17.999935	54.551584	0	0	10.82375	-5.484973	2122.758789
09/11/2007 8.15	11.320928	34.756947	35.434203	19.438076	57.922363	36.35	0	51.127911	17.999935	54.515864	0	0	10.882674	-5.473015	2105.477905
09/11/2007 8.15	11.35039	34.682274	35.6835	19.425964	57.800293	36.43	0	51.127911	17.999935	54.515864	0	0	10.79797	-5.473015	2105.664673
09/11/2007 8.16	11.427729	34.701824	35.536188	19.41843	57.861328	36.49	0	51.127911	17.999935	54.422992	0	0	10.764825	-5.452834	2111.359863
09/11/2007 8.16	11.523482	34.763145	35.116916	19.398403	57.922363	36.5	0	51.127911	17.999935	54.387272	0	0	10.908454	-5.435643	2114.16626
09/11/2007 8.16	10.989476	34.733963	35.604179	19.413471	58.441162	36.45	0	51.127911	17.999935	54.494432	0	0	10.676438	-5.451339	2130.180359
09/11/2007 8.16	11.328293	34.78384	35.377545	19.420815	57.800293	36.46	0	51.127911	17.999935	54.515864	0	0	10.89004	-5.460308	2107.398682
09/11/2007 8.17	11.471922	34.752369	34.992267	19.398212	57.220459	36.46	0	51.127911	17.999935	54.415848	0	0	10.849529	-5.451339	2086.257935
09/11/2007 8.17	11.387218	34.731293	35.116916	19.409084	57.739258	36.47	0	51.127911	17.999935	54.444424	0	0	10.842164	-5.46554	2105.750732
09/11/2007 8.17	11.265686	34.782505	35.796817	19.409561	58.013916	36.48	0	51.127911	17.999935	54.444424	0	0	10.849529	-5.457318	2116.347656

Table II.6: Calculation sheet produced by the DSP where are reported the main operating parameters of the CP-SOFC-5000 module (Part 2)

Completed the start-up phase, with control of the correct setting of all the operation parameters of the cogenerative module, successively the behavior of the cogenerative unit has been analyzed varying the electrical load connected (from 1.5 kW to 3.6 kW). From the operation value registered has been extracted the gross electrical efficiency (calculated beginning from the electric power produced by the cells in direct current, including the necessary energy to feeding the auxiliary ones) using the following relation:

$$\eta_{el(gross)} = \frac{\dot{P}_{el(gross)}}{\dot{m}_{CH_4,in} \times LHV} \quad (II.6)$$

where:

- $\eta_{el(gross)}$ = Gross electrical efficiency
- $\dot{P}_{el(gross)}$ = Gross Electric Power generated in direct current and measured by DSP
- $\dot{m}_{CH_4,in}$ = Mass flow rate of CH₄ at the inlet of the module (measured on board)
- LHV = Lower Heating Value.

The value shown in figure II.47, varies between 20% and 38%, increasing when the electric power of the external load raise. Similarly, varying the electrical load provided by the cogenerative module, the Fuel Utilization Coefficient (U_f) assumes values ranging between 38% and 80%. The calculation of the Fuel Utilization has been derived using the following relation:

$$U_f = \frac{I}{n_{el} \cdot \dot{n}_{fuel} \cdot F} \quad (II.7),$$

where:

- I = output current from the cell;
- n_{el} = number of charges exchanged for moles of gas reacted (2 for hydrogen and carbon monoxide);
- \dot{n}_{fuel} = Molar flow of fuel entering inside the cell;
- F = Faraday's constant (96,485 Coulomb / mol).

In order to determine the U_f parameter, the current value I is provided by the DSP and is listed in the table II.6, while n_{el} and F are constant values that do not vary with the operating conditions of the cogenerative unit. Different is the condition of the molar flow of fuel entering the cell (\dot{n}_{fuel}): this parameter represents the amount of H₂ and CO that is

sent to the anodic compartment of the tubular cells for carrying out electrochemical reactions.

The CP-SOFC-5000 module does not have the instrumentation that can provide the exact molar flow of reactant gases entering the tubular cells. In fact, the unit has only a volumetric flow meter that provides the amount of natural gas input to the cogenerative unit, upstream section of reforming: the module is equipped with a set of sample port through which, using a gas chromatograph, will be possible in the future to determine the precise composition of the gas reagents during the various stages of reforming and at the end of them. So at the moment the molar flow rate of reactant gases inlet the cell will be calculated on the basis of information provided by the same Acumentrics. The table II.7 shows the composition of the mixture at different stages of the reforming process occurring in the cogeneration module and the expected final composition at the entrance of the tubular fuel cells.

90% CPOX REFORMING (O/C=1,3)					
CH₄	(1,3/2) O₂	>	CO	2H₂	O₂
0.9	0.45	>	0.9	1.8	0.2
mol/s	mol/s		mol/s	mol/s	mol/s
	2.143			1.693	
	(mol/s of Air)			(mol/s of N₂)	
Residual			CO 1/2O₂	>	CO₂
			1 1/2	>	1
			mol/s mol/s		mol/s
O₂			0.133 0.067	>	0.133
	>		mol/s mol/s		mol/s
0.20			2H₂ O₂	>	H₂O
mol/s			2 1	>	2
			mol/s mol/s		mol/s
			0.267 0.133	>	0.267
			mol/s mol/s		mol/s
10% STEAM REFORMING					
CH₄	H₂O	>	CO	3H₂	
1	1		1	3	residual
mol/s	mol/s		mol/s	mol/s	H₂O
0.1	0.10	>	0.1	0.3	0.167
mol/s	mol/s		mol/s	mol/s	mol/s
From 1 mol/s of CH ₄ with O/C =1,3					
FINAL COMPOSITION (mol/s)					
CO	H₂	N₂	CO₂	H₂O	
0.9	1.8	1.693			CPOX Reaction
0.133	0.267		0.133	0.267	
0.1	0.3			0.100	Residual
0.867	1.833	1.693	0.133	0.167	Steam Reaction
18.5%	39.1%	36.1%	2.8%	3.6%	Final composition

From 1 mol/s of CH₄ > (0.897+1.833) = 2.73 mol/s fuel
--

Table II.7: Gas mixture composition during the different phases of the natural gas reforming process

The values obtained represents the expected final composition considering a molar flow of 1 mol/s of CH₄ entering into the system, assuming that all reactions are at equilibrium.

The results show a conversion factor of 2.73 between the moles of CH₄ at the inlet of the cogenerative module and the number of moles of H₂ and CO obtained at the outlet of the reforming section, value that will allow us to derive the molar flow that we have to replace in the previous relation:

$$\dot{n}_{\text{fuel}} = 2.73 \times \dot{n}_{\text{fuel,CH}_4} \quad (\text{II.9})$$

The coefficient obtained is lower than the value obtained in the case of complete partial oxidation (equal to 3 = 2 moles of H₂ + 1 mole CO) or that the value obtained in the event of complete steam reforming reaction (equal to 4 = 3 moles H₂ + 1 mole CO). This phenomenon is due to the excess of air used in the mixture under reforming: the excess of oxygen, reacting with part of the hydrogen and carbon monoxide formed by reactions, reduces the capacity of conversion of the entire system. However the excess of air is necessary to ensure that will be completed the entire reforming phenomenon. It is possible then to conclude that the solution adopted by Acumentrics, has the benefit of an easier plant solution, compared to the SMR solution taken by other manufacturers (no special section of heat exchange are necessary for the endothermic SMR reaction), at the expense of a less efficient conversion of the natural gas input.

The gas mixture at the inlet of the anodic compartment of the tubular fuel cells is composed by 57.6% of reagent gases (H₂ and CO), with a double quantity of hydrogen (39.1%) compared to carbon monoxide (18.5%); the remaining quote is made up of inert gases that do not participate at the anodic electrochemical reactions. This presence is a direct result of the choice made in the natural gas reforming process: the partial oxidation, carried out by air, rather than oxygen, is certainly a cheaper solution but that involves a residual quantity of N₂ equal to 36.1% of the total composition of the mixture. The nitrogen being inert occupies part of the area dedicated to electrochemical reactions (Three Phase Boundary) increasing the dwell time necessary at the molecules of CO and H₂ to reach the surface of reaction, slows down the speed of reactions to produce electricity and heat. This deleterious effect is partly offset by the possibility that the inert gases absorb the heat generated by electrochemical reactions, improving the cooling capacity of the cells themselves.

The presence of steam even if minimal, would provide the opportunity that may occur steam methane reforming reaction in the anodic compartment of tubular cells, in the event that small amounts of CH_4 fail to complete the reforming reactions in the previous sections, avoiding the occurrence of the carbon deposition phenomena on the anode surfaces.

Once analyzed the behavior of the CP-SOFC-5000 module in the start-up conditions and for sudden variations of the electric load, it has been valued instead the behavior of the cogenerative unit under steady state operation conditions (Figure II.48) with progressive variations of the electric load (step by step) from 2.1 kW to 3.8 kW. It is possible to observe as the value of the gross electrical efficiency is much more stable, with values ranging between 30% and 35%, while the Fuel Utilization Coefficient rise from 65% to almost 85%.

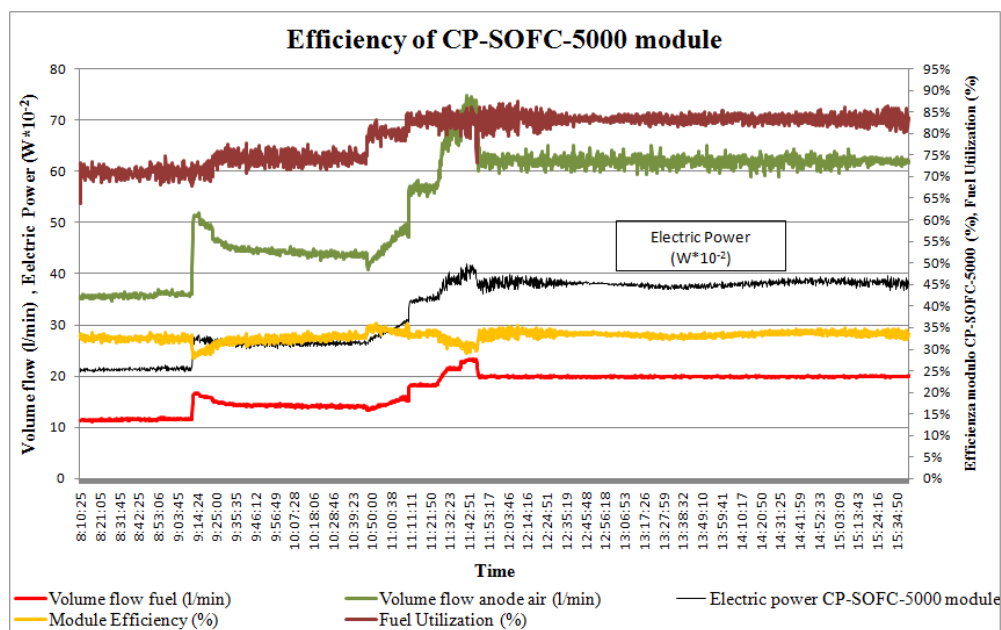


Figure II.48: Performance of the CP-SOFC-5000 module under steady state condition: step by step variation of the electric load

In the same figure are shown both the data of the natural gas volume flow sent to the anodic compartment and the anodic air volume flow required for the CPOX operations. The O/C ratio is maintained throughout the operation on values around 1.3. The natural gas flow during the steady state operation varies between $10 \text{ Scm}^3/\text{min}$ and $20 \text{ Scm}^3/\text{min}$ while the values recorded during the start-up phase amounted to $30\text{-}35 \text{ Scm}^3/\text{min}$. It is possible to observe as the natural gas volume flow trend follow in a very faithful way the evolution of the electric power provided by the cogeneration unit; from this behavior result that in the

regulation operations the DSP proceeds to sudden variations of the natural gas volume flow as soon as there are variations in electrical load. The increase is not entirely straightforward since the fuel utilization coefficient tends to increase as electrical power grows and conversely the value of cell voltage tends to decrease. All this can be translated into a shift toward right of the operation point into the polarization curve, as the electric power output grows.

Figure II.49 shows instead the trend, according to the electrical load, of the electric current and voltage output of the CP-SOFC-5000 module. It is clearly shows how the evolution of the stacks current output is perfectly overlapped with changes in the electrical load provided. On the contrary, the voltages of the stacks tends to fall slightly at each increment of the electric power, confirming the fact that, although gradually the point of operation moves on the right along the fuel cell polarization curve.

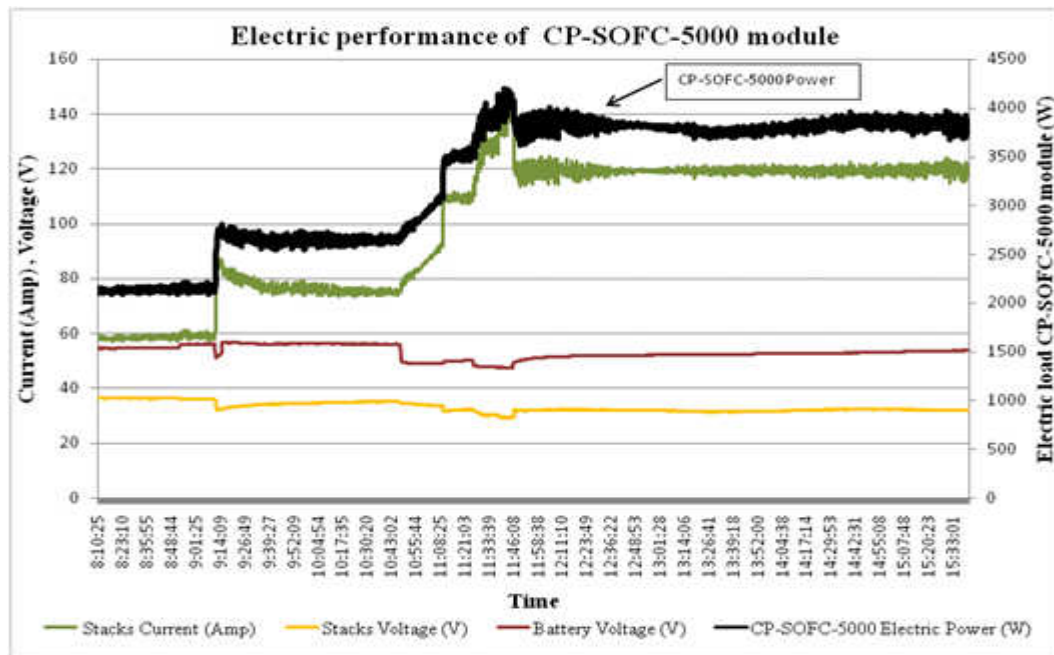


Figure II.49: Electric performance of the CP-SOFC-5000 module according to the electric load

In the same figure is shown the evolution of the batteries voltage placed between the CP-SOFC-5000 unit and the electrical load. It is possible to note that varying the electrical load always follows a sudden drop of the batteries voltage, reflecting the fact that are always these to intervene, initially, to supply the changes in the electric load, and only at a later time intervenes the cogenerative module, as it is also shown by the gradual growth of the batteries voltage successive to the variations of the load.

Similarly was obtained the electrical behavior for a single tubular SOFC (Figure II.50), under the same conditions of electrical load reported in the earlier figures. The trends reported in the figure are relative to the average values calculated on all 288 tubes inside the stacks, since the instrumentation on board of the module allows measuring the voltage of 48 files of tubular cells and the total current output from the stacks.

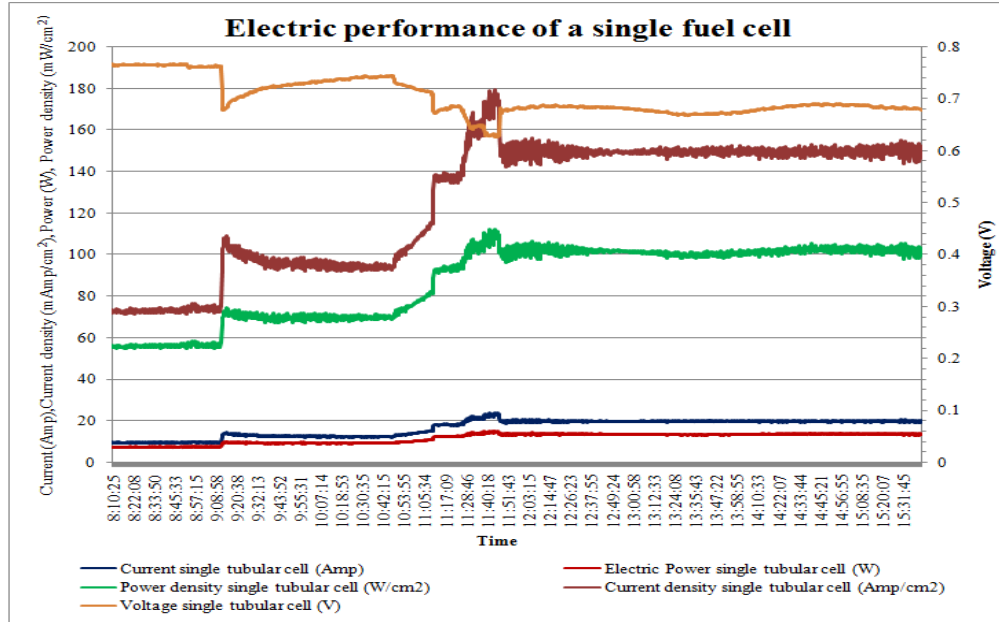


Figure II.50: Electric performance of a single tubular fuel cell according to electrical load

The voltage varies between 0.78 V and 0.68 V growing the electric power supplied, reflecting the fact that despite the load changes are significant (2.1 kW to 3.8 kW) the point of operation is moving just a little bit along the polarization curve, for reasons discussed above. The current output increased from about 9 Amp to 20 Amp; this change is due more to increase in the reagent gases flow available within the anode compartment than by the marked shift to the right of the operating point on the polarization curve. The single SOFC provides in these conditions an electric power between 10 W and 14 W. Much more interesting from the performance point of view are the specific values obtained: the current density varies between 75 mA/cm² and 150 mA/cm², with peak of 180 mA/cm²; the power density takes values between 55 mW/cm² and 100 mW/cm², with peaks of 110 mW/cm²: these values are obtained for reactants gas volume flow at the inlet of the single tubular cell between 110 Scm³/min and 190 Scm³/min.

Finally it was examined the temperature trends inside the cogeneration circuit and the production of heat by the CP-SOFC-5000 module. The results are related to a water volume flow of 7 Scm³/min (Figure II.51).

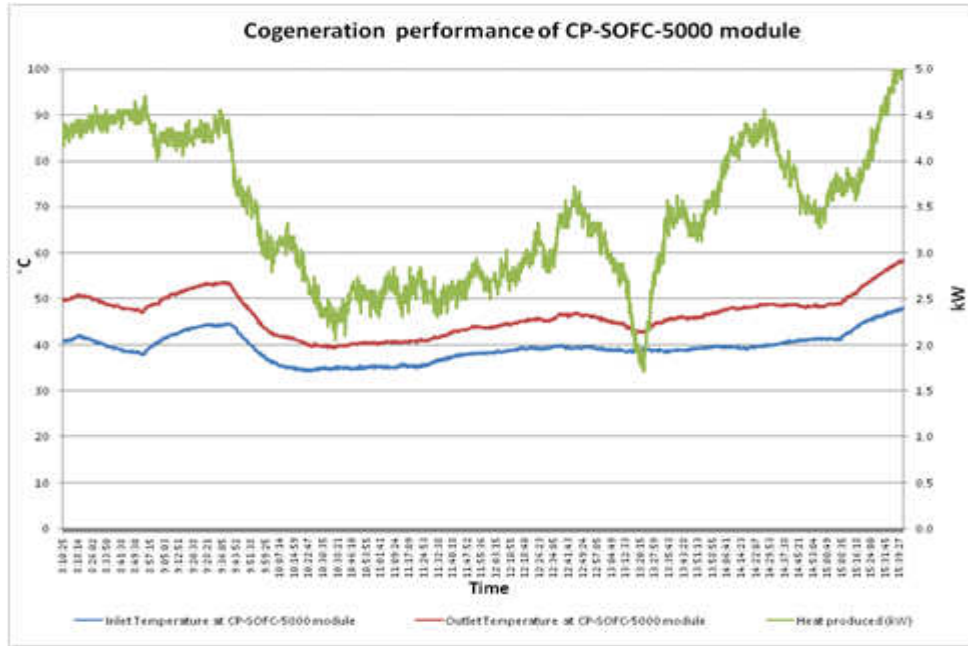


Figure II.51: Temperature trend of the cogenerative section and heat produced by the CP-SOFC-5000 module

The temperature levels, although not particularly high (40-50 °C) are sufficient to feed a thermal user operating at low temperature, confirming the possibility of using this unit mainly to feed domestic users. The heat generated, between 2.5 kW and 4.5 kW allows reaching values of the global energetic efficiency comprised between 65% and 76%.

$$\eta_g = \frac{\dot{P}_{el} + \dot{Q}}{\dot{m}_{CH_4,in} \cdot LHV} \quad (II.10)$$

2.13. Conclusion

The results obtained in the experimental activities confirm the potential of SOFC technology for the realization of innovative system with higher energetic efficiency, particularly to realize distributed energy plants on small scale (domestic applications).

The CP-SOFC-5000 unit, is capable of delivering a maximum power of 5 kW and, in cogenerative arrangement, a thermal power between 2.5 kW and 4.5 kW, showing a gross electric efficiency ranging between 20% and 40%, with global efficiency in cogenerative arrangement, ranging between 65% and 76%.

The solution of using a partial oxidation process (CPOX) for the natural gas reforming allows greater simplicity in the power plant design while ensuring adequate efficiency.

The timing for start-up operations (2 - 2.5 hours), lower than for other SOFC technologies, thanks to operating temperatures between 750 ° and 850 ° C and also to the

partial oxidation solution of the natural gas, are still high if compared with other technologies (engines, microturbines).

The experimental activities conducted on the CP-SOFC-5000 cogenerative have permitted to verify the energetic performance of the unit in different conditions of electric load, and the resulting variations of the main operating parameters of the unit (volume flow, temperature, Fuel Utilization Coefficient, etc.).

Future developments of the experimental activities will permit the trend evaluation of the average levels of voltage and current provided by the cell in the steady state condition for long term testing, in order to assess the level of degradation of the module with the time. It will also assess the behavior of CP-SOFC-5000 varying every single control parameter that is possible to modify in order to obtain a full characterization of the energetic performance of the cogenerative module.

In order to verify the system performance in dynamic condition, the cogenerative module will also be subject to different cycles of electric load.

2.14. Acknowledgments

Special thanks to ing. Stefan Wirth (Acumentrics) for the technical and scientific support and the effective cooperation shown during all phases of CP-SOFC-5000 testing.

2.15. Referenses

- [1] Norman Besette et al.: “*Acumentrics Technical Progress Report for DOE - March 2005*”;
- [2] R. Barrera et al.: “Performance and life-time test on a 5 kW SOFC system for distributed cogeneration”, HYSYDAYS – 2nd World Congress of Young Scientist on Hydrogen Energy Systems.
- [3] Singhal, S.C., Kendall, K.: “High temperature Solid Oxide Fuel Cells”, Elsevier, 2003.
- [4] Larminie, J., Dicks, A.: “Fuel cell system explained”, John Wiley & sons LTD, 2004.
- [5] “Fuel cell handbook (seventh edition)”, 2004, U.S. Department of Energy.

CHAPTER III

CHAPTER III.

Characterization of Electrochemical Properties of Intermediate and High Temperature Micro-tubular SOFCs

Summary

3.1. Introduction	3
3.2. General chemical principles	4
3.2.1. Thermodynamics	4
3.2.2. The oxidation steps.....	6
3.2.3. Reforming reactions and Carbon forming reactions	7
3.2.4. Catalytic activity	9
3.2.5. Steam Reforming on nickel catalysts	9
3.2.6. Support media for steam reforming catalysts.....	10
3.2.7. Methane Steam Reforming on nickel catalysts	11
3.2.8. Carbon formation and deposition.....	14
3.2.9. Filamentous Carbon formation.....	16
3.2.10. Graphitic (encapsulating) carbon formation	18
3.2.11. Additives and promotional effects (Cerium Oxide).....	19
3.3. Materials for SOFCs fabrication.....	20
3.3.1. Ceria Based Electrolytes	20
3.3.2. Anode materials.....	22
3.3.3. Operation of Anodes with Fuels other than Hydrogen	25
3.4. Fabrication Techniques for Tubular Solid Oxide Fuel Cells.....	26
3.4.1. Introduction	26
3.4.2. Formulation and Process Additives.....	28
3.4.3. Ceramic Powder	29
3.4.4. Liquid	30
3.4.5. Binders	30
3.4.6. Lubricant	33

3.4.7.	pH Control Agent	34
3.4.8.	Processing.....	34
3.4.9.	Mixing	35
3.4.10.	Die Design and Extrusion	36
3.4.11.	Cutting and Extrudate Handling.....	39
3.4.12.	Drying.....	39
3.4.13.	Sintering	39
3.4.14.	Thin Film Application	41
3.5.	Electrical Fuel cell characterization	43
3.5.1.	Current-Voltage Measurement.....	43
3.5.2.	Electrochemical Impedance Spectroscopy.....	44
3.6.	Experimental analysis of micro-tubular fuel cell's performance	57
3.6.1.	Solid Oxide Fuel Cells Test Stand	57
3.6.2.	Fabrication Process	65
3.6.3.	Experimental Results of the smaller micro-tubular SOFC test.....	72
3.6.4.	Effect of flow rate on SOFC's electrochemical performance at different temperature.	73
3.6.5.	Effect of temperature on SOFC's electrochemical performance at different flow rate	78
3.6.6.	Effect of temperature and flow rate on Open Circuit Voltage, Current and Power Density supplied by the SOFCs.....	81
3.6.7.	Efficiency and fuel utilization	85
3.6.8.	Electrochemical Impedance Spectroscopy measurement (EIS).....	89
3.6.9.	Electrochemical performance with different fuels	92
3.6.10.	Experimental Results of the bigger micro-tubular SOFC test.....	98
3.6.11.	Effect of temperature on SOFC's electrochemical performance at different flow rate.	100
3.6.12.	Effect of temperature and flow rate on Open Circuit Voltage, Current and Power Density supplied by the SOFCs.....	103
3.6.13.	Efficiency and fuel utilization	106
3.6.14.	Conclusion.....	107
3.7.	References	109

3. 1. Introduction

Solid Oxide Fuel Cell applications have long been limited by the necessity to operate at high temperatures, causing prolonged start up times and materials constraints, among other cost increasing constraints [1-3]. Considerably decreasing the operating temperature of SOFCs seems an absolute necessity for efficient power production specifically in mobile applications where start up time and materials cost is of increasing importance. Reducing the operating temperature of SOFCs below 650°C can extend the lifetime of the SOFC stack, lower cost by allowing the use of metal materials, and can decrease the degradation of SOFC and stack materials [4,5]. Tubular SOFC designs have been shown to be stable for repeated cycling under rapid changes in electrical load and in cell operating temperatures [6-8]. Micro-tubular SOFCs have also been shown to be able to endure the thermal stresses associated with rapid heating up to operating temperatures [9,10]. In contrast to planar SOFC designs, when the diameter of tubular SOFC is decreased, it is possible to design SOFC stacks for high volumetric power densities [1,11].

In this chapter are reported the main results of the experimental analysis conducted on micro-tubular solid oxide fuel cells tested at the Colorado Fuel Cell Center (CFCC) and at the Colorado Center for Advanced Ceramics (CCAC) of the Colorado School of Mines (Golden, CO – U.S.A.).

The experimental activities are part of a research program that focused on the analysis of the energetic performance of single tubular solid oxide fuel cells manufactured and tested in laboratory. The research program allowed analyzes the energetic performance of different SOFC operating at different temperatures and fed with different volume flow of gas entering the fuel cell. Furthermore, has been analyzed the behavior of the fuel cells when fed with different types of gas (hydrogen, methane, synthesis gas, etc.).

In particular, we were able to analyze the energetic performance of anodic supported tubular SOFCs, with a cermet anode made of a mixture of NiO (Nickel Oxide) and YSZ (Yttria Stabilized Zirconia), with a YSZ electrolyte and a cathode made of LSM (Strontium - doped Lanthanum Manganite). These cells were tested at operating temperatures ranging from 750 °C to 850 °C.

Subsequently we have analyzed the energetic performance of anodic supported micro-tubular SOFCs with a cermet anode of NiO and GDC (Gadolinium Doped Ceria), a GDC electrolyte and a cathode in LSCF ($\text{La}_{0.6}\text{Sr}_{0.4}\text{Co}_{0.2}\text{Fe}_{0.8}\text{O}_{3-y}$). These cells were tested at operating temperatures ranging from 450 °C to 550 °C.

Before to describe the main results of the experimental activities conducted at the laboratories of the Colorado School of Mines, in the next sections will be reported fundamental information about:

- chemical reaction that happen during the fuel cells operation when fed with hydrocarbon fuels, with particular attention to the carbon deposition phenomena;
- the typical materials used in the fabrication of fuel cells and the possibility to use different material that allow higher performance guaranteeing better resistance at the carbon deposition phenomena;
- the fabrication processes adopted for the construction of tubular fuel cells underlining the main parameter that should be controlled in order to obtain a better final result.

Subsequently will be shortly described the theory that governs the Electrochemical Impedance Spectroscopy (EIS) technique in order to measure experimentally the main losses present in the fuel cells operation (ohmic and activation polarization).

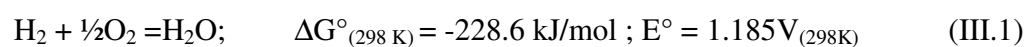
After the introduction of the themes listed above, will be finally presented the performance of the fuel cells (I-V curves, power curves, efficiency curves, etc.) and the EIS results, for a complete energetic performance analysis.

3.2. General chemical principles

In the next paragraphs will be shortly described the major chemical reaction that occurs on the anode surface of a solid oxide fuel cells when is fed with light hydrocarbon fuels, as methane, with particular attention at the carbon deposition phenomena that could occur at high temperature [13].

3.2.1. Thermodynamics

In the case of a fuel cell running on hydrogen the process is reasonably simple and straight forward, hydrogen is oxidized to produce water and electrical power.



For a SOFC running at an elevated temperature of 850°C (1123K), these values change slightly to: $\Delta G^\circ_{(1123\text{K})} = -179 \text{ kJ/mol}$ and $E^\circ = 0.928 \text{ V}_{(1123\text{K})}$. There are no side reactions, the reaction step is also the power production step and the reaction is well away from equilibrium and, therefore, goes to completion.

Things are not so simple for a fuel cell utilizing methane. The reaction mixture is a more complicated and leads to a series of at least 10 major reactions which can be happening, particularly at the elevated temperatures within a SOFC. A summary of these reactions is given below¹:

Reaction	$\Delta G^\circ_{(298\text{K})}$ [kJ mol ⁻¹]	$T_{\Delta G=0}$ [K]	$\Delta G^\circ_{(1123\text{K})}$ [kJ mol ⁻¹]
1. $\text{CH}_4 + 2\text{O}_2 = \text{CO}_2 + 2\text{H}_2\text{O}$	-800.9	154,3	-796.5
2. $\text{CH}_4 + \frac{1}{2}\text{O}_2 = \text{CO} + 2\text{H}_2$	-86.5	210	-277
3. $\text{H}_2 + \frac{1}{2}\text{O}_2 = \text{H}_2\text{O}$	-228.6	5.4	-179
4. $\text{CO} + \frac{1}{2}\text{O}_2 = \text{CO}_2$	-257.2	3.3	-186
5. $\text{CH}_4 + \text{CO}_2 = 2\text{CO} + 2\text{H}_2$	+170.7	963	-41
6. $\text{CH}_4 + \text{H}_2\text{O} = \text{CO} + 3\text{H}_2$	+142.1	960	-35
7. $\text{CO} + \text{H}_2\text{O} = \text{CO}_2 + \text{H}_2$	-55.3	955	+6
8. $\text{CH}_4 = \text{C} + 2\text{H}_2$	+50.7	926	-16
9. $\text{CO} + \text{H}_2 = \text{C} + \text{H}_2\text{O}$	-91.4	981	+19
10. $2\text{CO} = \text{C} + \text{CO}_2$	-120.5	980	+25

Table III. 1: ΔG° at 298 K and at 1123K and the equilibrium temperature for the major reactions of a SOFC powered by methane.

Note that the ΔG° 's of reaction at 1123K and the $T_{\Delta G=0}$ have been calculated from the thermodynamic data at 298K assuming that ΔH and ΔS are independent of temperature, as there is no phase change assumed, this should be reasonable, at least for a first approximation,

¹ Data taken from The Open University Data book – S247 Inorganic Chemistry: Concepts and Case Studies

in particular for the ΔS term. Throughout it is assumed that the lower heating value is operating due to the elevated operating temperatures of solid oxide fuel cells, i.e. the temperature is well above 100°C therefore the water remains as steam and the heat of condensation is not released.

At 298K this amounts to an energy release of -8.5 kJmol^{-1} of water condensing from steam. These reactions can be conveniently split into four groups, although there is some overlap between them.

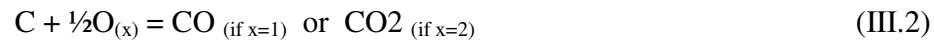
3.2.2. The oxidation steps

The oxidation steps are reactions 1-4 in table III.2. These reactions are the only ones which can produce a current within a SOFC as the electrons are carried through the cell by O^{2-} , completing the circuit. As can be seen from table III.1 all these reactions are favorable at room temperature (298K) and at the elevated temperatures at which most SOFC's operate (1123K). As these reactions contribute to the electrical power of the cell, to this end it is worth looking at the standard electrode potentials:

Reaction	$\Delta E^\circ_{(298\text{K})}$ [kJ mol ⁻¹]	$\Delta E^\circ_{(1123\text{K})}$ [kJ mol ⁻¹]
1. $\text{CH}_4 + 2\text{O}_2 = \text{CO}_2 + 2\text{H}_2\text{O}$	1.038	1.032
2. $\text{CH}_4 + \frac{1}{2}\text{O}_2 = \text{CO} + 2\text{H}_2$	0.448	1.176
3. $\text{H}_2 + \frac{1}{2}\text{O}_2 = \text{H}_2\text{O}$	1.185	0.928
4. $\text{CO} + \frac{1}{2}\text{O}_2 = \text{CO}_2$	1.333	0.964

Table III. 2: ΔE° values for the oxidation steps at 298 and 1123K.

All these reactions predict a standard electrode potential of around one volt for SOFC's running at temperatures of 850°C. Previous work suggests that the direct oxidation of methane (reactions 1 & 2) does not usually contribute to the power production of the cell leaving steps 3 & 4 as the power producing reactions. Thus reactions which produce hydrogen and carbon monoxide will indirectly contribute to the cell's electrical power production and efficiency. Although not a direct oxidation step, it is possible that as carbon is deposited within a fuel cell (reactions 8, 9 and 10), the carbon formed can then be oxidized to carbon monoxide and carbon dioxide:



3.2.3. Reforming reactions and Carbon forming reactions

Reactions which convert methane into the more usable hydrogen and carbon monoxide are known as reforming reactions. These are reactions 2, 5 & 6:

2. $CH_4 + \frac{1}{2}O_2 = CO + 2H_2$ - partial oxidation (or air reforming)
5. $CH_4 + CO_2 = 2CO + 2H_2$ - carbon dioxide reforming (or dry reforming)
6. $CH_4 + H_2O = CO + 3H_2$ - steam reforming

As a byproduct of some of the reactions shown in table III.2, from reactions 8, 9 & 10, carbon is formed, which if severe enough can block the small diameter tubes causing the system to fail:

8. $CH_4 = C + 2H_2$
9. $CO + H_2 = C + H_2O$
10. $2CO = C + CO_2$

As can be seen from table III.1 reactions 9 & 10 become thermodynamically less favorable as the temperature increases and become more unfavorable above 981K. Unfortunately reaction 8 becomes more favorable with increasing temperature and is thermodynamically favorable above 926K.

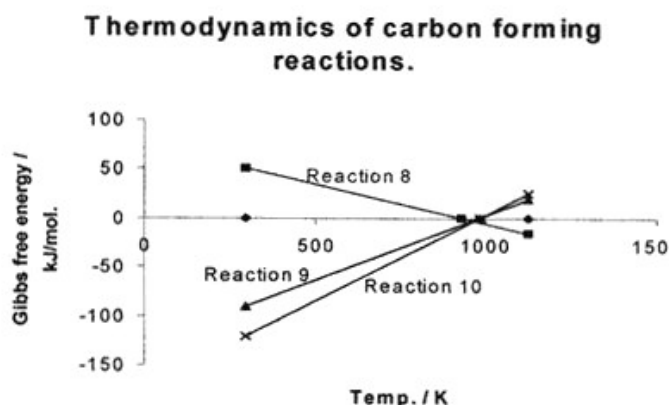


Figure III. 1: Effect of temperature on the Gibbs free energy of reaction of the carbon forming reactions.

Thus from a thermodynamic point of view, at no point are all the coking reactions unfavorable so temperature control alone cannot prevent the deposition of carbon. Even at temperatures below 926K the pyrolysis of methane to carbon can be significant. It should be remembered that even when ΔG is positive this is only a statement of equilibrium and some pyrolysis should be taking place, kinetics allowing. As one of the reaction products is solid (*i.e.* carbon) then it is effectively removed from the reaction mixture pulling the equilibrium over to the right:



Thus, even when the ΔG of reaction is positive, carbon formation can take place by pyrolysis. Certain possibilities to reduce carbon formation are suggested by table III.1, such as an increase in carbon dioxide levels to push reaction 10 further to the left. Another possibility resides in the fourth class of reaction, the water gas shift reaction. This reaction is important as it is a means of converting a carbon rich fuel (CO) into 'cleaner' hydrogen fuel:



This also has the bonus of removing carbon monoxide from reaction 9 and producing carbon dioxide, pushing reaction 10 to the left. Past work suggests that SOFC's are better able to utilize hydrogen as a fuel source, rather than carbon monoxide. So again this reaction is useful

for the running of a tubular SOFC. This reaction becomes thermodynamically unfavorable above 955K which is below the operating temperatures of HighTemperature-SOFC's (1000-1400K). Under cell operating conditions the hydrogen should be removed in the power production step (reaction 3) and water produced. This will unbalance reaction 7 such that, by LeChatelier's principle, the reaction will be driven to the right producing more hydrogen and carbon dioxide.

3.2.4. Catalytic activity

The catalytic activity of the cermet anode in a SOFC can be a major determining factor in the overall performance of the cell. The catalytic activity of the anode material used can influence the type of fuels that can be processed by the cell, the temperature at which the cell is operated, and the active lifetime of the cell. One of the major concerns with the long-term operation of SOFCs is the deactivation of the nickel anode either by sintering, poisoning by sulphur (when running on natural gas) and the formation of carbonaceous deposits (when using hydrocarbon fuels) [15,16].

3.2.5. Steam Reforming on nickel catalysts

In recent years supported nickel catalysts have been commonly used in industrial steam reforming, i.e. the reforming of methane to produce syngas (CO and H₂), which is very important to the chemical industry for the production of ammonia and methanol, and hydrogen for refineries, hydrogenation reactions and fuel cell applications [17]. Nickel has been recognized as probably the most suitable metal for the steam reforming of hydrocarbons for many years. Other metals have shown comparable and even high activity for steam reforming, these include Co, Pt, Pd, Ru and Rh. Some of the precious metals mentioned show much higher activity per unit weight than Ni, but Ni is much cheaper and has sufficient activity to provide a more economic option [18].

Unfortunately the reforming of hydrocarbons over nickel catalysts leads to carbon deposition [19, 20, 21], which in time deactivates the catalyst and renders it inactive. Sintering of the catalyst and metal-support interactions can also cause deactivation. Therefore one of the most important properties of a steam reforming catalysts is resistance to coking, leading to higher stability [22].

The recent trend in the steam reforming industry has been to reduce the steam to carbon ratio, in the reactant stream. This brings considerable economic advantages as energy is not wasted

heating excess water to provide vapour to the reformer and lower water content produces less CO₂ as a by-product. Unfortunately the lower ratio mixes encourage the formation of surface carbon on the catalyst [23].

An alternative which has generated interest is the use of CO₂ instead of water [24]. The reasons for this are twofold, the first, being that reforming with CO₂ yields a more desirable (lower) H₂/CO ratio in the syngas produced [25]. Lower H₂/CO ratios are better suited to the processes involved in methanol synthesis and other hydrocarbons. Secondly there may be considerable environmental benefit to be gained from producing a useful product from a known greenhouse gas [26]. Reforming with CO₂ may present a variety, of benefits, but it does suffer from one major flaw, namely the increased production of carbon which rapidly deactivates the catalyst during reforming. The increased rate of degradation is particularly marked in nickel catalysts [26].

One of the attractive features of SOFCs is their ability to oxidize methane efficiently without the need for an external reformer, but the problem of carbon deposition must be fully overcome for this to be economically viable. As mentioned above the nickel surface in Ni/YSZ anode can catalyze the steam reforming reaction in a similar way to the previously mentioned industrial catalyst.

3.2.6. Support media for steam reforming catalysts

The main objective of the catalytic steam reforming process is to extract the maximum amount of hydrogen from the water and the hydrocarbon being reformed. To achieve this objective a highly sintered, porous refractory oxide catalyst carrier, containing SiO₂ and/or Al₂O₃ is commonly used to support the nickel metal [24]. The main advantages of these supports are their high thermal and hydrothermal stability, accompanied by their mechanical strength. As a result of these properties these supports are the most commonly used in the catalytic conversion of hydrocarbons and also for catalysts used in a variety of extreme reaction conditions such as high temperature, steam environments and processes involving rapid temperature changes [27]. The choice of which support should be used is generally governed by the surface area required and the needs of stability in the chosen environment.

The most stable support material is α -alumina, which is ideally suited to the high temperature and steam rich environments of reforming [18]. Unfortunately the specific surface area of this support can be low and hence the specific activity of catalysts on this support tends to be low.

For higher specific activities different preparative methods can be employed producing, for example, γ -alumina as the support medium. This form of alumina is however thermodynamically less stable than the α form and at high temperature and high steam partial pressures the support converts to the α form. This hydrothermal sintering changes the microstructure of the catalyst and hence leads to the degradation of the catalyst's activity [18]. When these supported nickel catalysts are used at high temperature solid-solid interactions have been observed. The nickel or nickel oxide in the catalyst reacts with the support medium (Al_2O_3 or SiO_2), leading to nickel-aluminate (spinel) and nickel-silicate phases which are catalytically inactive with regard to the reforming of methane. These species are also thermally stable and hard to reduce, so the catalyst cannot be easily regenerated [27, 28]. In the case of fuel cells the nickel is supported on zirconia. With these compounds, solid-solid interactions, a higher nickel reduction temperature and deactivation of the catalyst at high temperature have been all observed.

Industrial Ni reforming catalysts supported on $\text{TiO}_2/\text{Al}_2\text{O}_3$ show a significant decrease in catalytic surface area due strong interaction with the support. This could be of considerable relevance to SOFCs as the nickel is supported on zirconia which is in the same periodic group as titanium and thus can be considered to have reasonably similar properties. This contributes to the observed deterioration of the nickel cermet anodes on cycling.

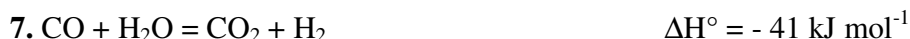
Another effect that must be taken into consideration is the acidic nature of the reactant gases. It is thought that a basic catalyst or support medium may well activate the adsorption of the reactant gases and prompt dissociation on the catalyst, hence increasing the reforming ability of the catalyst.

3.2.7. Methane Steam Reforming on nickel catalysts

When a mixture of methane and steam is passed over a nickel catalyst at high temperature, typically over 773 K, whether it is a traditional industrial catalyst or the Ni/YSZ cermets used in SOFCs, steam reforming occurs (reaction 6.). The reforming reaction is strongly endothermic and thus the high operating temperatures found in SOFCs favor the Steam Reforming Reaction (SMR). Decreased pressure will also enhance the reaction [13].

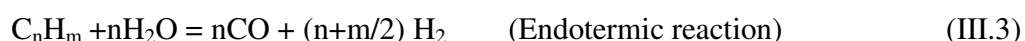


The nickel surface is also known to catalyze the Water Gas Shift reaction which enables the adjustment of the molar ratio of the gases presents (reaction 7.). Both reactions (6.) and (7.) are reversible.



The Water Gas Shift reaction is an exothermic reaction and is therefore promoted by low temperatures, but it actually is relatively unaffected by temperature. Reactions (6.) and (7.) are usually at equilibrium as the reaction rates are very fast. In the industrial process steam is usually added in excess of the stoichiometric requirement of reaction (6.); a steam to carbon ratio of 1.4:1 is common [29]. This excess of steam pushes reaction 2 towards H₂ and CO₂ production. Although the excess steam does pose economic problems as mentioned above it does in fact promote reaction (6.) hence giving a higher conversion rate. The water gas shift (WGS) reaction may be more important in SOFC applications as it increases the H₂ to CO ratio enhancing the fuel cell's performance. The WGS reaction alone eliminates a large part of the energy losses associated with the activation overpotential of the anodic reaction. This reaction is almost thermoneutral and is known to be promoted by doping the catalyst with alkali metals such as potassium [30, 31].

Natural gas is known to contain a small percentage of higher hydrocarbons as well as methane. These can, in principle, be reformed with steam at high temperatures in an analogous way to methane as shown in reaction (6.).



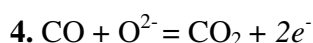
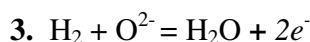
Using methane, and hence natural gas, as a fuel has its problems, the main one being the deposition of carbon on the anode during reforming. Under the operating conditions industrial steam reforming catalysts and SOFCs carbon deposition is thermodynamically favourable [29]. Carbon deposition on the anode is thought to occur via a variety of mechanisms which will be discussed in more detail in the next section [30, 32]. The principal routes to carbon deposition are the Boudouard reaction (reaction 10.), the catalytic methane decomposition (reaction 8.) and the direct reduction of CO species at the nickel surface (reaction 9.).

Carbon deposition can be limited, by adjusting the fuel mixture supplied to the reforming catalyst or SOFC anode. For maximum cell performance and minimum Cost, H₂O partial pressures p_{H₂O} must be kept low. However, unfortunately these conditions promote carbon deposition causing degradation of the industrial catalyst and destroying the anode in SOFCs. High p_{H₂O} give little or no carbon deposition, but due to the high p_{H₂O} in the fuel the cell performance is inhibited and the extra cost of producing water vapour makes this industrially unfavourable. Furthermore, when the p_{H₂O} increases, competitive adsorption of CH₄ as C(ad) and H₂O as OH(ad) becomes a problem [33]. In addition increased steam levels promote the sintering and even partially oxidize the nickel surface. These reactions lead to deactivation of the anode and hence loss of performance.

The steam reforming reaction may not be the only reaction route for the conversion of methane at the cermet surface. Methane partial oxidation (reaction2.) is also feasible as there is an oxygen ion supply to the anode and the operating temperature of the fuel cell makes the reaction thermodynamically possible [30, 32].



The reaction of CH₄ and O₂ at high temperatures (>973 K) principally yields H₂, CO, CO₂ and H₂O through partial and total oxidation. The ratios of these products can be altered by adjusting the reaction conditions [32]. With some catalysts and under certain reaction conditions, oxidative coupling to form C₂H₆ and C₂H₄ can occur [33, 34]. It has been observed that selectivity for H₂ and CO production increases with operating temperature, and methane conversion rates of 90% and selectivity > 90% to syngas can be achieved above 1000 K [32]. The products from the reforming reactions can be readily electrochemically oxidized at the catalytic three phase boundary (TPB), through the reaction (3.) e (4.).



Little is known about the kinetics of steam reforming on Ni/YSZ cermets but it is hoped that knowledge of the kinetics may help optimization of anode design in the future. Another problem that can arise with steam reforming is large temperature gradients along the anode.

As noted above the steam reforming reaction is endothermic. This can cause the anode at the fuel inlet to cool, severely inhibiting electrochemical performance, and setting up potential differences across the anode itself, as the conductivity of the anode is dependent on temperature [35]. The partial pressure of water present in the reaction stream has also been shown to influence the electrochemical performance of the SOFC [35].

3.2.8. Carbon formation and deposition

One of the major problems associated with the steam reforming of hydrocarbons over nickel based catalysts is that of carbon deposition. Hydrocarbons that are introduced to the catalyst at the operating temperatures involved will spontaneously decompose to form surface adsorbed carbon and gaseous hydrogen, via reaction (8.) in the case of methane.

This reaction is referred to as thermal cracking or methane decomposition [17]. The introduction of steam into the reactant stream inhibits this reaction, reducing carbon deposition and promoting the methane steam reforming process. The steam reforming process does however have associated side reactions, especially when the steam to fuel ratio is less than stoichiometric [17]. The Boudouard reaction (10.) is a disproportionation of CO. This reaction is also catalysed by nickel at high temperatures. This reaction can be controlled by manipulation of feed gases. As water content is increased the WGS reaction favors the production of CO₂ thus inhibiting the Boudouard process as stated earlier. The other possible route for the formation of surface carbon is the direct reduction of CO species at the nickel surface (reaction 9). This reaction is also inhibited by the addition of steam [17].

The carbon deposited during these reactions can, over time, deactivate the catalyst and render it useless for its intended purpose. This observed deactivation can be caused by:

- i. Fouling of the metal surface;
- ii. Blocking of active catalytic sites;
- iii. Destruction of the catalyst support.

The deactivation of the catalyst by any one of these mechanisms can occur rapidly in unfavorable conditions. Thus the need for understanding of these processes is of major importance [36]. Surface carbon and coke are defined conventionally by the origin of the carbon deposit. The decomposition of hydrocarbons such as methane (reaction 8.) leads to the formation of cokes, whereas, the disproportionation of CO (reaction 10.) gives carbon [36].

The nature of coke deposits on a catalyst can vary from graphite species to high molecular weight hydrocarbons, according to the reactions conditions the coke was deposited under [37, 38].

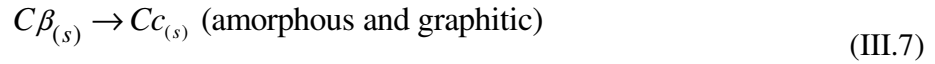
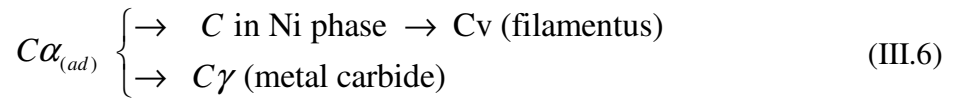
The high temperatures involved in steam reforming could potentially lead to gas phase reactions producing carbonaceous intermediates, which then condense onto the catalyst surface to form coke. These reactions rely on free radical polymerizations to occur in the gas phase, which can easily be controlled by the addition of water to the gas phase [37].

The vast majority of coke formation occurs at the catalyst surface. Carbonaceous deposits can be divided into three main types: amorphous, filamentous and encapsulating graphitic structures [38, 39]. Amorphous carbon is thought to be formed via condensation and polymerisation reactions, and is the product of thermal processes during steam reforming. There is a possibility that this deposit has significant hydrogen content, however, as the reaction temperature is increased the associated hydrogen content will decrease as dehydrogenation reactions become more thermodynamically favorable [38]. The formation of filamentous and graphitic carbon forms has been the subject of much discussion and is now thought to proceed only in the presence of a catalyst.

Early studies by Rostrup-Nielsen concluded that during steam reforming three different carbon species were formed, the aforementioned filamentous carbon was formed above 723 K, encapsulating hydrocarbon films formed below 773 K which dehydrogenate at higher temperatures and pyrolytic carbon above 873 K [39]. However, one of the main products of steam reforming is CO which will interact with the nickel surface to produce further carbon [40].

Carbon deposits from both the steam reforming reaction and the decomposition of CO and other carbon containing species may involve the generation and transformation and ageing of several different carbon species. There are several carbon species that must be considered within the system; the possible carbon species that may be formed during steam reforming are shown in reactions III.4-7.





At higher temperatures $C\alpha$ is more rapidly converted to $C\beta$ favouring the formation of amorphous carbon structures. A further increase in the reaction temperature will eventually see the conversion of $C\beta$ to Cc or graphitic carbon. Low density filamentous carbon and graphitic species have both been observed at elevated reaction temperatures. However it must be noted that prolonged exposure to higher temperatures can, make the filaments and amorphous film species become more graphitic [36].

3.2.9. Filamentous Carbon formation

The formation of filamentous carbon is fairly well understood. Decomposition and dissociation of hydrocarbons on the nickel surface of a steam reforming catalyst, produces an extremely reactive atomic carbon species ($C\alpha$). Due to the reactivity of this species most of the $C\alpha$ is gasified during the steam reforming reaction. The $C\alpha$ that is not gasified can be converted, probably via polymerization and rearrangement steps, to the less reactive $C\beta$ species. This less reactive species may then again be gasified or it may encapsulate the surface or dissolve into the bulk nickel phase of the catalyst [38].

It is the dissolved carbon that causes the growth of the observed filament structures. During the steam reforming reaction, methane is decomposed on specific faces, in this case the (100) and (110) planes of nickel. The carbon atoms then diffuse through the nickel phase to the (111) plane where nucleation and precipitation occurs [41]. This process leads to the formation of a fibrous structure, which eventually lifts the nickel particle from the support surface resulting in fragmentation of the catalyst.

The driving forces for the diffusion of dissolved carbon through the nickel particle to the depositing crystal face is not entirely clear [42]. It has been proposed that the diffusion of carbon is driven by a difference in solubility of carbon at the gas/metal surface and the filament/metal interface. A second proposed driving force for the diffusion of carbon in the

metal particle is a difference in temperatures of the relevant crystal faces, resulting from their different activities in hydrocarbon decomposition [43].

The rate determining step in the formation of filamentous carbon is the diffusion of carbon through the metal phase. Different catalysts and reaction conditions can produce a variety of filament structures with varying morphologies and degrees of crystallinity [38]. The gas composition that the nickel surface is exposed to has been shown to influence the formation of carbon filaments. Carbon filaments formed in pure methane conditions are usually small diameter dense structures with a globular nickel head, whereas filaments formed in a hydrogen/methane mixed reactant gas are wider and porous and the nickel head is clearly a faceted structure.

The temperature at which the filament is formed has also been shown to have a considerable effect on the structure of the end product [42]. Filaments formed at low temperatures tend to have a solid dense wishbone like structure, whereas filaments deposited at higher temperatures tend to have a hollow structure [42]. This can be explained in terms of the rate of carbon diffusion and nucleation. At lower temperatures the rate of nucleation is slower than the rate of diffusion so carbon is excreted uniformly along the metal/support interface. However, at high temperature, nucleation is rapid and is much faster than the rate of carbon diffusion through the nickel. Therefore, nucleation and filament growth occurs where the diffusion rate is at its fastest, i.e. the shortest distance between gas/metal interface and filament/metal interface. This leads to the formation of a hollow filament as no carbon is formed where the diffusion path lengths are long [42].

Work by Baker et al. [38] has suggested that the actual shape and crystallinity of the filamentous carbon produced during reaction is directly related to the crystallographic orientation of the metal surface that the filament is formed on. Filamentous carbon formation favors small well dispersed metal particles. Crystallites with grain diameters less than 0.5 μm will typically support filament growth [43, 44]. Therefore a catalyst with larger grain sizes and lower dispersity would show a much higher resistance to filament carbon formation and may not form any at all [43].

The formation of filamentous carbon causes physical destruction of the catalyst via fragmentation. As the unit volume of the catalyst increases pressure builds up in the catalyst bed. However, the rate of steam reforming over the catalyst may not change at all, as

the catalytically active nickel sites may not be blocked by filamentous carbon [45]. Filamentous carbon has several interesting properties; high absorbability, corrosion resistance, magnetic and electro physical properties. Due to these properties it is widely used in chemical, electronic, electrical and other industries [46]. Filamentous carbon has also been assessed as a catalyst support [41], where it was suggested that the rough nature of the carbon filaments provides extra active sites for catalysis to occur.

3.2.10. Graphitic (encapsulating) carbon formation

The basic mechanism for the formation of graphitic encapsulating carbon is not less important than the formation of filamentous carbon. Encapsulating carbon is in fact more catalytically deleterious, because, as its name suggests, it covers and surrounds the nickel particles thus reducing the catalytically active area of the catalyst, causing rapid degradation. It has been suggested that the mechanism for the growth of this type of carbon follows to an extent that of filamentous carbon, i.e. the decomposition of a hydrocarbon at one surface of the metal particle, then the diffusion of carbon through the bulk nickel phase to another crystal face where deposition occurs. The only difference being the relative amount of reactive and depositing faces on the crystal [38]. A factor which may play a part in the formation of the graphitic carbon is diffusion of carbon over the metal surface rather than just through the bulk. This has already been shown by Shaikhutdinov et al. [41] to influence the structure of filamentous carbon.

This form of carbon tends to be formed when the concentration of methane in the reactant phase is high [38]. The thickness of the observed shell structures required before total catalyst deactivation occurs is usually about 30 graphite layers. The actual mechanism for the formation of these shell structures has not been defined. However, work by Baker et al. has suggested two possible routes for formation [38]. The first of these assumes that during the precipitation and nucleation of carbon steps the nickel particle undergoes a progressive transformation in geometry whilst maintaining a constant volume. As the decomposition of methane continues, carbon migrates to the deposition face where it forms graphite. As decomposition and migration continue more carbon is deposited but the initial graphite deposit limits the available volume expansion. Therefore the only way that the decomposition and deposition can continue is if the particle shrinks in width and becomes taller. This however

reduces the active surface area of the catalyst which may account for the observed degradation [38].

The second proposed mechanism is a variation on the first. In this case the progressive modification of the catalyst particle's shape is accompanied by an overall decrease in volume. This loss of volume may be due to the formation of a strong interaction between the metal and graphite, leading to the metal wetting the surrounding carbon structure leaving monolayer coverage on each successive graphite edge [38].

3.2.11. Additives and promotional effects (Cerium Oxide)

The properties of a catalyst can be enhanced by careful preparation and changing the reaction environment, but the simplest way to enhance a catalyst is the introduction of additives or promoters [23]. Industry has utilized considerable resources in developing steam reforming catalysts which are resistant to coke formation at or near stoichiometric reaction ratios. Sulphur passivated, potassium doped and noble metal catalysts have all shown kinetic resistance to coke formation. However, high cost of materials has limited the widespread application of noble metal catalyst [47], but despite lower activities potassium doped catalyst are commonly used. Similarly a major obstacle to the long term feasibility of solid oxides fuel cells as a viable energy source is that of carbon deposition or coking during high temperature reforming of hydrocarbon fuels.

Increases in resistance to coking have been observed after the addition of 3-15 wt% of the oxides of certain metals [23]. These metal oxides include those of uranium, lanthanum and cerium. The introduction of additives can affect both the overall activity of the catalyst and its active surface area [23].

As known the life expectancy of a fuel cell powered by direct internal methane reforming gas is limited to few hours before carbon deposition blocks the cell and causes it to fail. For commercial purposes this situation needs to be dramatically improved.

It is possible to improve the situation by changing the flow rates and running temperature of the fuel cell system but a more perfect solution is to alter the chemistry within the fuel cell by the use of an appropriate catalyst.

The chemistry within a methane reforming fuel cell is complex with 10 major reactions taking place (Table III.1). This chemistry needs to be fine tuned to the fuel cells advantage. This can be achieved by one of 2 major ways:

- 1) Improve the rate of the reforming reactions, leaving less methane available for pyrolysis or other carbon forming reactions;
- 2) Lower the rate of the carbon forming reactions.

The main drawback with the use of nickel as a reforming catalyst is that it also promotes the formation of carbon. This leads to attempts to modify the nickel with various dopants to either increase the reforming reactions or decrease the carbon forming reactions. The attempts to decrease the carbon forming reactions usually revolve around lowering the activity of the nickel, which affects the carbon forming reaction more than the reforming reactions [48, 49].

Many different metal and metal oxide dopants have been employed to improve the reforming reactions catalytically and limit carbon deposition during methane reforming [50, 51]. One of the more commonly used *additive* to nickel is cerium oxide (ceria) [52-56]. Cerium oxide (ceria) is an excellent catalyst for oxidation reactions [57] both through its ability to exist in 2 reasonably stable electronic configurations, and also by its ability to donate and accept oxygen.

3.3. Materials for SOFCs fabrication

Yttria-Stabilised Zirconia (YSZ) represents the most favored electrolyte for SOFCs even though other oxide ion conductors seem to have better performance. These other oxides show disadvantages that need to be resolved in order to replace YSZ [14].

Ceria based electrolyte seem to have higher electrolyte conductivity and moreover, when ceria is used as anode dopant, show higher resistance at the carbon deposition phenomena. Furthermore this fuel cells operating at intermediate temperature show lower start up time, extending the lifetime of the SOFC stack, reducing cost by allowing the use of metal materials, and decreasing the degradation of SOFC and stack materials [14].

3.3.1. Ceria Based Electrolytes

The electrolyte for solid oxide fuel cells (SOFCs) must be stable in both reducing and oxidizing environments, and must have sufficiently high ionic with low electronic conductivity at the cell operating temperature. In addition, the material must be able to be formed into a thin, strong film with no gas leaks. Until now, Yttria-Stabilised Zirconia (YSZ),

has been the most favored electrolyte for SOFCs. Other oxide ion conductors, such as doped ceria, have also been proposed as the electrolyte materials for SOFCs, especially for reduced temperature operation (600—800°C).

Oxide ion conductivity was first observed in ZrO_2 containing 15 wt% Y_2O_3 (yttria-stabilised zirconia or YSZ) by Nernst [14] in the 1890s. Since that time, many oxide systems have been examined as potential electrolytes for SOFCs. Figure III.2 shows the temperature dependence of the ionic conductivity for several oxides, indicating that YSZ is by no means the best oxide ion conductor.

Several other formulations of oxide compositions show higher conductivity than YSZ, particularly at temperatures below 600°C [14].

However, these other oxides have disadvantages such as electronic conductivity, high cost, or difficulties in processing. Particularly, doped ceria has been suggested as an alternative electrolyte for low temperature SOFCs [14]. Reviews on the electrical conductivity and conduction mechanism in ceria-based electrolytes have been presented by Mogensen et al. [14] and Steele [14]. The conductivity of doped ceria systems depends on the kind of dopant and its concentration.

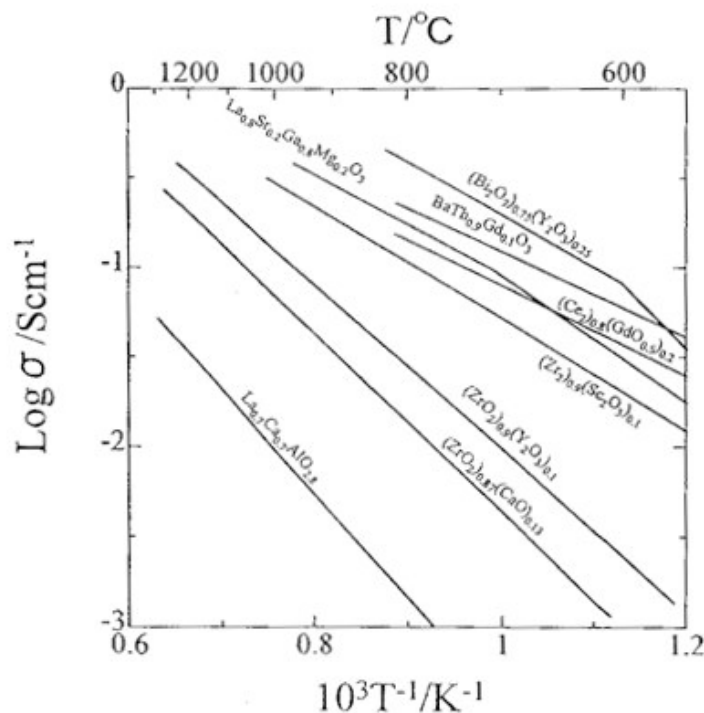


Figure III. 2: Temperature dependence of electric conductivity for selected oxide ion conductors.

In Table III.3, the conductivity data for doped ceria are summarized. CeO₂-Gd₂O₃ and CeO₂-Sm₂O₃ show an ionic conductivity as high as 5×10^{-3} S/cm at 500°C, corresponding to 0.2 Ω cm² ohmic loss for an electrolyte of 10 μ m thickness. These compositions are attractive for low temperature SOFCs.

	Mol%	Conductivity (S/cm)		Activation energy (kJ/mol)
		700°C	500°C	
Sm ₂ O ₃	10	3.5×10^{-2}	2.9×10^{-3}	68
	10	4.0×10^{-2}	5.0×10^{-3}	75
Gd₂O₃	10	3.6×10^{-2}	3.8×10^{-3}	70
Y ₂ O ₃	10	1.0×10^{-2}	0.21×10^{-3}	95
CaO	5	2.0×10^{-2}	1.5×10^{-3}	80

Table III. 3: Electrical conductivity data for CeO₂-Ln₂O₃

Ceria-based oxide ion conductors are reported to have purely ionic conductivity at high oxygen partial pressures. At lower oxygen partial pressures, as prevalent on the anode side of an SOFC, these materials become partially reduced. This leads to electronic conductivity in a large volume fraction of the electrolyte extending from the anode side. When a cell is constructed with such an electrolyte with electronic conduction, electronic current flows through the electrolyte even at open circuit, and the terminal voltage is somewhat lower than the theoretical value.

A SOFC with Ceria-based electrolyte should be operated at temperatures below about 600°C to avoid efficiency loss due to electronic leakage. Successfully ceria based electrolytes have been used in SOFCs operating at 550°C and lower.

3.3.2. Anode materials

The anode must combine catalytic activity for fuel oxidation with electrical conductivity. Catalytic properties of the anode are necessary for the kinetics of the fuel oxidation with the oxide ions coming through the solid electrolyte. Ionic conductivity allows the anode to spread the oxide ions across a broader region of anode/electrolyte interface, and electronic

conductivity is necessary to convey the electrons resulting from the electrode reaction out into the external circuit.

The role of an anode in a solid oxide fuel cell is to provide the sites for the fuel gas to react with the oxide ions delivered by the electrolyte, within a structure which also facilitates the necessary charge neutralization by its electronic conductivity. These functional considerations together with the operating environment of the anode are the key factors in the materials selection for the anode. It must evidently be refractory, given the high cell operating temperature to be sustained over a commercially useful lifetime, and be compliant with thermal cycling to ambient temperature. In addition, the equilibrium between fuel gas and oxidation products within the anode compartment results in an oxygen partial pressure which is very low, but variable over several orders of magnitude depending on the precise reactant and product conditions. Chemical and physical stability despite such variations is essential since certain metallic components of the anode could suffer corrosion by fuel oxidation products, while electrical properties and lattice geometry of oxide components of the anode could change by variation of stoichiometry.

For simplicity and reliability of operation, including start-up and shut-down as well as tolerance of transients, redox stability is a further desirable attribute of an anode material to permit brief excursions to high oxygen concentrations, even to air, without irreversible loss of structural coherence and electrochemical functionality. Stability implies the maintenance of structural integrity of the anode itself over the whole temperature range to which it is exposed, from the fabrication temperature through normal operating conditions, to the repeated cycling down to ambient temperature.

Throughout these ranges of temperature and gas environment there should also be maintained the necessary compatibility with the other materials with which the anode comes into contact, specifically the electrolyte, the interconnect and any relevant structural components. Physical compatibility requires a match of thermo-mechanical properties such as thermal expansion coefficient and an absence of phase-change effects which could generate stresses during temperature variations, For chemical compatibility there should be no solid-state contact reaction, inter-diffusion of constituent elements of those materials or formation of reaction product layers which would increase resistive losses or otherwise interfere with anode functionality, despite the extremes of temperature. After assembly into a series connected

stack, of course the same applies to the anode—interconnect interface. Compatibility must extend also to the behavior of the material towards the ambient gases including corrosion or poisoning by trace impurities such as sulphur.

Obviously the anode material should not only be an adequate electronic conductor, but also electro catalytically active such that a rapid charge exchange can be established. Resistive and over-potential losses are thereby minimized. However, the catalytic behavior of anode materials should not extend to the promotion of unwanted side reactions, hydrocarbon pyrolysis followed by deposition of carbon being an example. The electrochemical reaction takes place in the region where oxygen ions available from the electrolyte can discharge electrons to the conducting anode. This requires gas phase for the fuel access, electrolyte phase for oxide ion entry and metal phase for electron output the so-called ‘three-phase boundary’ zone.

Consequently, the fabrication of the anode is important in determining this complicated three-phase structure.

Given these stringent requirements, only a few metallic or ceramic candidate materials are available. As an alternative to a single-phase metallic or conductive ceramic electrode material, the accepted compromise has been the use of a porous composite of metal and ceramic, a ‘cermet’. In the SOFC anode most commonly used at present, the nickel—zirconia cermet, the primary role of the zirconia is structural, to maintain the dispersion of the nickel phase and its porosity by inhibition of the aggregation and grain growth of the metal and so to achieve an adequate anode lifetime. The adhesion of the zirconia part of the cermet to the electrolyte gives a structural ruggedness able to withstand the thermal stress due to differential thermal expansion, which anyway is lowered in the composite by the ceramic volume fraction. The provision of oxide ion conductivity complementary to the electronic conductivity and electro-catalytic action of the metal is a useful secondary role of the ceramic, enhancing the electrochemical performance by delocalization of the electrochemically active zone already mentioned. However, even as a compromise material the nickel—zirconia cermet does not fulfill all the requirements of an ideal anode. Fuel specification in particular is an important parameter. Most literature results report on hydrogen as fuel, but the commercial imperative requires hydrocarbons. These, however, are rapidly pyrolysed on nickel surfaces at high temperature, depositing a dense carbon which blocks the anode porosity and ultimately

disrupts the structural integrity of the cermet. Therefore the SOFC can be fuelled with gas mixtures rich in hydrogen and carbon monoxide derived from hydrocarbons by partial oxidation or by reforming reactions with steam or carbon dioxide.

There still remains a concern about impurities in the hydrocarbon fuels. Nickel at high temperature is sensitive to sulphur compounds at concentrations even as low as 0.1 ppm. These may occur at source in natural gas, for example, and thiophene and mercaptans are systematically added to it as odorants for safety reasons. Dependent on the origin of the fuel, for example from coal gasification, biomass pyrolysis or fermentation, other impurities may also occur, particularly ammonia and possibly hydrochloric acid. Inorganics may also be found, entrained as dust, which can then react with the ceramic components of the cell giving, for example, silicates.

It is therefore evident that adequate cell performance can only be achieved, and maintained, by careful fuel pre-treatment. Despite these compromises, however, the nickel—zirconia cermet has become the most common anode in SOFC technology.

3.3.3. Operation of Anodes with Fuels other than Hydrogen

The study of hydrogen-fuelled cells has provided essential information on the mechanisms. In the absence of a hydrogen distribution infrastructure, however, practical engineering requires compatibility with hydrocarbon fuels. Natural gas is favored for demonstration units, and interest in other fuels has already been noted. To avoid the growth of carbon on nickel cermet anodes exposed to hydrocarbons, a reforming process, to produce a hydrogen/carbon monoxide mixture, is standard practice.

Reforming of the hydrocarbon fuel does present a balance of plant requirement impacting on investment, maintenance and overall system efficiency, providing an incentive to develop systems and materials capable of sustaining direct oxidation on a fuel cell anode. It has been known for some time that at high current densities, with steam and carbon dioxide being formed electrochemically, and therefore with a higher $P(O_2)$ over the anode, methane can oxidize on a nickel cermet without serious carbon deposition [14]. It is presumed that the oxidation products of the cell reform the incoming fuel, though to maintain a current and therefore a power density above the necessary threshold [14] may not be a practical procedure in commercial operation. Admission of some steam with the fuel, or an autothermal process by partial oxidation, can extend the regime of operation, particularly with a co-catalyst as already

mentioned [14] through this distributed reforming over the anode [14]. However, it is now evident that such a direct oxidation process, without reforming, requires an innovation in anode materials, diverging from the established nickel—zirconia option.

Spacil's alternative transition metals for the cermet, iron and cobalt, though less active for the pyrolysis of hydrocarbons, do not have the corrosion resistance of nickel in a high-steam environment. Considering silver and copper, their oxides either decompose or melt at temperatures below the requirements for cermet sintering; neither are the metals refractory (Ag m.p. 962°C; Cu m.p. 1083°C). However, in catalytic technology the advantages of copper composites with ceria are recognised [14]. Partial reduction of copper oxide when exposed to fuel at elevated temperature, and the resulting redox properties, permit exchange of oxygen between the lattice and the gas phase, with availability for surface reactions. A copper—ceria composite anode [14] is a recent promising initiative. The difficulty of sintering a copper composite was avoided by forming a porous zirconia skeleton on a dense electrolyte substrate of the same material, then introduction of copper and cerium as their nitrate salts in solution, followed by drying and pyrolysis, similar to a procedure already demonstrated for anode and cathode catalysts [14]. Co-insertion of the two cations is possible since copper does not form a solid solution in ceria so the two phases remain separate as required for functionality of the electrode. The performance of cells using this zirconia-supported copper—ceria composite, show that the power density with methane fuel is significantly lower than that with hydrogen. There are also evidence of the stability of the composite anode, in contrast to a nickel cermet where the fuel cell operation is suppressed irreversibly within 30 min by the carbon accumulation. The ceria—copper system is now being further investigated for the direct oxidation of higher hydrocarbons [14].

3.4. Fabrication Techniques for Tubular Solid Oxide Fuel Cells

In this section of the chapter is reported a small overview of the various techniques for fabricating tubular solid oxide fuel cells (SOFCs) with particular emphasis on the ceramic extrusion process. Paste formulation, extrusion die design and thin film technology are also covered.

3.4.1. Introduction

Several ceramic and thin film techniques such as paste extrusion, slip casting, slurry coating, plasma spraying and electrochemical vapor deposition (EVD) have been adapted for tubular SOFC fabrication. When selecting or developing a fabrication technique, processing cost should be one of the major goals. Although the fuel cell stack itself is only about one third of the system costs [58], it is critical that the SOFC developmental activities recognize and address the issue of stack cost. Reducing the cost of cell components and simplifying of the process are important focus of ongoing development. There are two main processes for manufacturing tubular SOFCs (Table III.4): tubular support fabrication technique and thin film application.

Cell Structure	Electrolyte	Anode	Cathode
Electrolyte supported	Extrusion Slip casting	Slurry coating EVD Plasma spraying	Slurry coating EVD Plasma spraying
Anode supported	Slurry coating EVD Plasma spraying	Extrusion Slip casting	Slurry coating EVD Plasma spraying
Cathode supported	Slurry coating EVD Plasma spraying	Slurry coating EVD Plasma spraying	Extrusion Slip casting

Table III. 4: Tubular SOFC Structures and Associated Fabrication Techniques

Hollow ceramic tubes can be fabricated, using slip casting, isostatic pressing, powder pressing or paste extrusion methods. In slip casting, thick slurry is fed into a porous mould and the liquid is withdrawn through the porous surface, thereby forming an item of required shape. Although powder pressing is reproducible, product density is non-uniform and productivity is low. Isostatic pressing offers high and well distributed product-forming pressure but throughput rate is low. In extrusion, shaping occurs by forcing a cohesive plastic material through the orifice of a rigid die. Paste extrusion is particularly suitable for high-speed manufacturing of articles with constant cross section and the process has the following advantages [58]:

- Very complicated cross-sections can be formed;

- Relatively small amounts of liquid are added to the solid;
- Very hard powders can be shaped;
- A uniform density distribution is obtained;
- Long thin sections can be made;
- Capital costs and operating costs are generally competitive.

In contrast to forming methods, such as powder pressing and slip casting, paste and flow extrusion is not fully understood [58]. The plastic ceramic body has a complex structure and mechanisms for plastic flow are also complex [58]. Although many tests have been proposed to measure extrudate plasticity, methods for predicting the mechanical properties of ceramic extrudates under well defined stress conditions are limited [58].

3.4.2. Formulation and Process Additives

Because extrusion is a plastic forming method, the material to be extruded must have good flowability and the extrudate must have enough wet strength to resist deformation due to its own weight or handling stresses. If either of these conditions is not met, a good extrusion will not be obtained. Formulation is to select proper additives and to optimize processes for certain ceramic system.

Adsorbed organic additives such as binders, plasticizers and lubricants are critical for good compaction and green strength. Compaction behavior is controlled by deformability and lubricating effects of the additives. Binder properties are significant at every step of a production system. The strength imparted by the binder helps in handling the green extrudates. Microstructure developed during sintering is linked to the green microstructure formed during compaction. Many key properties of advanced ceramic parts depend on completely removing binder during the early stages of heat treatment [58]. The formulation for a zirconia casting slurry is given in Table III.5. This Section focuses on describing each component and its contribution to the forming process.

Composition	Volume (%)	Weight (%)
Zirconia powder	41.52	80.58
Water	52.33	16.92
Polyacrylate deflocculant	4.42	1.79
Polyvinyl alcohol binder	1.73	0.71
	100.00	100.00

Table III. 5: Compositions of a Zirconia Casting Slurry [58]

3.4.3. Ceramic Powder

Chemical and physical properties of a ceramic powder such as particle size, particle size distribution and particle shape affect extrusion flow and extrudate packing density. A criterion to identify the preferred physical properties of a powder for making electrolyte is to have high packing density with least liquid in the formulation.

For good extrusion, the largest particle must be much smaller than the smallest dimension of the extrudate. The maximum dimension of angular, needle-like, or plate-like particles should be less than a tenth of the smallest die cross-section such as the gap to form the tube-wall thickness [58]. Micron size particles are normally used in advanced ceramic extrusion. Particles in crushed or ground powders - are often angular while powders prepared by precipitation contain agglomerates. Spray dried powders are nearly spherical, the preferred shape for paste extrusion.

Particle size distribution significantly affects particle packing and pore structure. Theoretical packing densities for uniform spheres range from 52% to 74%, depending on the sphere arrangements (cubical, orthorhombic, tetragonal, pyramidal and tetrahedral) [58], while experimental densities, for non-ordered arrangements of uniform spheres, are between 60% and 64% [58]. Packing density can be increased by filling the interstitial pores with finer particles. When the ratio between nearest sizes is greater than 7, for example for a quaternary

sphere system (size ratio 320/39/7/1), a maximum packing density of 95% can be achieved [58]. In practice, continuous particle size distributions are used and their form and breadth also affect packing density. Rough surfaces prevent particle motion and reduce the extrudate packing density.

3.4.4. Liquid

Sufficient liquid must be added to wet the ceramic powder and obtain an extrudable paste. Liquid spaces the particles and lubricates particle movement and motion along the flow path. After extrusion, the liquid is removed by drying, which will usually shrink the extrudate and leave pores in the product. Thus, the amount of liquid is critical (Figure III.3). A mix with insufficient liquid requires higher shear stress for a given shear rate, which may exceed the pressure limits of the extruder [58]. If there is too much liquid, the paste has low cohesiveness and may become too soft to retain its shape after extrusion.

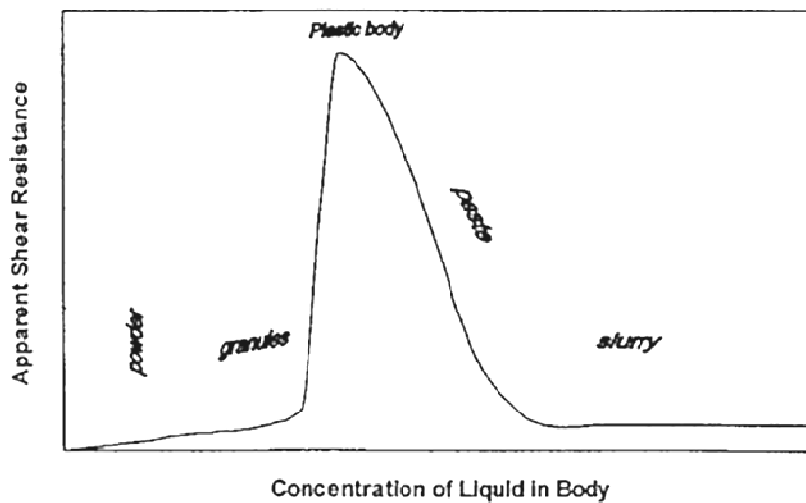


Figure III. 3: Effect of Liquid Concentration on Processing Consistency [58].

3.4.5. Binders

Binders provide green strength so the extrudate will retain its shape and can be handled. Average green strength after drying increases with binder concentration. This increase is rapid up to 4% binder. The selection of a binder system affects the internal and external rheological behavior of an extrudate. The internal flow property describes the stress-strain rate behavior of an extrudate when shear occurs between the particles. The external property describes the

shear between the extrudate and the die-wall. In general, binders for ceramic extrusion should have:

- (a) high green strength and high green density;
- (b) low viscosity;
- (c) insensitive to humidity;
- (d) mixing easily;
- (f) excellent burnout in air [58].

Widely used organic polymer binders include: polyvinyl alcohol (PVA), polyvinyl butyral (PVB), polyethylene glycol (PEG), methyl cellulose (Methocel[®]), and the specific ceramic extrusion binder Duramax[®] system. PVA and PVB are widely used in the fully hydrolysed form. The glass transition temperature for PVA is 75- 85°C. Methocel[®] and hydroxyethyl cellulose are commonly used for ceramic extrusion with high green strength. However, Methocel[®] adheres to metal in the die, which is undesirable. Adding an external lubricant may overcome this effect. PEG and polyethylene oxide (PEO) are water-soluble binders that can also act as plasticizers and lubricants. PEG has low residual ash compared with many other binders such as PVA [58].

Duramax acrylic extrusion binders, B1051 and B1052, are aqueous-based, ready-to-use emulsions made of 0.05-0.5 micron diameter polymer particles dispersed in water (Table III.6). Surfactants are added to control particle size, to stabilize emulsion particles during synthesis, and to prevent settling on storage. These binders impart high plasticity with sufficient adhesiveness and cohesiveness for the pates. Binder B1051 is an insoluble polymer gel made of more than 30% solids dispersed and suspended in water. It has a glass transition temperature of 81°C, which means that it produces a harder extrusion. Increasing the B1051 content in dough increases the hardness of the extrusion. Binder B 1052 is also an insoluble polymer gel of more than 55% solids suspended in water. It has a lower glass transition

temperature so it produces a softer extrusion but the extrusion is tougher. A binder level of 2-15% based on powder weight is recommended.

Additives	Duramax B1051	Duramax B1052
Appearance	Milky light yellow liquid	Milky white liquid
Total solids	30%	55%
Particle size, median	0.08 μm	0.3-0.4 μm
Glass transition temperature	81°C	6°C
Density at RT (23°C)	1.0 g/ml	1.1 g/ml
Viscosity (60 rpm)	40 cP (Brookfield #1)	<150 cP (Brookfield #2)
pH	2.7	5
Residue after firing	0.26% (air)	1.3% (air)

Table III. 6: Typical Properties of Duramax Extrusion Binders [58].

The mechanical properties of the extrudates can be tuned by varying the binder combinations (Figure III.4). For instance, B 1051 provides moderate plasticity and extrudability whilst B 1052 is a softer binder and provides high plasticity. Combining binders, as in the Duramax binder system, can improve performance. Extrudates with low B1051/B1052 ratios will have low elastic modulus and high ductility. To get round and straight green tubes or avoid wet green tube collapse due to the gravity, the ratio should be high.

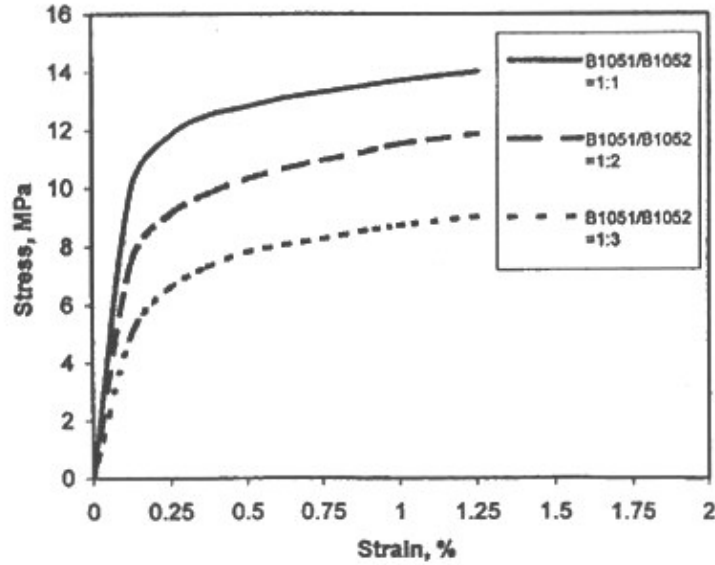


Figure III. 4: Mechanical Properties of Extruded Alumina with 4% Duramax Binders [58].

3.4.6. Lubricant

Lubricant is needed to enhance surface smoothness of the extrudates and reduce extrusion pressure. An internal lubricant reduces the pressure drop in the die-entry region, while an external lubricant decreases the pressure drop in the die-land (the section where cross-sectional area and shape are constant) [58]. The Benbow equation (Equation III.8) can be used to evaluate the die-land pressure loss (P_2) and analyse the effects of lubrication [58].

$$P_2 = 4(\tau_0 + \beta V) \left(\frac{L}{D} \right) \quad (\text{III.8})$$

Where τ_0 (wall shear stress at zero velocity) and β (wall velocity factor) are parameters characterizing the paste, V is the paste velocity in the die-land, D is die-land diameter and L is die-land length.

Polyethylene glycol (PEG) is often used as a lubricant and sometimes as binder. Flexibility of the dried extrudates can be tailored by adjusting lubricant level. Mechanical properties of polymers are temperature dependent. At low temperatures, polymers are elastic. As temperature increases, they go through a glass transition, T_g , to viscoelastic behaviour, becoming viscous liquids as temperature increases further. Good compaction depends on granule deformability, which is greater when granules are pressed at temperatures above the

T_g [58]. PEG's glass transition temperature (T_g) is less than 20°C , depending on the molecular weight [58]. PEG400 is mainly an external lubricant and has a slight internal lubricant function [58].

3.4.7. pH Control Agent

The electrical charge on fine ceramic particles is called zeta potential. The zeta potential is positive at low pH, negative at high pH and zero at the isoelectric point (IEP). For example, the IEP for silica (SiO_2), zirconia (ZrO_2), alumina (Al_2O_3) and magnesia (MgO) are pH 2, 4, 9 and 12 respectively [58]. The pH of pastes should be near the IEP to obtain maximum pseudo-plasticity and a pH control agent is usually needed for most ceramic powders. For example, the zeta potential of Ytria-Stabilized Zirconia (Figure III.5) can be adjusted with AMP-95, an organic amine with 90 wt% 2-amino-2-methyl-1-propanal, 5 wt% 2-(methylanino)-2-methyl-1-propanol and 5 wt% water. Usually 0.5-2% AMP-95 sufficient to coat the surface with charged particles so the ceramic particles repel each other.

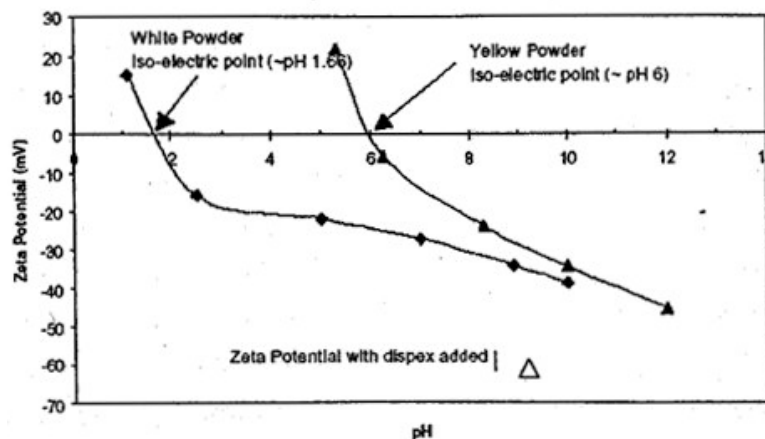


Figure III. 5: Zeta Potential of Ytria-Stabiized Zirconia [58].

3.4.8. Processing

Ceramic extrusion involves several steps including paste preparation, extrusion, drying and final sintering (Figure III.6). Preparing the paste is the critical step.

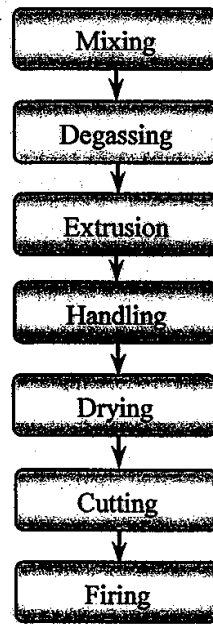


Figure III. 6: Basic Process of Paste Extrusion.

3.4.9. Mixing

The fundamental purpose of mixing is to produce a physically and chemically uniform extrusion batch. To improve uniformity and extrudability, each particle as well as die-land should be coated with a thin liquid film. The mean thickness of the liquid layer at die-land wall is estimated to be between 0.5-20 μm depending on the liquid content [58]. There are three steps in making a paste:

- (a) breaking and homogenizing agglomerates in the powder;
- (b) coating the particles with wetting agents;
- (c) producing a dough with further mixing and kneading [58].

High-shear may be needed to break agglomerates in the powder and obtain uniform dough. However, over mixing may cause the binder to drop out of the solution and form a gel of agglomerate. The average size of the dough (sometimes called lump) should be in 1.3-10 cm, depending on the mixer. A large lump indicates that too much liquid has been added whereas small lumps indicate that more liquid may be required. If the mixer wall is not clean at the end mixing, the formulation probably has too much liquid.

To predict accurately the manner in which dough behaves during extrusion, it is highly desirable to test their rheological behaviour under similar conditions, for example using

extrusion rheometer, at which extrusion is carried out at a series of steady speeds, and the equilibrium pressure required to extrude the material through the die at that speed is recorded via a pressure transducer [58].

Another extrusion route is to directly extrude spray-dried granules [58]. Slurry with water, powder, binder and other processing additives is sprayed into a warm drying medium to produce granules. Each near-spherical granule has a homogeneous coating of binder. Drying temperature and moisture in the dried material must be properly controlled so the granules can be extruded after evacuation.

3.4.10. Die Design and Extrusion

The extrusion die is critical for obtaining high quality extrudates such as straight, long and thin walled electrolyte tubes or porous tubular electrodes. Die entrance-angle, die-land length, ratio of die-land length and die diameter, die materials, and ram force/extrusion pressure influence the extrusion process and extrudate quality.

In a simplified ram extrusion system (Figure III.7), paste fed to cylinder (barrel) is packed and forced through a die-land to form an extrudate.

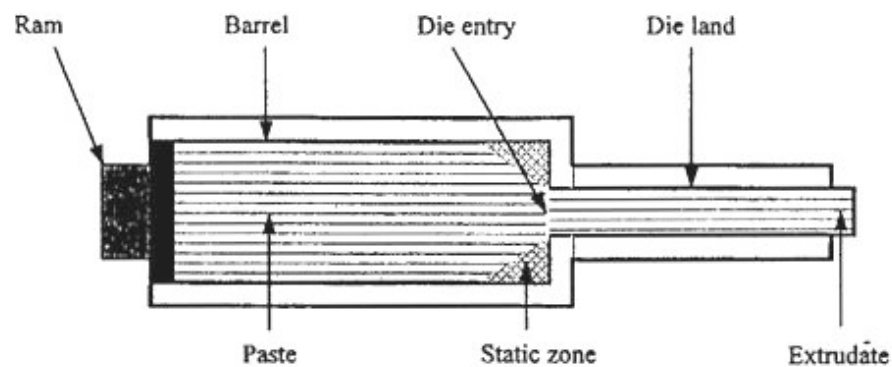


Figure III. 7: Illustration of a Basic Ram Extrusion System.

Pressure of the extrudate in a convergent conical die ($D=6$ mm, $L=59$ mm, and $\theta=30^\circ$) are shown in Figure III.8 and the effect of die entrance angle on extrusion pressure is shown in Figure III.9.

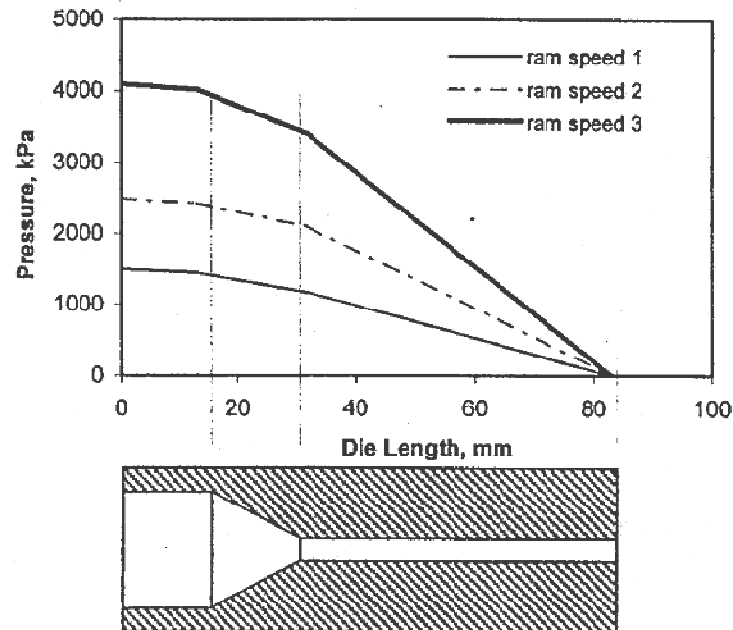


Figure III. 8: The Pressure of the Extrudate in a Convergent Conical Die [58].

The pressure generated in the paste packs the coated particles densely as well as forcing them through a die of suitable size and shape. Lower dough pressures (e.g. using a short die-land die) give less packing effect. Excessive pressures, however, may make liquid phase seep from the dough. Industrial extrusion pressures are up to about 4 MPa for porcelain bodies and up to 15 MPa for some organically plasticised materials [58].

The extrusion pressure for a given system (extruder, die design) is a function of paste rheologic properties (stiffness and uniformity). The overall pressure drop (P) for paste in a cylindrical die-land with a square entry (see Figure III.8) can be evaluated from the pressure drop at the die-entry (P_1) and the die-land (P_2) using Equation III.9, where pressure P_2 is used to shape and pack the extrudate [58].

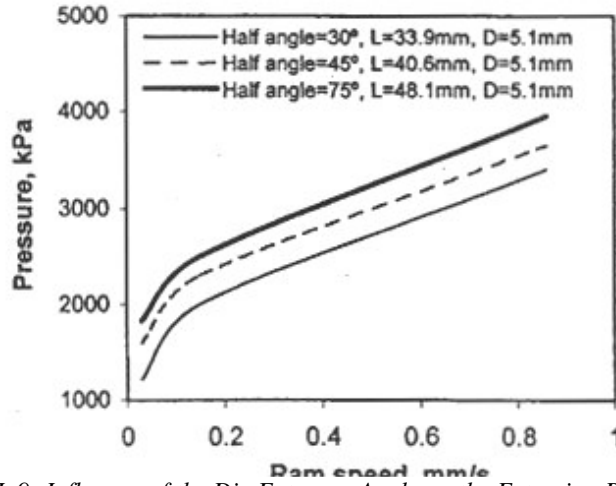


Figure III. 9: Influence of the Die Entrance Angle on the Extrusion Pressure [58].

To improve paste flow, tapered dies are preferred. Equation III.10 can be used to calculate the pressure drop at the die-entry P_1 , for a conical entry die cone half-angle, θ [58]. Reducing the die entrance angle will reduce the pressure drop at die entry. However, if the die entrance angle is too small (e.g. less than 20°), the extrudates are not packed sufficiently and do not retain their shape [58].

$$P = P_1 + P_2 = 2(\sigma_0 + \alpha V) \ln(D_0 / D) + 4(\tau_0 + \beta V)(L / D) \quad (\text{III.9})$$

$$P_1 = 2(\sigma_0 + \alpha V + \tau_0 \cot \theta) \ln(D_0 / D) + \beta V \cot \theta \quad (\text{III.10})$$

Where

P Extrusion pressure drop

D Die-land diameter

P_1 Pressure drop at die-entry

L Die-land length

P_2 Pressure drop in the die-land

V Paste velocity in the die-land

D_0 Barrel diameter

σ_0 Paste yield stress at zero velocity

τ_0 Wall shear stress at zero velocity

β Wall velocity factor

α Velocity factor

θ Die entry half-angle

Defects are imperfections formed during processing. The two major flow defects in paste extrusions are lamination and surface tearing. Lamination defects are formed by internal stresses where there is poor cohesion between adjacent layers in the extrudate. The streams

flowing around each arm of the spider (the mandrel support) are potential sources of laminations when extruding cylindrical tubes. Weak zones may develop into cracks during subsequent drying or firing. Reducing cross-section after the streams meet produces internal plastic flow, which may help reduce lamination. Surface tearing, which can occur in a wide variety of materials, produces periodic cracks on the surface. Material may curl from the extruder if the paste is not homogeneous or the mandrel pin is off centre.

3.4.11. Cutting and Extrudate Handling

Cutting the extrudate into short units always causes distortion. A 90° angle between the cut face and the die-land axis can reduce distortion [58]. Cutting also involves handling the extrudate. The extrudate can be difficult to handle, especially since it is usually not strong and deforms readily. If accurate cuts are required, the wet extrudate may be cut longer and exact dimensions cut after drying.

3.4.12. Drying

Drying removes liquid before the extrudate is fired. Dried green product has enough strength to allow further accurate cutting, machining and loading. Drying rate affects how the extrudate retains its shape. The extrudate shrinks as liquid between the particles is removed and inter-particle separation decreases. Differential shrinkage will give distortions or cracks.

3.4.13. Sintering

Sintering describes consolidation of material during firing while *firing* is a general describing heating a product to elevated temperatures. Sintering forms strong interparticle bonds in ceramics and usually requires high firing temperatures. In the firing process, organic binders burn out at low temperatures (Figure III.10) and strength gradually develops at higher temperatures. The product may be very weak as the binder is removed before the solid bonds are formed.

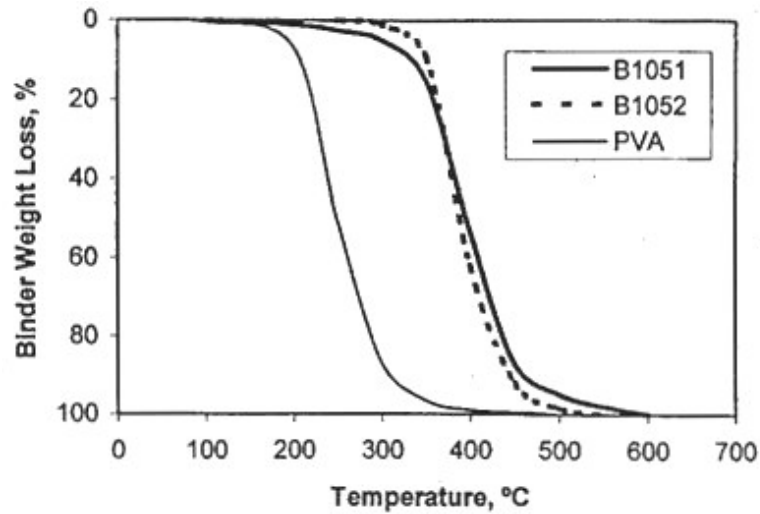


Figure III. 10: Binders Burnout Temperatures of Duramax and PVA [58].

Sintering strength and ceramic microstructure are related to maximum sintering temperature, time at this temperature, and chemical composition. The sintered product can be dense (e.g. for an electrolyte), or porous (e.g. for electrodes). Electrolytes used in SOFCs are typically made with a density of greater than 95% of theoretical density to minimize the crossover current and to separate the oxidant and the fuel gases (Figure III.11).

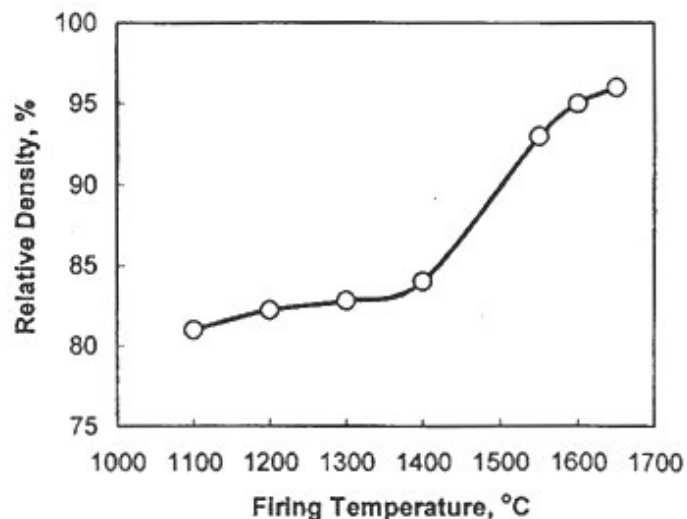


Figure III. 11: Effect of Firing Temperature on Relative Density of Slurry Cast YSZ Electrolytes [58].

Sintered density is also related to green density (Figure III.12) and pore size in the green body. A low green density means some particles compacted less dense, which will lead to a lower

sintering density and higher sintering shrinkage. Pores below a critical size are eliminated during sintering but large pores persist. Eliminating small pores reduces volume, so shrinkage occurs and is related to the matrix density.

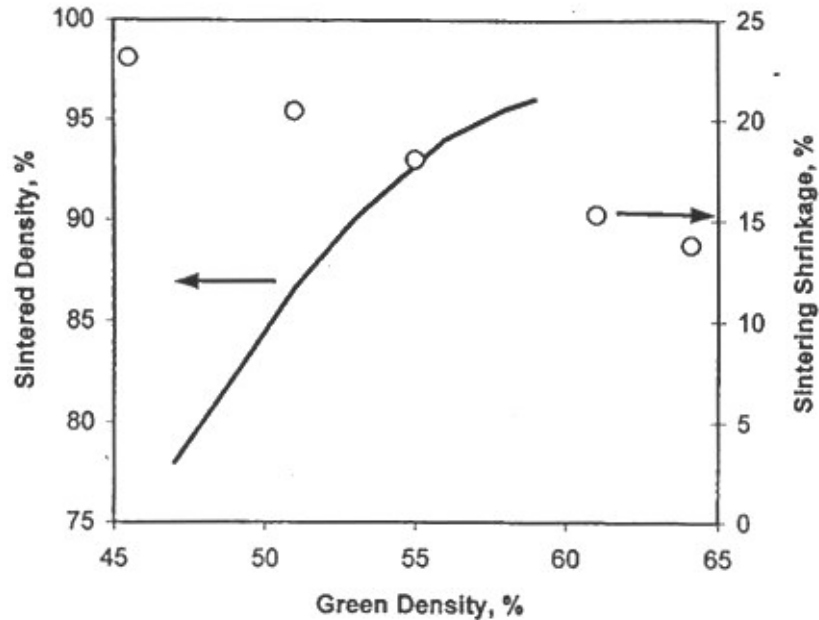


Figure III. 12: Relationship Between the Densities of Sintered and Green Body.

3.4.14. Thin Film Application

Present SOFC designs use thin film concepts to enhance cell performance and reduce material costs. Those thin films can be a single thin ceramic layer or multiple layers with a certain microstructures: as dense as possible for the electrolyte or with optimum porosity for electrodes. Both must have good mechanical integrity. Several thin film techniques have been used to fabricate SOFCs including EVD, chemical vapor deposition (CVD), jet vapor deposition (JVD), spray pyrolysis, electrophoretic deposition, dip coating, spin coating, tape calendaring, tape casting, vacuum slip casting, sputtering, and plasma spraying. The methods given in Table III.7 may be used for fabricating thin films on tubular supports.

Fabrication techniques differ depending on cell type, configuration and developer. For example, Siemens Westinghouse developed EVD technique, to produce thin layers for electrolyte, anode and interconnection in its early tubular SOFC development. After 1999, the company used an EVD process for electrolyte deposition only, and slurry deposition for anode and plasma spraying for interconnection [58]. For planar SOFCs, cost effective wet ceramic

techniques such as tape casting [58], screen printing [58] and spray painting [58] are widely used for the fabrication of thin films.

Process	Description
Spraying coating	Thin films are spray-coated onto outside surfaces of support tubes by a spray gun.
Spin coating	Thin films are coated onto inside surfaces of support tubes by spin coating a sol-gel precursor or slurry to spinning tube. For outside surface coating, fine brushes are used to carry slurries.
Dip coating	Films are formed on outside or inside surfaces by dipping or immersing support tube in slurries or colloidal suspensions.
Vacuum infiltration	The layers, especially electrolyte layers, are produced on inside or outside surfaces of partially sintered porous electrode tubes by vacuum slurry coating.
Electrophoretic deposition	A DC electrical field is applied to deposit preferred particles from a suspension onto a substrate electrode of opposite charge.
Sputtering	Thin films are sputter-deposited from metal targets onto porous electrode substrate using an electric discharge in an oxygen/argon mixture.
EVD	Thin films are deposited on a substrate by spraying atomized precursor droplets across a heated environment.
Plasma spraying	Thin films are produced using a plasma spray gun and powder injected. The fine particles become molten and adhere to the prepared surface. Using this technique can eliminate firing process.
Screen printing	A squeegee forces a thick paste through a stencil screen to form a thin film on the surface below.

Table III. 7: Thin Film Techniques for Fabrication Tubular SOFCs.

Many researchers have investigated plasma spraying. The Electrochemical Laboratory in Japan [58] applied YSZ to a substrate and found the sprayed material maintained its crystalline

structure during the process. Multilayer coatings can be formed, so electrolyte and electrode layers can be laminated without needing additional firing [58]. The technique is currently limited to R&D scale because it is costly and difficult to mass-produce.

EVD can be carried out above 1200°C with metal halides in an H₂/CO₂ atmosphere to produce excellent but very expensive thin electrolyte layers. Alternative cheaper fabrication methods, such as CVD and JVD are receiving more attention. CVD is one of the most versatile processes for manufacturing thin films and is currently used to manufacture products ranging from semiconductors to low-emissivity coatings on glass [58]. JVD is a thin film technique where sonic gas jets serve as the deposition source. It can be used to make dense and pinhole free YSZ films that seal highly porous electrode surfaces and are gas tight [58].

All thin film processes, other than plasma spraying and EVD, need a final sintering step to create a strongly bonded structure. One approach for decreasing densification temperature of electrolyte coatings is to use submicron active powers, preferably nanosize powders. High densities may be achieved at 1300°C and below with nanosize powder compared with 1500°C or above for micron YSZ powder.

3.5. Electrical Fuel cell characterization

Characterization techniques permit the quantitative comparison of fuel cells systems, discriminating between the various sources of loss within a fuel cell (activation, ohmic and concentration polarization), providing information about operational fuel cells behavior [59].

3.5.1. Current-Voltage Measurement

The performance of a fuel cell is best summarized by its current-voltage response, or i-V curve. The i-V curve shows the voltage output of the fuel cell for a given current density loading. High performance fuel cells will exhibit less loss and therefore a higher voltage for a given current load. Fuel cells i-V curves are usually measured with a potentiostat/galvanostat system. This system draws a fixed current from the fuel cell and measures the corresponding output voltage. By slowly stepping the current demand, the entire i-V response of the fuel cell can be determined [59].

In taking i - V curve measurements of fuel cells, the following important points must be considered:

- Steady state system must be ensured. When current is demanded from a fuel cell, the voltage of the cell drops to reflect the higher losses associated with producing current. However this drop is not instantaneous and it can take seconds, minutes or even hours;
- Temperature must be maintained constant during measurement;
- Gas pressure generally must be monitored at both the fuel cells inlet and outlet;
- Gas flow rate must be generally set using mass flow controllers. Flow rates are usually held constant during the entire test at a flow rate that is sufficiently high so that even at the largest current densities there is sufficient supply.

At first glance, appears impossible to individually separate the various loss contributions from the i - V curve. Nevertheless, careful data analysis permits approximate evaluation of the activation, ohmic and concentration polarization [59].

3.5.2. Electrochemical Impedance Spectroscopy

While the i - V curve provides general quantification of fuel cell performance, a more sophisticated test is required to accurately differentiate between all the major sources of loss in a fuel cell. Electrochemical impedance spectroscopy is the most widely used technique for distinguishing the different losses [59].

EIS Basics. Like resistance, impedance is a measure of the ability of a system to *impede* the flow of electrical current. The impedance Z is given by the ratio between a time-dependent voltage and a time-dependent current:

$$Z = \frac{V(t)}{i(t)} \tag{III.11}$$

System linearity is required for simple impedance analysis. Obviously, electrochemical systems are not linear. (Consider Butler—Volmer kinetics, which predicts an exponential relationship between voltage and current.) We circumvent this problem by using small-signal

voltage perturbations in our impedance measurements. As Figure III.13 illustrates, if we sample a small enough portion of a cell's $i-V$ curve, it will *appear linear*. In normal EIS practice, a 1-20- mV AC signal is applied to the cell. This signal is generally small enough to confine us to a pseudo-linear segment of the cell's $i-V$ curve.

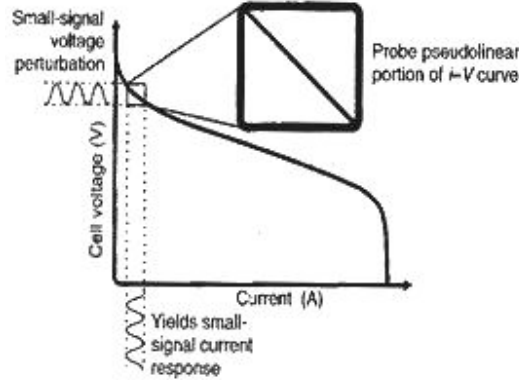


Figure III. 13: Application of a small signal voltage perturbation confines the impedance measurement to a pseudolinear portion of a fuel cell's $i-V$ curve.

Impedance measurements are usually made by applying a small sinusoidal voltage perturbation, $V(t) = V_0 \cos(\omega t)$, and monitoring the system's resultant current response, $i(t) = i_0 \cos(\omega t - \phi)$. In these expressions, $V(t)$ and $i(t)$ are the potential and current at time t , V_0 and i_0 , are the amplitudes of the voltage and current signals, and ω is the radial frequency ($\omega = 2\pi f$).

In general, the current response of a system may be shifted in phase compared to the voltage perturbation. Following equation III.11 it is possible to write the sinusoidal impedance response of a system as:

$$Z = \frac{V_0 \cos(\omega t)}{i_0 \cos(\omega t - \phi)} = Z_0 \frac{\cos(\omega t)}{\cos(\omega t - \phi)} \quad (\text{III.12})$$

Alternatively, we can use complex notation to write the impedance response of a system in terms of a real and an imaginary component:

$$Z = \frac{V_0 e^{j\omega t}}{i_0 e^{j(\omega t - \phi)}} = Z_0 e^{j\phi} = Z_0 (\cos \phi + j \sin \phi) \quad (\text{III.13})$$

The impedance of a system can therefore be expressed in terms of an impedance magnitude Z_0 and a phase shift ϕ , or in terms of a real component ($Z_{\text{real}} = Z_0 \cos \phi$) and an imaginary component ($Z_{\text{imag}} = Z_0 \sin \phi j$). Typically, impedance data are plotted in terms of the real and imaginary components of impedance (Z_{real} on the x axis and Z_{imag} on the y axis). Such graphical representations of impedance data are known as *Nyquist plots*. Because impedance measurements are made at dozens or even hundreds of different frequencies, Nyquist plots generally summarize the impedance behavior of a system over many orders of magnitude in frequency [59].

EIS and Fuel Cells. Consider a hypothetical fuel cell which suffers from three loss effects:

1. Anode activation loss;
2. Ohmic electrolyte loss;
3. Cathode activation loss.

Figure III.14 shows what the EIS Nyquist plot for this fuel cell might look like.

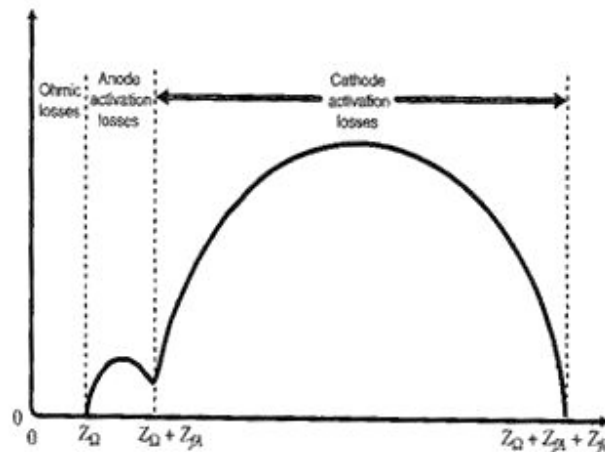


Figure III. 14: Example Nyquist plot from a hypothetical fuel cell with ohmic resistance, anode activation, and cathode activation losses.

The key thing to note is that two semicircular peaks are visible in the plot. For the hypothetical fuel cell in this example, the size of these two semicircles can be attributed to the magnitude of the two (anode and cathode) activation losses. Looking more closely at the diagram, you will

see that the three x-axis intercepts defined by the semicircles mark off three impedance regions which are denoted by Z_{Ω} , Z_{fA} , and Z_{fC} . The size of these three impedances correspond to the relative size of η_{Ohmic} , $\eta_{\text{act.anode}}$, and $\eta_{\text{act.cathode}}$ in our fuel cell. Thus, in this hypothetical EIS example, it is clear that the cathode activation loss dominates the fuel cell's performance while the ohmic and anode activation losses are small.

How it is possible to generate this spectrum using EIS and how it could be assign a value at the various intercepts in the spectrum to the various loss processes in the fuel cell, requires a discussion on impedance theory and the equivalent circuit modeling [59].

EIS and Equivalent Circuit Modeling. The processes that occur inside a fuel cell can be modeled using circuit elements. For example, it is possible to assign groups of resistors and capacitors to describe the behavior of electrochemical reaction kinetics, ohmic conduction processes, and even mass transport. Such circuit-based representations of fuel cell behavior are known as equivalent circuit models. If we measure a fuel cell's impedance spectrum and compare it to a good equivalent circuit model, it is then possible to extract information about the reaction kinetics, ohmic conduction processes, mass transport, and other properties.

In order to build a sample equivalent circuit model of a fuel cell it is necessary to introduce the common circuit elements used to describe fuel cell behavior.

Beginning with the ohmic conduction processes (ohmic Resistance), the equivalent circuit is represented by a simple resistor.

$$Z_{\Omega} = R_{\Omega} \tag{III.14}$$

A Nyquist diagram plots the real component of impedance versus the negative of imaginary component of impedance over a range of frequencies. For the case of a simple resistor, the imaginary component of resistance is zero, and the impedance does not change with frequency. The Nyquist plot for a resistor is therefore a single point on the real axis (x-axis) with value R (Figure III.15) [59].

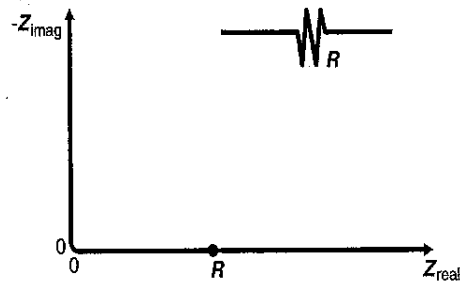


Figure III. 15: Circuit diagram and Nyquist plot for a simple resistor.

Electrochemical Reaction. The equivalent circuit representation of an electrochemical reaction is more complicated. Figure III.16 depicts the typical electrochemical reaction interface. As illustrated in this figure, the impedance behavior of the reaction interface can be modeled as a parallel combination of a resistor and a capacitor (R_f and C_{dl}). Here, R_f the *Faradaic resistance*, models the kinetics of the electrochemical reaction while C_{dl} , the *double-layer capacitance*, reflects the capacitive nature of the interface.

As Figure III.16 illustrates, during an electrochemical reaction, a significant separation of charge occurs across the reaction interface, with electron accumulation in the electrode matched by ion accumulation in the electrolyte. The charge separation causes the interface to behave like a capacitor. The strength of this capacitive behavior is reflected in the size of C_{dl} .

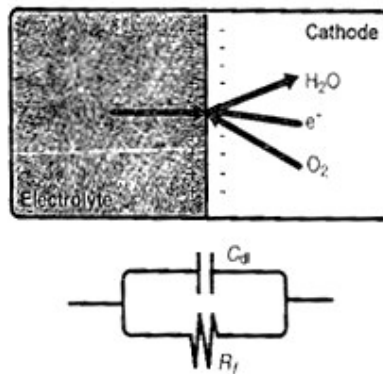


Figure III. 16: Physical representation equivalent circuit model of an electrochemical reaction interface.

The impedance response of a capacitor is purely imaginary. The equation relating voltage and current for a capacitor is:

$$i = C \frac{dV}{dt} \quad (\text{III.15})$$

For a sinusoidal voltage perturbation ($V = V_0 e^{j\omega t}$) this gives:

$$i(t) = C \frac{d(V_0 e^{j\omega t})}{dt} = C(j\omega)V_0 e^{j\omega t} \quad (\text{III.16})$$

which yields an impedance of:

$$Z = \frac{V(t)}{i(t)} = \frac{V_0 e^{j\omega t}}{C(j\omega)V_0 e^{j\omega t}} = \frac{1}{j\omega C} \quad (\text{III.17})$$

If this capacitor is placed in series with a resistor, the net impedance will be given by:

$$Z = R + \frac{1}{j\omega C} \quad (\text{III.18})$$

The equivalent circuit diagram and corresponding Nyquist impedance plot of the resistor-capacitor series combination is shown in Figure III.17.

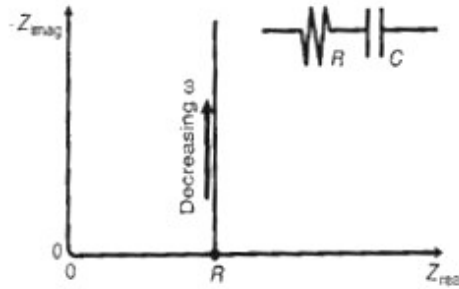


Figure III. 17: Circuit diagram and Nyquist plot for a series RC.

The impedance is a vertical line that increases with decreasing ω . The real component of the impedance is given by the value of the resistor. As frequency decreases, the imaginary component of the impedance (as given by the capacitor) dominates the response of the circuit.

To understand how the reaction process can be modeled by the Faradaic resistance R_f , recall the Tafel equation utilized as simplification of reaction kinetics (activation losses):

$$\eta_{act} = -\frac{RT}{\alpha nF} \ln i_0 + \frac{RT}{\alpha nF} \ln i \quad (\text{III.19})$$

For a small-signal sinusoidal perturbation, the impedance response $Z = V(t)/i(t)$ can be approximated as $Z = dV/di$ (instantaneous slope of the i — V response at the point of interest). Thus the impedance of the kinetic process may be calculated as:

$$Z_f = \frac{d\eta}{di} = \frac{RT}{\alpha nF} \frac{1}{i} \quad (\text{III.20})$$

Substituting $i = i_0 e^{\alpha nF \eta_{act} / (RT)}$ into this expression yields:

$$Z_f = R_f = \left(\frac{RT}{\alpha nF} \right) \frac{1}{i_0 e^{\alpha nF \eta_{act} / (RT)}} \quad (\text{III.21})$$

Notice that Z_f has no imaginary component and therefore can be represented as a pure resistor (R_f). The size of R_f depends on the kinetics of the electrochemical reaction. A high R_f indicates a highly resistive electrochemical reaction. A large i_0 or a large activation overvoltage (η_{act}) will decrease R_f , decreasing the kinetic resistance of the reaction.

For the case of the reaction interface shown in Figure III.16, the total impedance of the electrochemical interface model is given by the parallel combination of the capacitive double layer impedance and the resistive Faradaic impedance. Just like combining parallel resistances, the parallel combination of two impedance elements is given by:

$$\frac{1}{Z} = \frac{1}{R_f} + j\omega C_{dl} \quad (\text{III.22})$$

$$Z = \frac{1}{1/R_f + j\omega C_{dl}} \quad (\text{III.23})$$

The equivalent circuit and corresponding Nyquist diagram of this reaction interface model is given in Figure III.18. Note that the impedance shows a characteristic semicircular response. The leftmost point on the diagram corresponds to the highest frequency; frequency then steadily decreases as the points progress from left to right across the diagram. In most electrochemical systems, the real component of impedance will almost always increase (or remain constant) with decreasing frequency.

The high-frequency intercept of the semicircle in Figure III.18 is zero, while the low-frequency intercept is R_f . Thus, the diameter of the semicircle provides information about the size of the activation resistance of a fuel cell. A fuel cell with highly facile reaction kinetics will show a small impedance loop. In contrast, a *blocking electrode* (one where $R_f \rightarrow \infty$ because the electrode “blocks” the electrochemical reaction) shows an impedance response similar to the pure capacitor in Figure III.17.

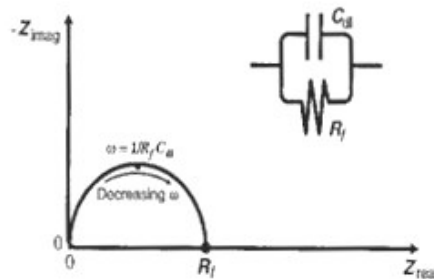


Figure III. 18: Circuit diagram and Nyquist plot for a parallel RC.

At intermediate frequencies, the impedance response contains both real and imaginary components. The frequency at the apex of the semicircle is given by the RC time constant of the interface ($\omega=1/(R_f C_{dl})$). From this value, C_{dl} may be determined.

The impedance behavior illustrated in Figure III.18 can be understood intuitively by examining the RC circuit model. At extremely high frequencies, capacitors act as short circuits; at extremely low frequencies, capacitors act as open circuits. Thus, at high frequency,

the current can be completely shunted through the capacitor and the effective impedance of the model is zero. In contrast, at extremely low frequencies, all of the current is forced to flow through the resistor and the effective impedance of the model is given by the impedance of the resistor. For intermediate frequencies, the situation is somewhere in-between, and the impedance response of the model will have both resistive and capacitive elements [59].

Mass Transport. Mass transport in fuel cells can be modeled by *Warburg* circuit elements. They are based on diffusion processes. The impedance of an “infinite” Warburg element (used for an infinitely thick diffusion layer) is given by the equation:

$$Z = \frac{\sigma_i}{\sqrt{\omega}}(1 - j) \quad (\text{III.24})$$

where σ_i in this equation is the *Warburg coefficient* for a species i and is defined as:

$$\sigma_i = \frac{RT}{(n_i F)^2 A \sqrt{2}} \left(\frac{1}{c_i^0 \sqrt{D_i}} \right) \quad (\text{III.25})$$

where A is the electrode area, c_i is the bulk concentration of species i , and D_i is the diffusion coefficient of species i . Thus, c_i characterizes the effectiveness of transporting species i to or away from a reaction interface. If species i is abundant (c_i^0 is large) and diffusion is fast (D_i is high), then σ_i will be small and the impedance due to mass transport of species i will be negligible. On the other hand, if the species concentration is low and diffusion is slow, σ_i will be large and the impedance due to mass transport can become significant. Note from Equation III.24 that the Warburg impedance also depends on the frequency of the potential perturbation. At high frequencies the Warburg impedance is small since diffusing reactants do not have to move very far. However, at low frequencies the reactants must diffuse farther, thereby increasing the Warburg impedance.

The equivalent circuit and corresponding Nyquist diagram of the infinite Warburg impedance element are given in Figure III.19. Note that the infinite Warburg impedance shows a characteristic increasing linear response with decreasing ω . The infinite Warburg impedance

appears as a diagonal line with a slope of 1. Impedance increases from left to right with decreasing frequency.

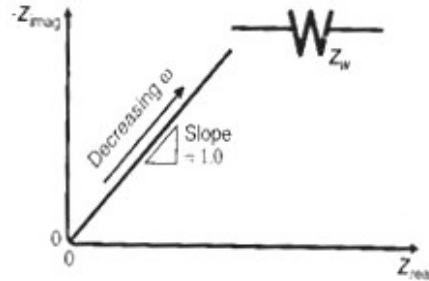


Figure III. 19: Circuit diagram and Nyquist plot for a Warburg element used to model diffusion processes.

The infinite Warburg impedance is only valid if the diffusion layer is infinitely thick. In fuel cells, this is rarely the case. Convective mixing in fuel cell flow structures usually restricts the diffusion layer to the thickness of the electrode. For such situations, the impedance at lower frequencies no longer obeys the infinite Warburg equation. In these cases, it is better to use a *porous bounded Warburg* model (also called the “0” diffusion element), which has the form:

$$Z = \frac{\sigma_i}{\sqrt{\omega}} (1 - j) \tanh \left(\delta \sqrt{\frac{j\omega}{D_i}} \right) \quad (\text{III.26})$$

where δ is the diffusion layer thickness. As shown in Figure III.20, at high frequencies or cases where δ is large, the porous bounded Warburg impedance converges to the infinite Warburg behavior. However, at low frequencies or for small diffusion layers, the porous bounded Warburg impedance moves back toward the real axis [59].

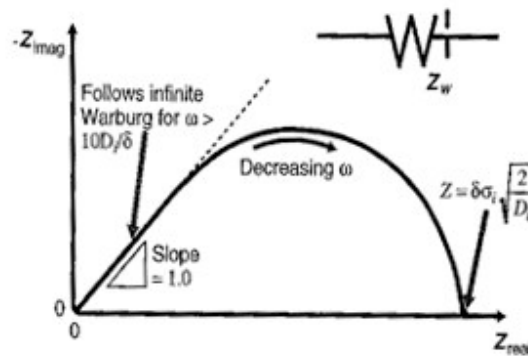


Figure III. 20: Circuit diagram and Nyquist plot for a porous bounded Warburg element, which is used to model finite diffusion processes

Simple Equivalent Circuit Fuel Cell Model. We have now assembled enough tools to describe basic fuel cell processes using equivalent circuit elements. It is possible to construct a simple equivalent circuit model for a complete fuel cell using the elements described previously. Assuming that our fuel cell is affected from the following loss processes:

1. Anode activation;
2. Cathode activation;
3. Cathode mass transfer;
4. Ohmic loss;

If for simplicity, we assume that the cathode mass transfer process can be modeled with an infinite Warburg impedance element; also, we assume that the anode kinetics are fast compared to the cathode activation kinetics. The physical picture, equivalent circuit model, and corresponding Nyquist plot for our fuel cell are shown in Figure III.21. The Nyquist plot was generated using the equivalent circuit showed in Figure III.21. Note how the impedance response of this fuel cell model is given by a combination of the impedance behaviors from each individual element in our circuit. The Nyquist plot shows two semicircles followed by a diagonal line. The high-frequency, real-axis intercept corresponds to ohmic resistance of our fuel cell model. The first loop corresponds to the RC model of the anode activation kinetics while the second loop corresponds to the RC model of the cathode activation kinetics. The

diameter of the first loop gives R_f for the anode while the diameter of the second loop gives R_f for the cathode. Note how the cathode loop is significantly larger than the anode loop. This visually indicates that the cathode activation losses are significantly greater than the anode activation losses. From the R_f values, the kinetics of the anode and cathode reactions can be extracted using Equation III.21 Fitting the C_{dl} values gives an indication of the effective surface area of the fuel cell electrodes.

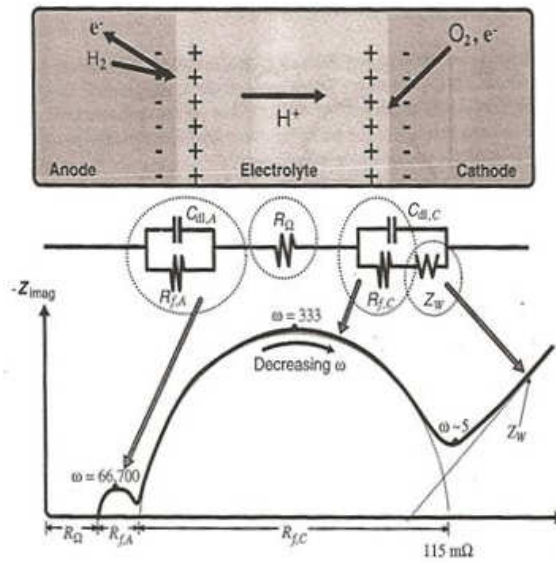


Figure III. 21: Physical picture, circuit diagram, and Nyquist plot for a simple fuel cell impedance model.

The diagonal line at low frequencies is due to mass transport as modeled by the infinite Warburg impedance. From the frequency-impedance data of this line, the mass transport properties of the fuel cell can be extracted. If a porous bounded Warburg is used instead, a diffusion layer thickness could also be extracted.

For clarity in this example, we deliberately chose RC values for the anode and cathode that allowed the two semicircles to be distinguished from one another. In many real fuel cells, however, the RC loop for the cathode overwhelms the RC loop for the anode, as shown in Figure III.22.

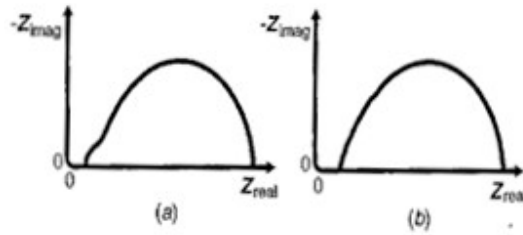


Figure III. 22: In H_2 — O_2 fuel cells the cathode impedance is often significantly larger than the anode impedance. In these cases, the cathode impedance can mask the impedance of the anode

To fully understand fuel cell behavior, it is important to measure the impedance response at several different points along a fuel cell’s i — V curve. The impedance behavior of a fuel cell will change along the i — V curve, depending on which loss processes are dominant. Figure III.23 gives several illustrative examples. At low currents, the activation kinetics dominates and R_f is large, while the mass transport effects can be neglected. In these situations an impedance response similar to that shown in Figure III.23a is typical. At higher currents (higher activation overvoltages), R_f decreases since the activation kinetics improve with increasing η_{act} (refer to Equation III.21). Thus, the activation impedance loop decreases, as shown in Figure III.23b. A decreasing impedance loop with increasing activation overvoltage is indicative of an activated electrochemical reaction. At high currents, mass transport effects occur and the impedance response may look something like Figure III.23c [59].

While the power of EIS is considerable, the technique is complex and fraught with pit falls.

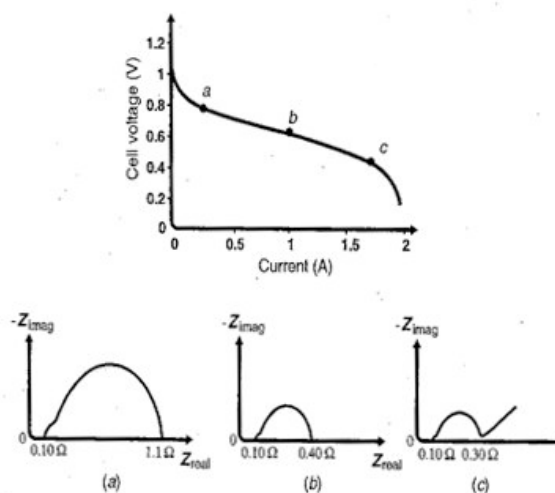


Figure III. 23: EIS characterization of a fuel cell requires impedance measurements at several different points along an i — V curve. The impedance response will change depending on the operating voltage.

3.6. Experimental analysis of micro-tubular fuel cell's performance

Finally, in this section are reported the main results of the experimental analysis conducted on micro-tubular solid oxide fuel cells manufactured and tested in the laboratories of the Colorado School of Mines (Golden, CO – U.S.A.).

In particular, we were able to analyze the energetic performance of anodic supported tubular SOFCs, with a cermet anode made of a mixture of NiO (Nickel Oxide) and YSZ (Yttria Stabilized Zirconia), with a YSZ electrolyte and a cathode made of LSM (Strontium - doped Lanthanum Manganite). Subsequently we have analyzed the energetic performance of anodic supported micro-tubular SOFCs with a cermet anode of NiO and GDC (Gadolinium Doped Ceria), a GDC electrolyte and a cathode in LSCF ($\text{La}_{0.6}\text{Sr}_{0.4}\text{Co}_{0.2}\text{Fe}_{0.8}\text{O}_{3-y}$).

The energetic performances were evaluated at different operating temperatures and for different volume flow of gas entering the fuel cell. Furthermore, has been analyzed the behavior of the fuel cells when fed with different types of gas (hydrogen, methane, synthesis gas, etc.).

3.6.1. Solid Oxide Fuel Cells Test Stand

The performance of the fuel cells were analyzed using a SOFC Test Stand present at Colorado Fuel Cell Center and subsequently replicated at the Colorado Center for Advanced Ceramic of the Metallurgical and Material Department (MME) - Colorado School of Mines (Golden, CO – USA).

The figures III.24 and III.25 show both the test stand realized in laboratories with the most important component necessary for a complete characterization of the energetic performance of a tubular fuel cell.

In particular, test stands were realized with the instruments and equipments reported below:

- *Furnace*: in order to control the operating temperature during the experiments;
- *Electrical Load*: this system is capable to draw a fixed current amount from the fuel cell and measures the corresponding output voltage;
- *Potentiostat/Galvanostat*: this system is capable applying a small sinusoidal voltage perturbation on fuel cell, monitoring the system's resultant current response in order to determine the EIS (Electrochemical Impedance Spectroscopy);

- *Gas flow distribution network*: essential to supply the necessary gases for the fuel cell operation. This system includes hydrogen, carbon monoxide, carbon dioxide, methane and nitrogen pipe lines. Furthermore was installed a bubbler system for steam production;
- *Volume flow gas controllers*: each line is equipped with a gas flow controller linked to a general control panel capable to set the expected volume flow and change eventually the correction factor in case it is necessary to use different gases with the same gas flow controller;
- *PC data acquisition system*: in order to control each single instrument and save the data produced during the experiments.



Figure III. 24: Fuel cell test stand realized at the Colorado Center for Advanced Ceramic



Figure III. 25: Fuel cell test stand realized at the Colorado Fuel Cell Center

All furnaces used are equipped with a control system for accurate and stable temperature response and have the option of a choice of programmer. The furnaces are equipped with advanced setpoint programming temperature controller and it is possible to fix beforehand the configuration of ramp rate, ramp time and dwell time for each program. Power feedback is used to stabilize the output power and hence the controlled temperature against supply voltage fluctuations.

Ramp rate temperature control is especially important for fuel cell testing in order to avoid possible rupture for thermal stress during start-up and shut down procedures. A ramp rate of 1.5-2 °C/min was used both for heat-up and cools down fuel cell's procedure.

The Electrical Load used to determine the performance of fuel cells (I-V curve) is a Chroma 6310 series instrument. The instrument is capable to draw current from fuel cells, measuring the corresponding output voltage, both in static and dynamic condition. The electric load is equipped with advanced programmer for current and voltage cycle control that allow fixing properly the current drawing in order to measure correctly the I-V curve. The

instrument is perfectly controlled by PC allowing program the duration and the ramp rate of the current drawing.



Figure III. 26: Chroma (6310 series) electrical load front panel (OCV = 1.1650)

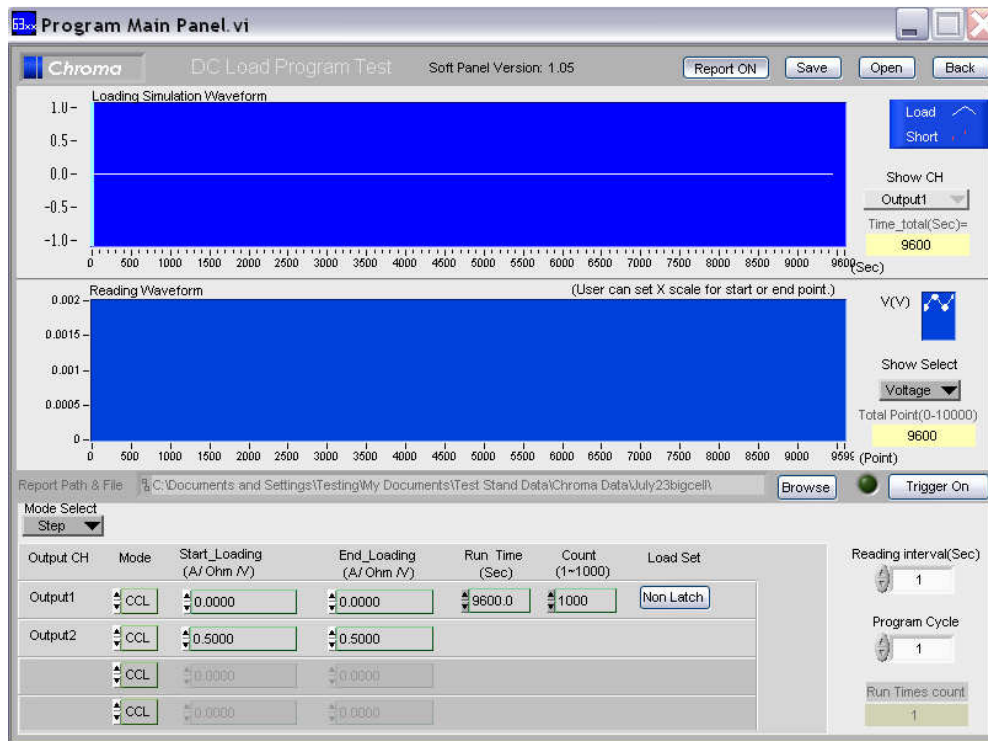


Figure III. 27: PC software for Chroma electrical load control

The Electrochemical Impedance Spectroscopy has been measured by a Gamry 600 Potentiostat/Galvanostat. The system, applying a small sinusoidal voltage perturbation on fuel cell, monitoring the system's resultant current response, for different frequency, is able to determine the EIS typical shape. The instrument is perfectly controlled by PC allowing program the range of frequency, and the amplitude of the signal to apply at the fuel cell in order to determine the EIS.



Figure III. 28: Gamry Potentiostat/Galvanostat for Electrochemical Impedance Spectroscopy

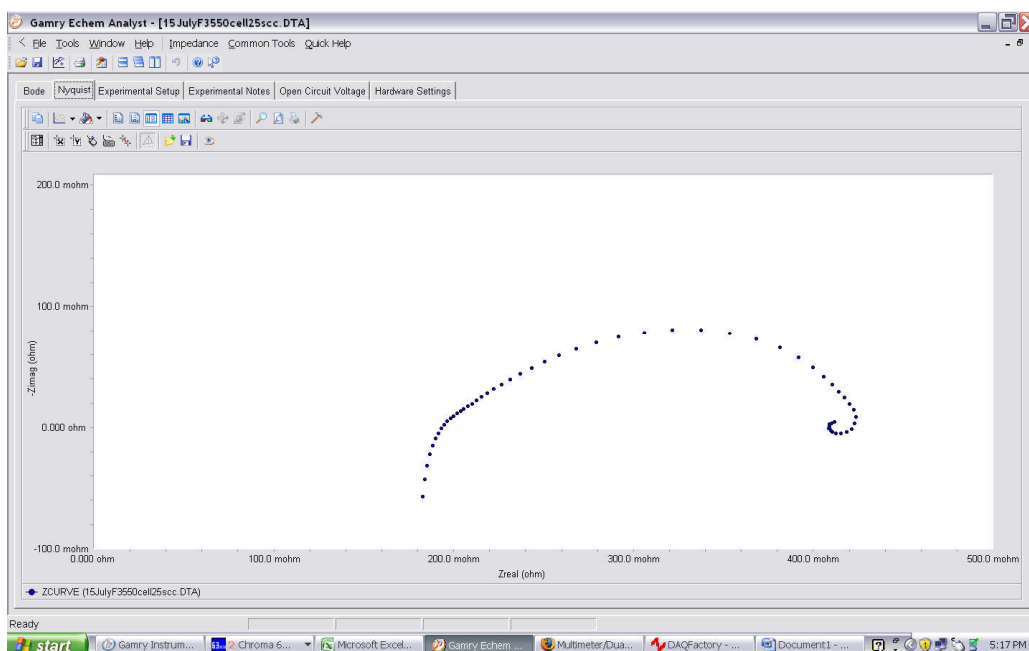


Figure III. 29: PC software for Gamry potentiostat control – EIS response curve

The Gas flow distribution network has been realized with stain steel pipe lines of ¼” linked to single cylinders containing each one different gas. On the top of each cylinder has been applied a pressure reducer (regulator) in order to obtain a pressure inside the circuit bigger than the environmental pressure. As shown in the figure below, have been realized dedicated lines for each one of the 3 different furnaces. Moreover, a specific circuit has been conceived for carbonaceous gases in order to experiment the electrochemical performance and the carbon deposition phenomena when fuel cells are fed with hydrocarbon fuels.



Figure III. 30: Gases distribution panel – 3 lines, one for each furnace and the auxiliary line.

Each line is controlled with solenoid valves and MKS Thermal Mass Flow Meters (type 179) that sense flow by measuring the rate of heat transfer from a heated tube to the flowing gas inside the tube. All the mass flow meters are connected with an MKS mass flow controller (MFC) power supply and display electronics, in order to control the gas flow rate, the zero adjustments and eventually to change the correction factor in case it is necessary to use the same gas flow meter for different gases.

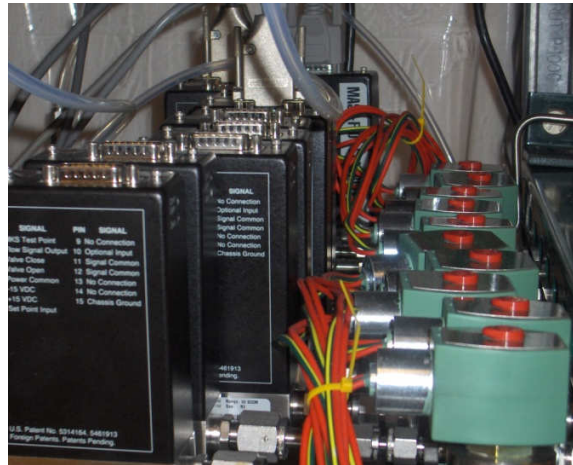


Figure III. 31: MKS mass flow meters and solenoid valves

Each pipe line, through a data acquisition system, is remotely controlled by PC. The figure below shows the possibility to activate/deactivate each solenoid valve; it is also clearly displayed how the auxiliary line (carbonaceous gas) are connected to the 3 pipe lines of the furnaces.

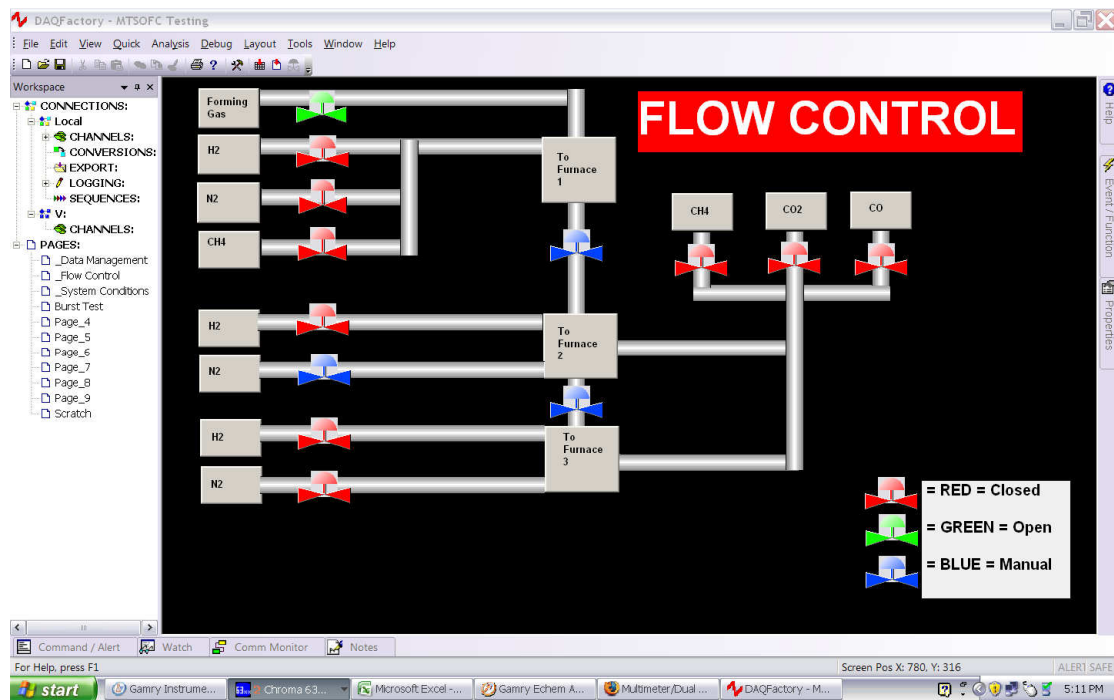


Figure III. 32: PC Gas distribution panel control

All the pipe lines are equipped with a “bubbler system” capable to introduce different quantity of steam inside the gas mixture that feed the fuel cells. This system is used during the fuel cell I-V curve measurement to introduce a small amount (2-3% of total mass flow) of steam in the hydrogen stream in order to reach a more stable trend of the voltage during the current drawing. The operating principle is really simple: the gas flow, coming from the gas flow meter, is made bubbling inside the steel tank (full of water), and subsequently a small amount of water evaporate depending on the water saturation pressure for a given water’s temperature. The water tank is surrounded by a heating type with adjustable thermostat, capable to control the water temperature, that allows to fix properly the amount of steam desiderate in the gas stream. This system is really useful in case of fuel cell feeding with methane and carbon monoxide, allowing the control of the steam/carbon ratio.



Figure III. 33: Bubbler for steam production – a thermocouple control the temperature to determine the amount of steam in the gas mixture

The relationship between the water saturation pressure and the temperature is represented by the Clausius-Clapeyron relation that could be approximate by the Magnus formula:

$$p(\text{sat}) = 6.112 \cdot 10^{\frac{7.5 \cdot t}{237.7 + t}} \quad (\text{III.27})$$

with:

- $p(\text{sat})$ = water saturation pressure [mbar];
- t = temperature [$^{\circ}\text{C}$]

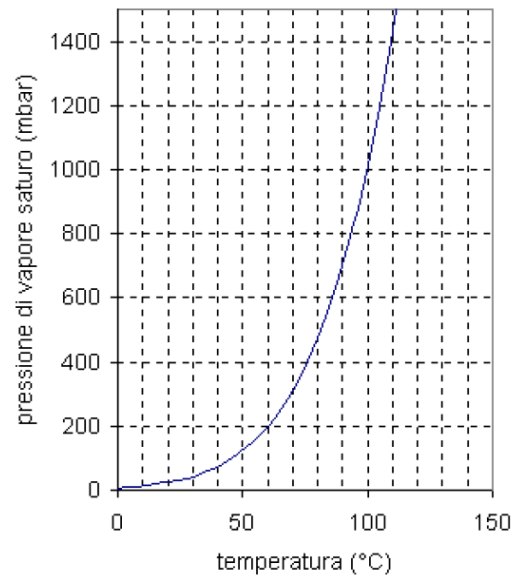


Figure III. 34: Trend of water saturation pressure with the temperature

3.6.2. Fabrication Process

The aforementioned considerations reported on previous paragraph have lead to the development of micro-tubular SOFCs with diameters in the millimeter to sub-millimeter ranges for intermediate temperatures operation between $450\sim 550^{\circ}\text{C}$ [1,11,12]. In this study, micro-tubular SOFCs measuring 1.8 mm in diameter and 1.2 cm in length have been fabricated using traditional extrusion and coating techniques and cells are tested in the intermediate temperature region between $450\sim 550^{\circ}\text{C}$. The micro-tubular SOFC used is anode supported, consisting of a NiO and $\text{Gd}_{0.2}\text{Ce}_{0.8}\text{O}_{2-x}$ (GDC) cermet anode, thin GDC electrolyte, and a $\text{La}_{0.6}\text{Sr}_{0.4}\text{Co}_{0.2}\text{Fe}_{0.8}\text{O}_{3-y}$ (LSCF) and GDC cermet cathode.

The energetic performance measured during the experimental activities were compared with the result of test conducted on anodic supported tubular SOFCs realized with a cermet anode made of a mixture of NiO (Nickel Oxide) and YSZ (Yttria Stabilized Zirconia), with a YSZ electrolyte and a cathode made of LSM (Strontium - doped Lanthanum Manganite). These cells were tested at operating temperatures ranging from 750°C to 850°C .

Micro-tubular SOFCs were fabricated using a process similar to that described by Suzuki et al. (*J. Power Sources* 160 (2006) 73). This process is briefly outlined with changes to fabrication processes noted. Anode slurry was prepared and consisted of NiO powder, GDC powder, and cellulose as the binder. The anode components were mixed with water using an industrial mixer for 1–2 hours and left to age overnight. Placing a vacuum over the anode mixture allowed for excess air to be removed.

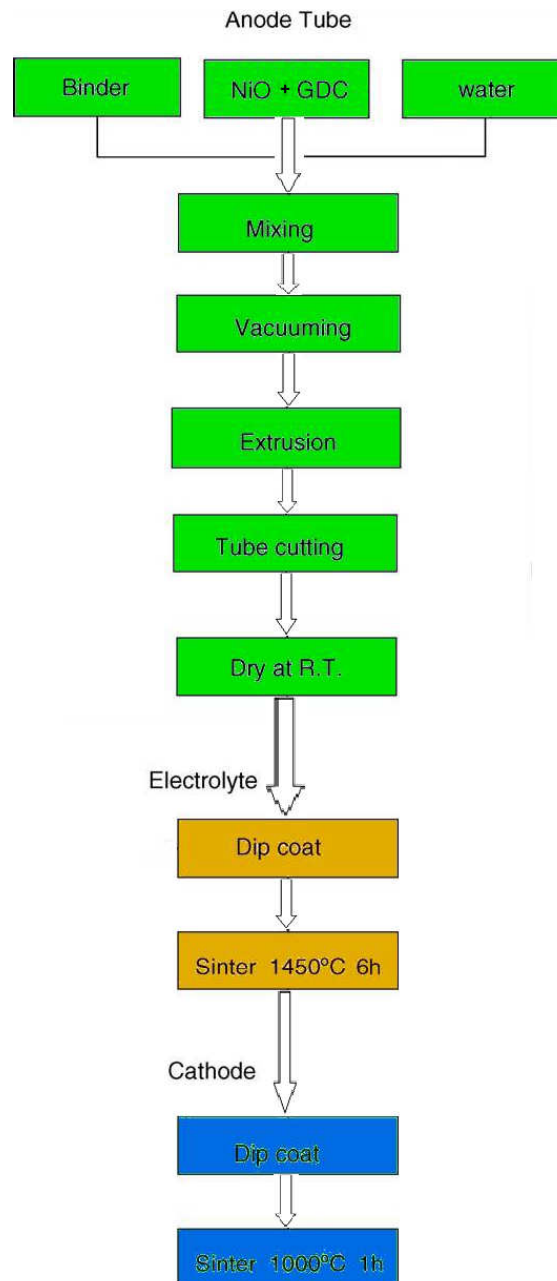


Figure III. 35: Flow Chart of the micro-tubular fabrication process

Anode tubes were extruded from the anode mixture using a ram extruder and a custom made die. The anode tubes were allowed to dry, were cut to the desired length, then dip-coated in GDC electrolyte slurry and allowed to dry. The GDC electrolyte slurry is composed of the same GDC powder described above, and organic ingredients such as binder (poly vinyl butyral), dispersant (fish oil) and solvents (toluene and ethanol). The desired electrolyte thickness was acquired through multiple electrolyte coatings and subsequently the tubes were sintered at 1450°C for 6 hours in air. Next, the electrolyte coated anode tubes were dip-coated in a cathode slurry consisting of $\text{La}_{0.6}\text{Sr}_{0.4}\text{Co}_{0.2}\text{Fe}_{0.8}\text{O}_{3-y}$ (LSCF) and GDC powder, and organic ingredients similar with those of the electrolyte slurry. The cathode dip-coated tubes were dried in air and sintered at 1000°C for 1 hour in air to complete the fuel cell fabrication.

An Environmental Scanning Electron Microscope (ESEM) was used to check the electrode and electrolyte microstructure. Figure III.36 shows cross sectional ESEM images of the fabricated micro-tubular SOFC, with porous electrodes and a dense electrolyte. The size of each cell was 1.8 mm diameter and 12 mm length with active cathode length of 8 mm, whose active cell area is estimated to be 0.45 cm².

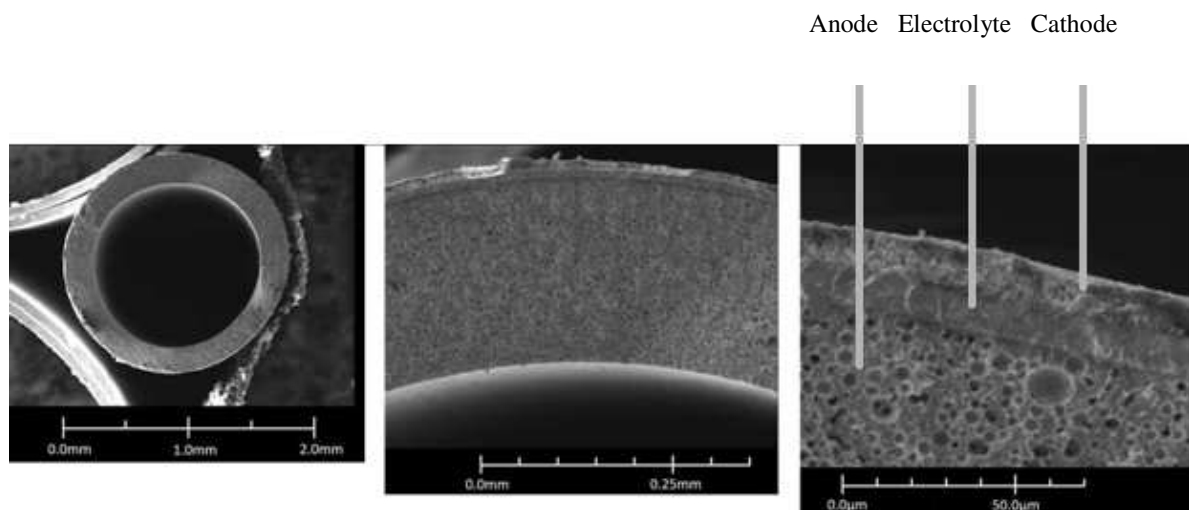


Figure III. 36: SEM Microstructure Images of the Micro-Tubular SOFC

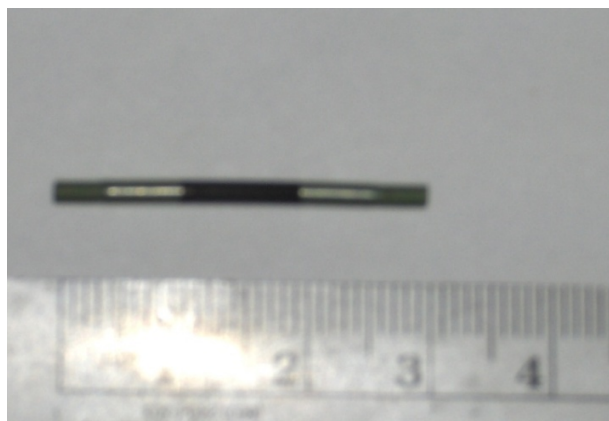


Figure III. 37: Micro tubular fuel cell – NiO-GDC anode support

The others micro-tubular SOFCs, tested at operating temperatures ranging from 750 °C to 850 °C, measuring 1.0 cm in diameter and 5.0 cm in length, have been fabricated using a process similar to the intermediate temperature micro-tubular SOFCs.

High purity monoclinic zirconia powder (Advanced Material Resources, Toronto, Ontario) and high purity yttria powder (Advanced Material Resources, Toronto, Ontario) were ball-milled together using zirconia media to ensure that the yttria and zirconia were well mixed. After drying and screening, the yttria-zirconia powder was then blended with 65wt% nickel oxide (OMG, Westlake, OH). For extrusion, the anode powder was blended with an aqueous binder system in a K-Lab mixer, let the powder sit overnight and then extruded using a ram extruder. The tubes were then cut and dried for 3 days. After drying, green anode tubes were coated with the electrolyte using a basic external mix spray nozzle from Spraying Systems Co. The electrolyte spray mix was prepared from 8 mole percent yttria stabilized zirconia (TZ-8Y, Tosoh Inc.), calcined to reduce the reactivity of the powder and match the shrinkage of the anode. The anode and electrolyte were sintered between 1400 °C and 1550 °C for 4 hours, creating an anode composition of 65wt% NiO and 35wt% 8YSZ covered by a dense 20 µm layer of 8YSZ. After coating, the tubes were hang-fired at a temperature between 1400 °C and 1500 °C. The cathode LSM/8YSZ + LSM, was deposited at the Colorado Fuel Cell Center, by a spray-coating deposition technique.

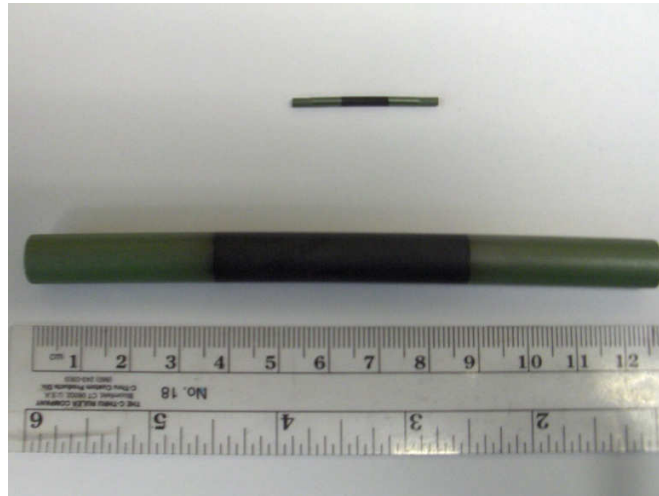


Figure III. 38: Comparison between the smaller and the bigger micro-tubular SOFC fabricated

In order to conduct the experimental activities, measuring the fuel cell's electrochemical performances, has been realized a specific support capable to sustain the fuel cell when it is mounted in the furnace, guaranteeing the gas distribution on the anode and cathode sides and assuring the electrical connection with the electrical load and potentiostat. Each tube has been connected to 2 alumina tubes allowing the inner anode gas distribution sustaining the cell in the furnace. The entire system has been placed on an alumina half tube support in order to yield stronger the structure.

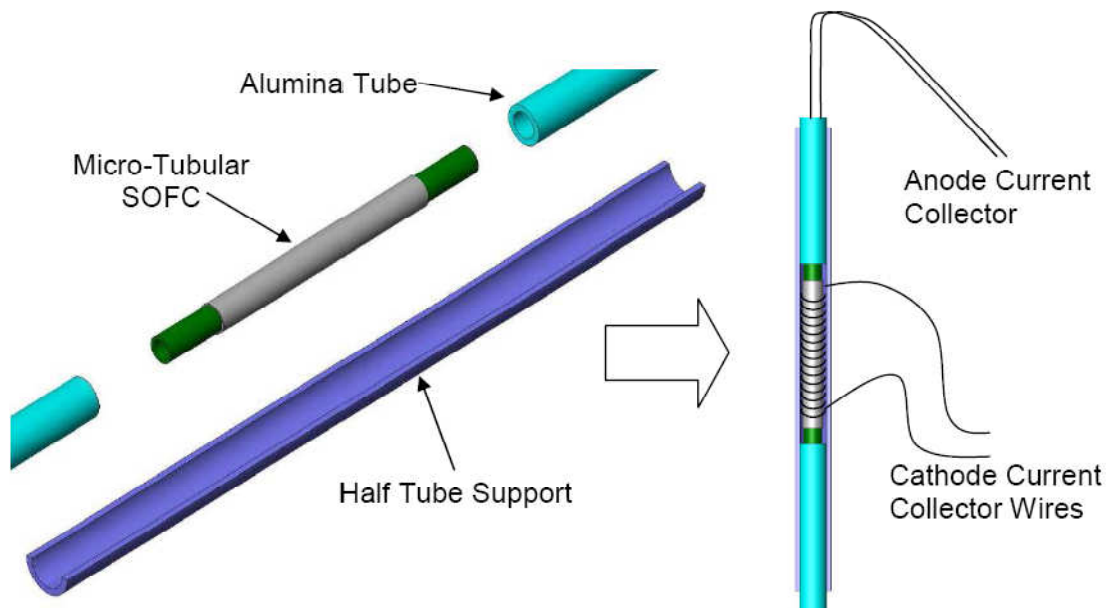


Figure III. 39: Individual Micro-Tubular SOFC Mount Setup

Figure III.40 shows how each micro-tube was mounted for testing within a vertically mounted micro-tube furnace (Carbolite). Cells were tested vertically as shown in Figure III.40 in order to ensure evenly distributed flow of fuel gas across the anode surface (horizontally oriented cells are subject to uneven fuel gas distribution due to gravity).

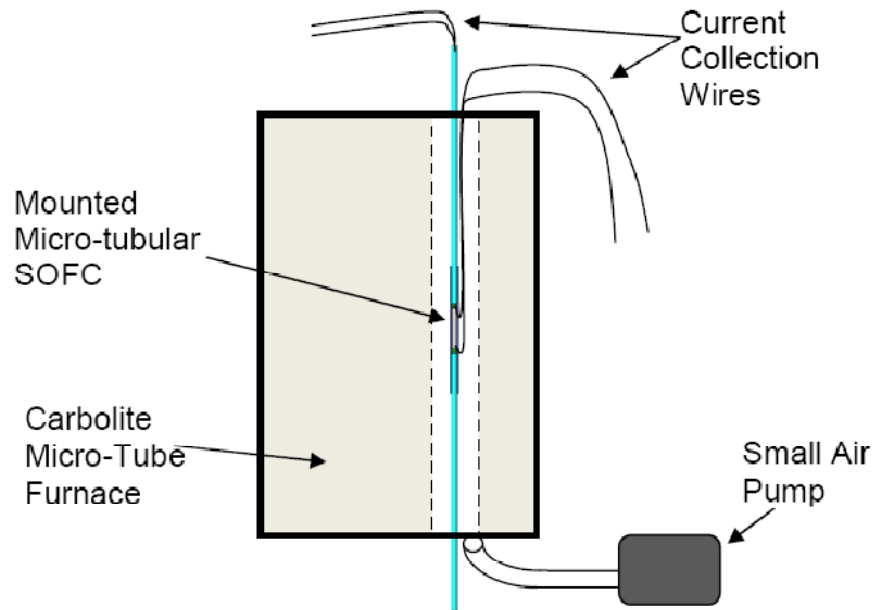


Figure III. 40: Setup of Micro-Tubular SOFC Inside of a Vertical Micro-tube Furnace

Each tube have four 0.5mm silver sensor wires attached for collecting current for anode and cathode sides. The anode electrical connection has been realized using 2 long silver wires fixed using nickel paste; in the case of the bigger micro-tubular cell, was also applied a nickel mesh inside the anode to improve the electrical contact surface. A silver wire has been wrapped around the tubular fuel cell (on the cathode), as a reel, and fixed with silver paste for the cathode electrical connection. The silver paste and nickel paste were brush painted on the cathode and anode surfaces to reduce the contact resistance between the silver sensor wires and the electrode surfaces. The pastes are porous enough at operating temperatures that fuel and oxygen are able to pass through the pastes to arrive at their respective electrodes. The Ceramabond 552 (Aremco) was used as sealant between anode, alumina tubes and alumina half tube support.



Figure III. 41: Anode and Cathode electrical connection – Alumina tubes application

The four current collecting wires from the cell shown in Figure III.39 were connected to the impedance analyzer (Gamry 600) and the electrical load (Chroma 6310 series) at operating temperature ranges between 450~550°C for the smaller tubular SOFCs and between 750-850°C for the bigger tubular SOFCs. Individual cells were run using humidified gases (with various percentage of H₂O depending by the type of test) as fuel to the anode side, while the cathode side (outside surface of tube) was exposed to atmospheric conditions. The type of air pump normally used for small aquariums was used to facilitate new air into the bottom of the micro-tube furnace to assist convective flow of air through the furnace.

The anode of the smaller SOFC was reduced at 450°C for 10 hours before measurement of the I-V information while the anode of the bigger SOFC was reduced at 750°C for 24 hours.

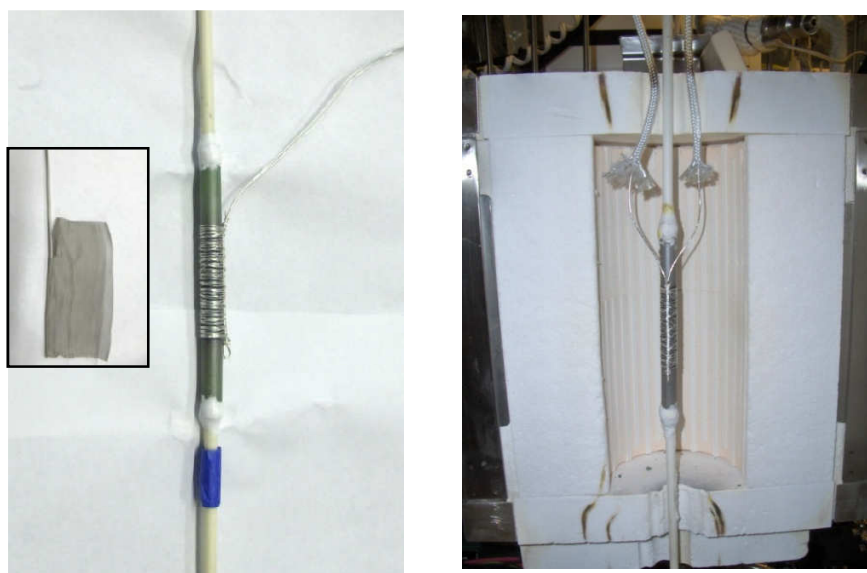


Figure III. 42: Bigger micro-tubular SOFC electrical connection – Mount into the big Furnace. The anode color is green before sintering and gray after sintering process

Impedance information was gained using AC impedance spectroscopy (Gamry 600) in the frequency range from 100 kHz to 0.2 Hz with signal amplitude of 10 mV under open circuit conditions.

Power density and impedance information has been acquired for the micro-tubular SOFCs to quantitatively characterize performance and gain insight into methods for optimization of the microtubular SOFCs.

3.6.3. Experimental Results of the smaller micro-tubular SOFC test.

The start up behavior of the smaller micro-tubular cell was investigated at 450°C and is shown in Figure III.43. For testing of the start up behavior, the anode of the cell was subjected to N₂ while heating up to operating temperature. After arriving at an operating temperature of 450°C, the cell anode was taken off of N₂ and subjected to pure H₂. The cell was able to be reduced in less than 1 min and reached an open circuit voltage (OCV) close to 1.0V in that time.

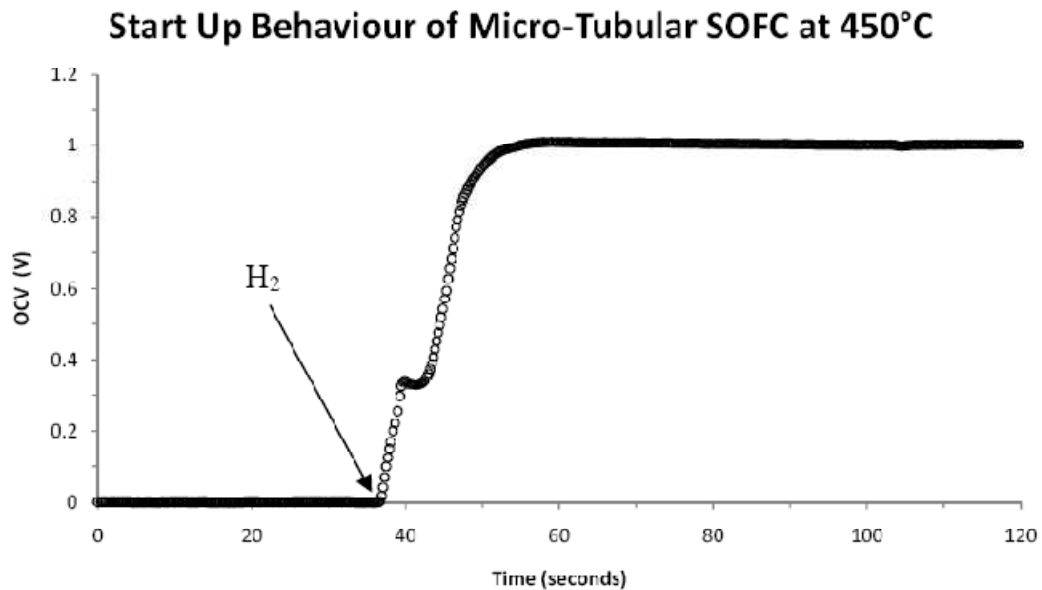


Figure III. 43: Start-up behavior of the smaller micro-tubular fuel cell, reduced with N₂ and after fed with H₂

The maximum performance of the smaller micro-tubular cell, fed by hydrogen, is shown in Figure III.44. The i-V (current density-voltage) curve shape and the power density curve shape are similar to the typical trends registered for others types solid oxide fuel cells. The maximum power densities were measured to be 0.263 W/cm², 0.518 W/cm², and 1.310 W/cm² at 450 °C, 500 °C, and 550°C respectively, obtained for a fuel volume flow of 25 Scm³/min of H₂. These

values show excellent power density performance, with great growing with the temperature: a variation of 100 °C increase the power density of more than 1 W/cm² (the value at 550 °C is about 5 times bigger than the value at 450 °C).

However, the OCV performance of the cell was somewhat low compared to previous studies [11,12]. The OCV dropped from 0.892 to 0.8275 V as the temperature was increased from 450 °C to 550 °C. This drop in OCV can probably be explained by increases in electronic conductivity of the ceria electrolyte with increasing temperature in reducing environments.

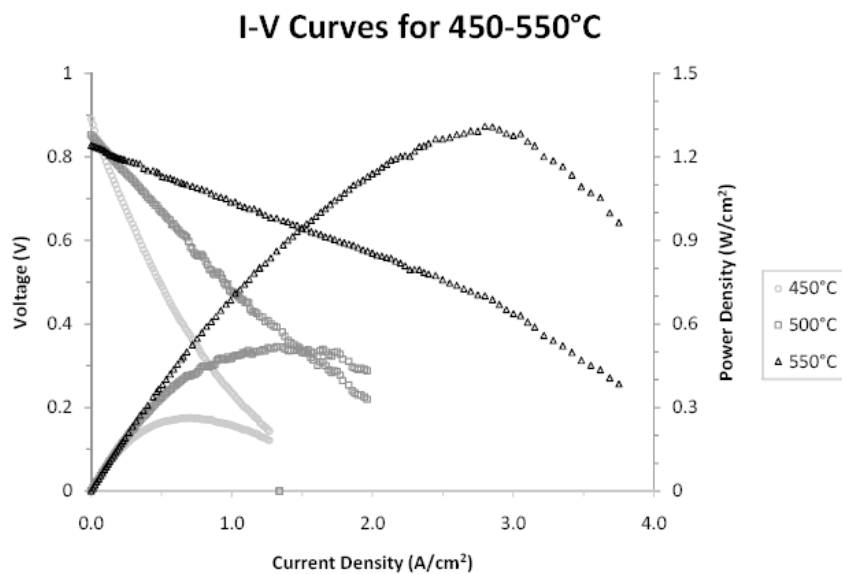


Figure III. 44: *i*-V curves and power density curves for micro-tubular SOFC operating between 450 °C and 550 °C

3.6.4. Effect of flow rate on SOFC's electrochemical performance at different temperature.

Different flow rates of hydrogen were employed, from 1 Scm³/min to 25 Scm³/min, at varying temperature, from 450 °C to 550 °C, in order to measure the electrochemical performance of the smaller micro-tubular SOFC.

The electrical performance was measured by the Chroma electric load over the range from open circuit voltage to 0.15 volts: has been used a minimum value of 0.15 V in order to avoid great degradation in the fuel cells performance.

The electrochemical impedance spectroscopy was measured by galvanostat/potentiostat. Single cells were employed for these experiments. The cells used were 3 cm long (0.9 cm of reactive area length) with a 1.8 mm diameter for an active cell area of 0.5 cm^2 .

In general the more fuel put into a generating system the more electrical power the system will put out. Again in the case of batteries and fuel cells it will be expected that eventually the system will be “overwhelmed” and the power production will flatten out or even fall off. The effect of increasing hydrogen flow rate on the electrical power produced by a 0.5 cm^2 fuel cells, at different temperatures, is shown in the following figures (Figure III.45-III.50).

As expected, the graph shows an increase in power output with increasing fuel flow: at $550 \text{ }^\circ\text{C}$ and for a fuel volume flow of $25 \text{ Scm}^3/\text{min}$ of H_2 , the maximum power density is 1.13 W/cm^2 while, for a fuel volume of $1 \text{ Scm}^3/\text{min}$, the maximum power density is 0.13 W/cm^2 , with a growth of almost one order of magnitude. The rate of increase fall off at the higher fuel flow rates. In fact the difference is less prominent between $15 \text{ Scm}^3/\text{min}$ and $25 \text{ Scm}^3/\text{min}$, while there is a greater difference between the maximum power density at $1 \text{ Scm}^3/\text{min}$, $2 \text{ Scm}^3/\text{min}$, $5 \text{ Scm}^3/\text{min}$ and $15 \text{ Scm}^3/\text{min}$.

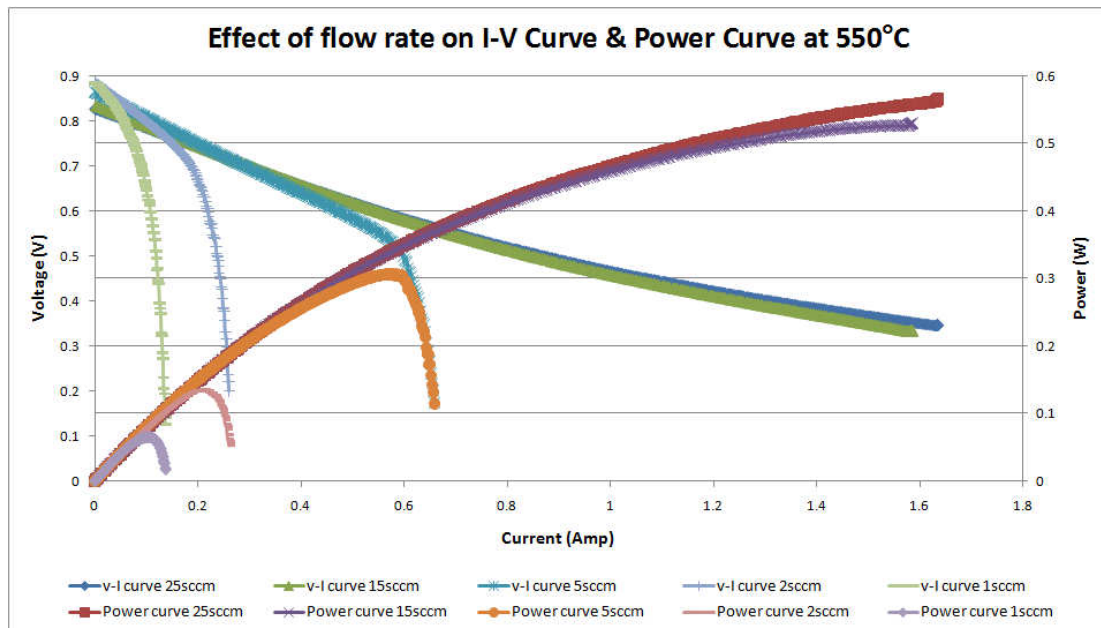


Figure III. 45: Current-Voltage curve and Current-Electric Power curve measured at $550 \text{ }^\circ\text{C}$ for different H_2 volume flow

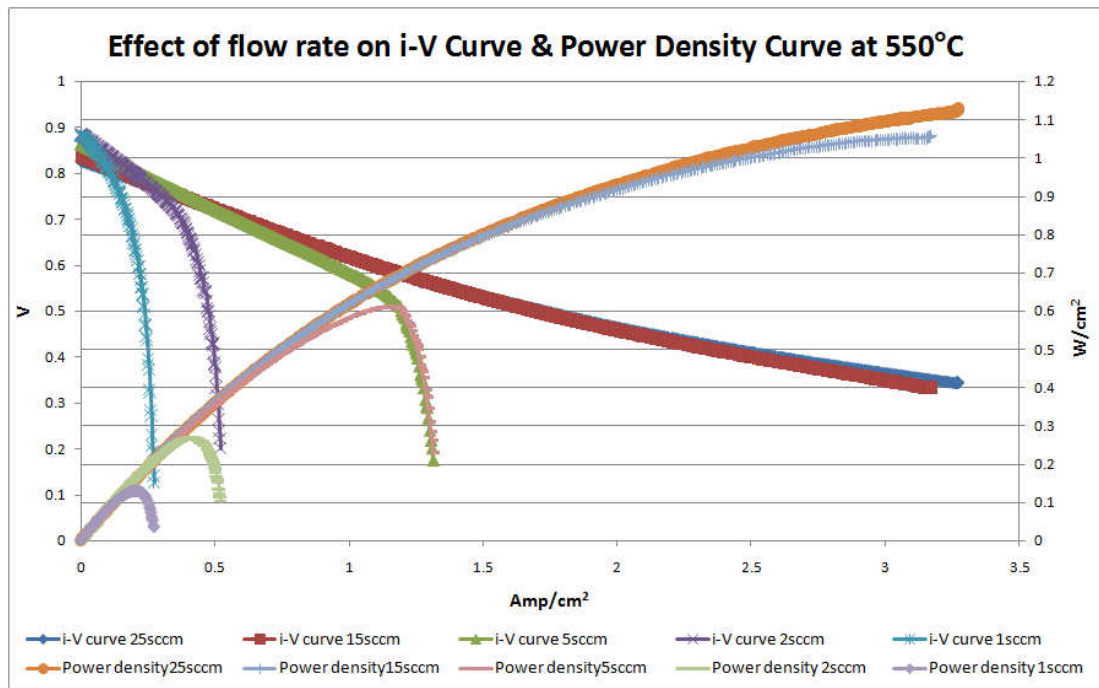


Figure III. 46: Current Density-Voltage curve and Current Density-Power Density curve at 550 °C for different H_2 volume flow rates

The figures III.45-46 show as at 15 Scm^3/min and 25 Scm^3/min the rate of increase falling off and both I-V curve and power curve are almost placed one upon another. Furthermore, at lower fuel flow rate, is clearly shown the effect of the concentration polarization while at higher flow rate the maximum current density is far away from anode and cathode limiting current density.

Figure III.47 and III.48 show SOFC's performance at 500°C while figures III.49 and III.50 report the same current-voltage current-electric power, current density-voltage and current density-power density curves, evaluated anyway at 450°C.

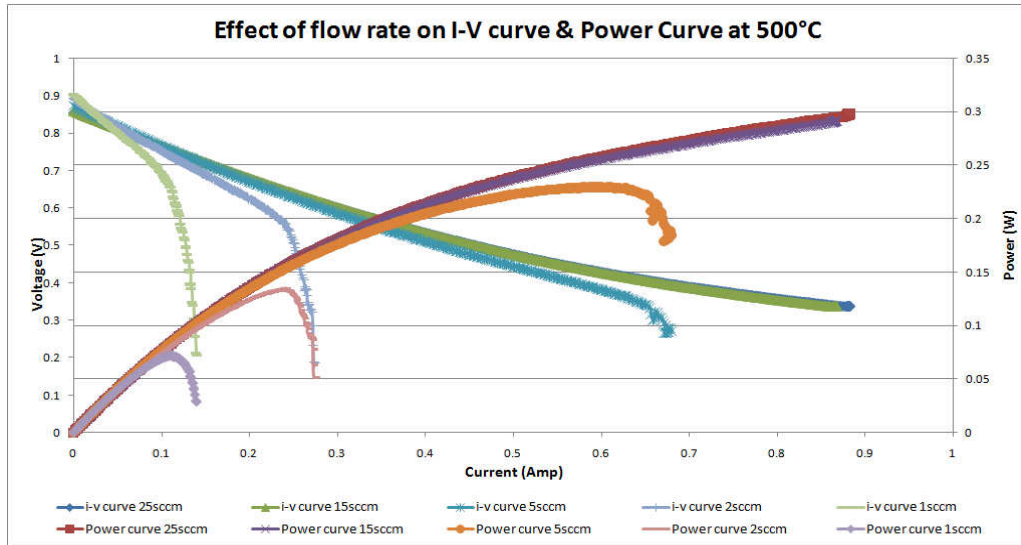


Figure III. 47: Current-Voltage curve and Current-Electric Power curve measured at 500 °C for different H_2 volume flow

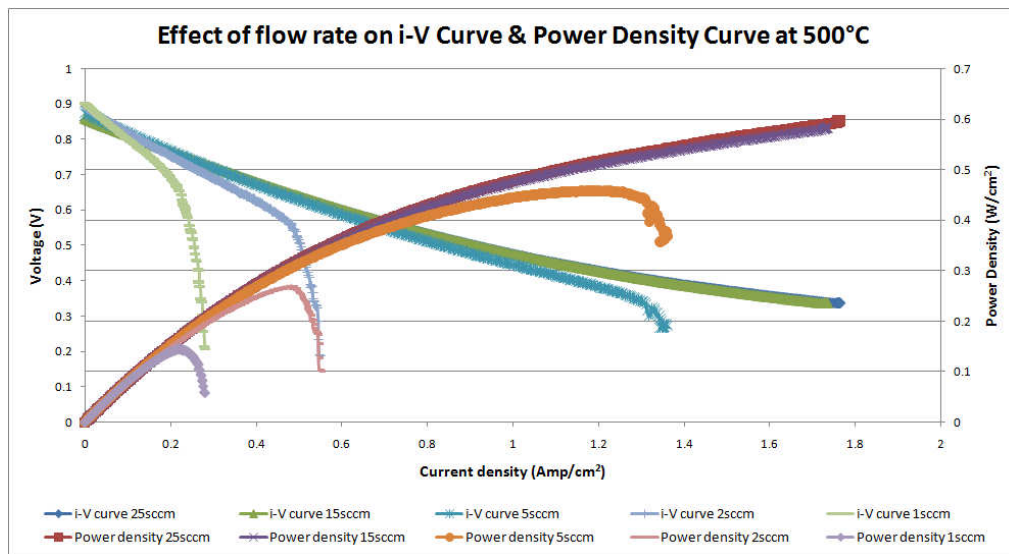


Figure III. 48: Current Density-Voltage curve and Current Density-Power Density curve measured at 500 °C for different H_2 volume flow

The difference between the maximum power measured at the highest and the lowest flow rate is lower (0.47 W/cm^2 at $500 \text{ }^\circ\text{C}$ and 0.10 W/cm^2 at $450 \text{ }^\circ\text{C}$) than the difference's value measured at $550 \text{ }^\circ\text{C}$ ($\approx 1.0 \text{ W/cm}^2$).

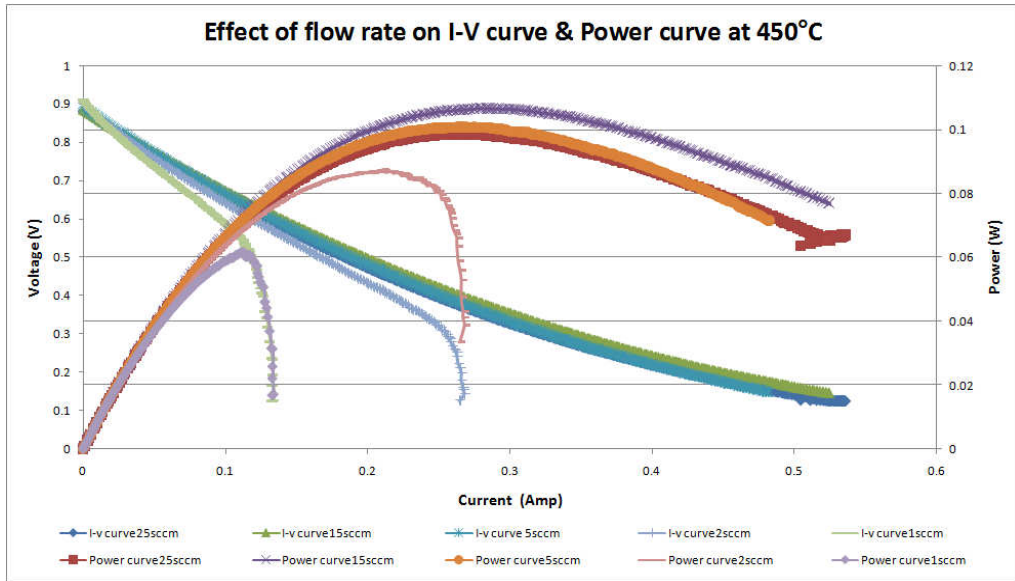


Figure III. 49: Current -Voltage curve and Current –Electric Power curve measured at 450 °C for different H_2 volume flow

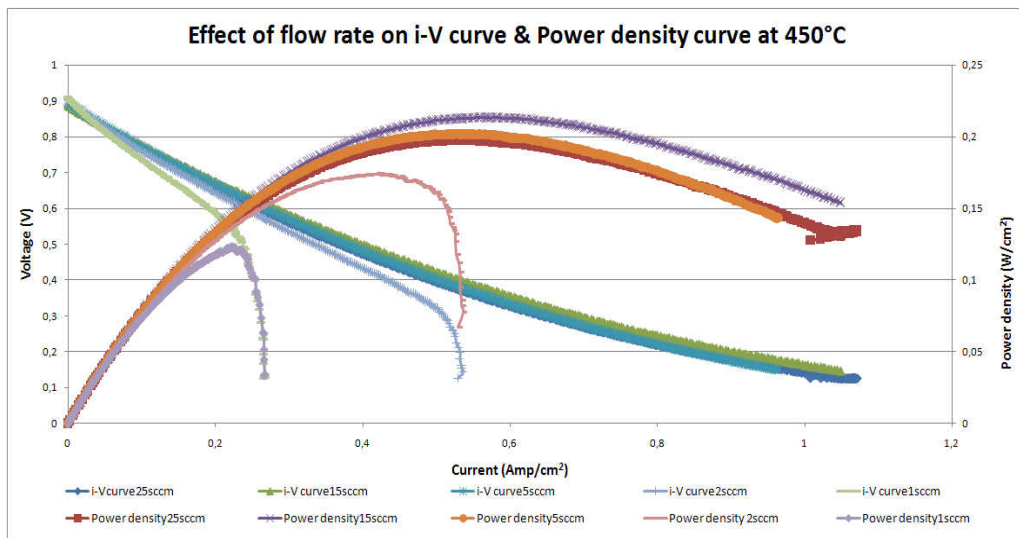


Figure III. 50: Current Density-Voltage curve and Current Density-Power Density curve measured at 450 °C for different H_2 volume flow

At 450 °C, for hydrogen volume flow of 5 Scm^3/min , 15 Scm^3/min and 25 Scm^3/min , both I-V curve and power curve are almost placed one upon another. Instead at 500 °C only the curves at 15 Scm^3/min and 25 Scm^3/min are almost superimposables.

At 500 °C, for 1 Scm^3/min , 2 Scm^3/min and 5 Scm^3/min , is clearly shown the effect of the concentration polarization while at 450 °C, only for 1 Scm^3/min and 2 Scm^3/min this phenomena is clearly visible.

3.6.5. Effect of temperature on SOFC's electrochemical performance at different flow rate

In the next figures is reported the trend of the I-V curves and the electric power curves of a single fuel cell valued at constant hydrogen volume flow and at different temperatures. The trend shows behavior substantially different depending on whether use low or high volume flow.

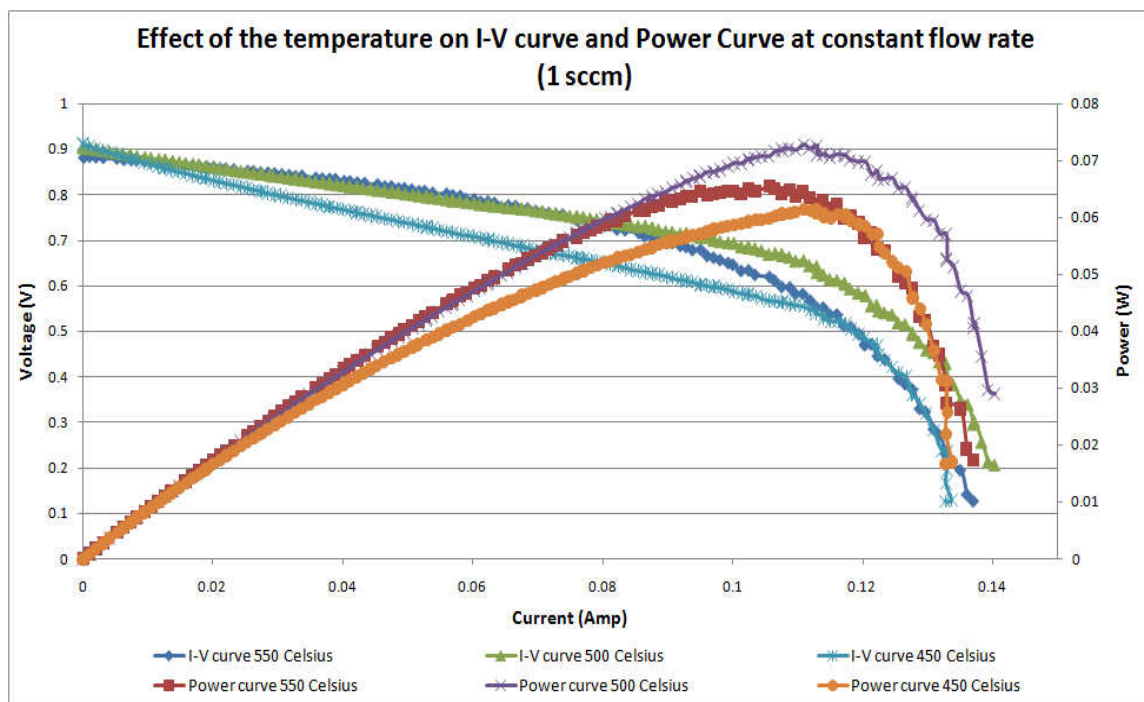


Figure III. 51: Current-Voltage and Current-Electric power curves at constant volume flow ($1 \text{ Scm}^3/\text{min}$) and at 450°C , 500°C and 550°C

In particular, it is possible to notice how, at low volume flow, the effect of temperature is not so much evident or completely absent. The fluctuations in the electrical power output (less than 10 mW), revealed at the volume flow of $1 \text{ Scm}^3/\text{min}$ and reported in Figure III.51, can be attributed much more to intrinsic uncertainties of measuring instruments (flow meter, electric load) than at changes in the electrochemical properties of the cell.

At $2 \text{ Scm}^3/\text{min}$, the maximum electric power supplied by the cell increase of 55% from 450°C to 550°C , passing from 90 mW to 140 mW.

Both at 1 Scm³/min and at 2 Scm³/min the maximum electric power for different temperature is reached in a small interval of current: 0.10-0.12 Amp at 1 Scm³/min and 0.20-0.25 Amp at 2 Scm³/min.

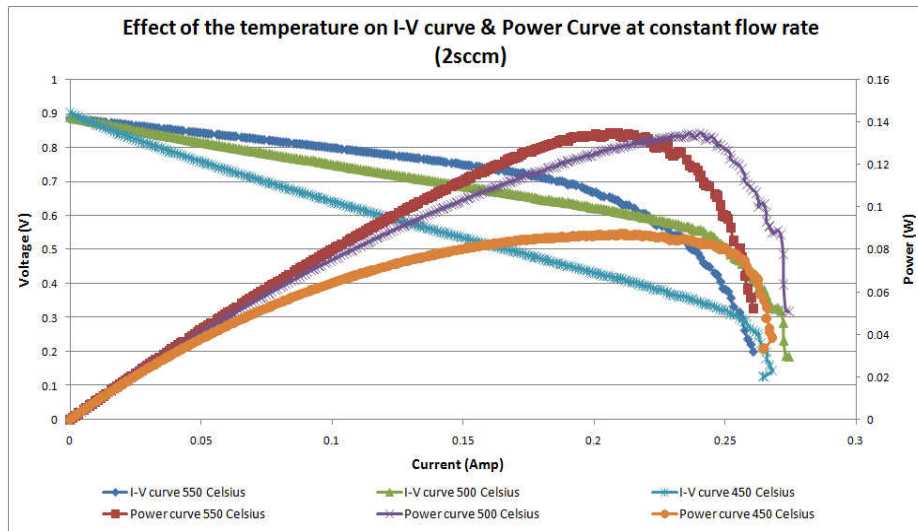


Figure III. 52: Current-Voltage and Current-Electric power curves at constant volume flow (2 Scm³/min) and at 450°C, 500°C and 550 °C

The temperature effect becomes significant as the hydrogen volume flow increase. At volume flow of 5 Scm³/min the maximum electric power supplied at 550 °C is 3 times higher than the maximum power provided at 450 °C. At 15 Scm³/min and at 25 Scm³/min the maximum electric power supplied at 550 °C is 5 times higher than the maximum power provided at 450 °C.

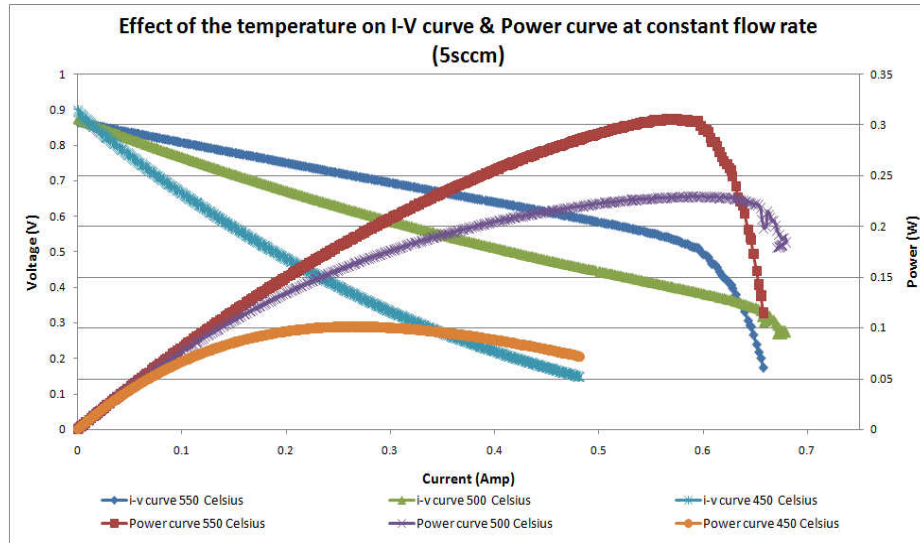


Figure III. 53: Current-Voltage and Current-Electric power curves at constant volume flow ($5 \text{ Scm}^3/\text{min}$) and at 450°C , 500°C and 550°C

Once again the trend show as the current-voltage and the current-electric power curves at $15 \text{ Scm}^3/\text{min}$ and at $25 \text{ Scm}^3/\text{min}$ are almost superimposables with similar differences between the maximum power registered at 450°C and at 550°C .

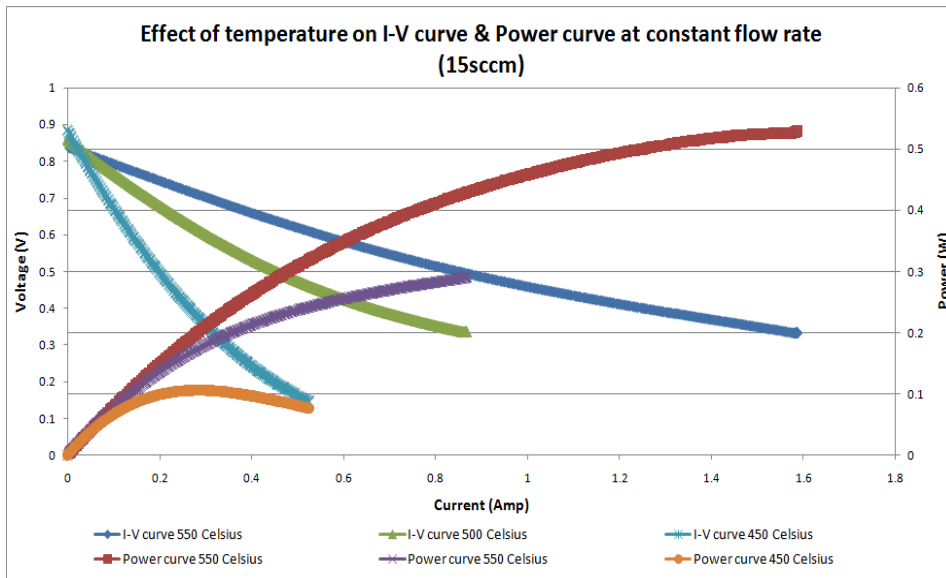


Figure III. 54: Current-Voltage and Current-Electric power curves at constant volume flow ($15 \text{ Scm}^3/\text{min}$) and at 450°C , 500°C and 550°C

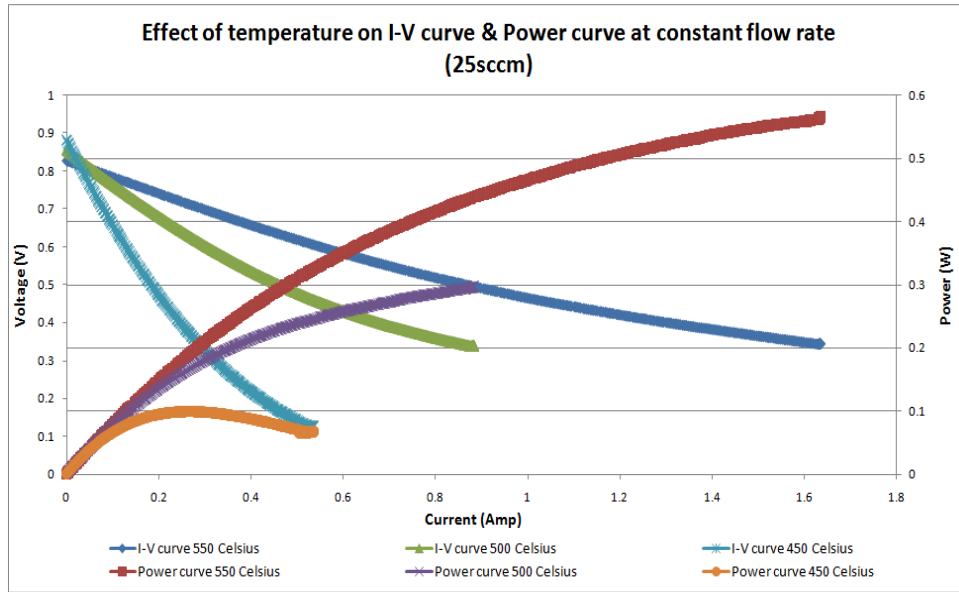


Figure III. 55: Current-Voltage and Current-Electric power curves at constant volume flow (15 Scm³/min) and at 450°C, 500°C and 550 °C

At high flow rate is clearly shown as the maximum electric power, at different temperatures, is reached at diverse value of current. At 5 Scm³/min, the maximum electric power supplied at 550 °C is reached for a current value of 0.6 Amp that is 2 times the value registered at 450 °C (0.3 Amp). At 15 Scm³/min and 25 Scm³/min the value at 550 °C is 5 times greater that the value at 450 °C.

3.6.6. Effect of temperature and flow rate on Open Circuit Voltage, Current and Power Density supplied by the SOFCs.

Figure III.56 show the effect of temperature on the Open Circuit Voltage for different value of the hydrogen volume flow. As can be seen from the graph below the open circuit voltage has the expected downwards trend with temperature for all the different flow rate of fuel.

Looking at the Nernst equation for the hydrogen reaction:

$$E = E^0 - \frac{RT}{2F} \ln \left(\frac{p(\text{H}_2\text{O})}{p(\text{H}_2)p(\text{O}_2)} \right) \quad (\text{III.28})$$

It can be seen that as the partial pressure of hydrogen is increased E will be expected to increase, by the result of the experimental activities seems that the OCV trend is opposite to the Nernst equation indication. In fact for all the different temperature, the OCV became lower when the flow rate of hydrogen increase and this phenomenon is greater at higher temperature.

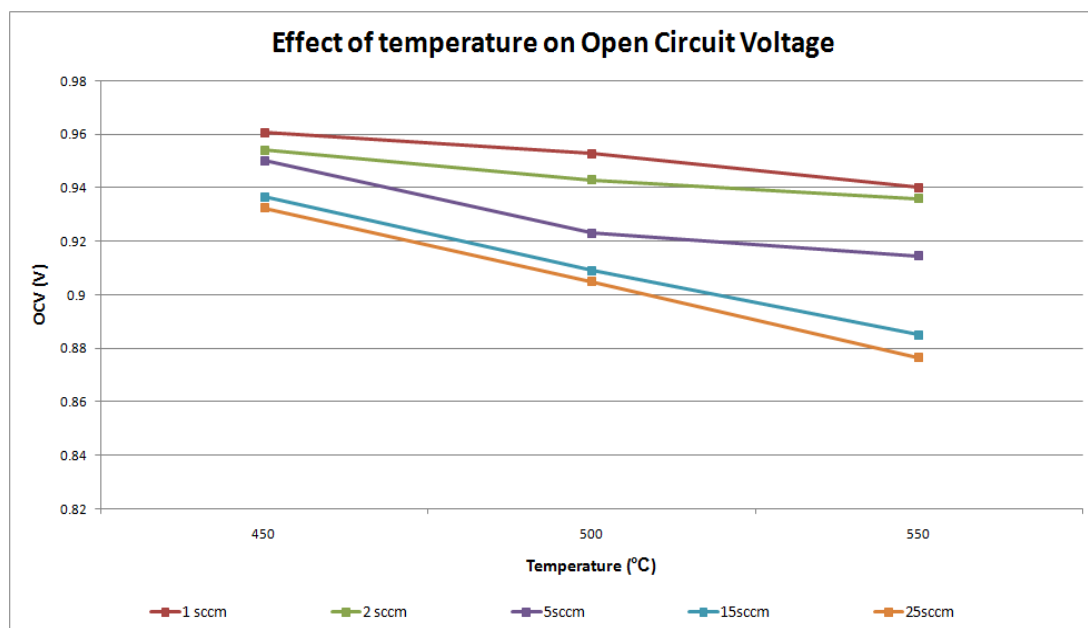


Figure III. 56: Effect of temperature on OCV for different hydrogen volume flow

This phenomena, opposite to the theoretical trend of Nernst equation, could be explained with the fact that the electrolyte used in this cell is a Ceria-based (GDC) oxide ion conductor. This material could lead to electronic conductivity and electronic current could flow through the electrolyte even at open circuit, with the result that the final voltage is somewhat lower than the theoretical value. The greater difference measured on the OCV at 550°C, for different hydrogen volume flow, compared with the values at 450°C, seems to confirm this possibility, with greater electronic conductivity of the ceramic materials at higher temperature.

The Figure III.57 shows the effect of the hydrogen volume flow on the Open Circuit Voltage for different value of temperature. As mentioned before the graph shows an expected decrease in the OCV value with increasing fuel flow rate, with the slope of decrease that fall off at the higher fuel flow rates.

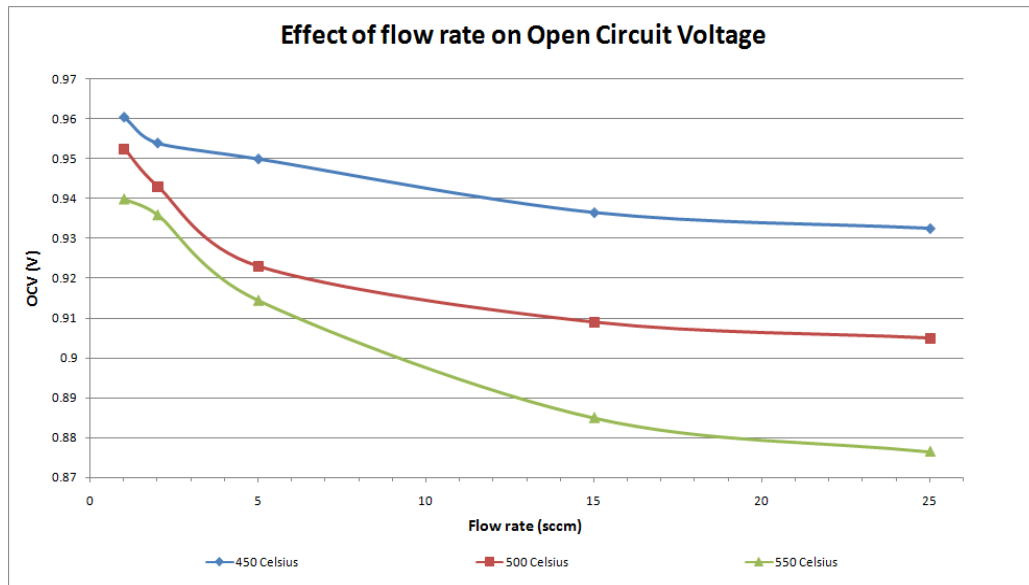


Figure III. 57: Effect of flow rate on OCV at different temperature

The Amps produced in an electrical system is directly related to the numbers of electrons involved. According to Faraday's law of electrolysis, 96,490 Coulombs are produced per mole of electrons. Oxygen ions carry 2 electrons per ion, therefore one mole of oxygen ions will produce 192,980 Coulombs. In turn, the amounts of oxygen ions that can pass through a Gadolinium Doped Ceria electrolyte depend on the temperature of the electrolyte as well as on the dopant level and thickness of electrolyte. Thus the amount of current produced by a tubular solid oxide fuel cell should increase with temperature. To investigate this, the current delivered by the cell is reported on figure III.58; the current value was measured at 0,7 volts for different temperature and different fuel flow rate.

The oxygen flux through a particular thickness of electrolyte is exponential with respect to temperature. As current is directly dependent on the flux of oxygen ions it would be expected that this should show a hyperbolic trend as the temperature of fuel cell is increased. In fact the graph shows, as expected, an exponential relationship between increasing temperature and increasing current produced by the cell, but only for high flow rate (5-15-25 Scm³/min).

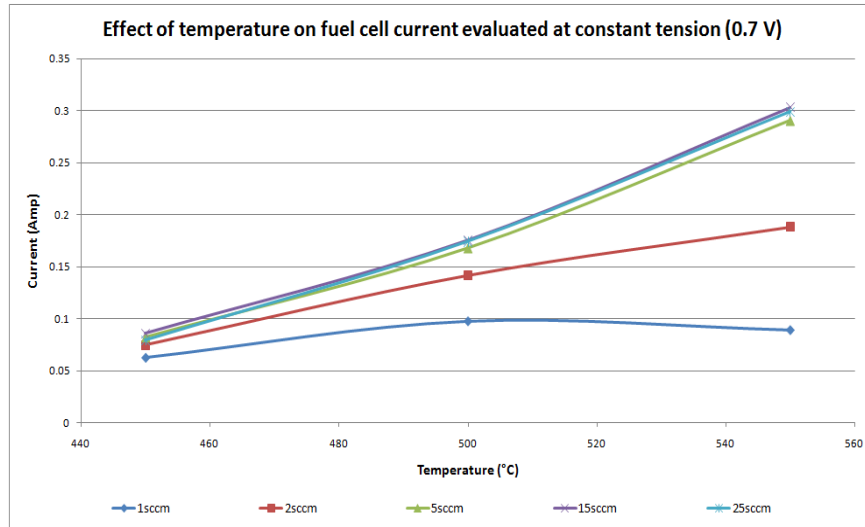


Figure III. 58: Current supplied by the fuel cell at 0.7 V, at different temperature and for different H₂ volume flow.

It is possible that other factors are mitigating against the increase of ion flow, this include the increases resistance within the current collection wires as the temperature is increased and the limiting effects of the kinetics of reaction. For example the amount of hydrogen adsorbed onto the catalytic surface may already be the limiting factor rather the oxygen flux through the electrolyte.

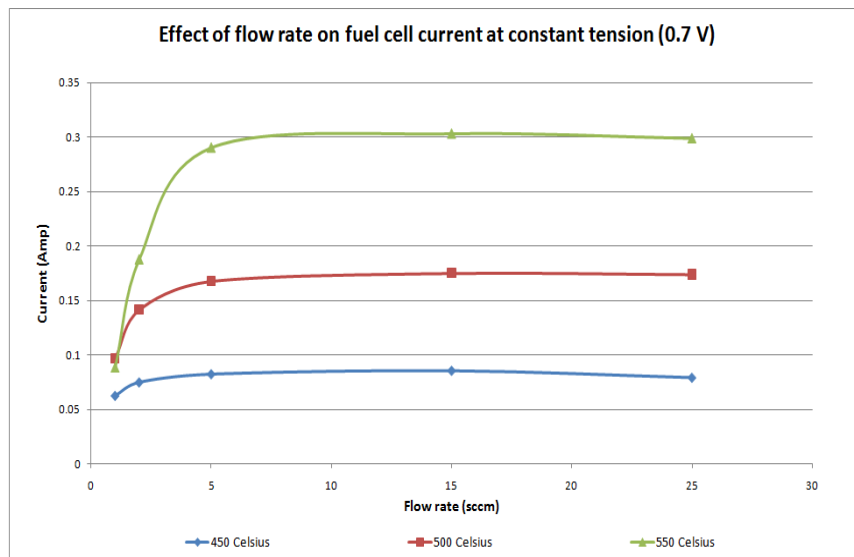


Figure III. 59: Current supplied by the cell at 0.7 V, at different H₂ volume flow and for different temperature.

Finally, the effect of increasing hydrogen flow rate on the current and the power supplied by the cell at 0,7 volts, at different temperature (450°C, 500°C and 550°C), is shown in Figures III.59 and III.60.

The graphs show an increase in current and power output with increasing fuel flow rate, with the increase falling off, as expected, at the higher fuel flow rates.

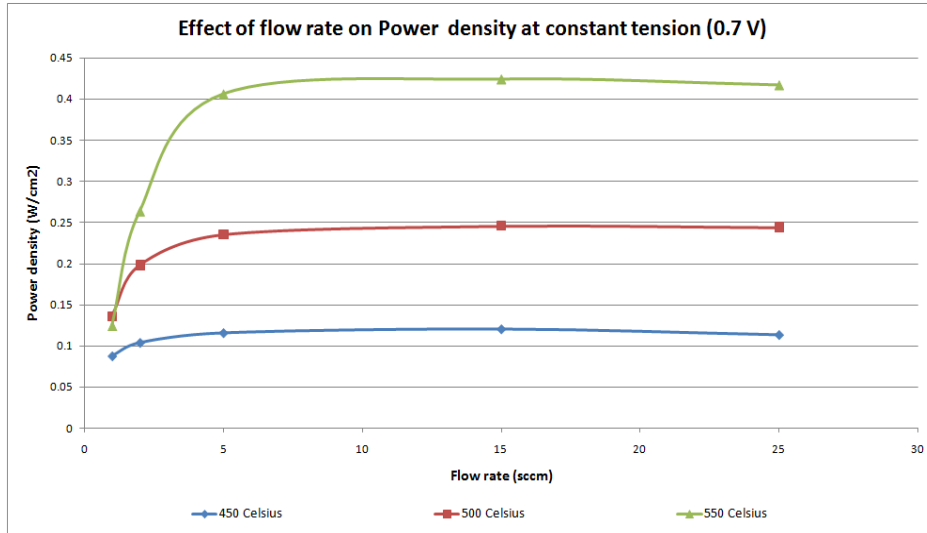


Figure III. 60: Trend of Power Density at 0.7 V for different H₂ volume flow and for different temperature.

3.6.7. Efficiency and fuel utilization

Because a fuel cell converts fuel direct to electricity in an isothermal process the amount of energy available depends not on ΔH of the reaction but on the ΔG of the reaction. Thus the losses normally associated with the heat engines do not apply and higher efficiencies can be obtained. When compared to a heat engine the maximum efficiency of a fuel cells is given simply by:

$$\eta_{\max} = \frac{\Delta G}{\Delta H} \quad (\text{III.29})$$

Thus for the reaction of a solid oxide fuel cell running on hydrogen the maximum efficiency at 298 K and 1123 K is:

$$\eta_{\max(298\text{K})} = \frac{229}{242} = 95\% \quad \eta_{\max(1123\text{K})} = \frac{179}{242} = 74\% \quad (\text{III.30})$$

In order to value the real efficiency of a fuel cells is necessary to consider the real electric power produced by the cell cleaned out by the three principal source of irreversibility present on the cell:

- Ohmic polarization;
- Concentration polarization;
- activation polarization

Thus the final electric power produced by the cell can be valued multiplicand the current and the voltage of the cell measured by the electric load instrument; the real efficiency can be valued by:

$$\eta_{el,real} = \frac{P_{el}}{\dot{n}_{fuel} \times \Delta H} \quad (III.31)$$

with:

- P_{el} = Electric power produced by the fuel cell;
- \dot{n}_{fuel} = fuel molar flow;
- ΔH = variation of enthalpy of reaction.

As shown before, fuel cells are unable to use 100% of the fuel fed at the anode compartment and for this reason has been introduced the fuel utilization factor:

$$U_f = \frac{\dot{n}_{fuel,reacted}}{\dot{n}_{fuel}}; \quad 0 < U_f < 1;$$

with:

- $\dot{n}_{fuel,reacted}$ = fuel molar flow reacted on the fuel cell;
- \dot{n}_{fuel} = fuel molar flow fed at the anode compartment.

In order to valued the effective ratio of conversion of a fuel cell is possible to introduce another efficiency factor that take in count the real fuel flow rate that reacted on the cell:

$$\eta = \frac{P_{el}}{U_f \times \dot{n} \times \Delta H} \quad (III.32)$$

The utilization of available fuel will depend on the amps produced by the cell and could be valued by the following relation:

$$U_f = \frac{I}{n^{el} \times \dot{n}_{fuel} \times F} \quad (III.34)$$

with:

- I = current produced by the fuel cell (measured by the electric load instrument);
- n^{el} = number of electrons for mole of fuel reacted (2 for hydrogen);
- \dot{n}_{fuel} = fuel molar flow fed at the anode compartment;
- F = Faraday's constant.

This means that as the voltage of a cell is reduced, increasing the amps produced, a greater portion of the available fuel should be utilized. This efficiency factor take in count the fact that the remaining fuel that not react in the cell, could be used in another fuel cell or in a different devise to produce additional electrical energy.

The electrical efficiency of the fuel cell has been evaluated starting from the consideration listed before. The figure III.61 shows the trend of the electrical efficiency versus the fuel utilization factor, evaluated using the current I produced by the cell and the molar flow of hydrogen provided to the cell. Here, it is clearly shown as at the higher flow rate correspond the lower electrical efficiency. The maximum η_{el} is 12% at 25 Scm³/min and less than 20% at 15 Scm³/min. At lower flow rate the electrical efficiency and the fuel utilization is much higher: η_{el} is around 37% at 1-2 Scm³/min and 33% at 5 Scm³/min, with fuel utilization factors respectively of 73% and 81%.

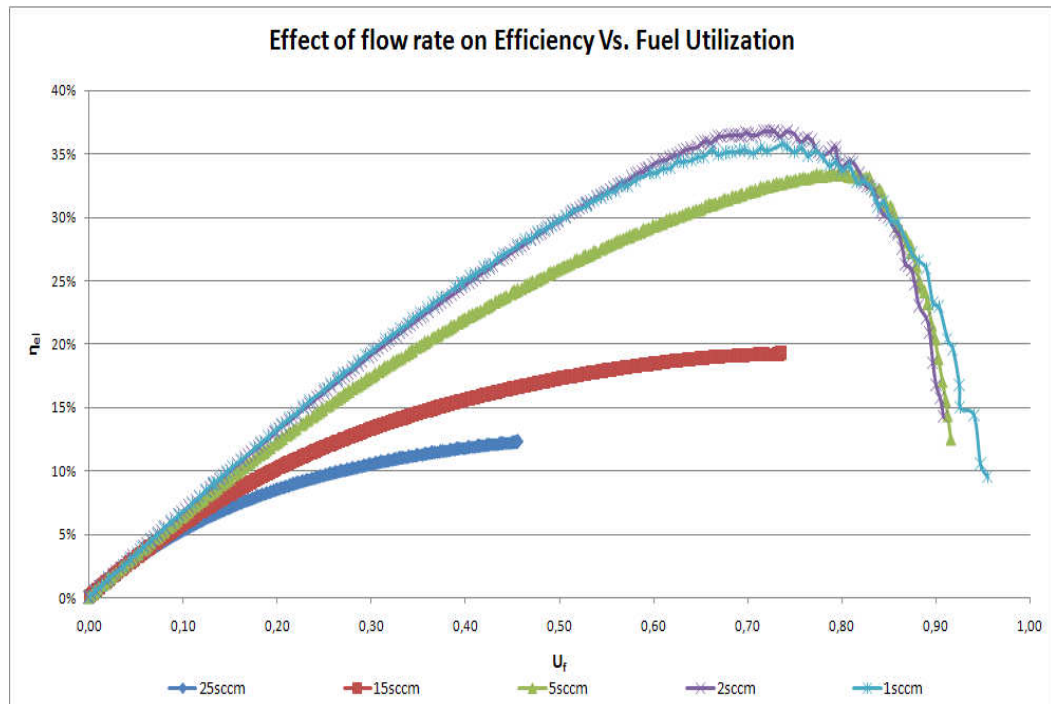


Figure III. 61: Efficiency of fuel cell at 550 °C for different fuel flow rates.

As mentioned in the paragraph 3.6.4, vice versa the maximum power density is obtained for higher fuel volume flow. So depending on the operation condition its possible to decide which fuel volume flow is necessary to use: if it is necessary to have the maximum power it is required to work with high flow rates, but if it is necessary to have the maximum efficiency instead it is necessary to operate at lower flow rates. Probably, the fuel flow rate of 5 Scm^3/min represent the best compromise: the efficiency is 33% with a fuel utilization of 81% and a power density of 600 W/cm^2 and a current density of 1.2 Amp/cm^2 .

Besides the electrical efficiency reported in Figure III.61, it is possible to obtain the gross electrical efficiency taking in count that a quote of the inlet fuel not react in the cell and could be used to produce additional electrical energy. The figure III.62 shows the gross electrical efficiency versus the fuel utilization factor. Clearly, in this case the trend decrease because when produce small current the system is capable to convert the chemical energy much more efficiently; at high current density more losses are present and reduce the efficiency.

In this case the maximum efficiency, at 70% of fuel utilization, is around 50% at 1-2 Scm^3/min and 45% at 5 Scm^3/min .

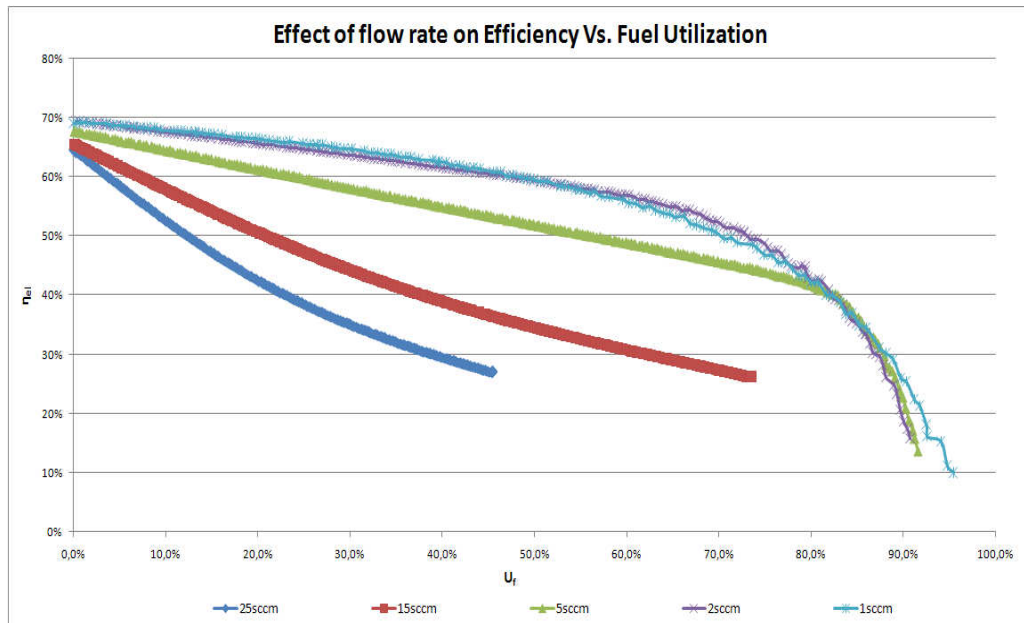


Figure III. 62: Gross electrical efficiency, calculated taking in count the real amount of fuel that react on the cell

The limit of the procedure used to value the efficiency of a fuel cell could be the way the fuel utilization was calculated. In fact the expression used doesn't take in count the internal and fuel crossover current caused by leakage and electronic conductivity between anode and cathode.

For solid oxide fuel cells these value are generally negligible; in the case of GDC electrolyte nevertheless is possible that the electronic conductivity is not so negligible, causing a difference between the theoretical and real value. In order to value the real fuel utilization factor will be necessary to conduct a gas chromatography analysis of the outlet gas of the fuel cell in order to determine the real percentage of hydrogen converted in the cell (this analysis is out of the scope of this study).

3.6.8. Electrochemical Impedance Spectroscopy measurement (EIS)

The impedance spectra gathered from the micro-tubular SOFCs is shown in Figure III.63, III.64 and III.65. The ohmic resistances of the micro-tubular cell were measured to be approximately 0.65 Ω, 0.33 Ω, and 0.2 Ω at 450 °C, 500 °C, and 550°C respectively. These measured resistances show improvement over resistances quoted in previous studies [11,12]. The reason for this improvement is likely due to decreased contact resistance obtained in this cell through careful preparation with silver and nickel pastes. The decreased contact resistance

would lead to better current collection from the cell and the improved cell I-V performance confirms this notion.

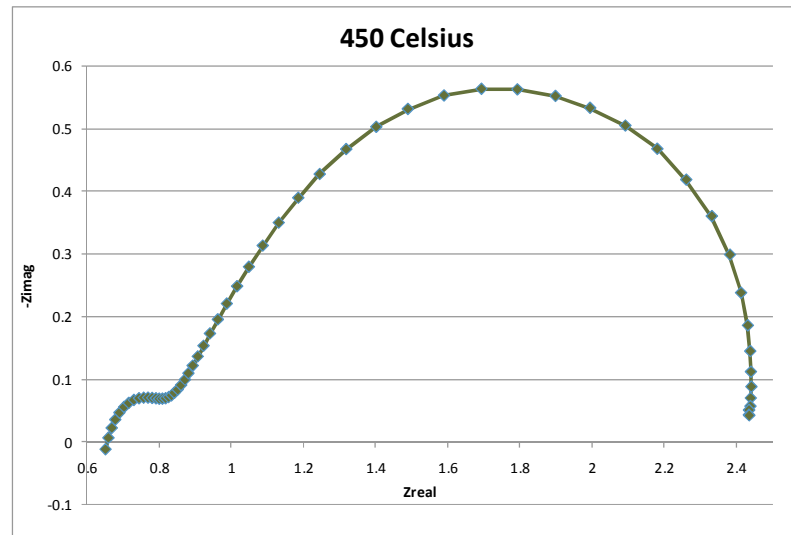


Figure III. 63: Electrochemical Impedance Spectroscopy measured at 450°C

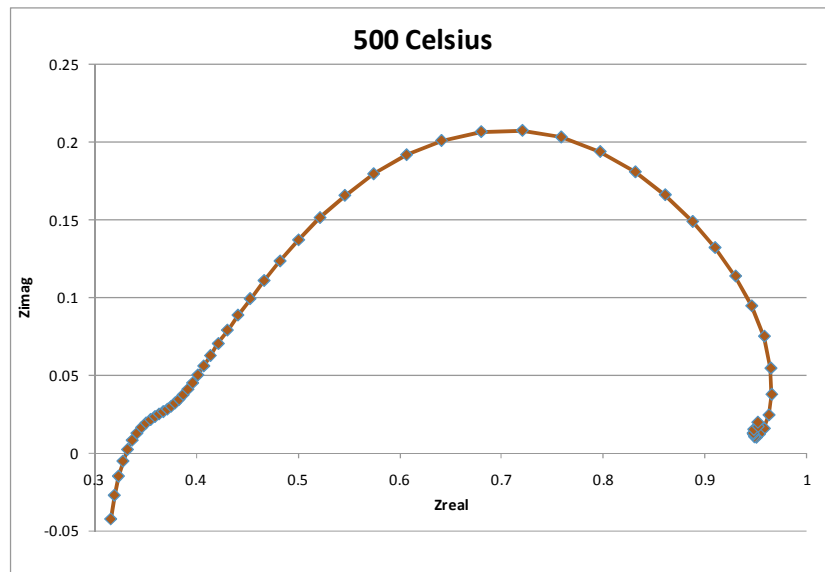


Figure III. 64: Electrochemical Impedance Spectroscopy measured at 500 °C

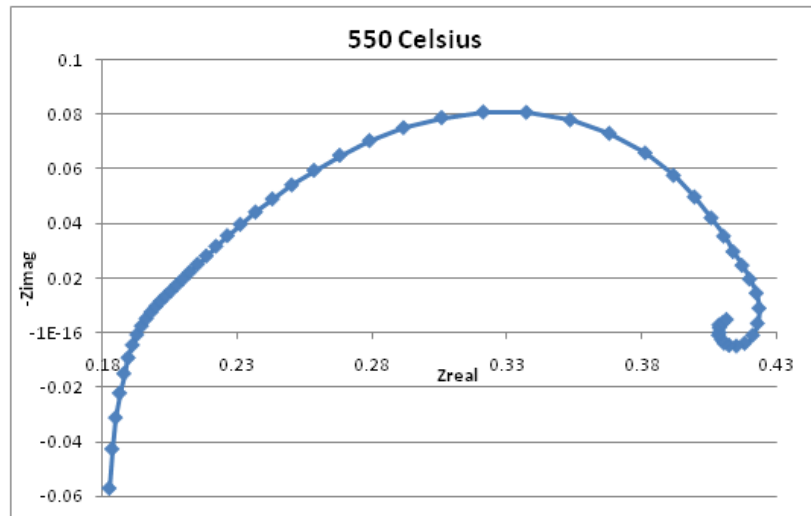


Figure III. 65: Electrochemical Impedance Spectroscopy measured at 550°C

Figure III.66 shows clearly the comparison between the impedance spectra gathered at 450°C, 500 °C and 550 °C. Increasing the operating temperature the shape of the impedance curve became smaller reducing both ohmic and activation polarization. At 450 °C it is possible to distinguish both the anodic and cathodic activation polarization curve represented by the two semi circle. At higher temperature the cathode impedance masks the impedance of the anode.

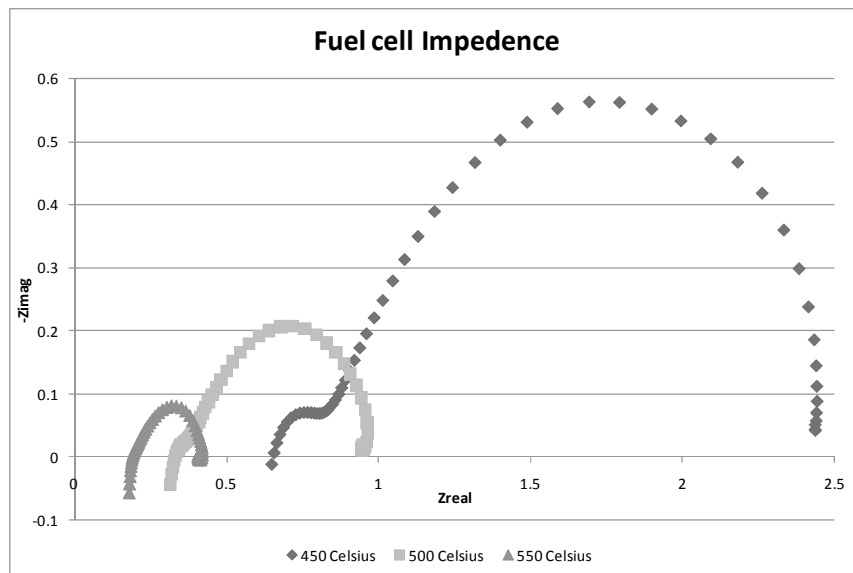


Figure III. 66: Impedance Spectroscopy of Micro-tubular SOFC from 450-550°C

3.6.9. Electrochemical performance with different fuels

In order to value the ability of this type of solid oxide fuel cells to work with different kind of fuels, have been conducted different experimental tests to understand the ability of this SOFC to resist at carbon depositions phenomena and to determine the ability of this cell to carry out the internal reforming of carbonaceous fuels.

The performance of a fuel cell was measured at 550°C, before with 25 Scm³/min of hydrogen and after with gas mixture that gradually grow carbon monoxide presence reducing the hydrogen composition. The Figure III.67 shows the current-voltage (I-V) curve and the Current-Electric Power Curve measured with 25 Scm³/min of hydrogen and after with a mixture of 20 Scm³/min of hydrogen and 5 Scm³/min of carbon monoxide for three times . The values with hydrogen are the higher shown in Figure III.67 but is clearly visible as the other curve are perfectly superimposable. These curves show the ability of this micro-tubular cell to work with carbon monoxide fuel reproducing the same performance as with hydrogen.

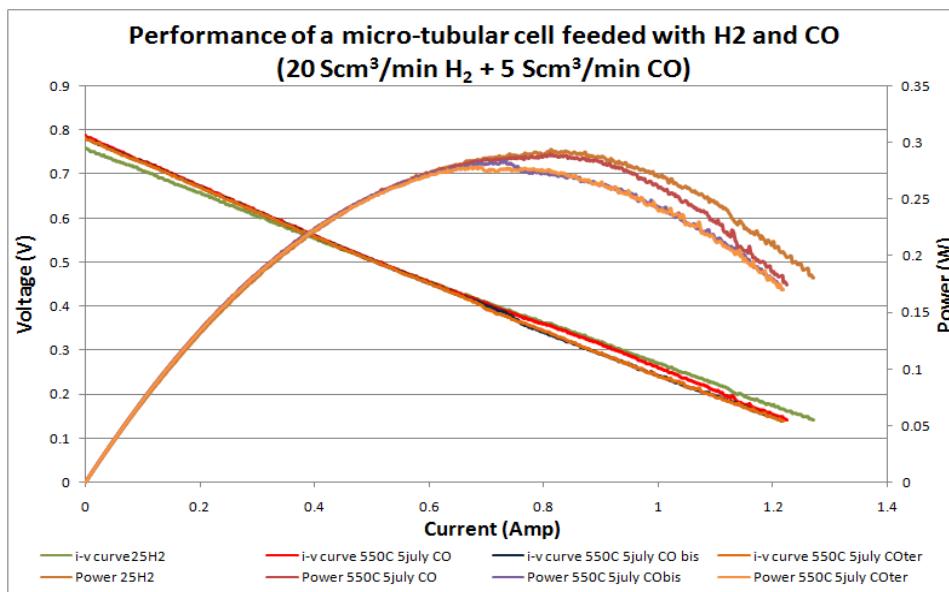


Figure III. 67: Fuel cell performance with hydrogen – carbon monoxide.

The Figure III.68 shows the current-voltage (I-V) curve and the Current-Electric Power Curve measured with 25 Scm³/min of hydrogen and after with a mixture of 15 Scm³/min of hydrogen and 10 Scm³/min of carbon monoxide for three times . The values with hydrogen are again the higher shown in Figure III.68; the other curve show still good performance but decreasing at each load cycle. The micro-tubular cells seem to have great compatibility with

carbon monoxide fuel but reducing the performance after many cycles and after hours of operation under the carbonaceous gas.

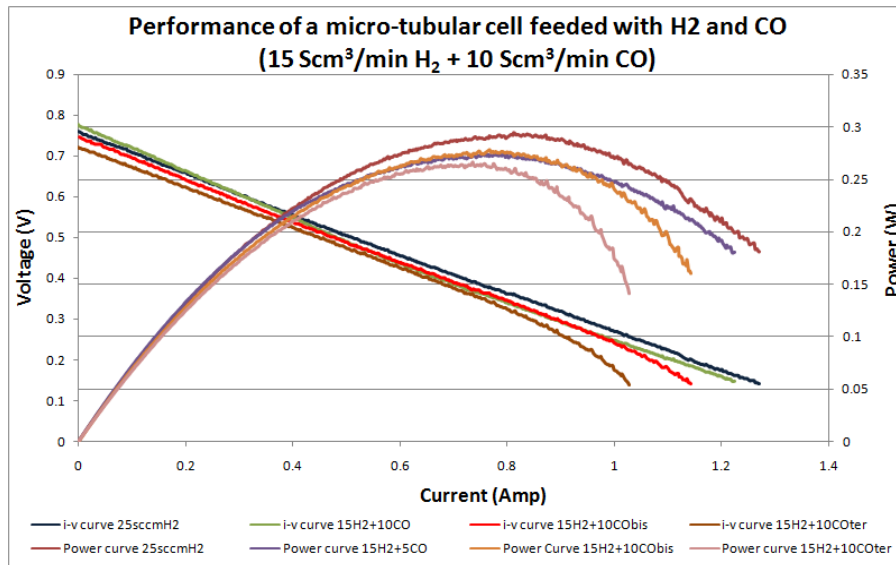


Figure III. 68: Fuel cell performance with hydrogen and carbon monoxide (10 Scm³/min)

This condition is more clearly shown in Figure III.69 where all the curves of the load cycles are put together; it is plainly visible as the performance decrease at each electric load cycle applied.

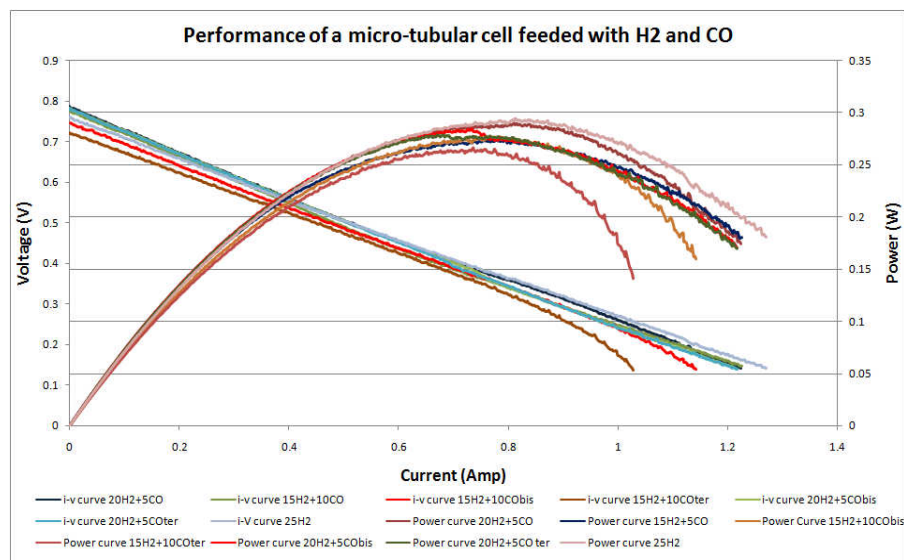


Figure III. 69: Comparison of electrochemical performance under diverse load cycles and with CO fuel.

Subsequently, the performance of a fuel cell was measured at 550°C, before with 25 Scm³/min of hydrogen and after with gas mixture of hydrogen and methane with presence of methane growing proportionally with the reducing presence of hydrogen. The Figure III.70 shows the current-voltage (I-V) curve and the Current-Electric Power Curve measured with 25 Scm³/min of hydrogen and after with a mixture of 20 Scm³/min of hydrogen and 1 Scm³/min of methane: regulating properly the temperature of the bubbler is introduced steam on the gas mixture to satisfy the S/C = 2-3. For a stoichiometric reaction from 1 Scm³/min of methane are produced 4 Scm³/min of H₂. The values with hydrogen are the higher shown in Figure III.70; is clearly visible as the other curve are superimposable but with reducing performance at each electrical load cycle. The Figure III.71 shows the performance for a gas mixture of 15 Scm³/min of hydrogen and 2.5 Scm³/min of methane. In this case the difference between the performance of each electrical load cycle is much more pronounced, with reduced OCV values and power production. Finally, the Figure III.72 shows the performance for a gas mixture of 5 Scm³/min of hydrogen and 5 Scm³/min of methane. These curves show clearly the strong performance reduction caused by carbon deposition phenomena.

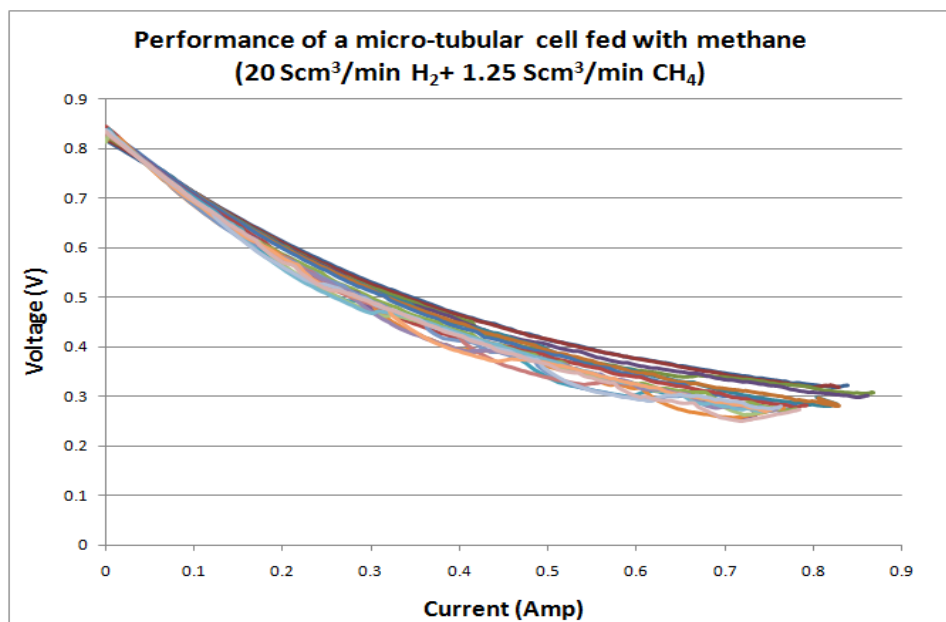


Figure III. 70: Comparison of electrochemical performance under 20 load cycles, with 1 Scm³/min of CH₄

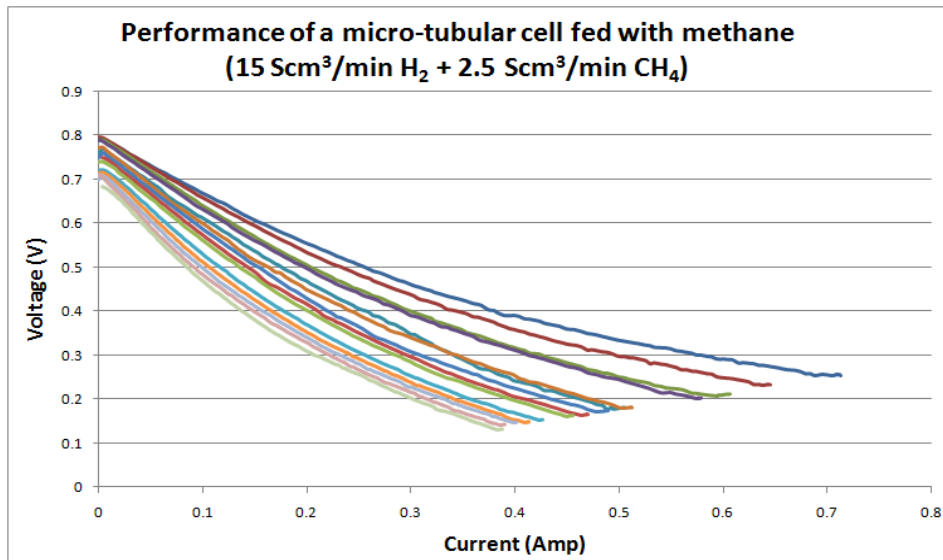


Figure III. 71: Comparison of electrochemical performance under 15 load cycles, with 2.5 Scm³/min of CH₄

Figure III.73 shows a recapitulation of the micro-tubular SOFC electrochemical performance fed with increasing volume flows of methane. It is clearly shown the presence of the carbon deposition phenomena. For each volume flow of methane used is reported the maximum and minimum I-V curve.

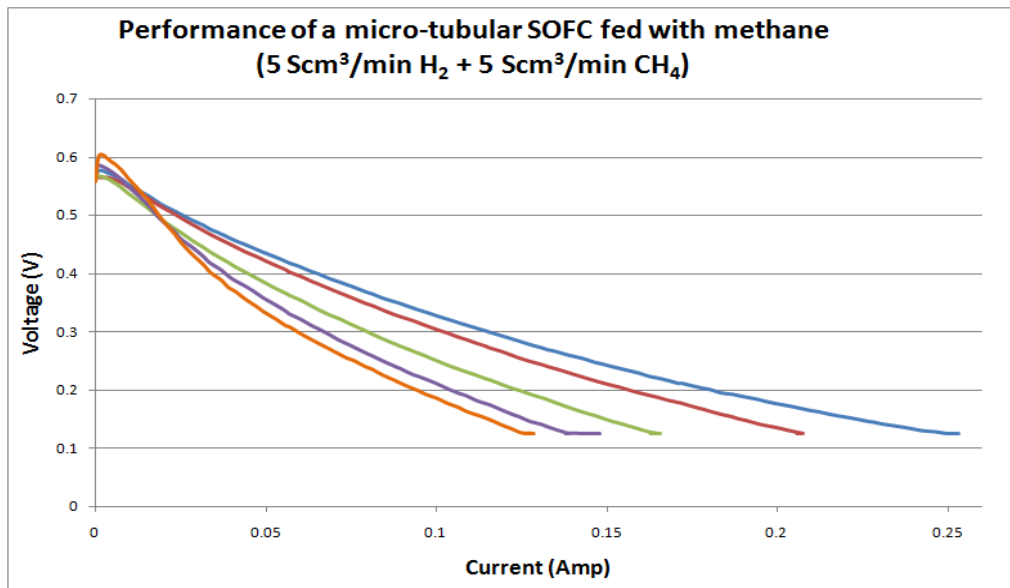


Figure III. 72: Comparison of electrochemical performance under 5 load cycles, with 5 Scm³/min of CH₄

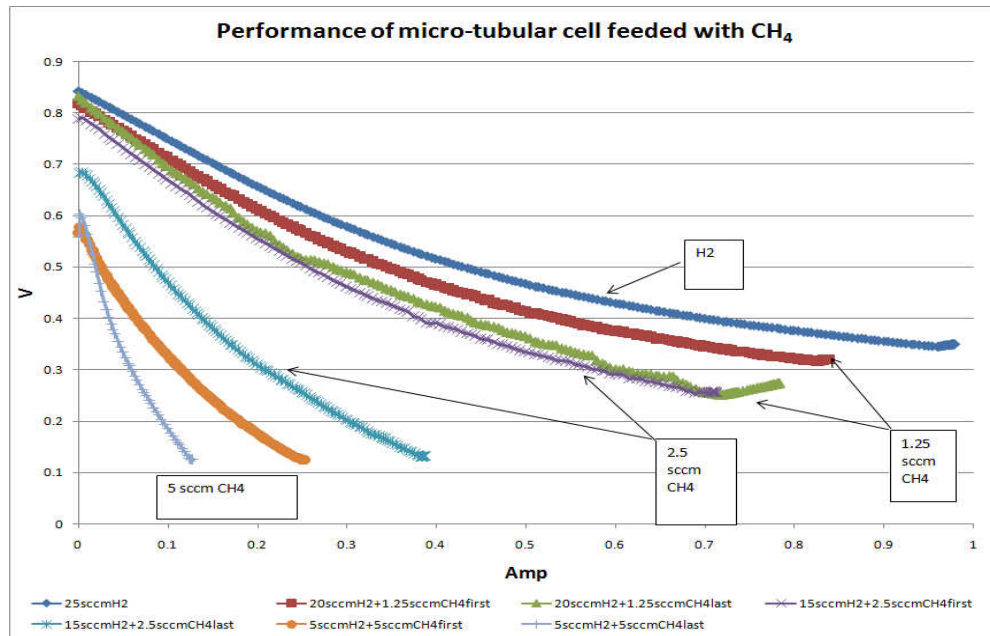


Figure III. 73: Recapitulation of SOFC performance fed with increasing volume flow of methane.

The figure III.74 shows the performance of the SOFC at constant current in order to measure the long term resistance and degradation of the ceramic materials and the resistance at the carbon deposition phenomena. The fuel gas mixture is composed of 20 Scm³/min of hydrogen and 5 Scm³/min of CO with enough steam produced in the bubbler to maintain a S/C ratio of 2-3. After about 3 hours the performance suddenly decreases (carbon deposition). Subsequently has been interrupted the CO feeding, leaving the cell only with 25 Scm³/min of hydrogen.

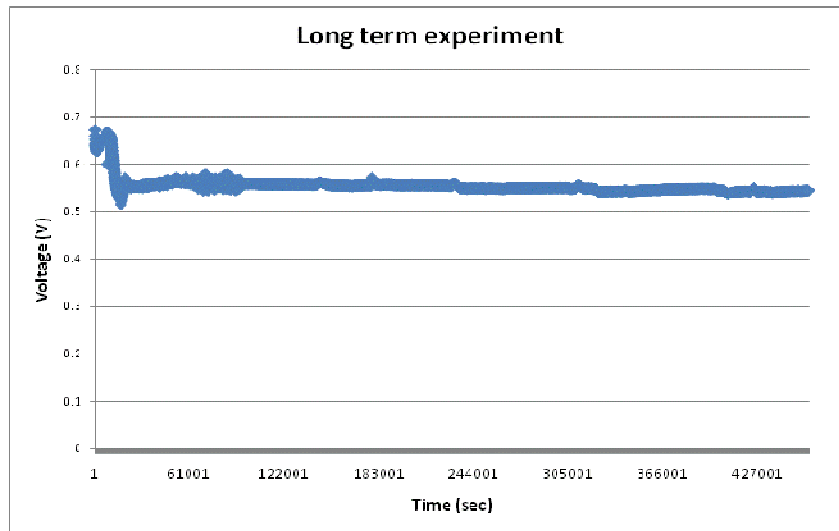


Figure III. 74: Long term experiment of a SOFC fed with a mixture of 20 Scm³/min hydrogen and 5 Scm³/min of CO with S/C =2-3and, after the first part, only with 25 Scm³/min of hydrogen.

Figure III.75 shows the long term performance of a SOFC fed by 25 Scm³/min of hydrogen obtained drawing a constant value of current from the cell. In this case, after each day of constant current drawing, has been measured the I-V performance of the cell. The figure clearly shows as after each electric load cycle the performance in the day after is lower than the day before. So the application of the electric load cause a degradation of the SOFC performance, especially if the lower voltage obtained is lower than 0.15 V. At constant current, degradation of 3% for 100 hours was registered.

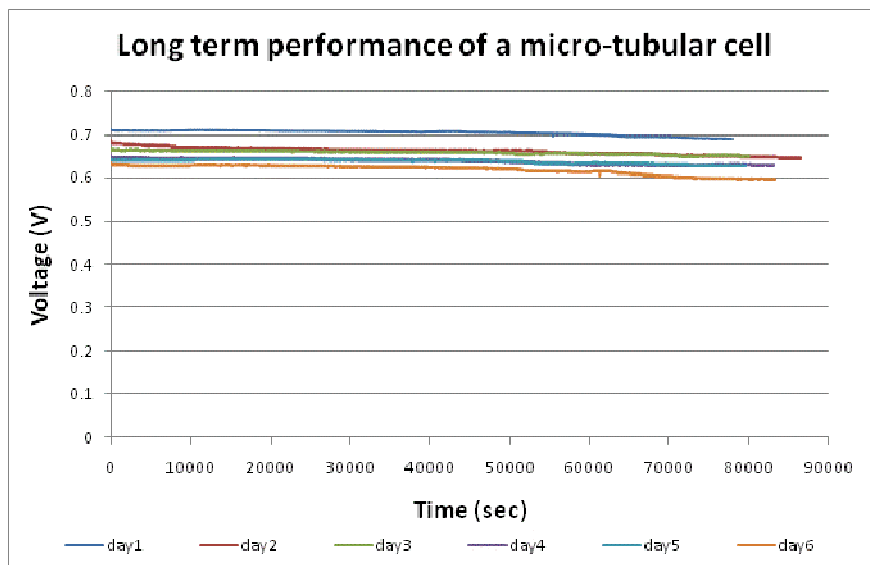


Figure III. 75: Long term experiment of a SOFC fed only with 25 Scm³/min of hydrogen.

3.6.10. Experimental Results of the bigger micro-tubular SOFC test

Different flow rates of hydrogen were employed, from 15 Scm³/min to 100 Scm³/min, at varying temperature, from 750 °C to 900 °C, in order to measure the electrochemical performance of the bigger micro-tubular SOFC.

Single cells were employed for these experiments. The cells used were 12 cm long (5 cm of reactive area length) with a 0.9 cm diameter for an active cell area of 14.1 cm².

As expected, the Figure III.76 shows an increase in power output with increasing fuel flow: at 750 °C and for a fuel volume flow of 100 Scm³/min of H₂, the maximum power density is 50 mW/cm² while, for a fuel volume of 15 Scm³/min, the maximum power density is 0.40 mW/cm². The rate of increase doesn't seem to be prominent and there is no difference at various flow rate.

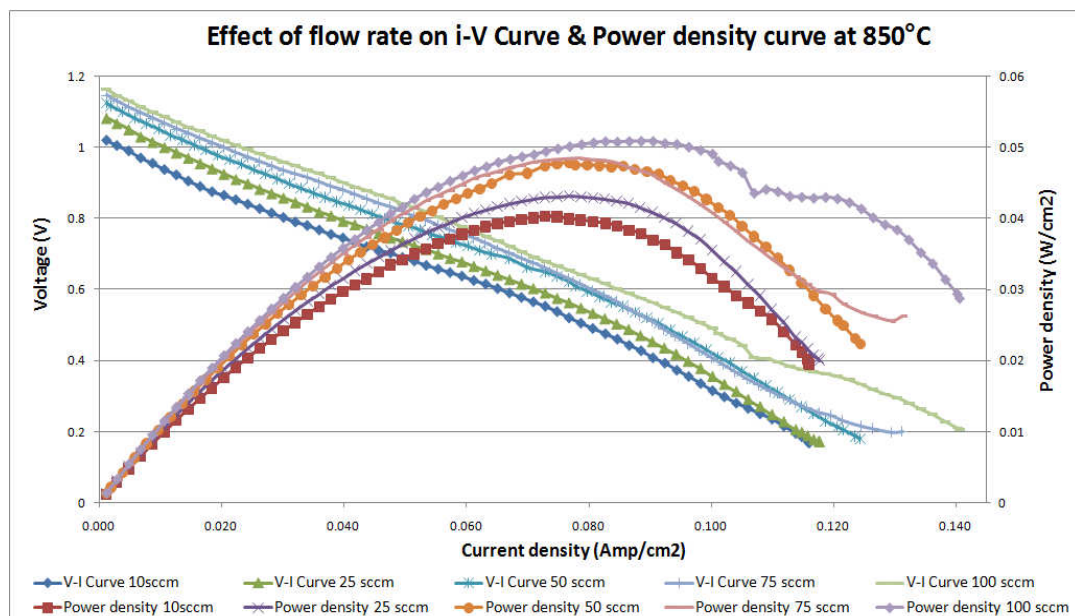


Figure III. 76: Current Density-Voltage curve and Current Density-Power Density curve at 850 °C for different H₂ volume flow rates

Figure III.77 shows SOFC's performance at 900°C while figures III.78 and III.79 report the same current density-voltage and current density-power density curves, evaluated anyway at 800°C and 750°C. The values obtained at 900 °C, though higher than at 850 °C, cannot be used in the real operation because the melting point of the silver wires is only 960°C, too close of the operating temperature, causing a decrease in the performance in the long term running.

In general the power density for different volume flows, at constant temperature, has not so evident variation as happened with the smaller micro-tubular cell.

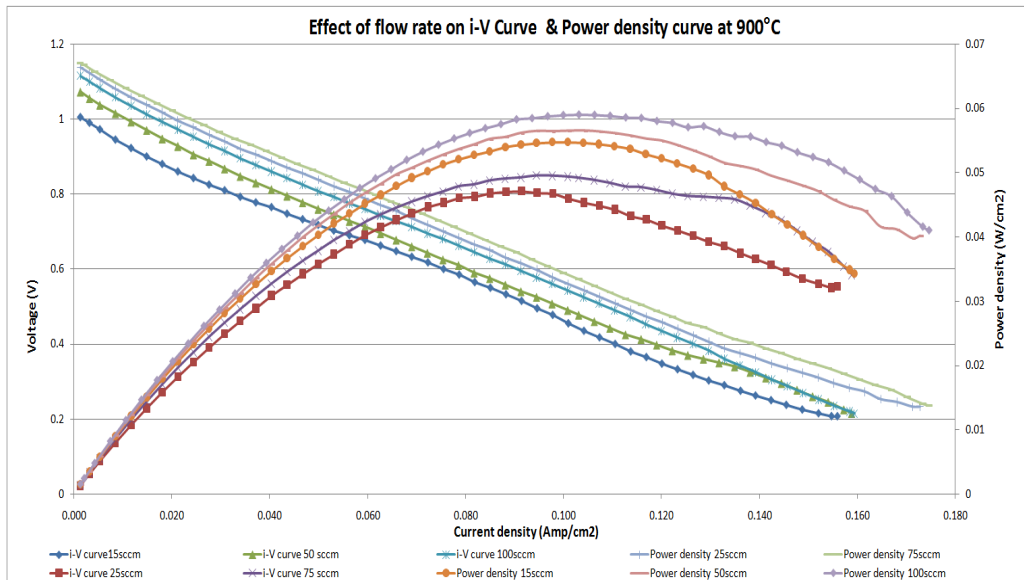


Figure III. 77: Current Density-Voltage curve and Current Density-Power Density curve at 900 °C for different H₂ volume flow rates

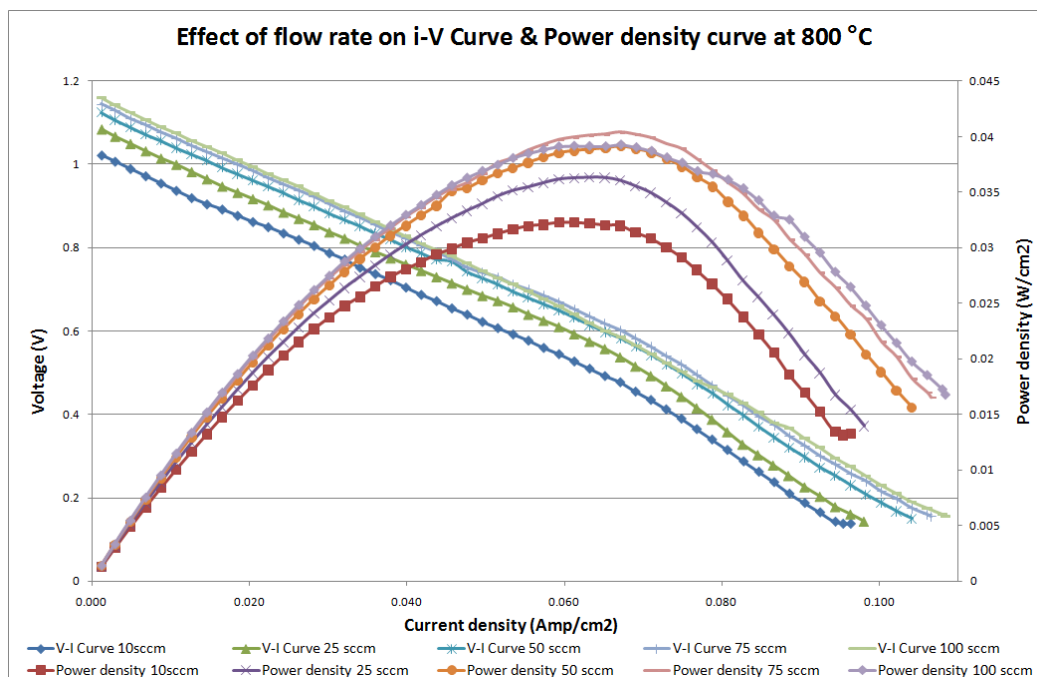


Figure III. 78: Current Density-Voltage curve and Current Density-Power Density curve at 800 °C for different H₂ volume flow rates

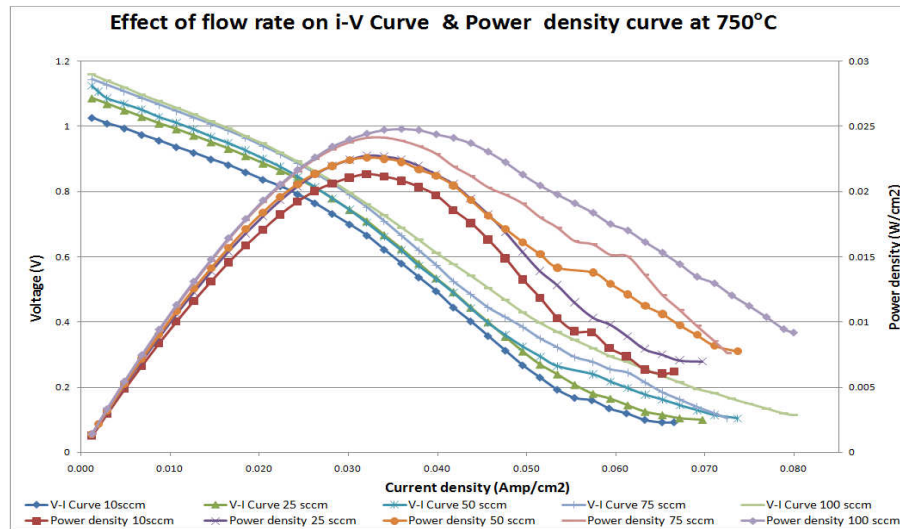


Figure III. 79: Current Density-Voltage curve and Current Density-Power Density curve at 800 °C for different H_2 volume flow rates

The maximum power density increases of about 3 times, changing the temperature from 750 °C to 900 °C and of about 2.5 times, from 750 °C to 850 °C.

3.6.11. Effect of temperature on SOFC's electrochemical performance at different flow rate.

In the next figures is reported the trend of the I-V curves and the electric power curves of a single fuel cell valued at constant hydrogen volume flow and at different temperatures. The trend shows behavior substantially different depending on whether use low or high volume flow.

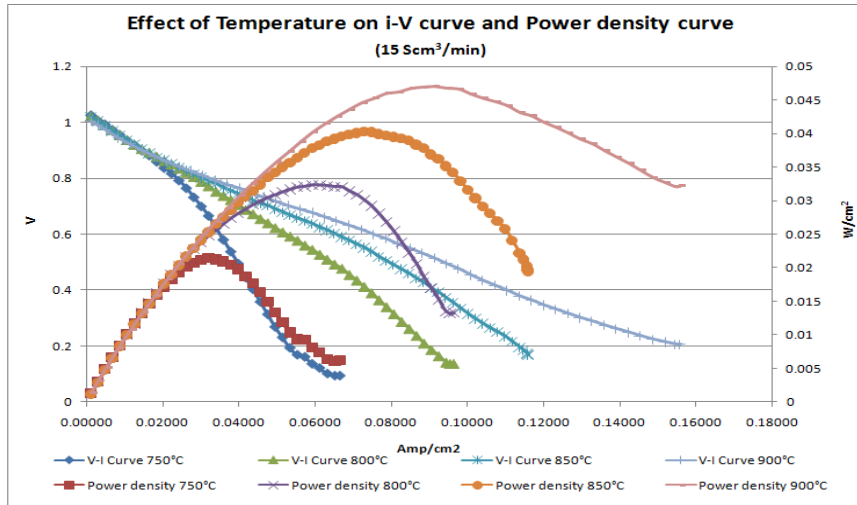


Figure III. 80: Current Density -Voltage and Current Density – Electric Power Density curves at constant volume flow (15 Scm³/min) and at 750°C, 800°C, 850 °C and 900°C.

The performance of the bigger micro-tubular SOFC is much more affected by the temperature that by the fuel volume flow. The figures clearly show the differences in the maximum power and the various values of the current corresponding to the maximum power.

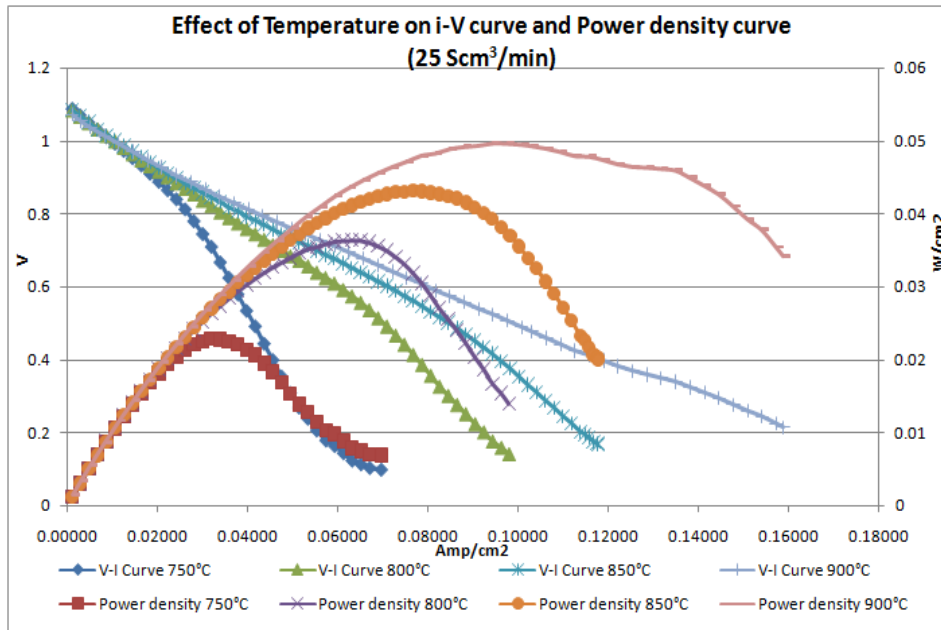


Figure III. 81: Current Density -Voltage and Current Density – Electric Power Density curves at constant volume flow (25 Scm³/min) and at 750°C, 800°C, 850 °C and 900°C.

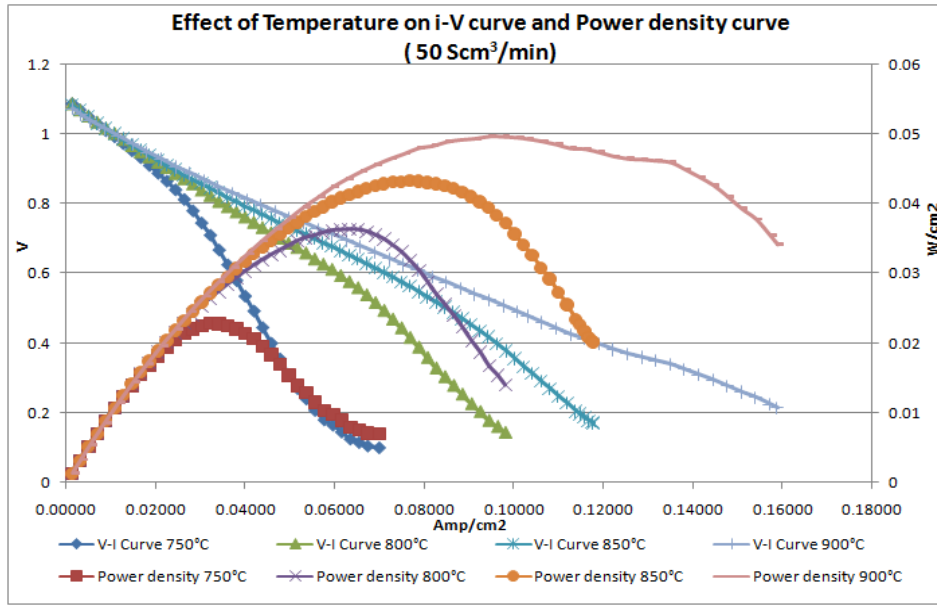


Figure III. 82: Current Density -Voltage and Current Density – Electric Power Density curves at constant volume flow (50 Scm³/min) and at 750°C, 800°C, 850 °C and 900°C.

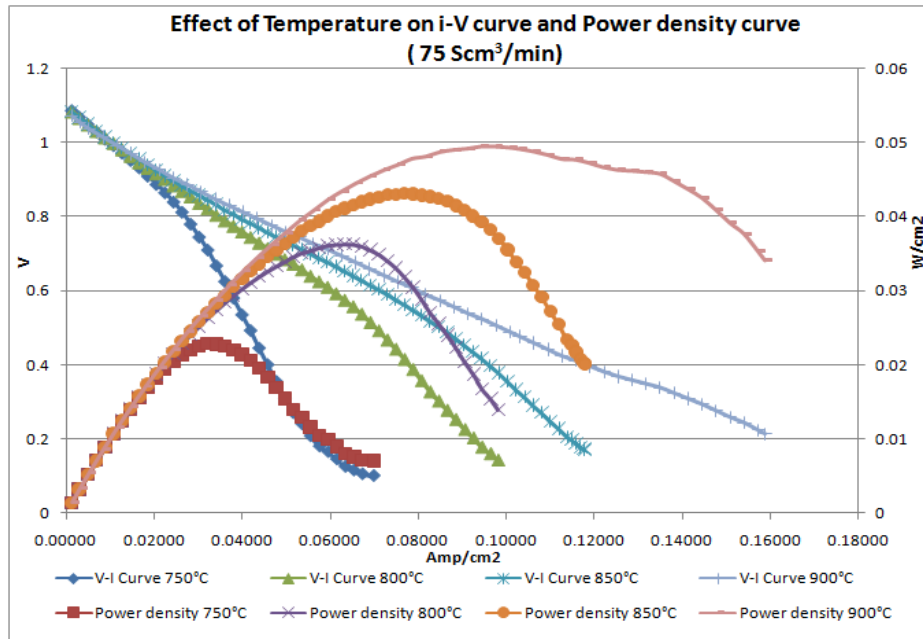


Figure III. 83: Current Density -Voltage and Current Density – Electric Power Density curves at constant volume flow (75 Scm³/min) and at 750°C, 800°C, 850 °C and 900°C.

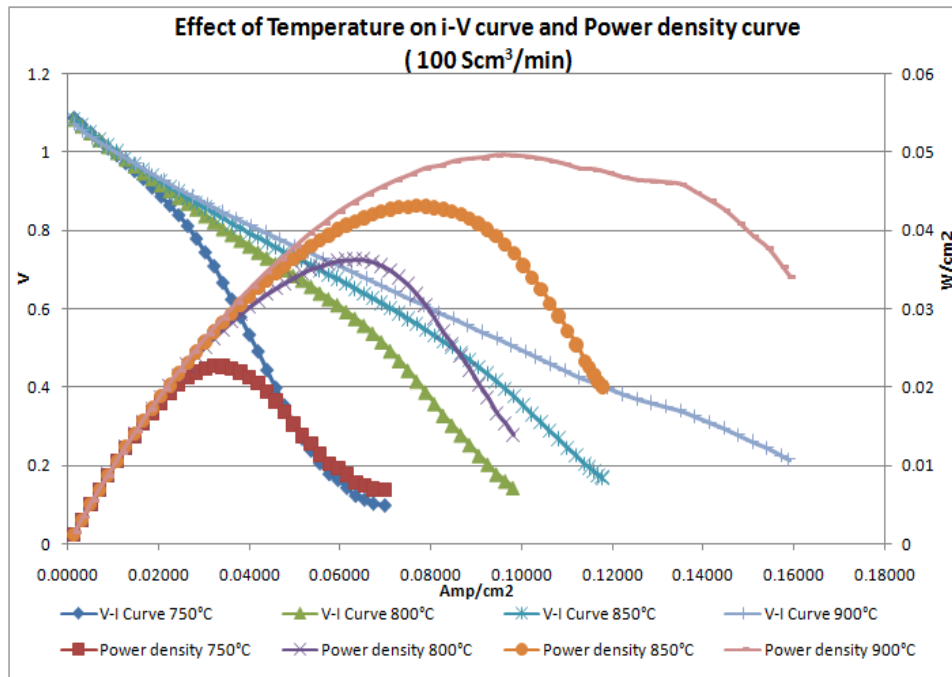


Figure III. 84: Current Density -Voltage and Current Density – Electric Power Density curves at constant volume flow (100 Scm³/min) and at 750°C, 800°C, 850 °C and 900°C.

3.6.12. Effect of temperature and flow rate on Open Circuit Voltage, Current and Power Density supplied by the SOFCs.

As mentioned in the paragraph 3.6.6, when the partial pressure of hydrogen is increased the OCV value will be expected to increase and this is confirmed by the result of the experimental activities conducted on the bigger micro-tubular SOFC.

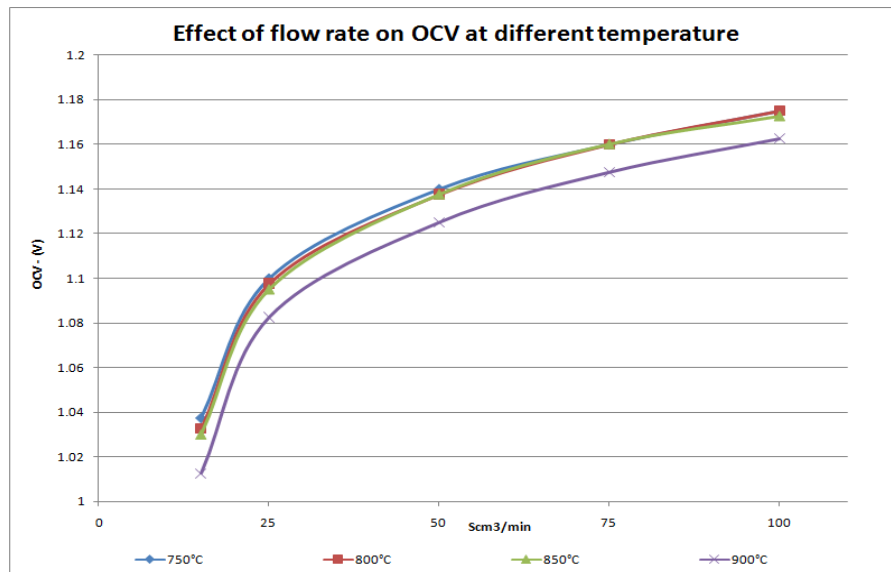


Figure III. 85: Effect of flow rate on OCV at different temperature

Figure III.86 show the effect of temperature on the Open Circuit Voltage for different value of the hydrogen volume flow. As can be seen from the graph below the open circuit voltage has the expected downwards trend with temperature for all the different flow rate of fuel.

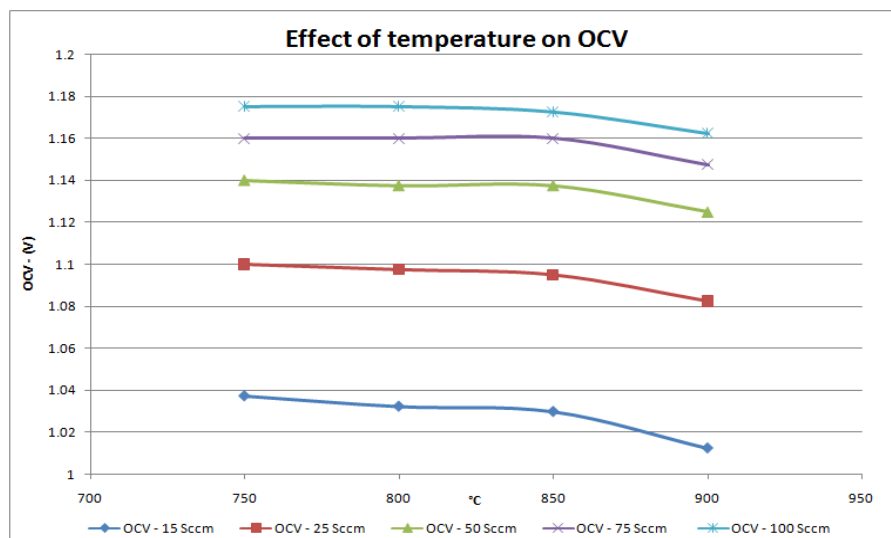


Figure III. 86: Effect of temperature on OCV for different hydrogen volume flow

Differently of the smaller micro-tubular SOFC the relationship between increasing temperature and increasing current is not exponential, as expected. Finally, the effect of increasing hydrogen flow rate on the current and the power supplied by the cell at 0,7 volts,

show an increase in current and power output with increasing fuel flow rate. No falling off effect is noted at the higher fuel flow rates.

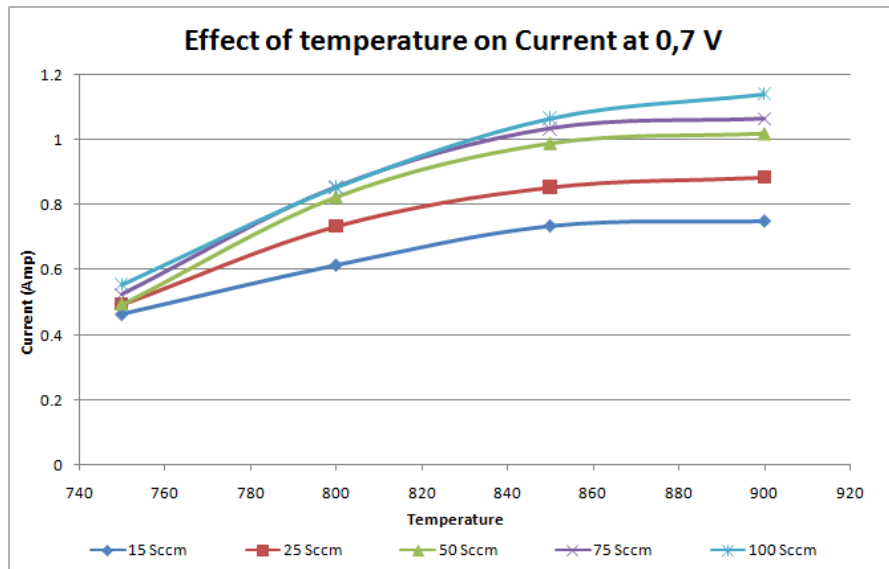


Figure III. 87: Current supplied by the fuel cell at 0.7 V, at different temperature and for different H₂ volume flow.

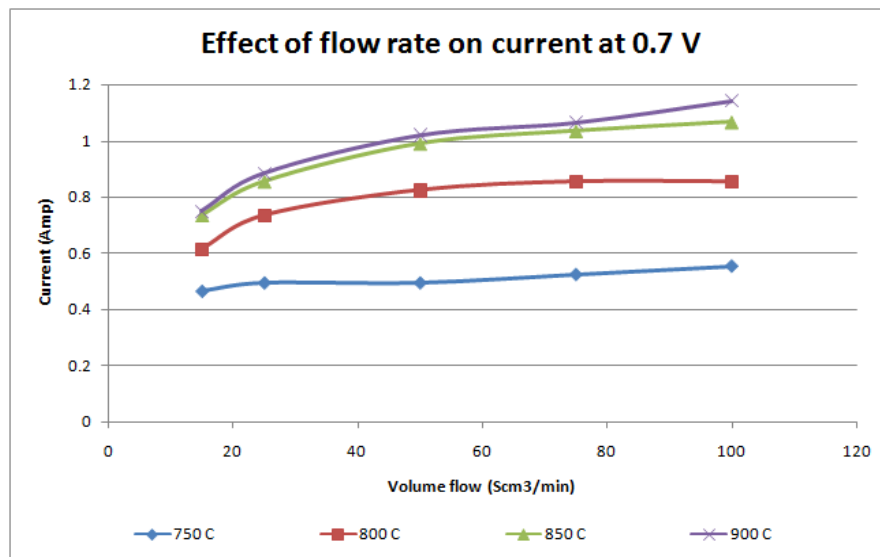


Figure III. 88: Current supplied by the cell at 0.7 V, at different H₂ volume flow and for different temperature.

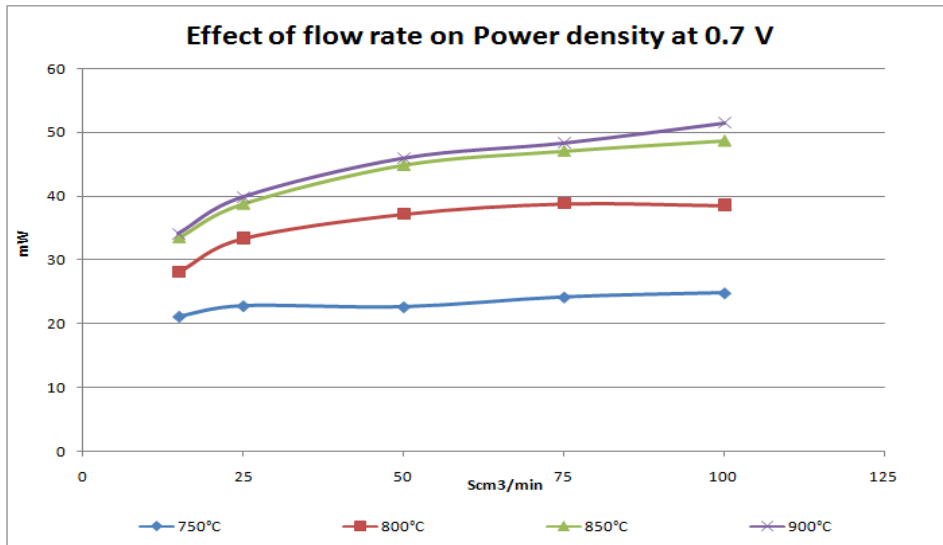


Figure III. 89: Trend of Power Density at 0.7 V for different H₂ volume flow and for different temperature.

3.6.13. Efficiency and fuel utilization

The figure III.89 shows the trend of the electrical efficiency versus the fuel utilization factor, evaluated using the current I produced by the cell and the molar flow of hydrogen provided to the cell. Here, it is clearly shown as at the higher flow rate correspond the lower electrical efficiency. The maximum η_{el} is 5% at 100 Scm³/min and less than 23% at 15 Scm³/min with a fuel utilization factor of 55%.

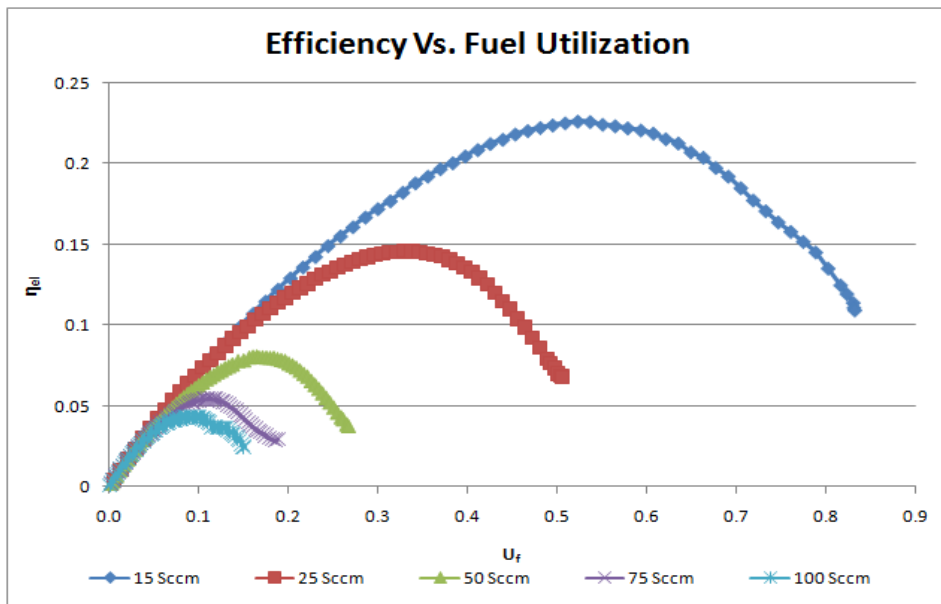


Figure III. 90: Efficiency of fuel cell at 550 °C for different fuel flow rates.

Besides the electrical efficiency reported in Figure III.89, it is possible to obtain the gross electrical efficiency taking in count the quote of the inlet fuel not reacted that could be used to produce additional electrical energy. The figure III.90 shows the gross electrical efficiency versus the fuel utilization factor. In this case the maximum efficiency, at 55% of fuel utilization, is around 40% at 15 Scm³/min.

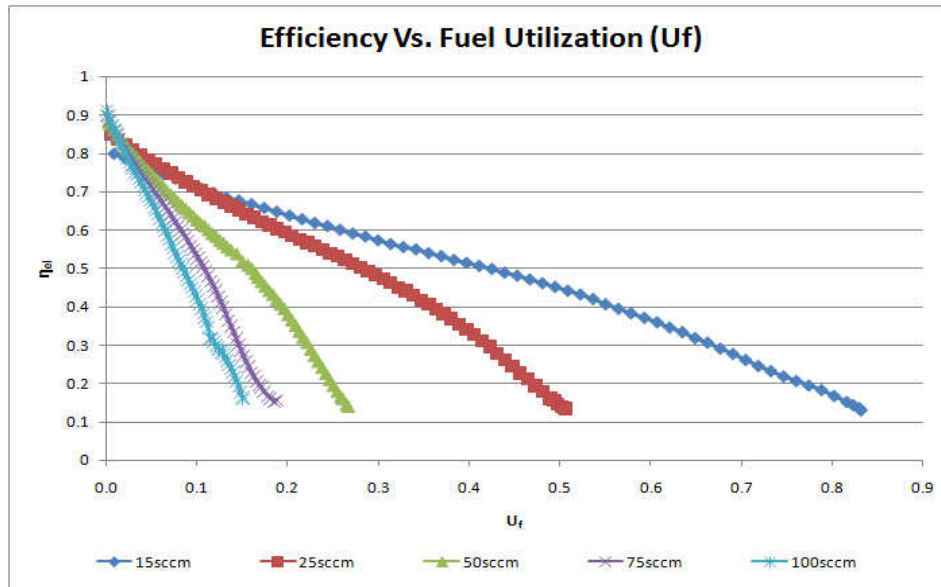


Figure III. 91: Gross electrical efficiency, calculated taking in count the real amount of fuel that react on the cell

3.6.14. Conclusion

Micro-tubular SOFCs were successfully fabricated to dimensions of 1.8 mm diameter, 1.2 cm length using traditional extrusion techniques [11]. Electrochemical testing of micro-tubular SOFCs 1.8 has been conducted successfully in the intermediate temperature range under 600°C and at higher temperature (750-900 °C).

The results of the experimental activities conducted at the Colorado School of Mines show significantly higher performance for the SOFCs realized with GDC electrolyte and with a cermet anode composed of NiO and GDC powders. The lower operating temperatures (550°C) allow small start-up times and greater simplicity in the "sealing" of the various components of the stack. The maximum power densities for temperatures between 450 °C and 550°C were between 0.263 W/cm² and 1.310 W/cm². This means that a stack of 3 x 3 cell arrangement could have a volume of 1 cm³, and could possibly generate over 10 W at 550°C. This power density performance would be excellent for a SOFC system.

Tests conducted with different gas confirm the ability of the "Ceria" to inhibit the phenomenon of carbon deposition on the anode side. It should be remembered, however, as the presence of nickel on the anode is still the main obstacle to the possibility of direct feed these types of fuel cells with carbonaceous fuels. Tests conducted in fact confirm the ability of the "ceria" to improve the performance of the cells when directly fed with hydrocarbons but this behavior is guaranteed for a number of hours still insufficient.

The results obtained show an increase in the electrical efficiency with decreasing fuel flow rate, with the increase falling off, as expected, at the lower fuel flow rates. An electrical efficiency of 37% with a fuel utilization of 73% was reached at 1-2 Scm³/min. At 5 Scm³/min an efficiency of 33% with a fuel utilization of 81% was measured.

The gross electrical efficiency shows clearly value much higher, with value that became higher for lower value of current production. For fuel utilization of 70% and fuel flow rate of 1-2 Scm³/min the efficiency is higher than 50%. At 5 Scm³/min is possible to reach a 40% of efficiency with a fuel utilization of 81%.

The smaller SOFCs shows a great variability of performance varying fuel flow rate and operation temperature. The maximum power density of 1.13 W/cm² reached at 25 Scm³/min and 550°C is much higher than the maximum power density of different solid oxide fuel cells manufactured with an yttria stabilized zirconia (YSZ) electrolyte and reported on literature. For this value the electrical efficiency of the cell is around 12.5% and the gross efficiency is 27%, with a fuel utilization of 46%; this value are not feasible for commercial purpose.

If the target of the fabrication process is the realization of a SOFC with high electrical efficiency, the only solution is the reduction of the fuel flow rate. In this case is possible to achieve an electrical efficiency of about 37% and a net efficiency higher than 50% with a fuel utilization of 73%. The maximum power density at 2 Scm³/min is 260 mW/cm².

At 5 Scm³/min the electrical efficiency is 33% and the net efficiency is higher than 40%, with a fuel utilization of 81% and a maximum power density higher than 600 mW/cm². Reducing the fuel flow rate of 5 time, the electrical efficiency increase from 12.5% to 33%, the gross efficiency change from 27% to 41%, the fuel utilization increase from 46% to 81% and the power density halves.

As expected, the open circuit voltage (OCV) fall with temperature while the effect of fuel flow rate is opposite of what predicted by the Nernst equation. In fact increasing the hydrogen

flow the OCV decrease. The cause of this behavior could be imputed to the nature of the electrolyte; in the case of GDC electrolyte is possible that the electronic conductivity is not so negligible, causing a difference between the theoretical and the real value.

The current output of the cell increases with increasing temperature as more oxygen ions pass through the cell per unit time. The amps and the power output also increase with increasing flow rate. Furthermore, at lower fuel flow rate, is clearly shown the effect of the concentration polarization while at higher flow rate the maximum current density is far away from anode and cathode limiting current density.

3.7. References

- [1]. Y. Funahashi et al., 2007. *Journal of Power Sources*, 163, 731 (2007).
- [2]. M.C. Williams et al., 2006. *Solid State Ionics*, 177, 2039 (2006).
- [3]. M. Masashi, H. Yoshiko, N.M. Sammes, 2000. *Solid State Ionics*, 135, 743 (2000).
- [4]. J. Turner, M.C. Williams, K. Rajeshwar, 2004. *Electrochem. Soc. Interface*, 13-3, 24 (2004).
- [5]. K. Kendall, M. Palin, 1998. *Journal of Power Sources*, 71, 268 (1998).
- [6]. X. Zhou et al., 2006. *Journal of Power Sources*, 279, 162 (2006).
- [7]. S. Livermore, J. Cotton, R. Ormerod, 2000. *Journal of Power Sources*, 86, 411 (2000).
- [8]. U.B. Pal, S. Gopalan, W. Gong, 2004. FY 2004 Annual Report, Office of Fossil Energy Fuel Cell Program, 262(2004).
- [9]. J. Pusz, A. Mohammadi, N.M. Sammes, 2006. *Journal of Fuel Cells*, In Press, (2006).
- [10]. N.M. Sammes, Y. Du, R. Bove, 2005. *Journal of Power Sources*, 145, 428 (2005).
- [11]. T. Suzuki et al., 2006. *Journal of Power Sources*, 160, 73 (2006).

- [12]. T. Suzuki et al., 2006. *Journal of Electrochem. Soc.*, 153, A925 (2006)
- [13]. J. Staniforth, PhD Thesis: THE USE OF BIOGAS TO POWER A SMALL TUBULAR SOLID OXIDE FUEL CELL (2000, Keele University)
- [14]. Singhal S.C., Kendall, K., *High temperature Solid Oxide Fuel Cells*, ed. Elsevier. 2003.
- [15]. Caine. M. Finnerty , PhD Thesis: The catalysis and electrical performance of nichel-based/zirconia fuel reforming anodes in solid oxide fuel cells running on methane – Keele University.
- [16]. D. Huang, K.R. Venkatachari and G.C. Stangle, *J. Mater. Res.*, 10, (1995) 762-773
- [17]. M.V. Twigg, *Catalyst Handbook*, 2th Edition, Manson Publishing, 1996
- [18]. S.H. Clarke, A.L. Dicks, K. Pointon et al., *Catalysis Today*, 38, (1997), 411-423
- [19]. K. H. Cunningham, C. M. Finnerty and R. M. Ormerod, *Proc. 5th Int. Symp. on SOFCs, the electrochemical Society*, vol 97-48, (1997), 973-982. I
- [20]. E . Riensche, P . Cremer, J. Meusinger, *Proc. 3th European Solid Oxide Fuel Cell Forum*, (1998), 193 -204.
- [21]. A. Scholten, S. T. van Schaaik and Ir. M. van Driel, *Proc. 3th European Solid Oxide Fuel Cell Forum* , (1998), 205-216.
- [22]. D. Duprez, M. C. Demicheli, P. Marecot, J. Barbier, O. A. Ferretti and E. N. Ponzi, *Journal of Catalysis*, 124 (1990) 324-325.
- [23]. T. Borowieckj and A. Gotebiowski, *Catalysis Letters*, 25 (1994) 309-313.
- [24]. H. M. Swaan, V. C. H. Kroll, G. A. Martin and C. Mirodatos, *Catalysis Today*, 21(1994)571-578.
- [25]. L.M. Aparicio, *Journal of catalysis*, 165, (1997), 262-274.

- [26]. V. R. Choudhary and A. M. Rajput, *Ind. Eng Chem.Res.*, 35, (1996), 3934-3939
- [27]. V. R. Choudhary, B. S. Uphade and A. S. Mamman. *Catalysis Letters*, 32(1995), 387-390.
- [28]. L. Zhang, J. Lin and Y. Chen, *J. Chem. Soc. Faraday Trans.*, 88, (1992), 2075-2078.
- [29]. Yamazaki, K. Tomishige and K. Fujimoto, *Applied Catalysis A: General*, 136, (1996), 4956.
- [30]. G. A. Somorjai, *Introduction to Surface Chemistry and Catalysis*, John Wiley and Sons Inc., New York 1994 .
- [31]. J R. Rostrup-Nielsen and L. J. Christiansen, *J Catalysis*, 126, 2 (1995) 381-390.
- [32]. S. Tsang, J. B. Claridge and M. L. H. Green, *Catalysis Today* 23 (1995) 3-15.
- [33]. X. Li, K. Tomishige and K. Fujimoto, *Catalysis Letters*, 36, (1996), 21-24.
- [34]. A. M. Maitra, *Applied Catal.* 104, (1993), 11.
- [35]. I.V. Yentekths, Y. Jiang, S. Neophytides, S. Bebelis and C.G. Vayen. *Proc. 3rd Int. Symp. on SOFC* (1993) 904 -912.
- [36]. C. H. Bartholomew, *Catal. Rev. ScL Eng*, 24, (1982), 68-112. .
- [37]. D. L. Trimm, *Catalysis Today*, 37, (1997), 233-238.
- [38] R T. K. Baker, M. S. Kim, A. Chambers, C. Park and N. M. Rodriguez, *Studies in Surface Science and Catalysis*, 111, (1997), 99-109.
- [39]. J. R. Rostrup-Nielsen, *Symposium on the Science of Catalysis and its Application in Industry, FPDIL, Sindri, February, 22-24, (1979), paper 39.*
- [40]. J. Zielinski, *Journal of Molecular Catalysis*, 79, (1993), 187-198.

- [41] Sh. K. Shaikhutdinov, V. I. Zaikovskii and L. B. Avdeeva, *Applied Catalysis A : General*, 148 , (1996), 123-133.
- [42]. J. W. Snoeck, G. F. Froment, M. Fowles, *Journal of Catalysis*, 169, (1997), 240-249.
- [43]. G. G. Kuvshinov, Y. I Mogilnykh, D.G. Kuvshinov, V. I. Zaikovskii and L. B. Avdeeva, *Carbon*, 36, 1-2, (1998), 87-97.
- [44]. R. T. Yang, 3. P. Chen, *Journal ofCatalysis*, 1 15, (1989), 52-64.
- [45]. S. C. Tsang, J. B. Claridge and M. L. H. Green, *Catalysis Today*, 23, (1995), 3-15.
- [46]. A. V. Mkliaailova, A. M. Alekseev and V. S. Beskov, *Theoretical foundations of chemical Engineering*, vol. 30, (1996), 174-178.
- [47]. A. P. E. York, J. B. Claridge, A. J. Brungs, S. C. Tsang and M. L. H. Green, *Chemical Communication*, (1997), 39-40.
- [48]. M.Mogensen et al., Proceedings of 17th Riso International Symposium, (1996), 77-100.
- [49]. J. Misuzaki et al., *Journal of electrochemical Soc.*, 14, (1994), 2129-2134.
- [50]. J.Divisek et al., *Journal of Power Sources*, 49, (1994), 257-270
- [51]. R.J.Aalberg et al., Proc. 5th Int. Symp. On SOFCs, The Electrochemical Society, vol 97-18, (1997), 557-564.
- [52] M. Mogensen, High Temperature electrochemistry, Riso, (1993), 117-133.
- [53]. R.J. Alberg et al., 3th European Solid oxide Fuel Cell Forum, Nantes France, (1998), 291-300.
- [54]. T. Setoguchi et al. *Journal of Electrochemistry Soc.* 139, (1992), 2875-2880.
- [55]. E. Achenbach et al., *Journal of Power Sources*, 52, (1994), 283-288.

- [56]. V.D. Belyaev, *Applied Catalysis A: General*, 133, (1995), 47-57.
- [57]. K.Eguchi et al., *Denki Kagaku*, 6, (1996), 596-601.
- [58]. Yanhai Du, PhD Thesis: Fabrication and Characterization of Micro-Tubular Solid Oxide Fuel Cells, University of Waikato, New Zealand (2004).
- [59]. *FUEL CELL Fundamentals*, R. O'Haire, S. Cha, W. Colella, F. Prinz.- Wiley (2005).